

The relation between natural fracturing
and stress heterogeneities in deep-seated
crystalline rocks at Soultz-sous-Forêts
(France)

Benoît Christian Valley

Dissertation ETH Number 17385

The relation between natural fracturing and stress heterogeneities in deep-seated crystalline rocks at Soultz-sous-Forêts (France)

A dissertation submitted to the
SWISS FEDERAL INSTITUTE OF TECHNOLOGY ZURICH

for the degree of
DOCTOR OF SCIENCES

presented by

BENOÎT CHRISTIAN VALLEY

Dipl. en Sciences de la Terre, Université de Neuchâtel, Switzerland
born March 2, 1979
citizen of Chevenez (JU), Switzerland

accepted on the recommendation of

Prof. Dr. Simon Löw, examiner
Dr. Keith F. Evans, co-examiner
Dr. Albert Genter, co-examiner
Dr. François H. Cornet, co-examiner

2007

Copyright © 2007 Benoît Christian Valley
Group of Engineering Geology (ETH Zurich)
All rights reserved.

The relation between natural fracturing and stress heterogeneities in deep-seated crystalline rocks at Soultz-sous-Forêts (France)

Doctoral defense: 21/08/2007
Final manuscript: 03/04/2008

Published and distributed by:

Group of Engineering Geology
Institute of Geology
Swiss Federal Institute of Technology (ETH) Zurich
ETH Hoenggerberg, HIL
8093 Zurich
Switzerland
<http://www.erdw.ethz.ch/>

Printed in Switzerland by:

ETH Reprozentrale Hönggerberg
HIL C45
8093 Zurich
Switzerland

La qualité d'un modèle scientifique n'est jamais, en dernière analyse, une affaire de statistique. (...) Pour un géomètre, le meilleur test reste (...) le jugement de ce que son oeil transmet à son cerveau.

Benoît Mandelbrot (1975, p. 116)

Contents

List of Figures	xi
List of Tables	xv
Notations	xvii
Abstract	xxi
Résumé	xxiii
Zusammenfassung	xxvii
Acknowledgements	xxxix
1 Introduction	1
1.1 Motivations	1
1.2 Objectives	3
1.3 Structure of the thesis	4
2 Foundation Studies	5
2.1 The Soultz-sous-Forêts Geothermal project	5
2.2 Geological context and tectonic settings	8
2.2.1 General morphology of the Rhine Graben	8
2.2.2 Emplacement of the Soultz granite in Visean time	10
2.2.3 Tectonic history of the Soultz granite	13
2.2.4 Various tectonic models for the Cenozoic formation of the URG	17
2.3 The 5 km deep borehole image data set at Soultz-sous-Forêts	30
2.3.1 Acoustic imaging measurement principle	30
2.3.2 Technical information on the 3 deep boreholes	33
2.3.3 Description of the images acquired in the deep boreholes of Soultz-sous-Forêts	34
3 Multi-scale fracturing from borehole images analyses	41
3.1 Abstract	41
3.2 Introduction	41

3.3	Background	43
3.4	Description of the data set	45
3.4.1	Ultrasonic borehole images	45
3.4.2	Measurements of fracturing on wellbore images	47
3.5	Analysis of the individual fractures characteristics	48
3.5.1	Clustering of the fracture data to derive orientation sets	50
3.5.2	Spacing distributions	52
3.5.3	Variogram analysis on fracture spacing	58
3.5.4	Fracture correlations	58
3.5.5	Fracture size	62
3.6	Analysis of the fractures zones from wellbore images	65
3.7	Synthesis	72
3.8	Conclusions	74
4	State of stress from wellbore failure and hydraulic measurements	77
4.1	Abstract	77
4.2	Introduction	78
4.3	Background	79
4.3.1	Previous knowledge of the stress state at Soultz	79
4.4	Description of the data set	82
4.4.1	Ultrasonic borehole images	83
4.4.2	Description of wellbore failure	84
4.5	Interpretation of the wellbore failure observations to constrain the stress state	86
4.5.1	Principal stress orientation	86
4.5.2	Natural formation pressure	89
4.5.3	Vertical stress magnitude	89
4.5.4	Minimum horizontal stress magnitude	92
4.5.5	Maximum horizontal principal stress magnitude	95
4.5.5.1	Estimation of thermal stress component	96
4.5.5.2	Strength criteria and effective stress	100
4.5.5.3	Constraints on maximum horizontal principal stress magnitude imposed by wellbore failure	102
4.6	Additional Results	105
4.6.1	Constraints on the effective stress law for tensile failure	105
4.6.2	Evaluation of breakout geometry as a stress indicator	107
4.6.2.1	Depth of failure	109
4.6.2.2	Width of failure	112
4.7	Conclusions	118
5	Stress heterogeneities inferred from analysis of wellbore failure	121
5.1	Abstract	121

5.2	Introduction	122
5.3	Background	123
5.4	Presentation of the data	127
5.5	Analysis of variability of stress induced failure orientation	129
5.5.1	General variability in the orientation of stress indicators	129
5.5.2	Deviation of one principal stress from verticality and E-DITFs linkage	132
5.5.3	Variability with depth of the stress orientation indicators	134
5.5.4	Large scale stress variations	138
5.5.4.1	Large scale stress variations in the lower wells sections	138
5.5.4.2	Large scale stress variations in the upper wells sections	139
5.5.5	Small scale stress variations	144
5.5.5.1	Characteristics of DITF changes at natural fractures	144
5.5.5.2	E-DITFs parallel to natural fractures	145
5.5.5.3	Stress perturbation around fractures correlated between the wells	154
5.6	Stress-perturbing fractures	158
5.7	Conclusions	161
6	Conclusions and outlook	163
6.1	Multi-scale fracturing from borehole images analyses	164
6.2	Stress characterisation	165
6.3	Stress heterogeneities	168
6.4	Suggestions for improvements and further investigations	170
	Bibliography	173
	Appendix	195
A	First appendix - Typology of natural fractures characterised on UBI images	197
A.1	Some other reflection on significance of UBI-images	198
B	Second appendix - Variogram analysis of synthetic data	203
C	Third appendix - Methodology for fracture correlation	211
C.1	Description of the method	211
C.2	Complete example of correlation	212
C.3	Processing of the GPK3 and GPK4 data set	216
D	Fourth appendix - Stress around a wellbore	223

D.1	Stress transformation between principal stress, geographical and borehole coordinate system	223
D.2	Stress concentration around a wellbore	226
D.3	Thermal stress component	229
E	Fifth appendix - Strength and elastic properties of the Soultz granite	231
E.1	Abstract	231
E.2	Introduction and previous works	231
E.3	Sample description and preparation	233
E.4	Tests description	235
E.5	Calibration and corrections of E-modulus	236
E.6	Results and discussion	238
	E.6.1 Uniaxial compressive strength	238
	E.6.2 Yougn's modulus	238
E.7	Conclusions	241

List of Figures

2.1	Conceptual model of fracture zones in <i>Genter et al. (1998)</i>	6
2.2	West european Rift system	9
2.3	General structure of the Upper Rhine graben.	10
2.4	Map of the Upper Rhine Graben	11
2.5	Rhine Graben crosssections after <i>Brun et al. (1992)</i>	12
2.6	Rhine Graben crosssection going through Soultz-sous-Forêts	13
2.7	Synthesis of tectonic phases	17
2.8	Map of hercynian structures	19
2.9	Fault data from EPS1	20
2.10	Sedimentary filling of the Rhine Graben	21
2.11	Simple graben formation model after <i>Illies (1965)</i>	22
2.12	Stress history after <i>Illies (1975)</i>	23
2.13	Recent time movements in the Rhine Graben after <i>Illies and Greiner (1979)</i>	24
2.14	Cenozoic formation of the URG after <i>Villemain and Bergerat (1987)</i>	26
2.15	Cenozoic development of the URG after <i>Schumacher (2002)</i>	28
2.16	Description of the UBI tool principle	30
2.17	Example of UBI images	32
2.18	Characteristics of the three deep wells	34
2.19	Borehole trajectory and UBI data	36
2.20	Example of key-seat	39
3.1	Fault trace map of the URG	44
3.2	3D block diagram of the Soultz-sous-Forêts Area	46
3.3	Presentation of the entire fracture data set from GPK3 and GPK4	49
3.4	Result of the clustering process performed on the fracture data	52
3.5	Repartition of the sets and their type	53
3.6	Repartition of fracture sets versus depth	54
3.7	Spacing statistic of fracture sets	55
3.8	Variograms analysis of fractures spacings	59
3.9	Correlated fractures	61
3.10	Histogram of minimum radius of correlated fractures	63
3.11	Scheme for fracture size inferences	63
3.12	Computation of fracture radius	65

3.13	Fracture zone examples	67
3.14	Example of correlated fractures zones	68
3.15	Fracture zones and cross-section	69
3.16	Fracture zones and logs	72
3.17	Synthesis of the scale of features	73
4.1	Soultz site location	80
4.2	Examples of stress induced wellbore failure	85
4.3	Summary of wellbore failure observations in the borehole GPK3.	86
4.4	Summary of wellbore failure observations in the borehole GPK4	87
4.5	Circular histograms of breakout and A-DITF orientations along sub- vertical sections of GPK3 and GPK4	88
4.6	Estimation of the density profile for the sedimentary section	90
4.7	Estimates of the Sh_{min} profile	94
4.8	Temperature profile in GPK4 borehole	100
4.9	Constraints on SH_{max} magnitude	103
4.10	Constraints for the effective stress law for tensile failure (1)	106
4.11	Constraints on the effective stress law for tensile failure (2)	107
4.12	Analysis of breakouts depth of failure	111
4.13	Sensitivity of SH_{max} magnitude to the breakouts width	114
4.14	Results of the analysis of breakouts width	115
4.15	Results of the analysis of breakouts width with smoothing	116
4.16	Results of the analysis of breakouts width, expanded view	117
5.1	Borehole failure data for GPK3	127
5.2	Borehole failure data for GPK4	128
5.3	Orientation of stress induced failure	131
5.4	Offset angle between A-DITFs and E-DITFs	132
5.5	Computation of DITFs linkup angle	133
5.6	Power spectral analysis of orientation variations in GPK3	135
5.7	Power spectral analysis of orientation variations in GPK4	136
5.8	Correlation of the strike variations between 1450 and 2500 m	140
5.9	Long wavelength signal comparisons between GPK3 and GPK4	142
5.10	Comparison of gaps in wellbore failure between GPK3 and GPK4	143
5.11	Example of short wavelength variations	145
5.12	Terminations and transformations of DITFs	146
5.13	Terminations and transformations of DITFs	147
5.14	Simulation of E-DITFs parallel to natural fractures	149
5.15	Histogram of relative dip angles and dip directions	150
5.16	Fractures with parallel E-DITFs	152
5.17	Analysis of stress perturbation around correlated fractures	155
5.18	Model of the stress perturbation around a fault	157

5.19	Stress induced failure of a borehole going through a fault (1)	159
5.20	Stress induced failure of a borehole going through a fault (2)	160
5.21	Analysis of influencing fractures	161
6.1	Conceptual general organisation of faults in the URG	165
6.2	Stress characterisation at Soultz-sous-Forêts	167
6.3	Stress orientation in Central Europe	169
A.1	Open-Close concept for BHTV image	201
B.1	Schematic variogram	204
B.2	Variogram for synthetic data	205
B.3	Variogram for sorted synthetic data	206
B.4	Variogram for sorted synthetic data, one cycle	207
B.5	Variogram for sorted synthetic data, many cycles	208
B.6	Variogram for noisy synthetic multi-cycled data	209
C.1	Cross-hole fracture correlation process	213
C.2	Example of fracture correlation	214
C.3	Scatter plot of result of correlation	217
C.4	Fracture correlation with high differences in correlation index	219
C.5	Histogram of index of relative correlation	219
C.6	Correlated fracture between GPK3 and GPK4	220
C.7	Index of goodness of correlation for the 101 correlated fractures	221
D.1	Coordinate systems	224
D.2	Borehole stresses	227
E.1	Example of a test record	236
E.2	Test settings	237
E.3	Test results	239
E.4	Results in the view of alteration grade	240

List of Tables

2.1	UBI image quality classes	36
2.2	GPK3 UBI image quality	38
2.3	GPK4 UBI image quality	39
3.1	Abutting relations.	56
3.2	Spacing statistics	57
3.3	Description of the six type of fractures zone	66
3.4	List of correlated fractures zone in the upper part of the boreholes	70
4.1	Summary of UBI logging in GPK3 and GPK4	84
4.2	Maximum pressures recorded at the casing shoe during the stimulation injections of the three deep wells	93
4.3	Sensitivity of SH_{max} magnitude to the breakouts width	113
5.1	Summary of the power spectral density analysis	137
5.2	Relation of angle between natural fracture and E-DITFs and shear stress on fracture	148
A.1	Fracture typology	197
C.1	Example of fractures correlation	214
E.1	Literature review of E-modulus determinations of Soultz granite	232
E.2	Properties of samples	234
E.3	Classification of alteration	235

Notations

Physical quantity

Symbol	Unit	Meaning
α, β, γ	°	Euler angles
β_c	-	coefficient in the effective stress law for compressive failure
β_T	-	coefficient in the effective stress law for tensile failure
CV	-	Coefficient of variation
D	-	Fractal dimension
d	m	Distance between boreholes in fracture plane (Section 3.5.5)
i	m	Maximum theoretical spacing
k	-	Factor of proportionality between r and d (Section 3.5.5)
N_a	-	Total number of fractures within a certain range of d (Section 3.5.5)
N_c	-	Number of correlated fractures within a certain range of d (Section 3.5.5)
P_p	MPa	Natural formation pressure
P_w	MPa	Pressure in the wellbore
p	-	Probability that a fracture observed in one borehole cross the other borehole (Section 3.5.5)
p_e	-	Estimate of the probability p (Section 3.5.5)
r	m	Fracture radius (Section 3.5.5)
S_1	MPa	Maximum principal total stresses
S_2	MPa	Intermediate principal total stresses

continued on next page

Notations

Symbol (cont.)	Unit (cont.)	Meaning (cont.)
S_3	MPa	Minimum principal total stresses
$S_{\Delta T}$	MPa	Induced thermal stress tangential to wellbore wall
SH_{max}	MPa	Maximum horizontal total stress
Sh_{min}	MPa	Minimum horizontal total stress
S_v	MPa	Vertical total stress
\mathbf{S}	MPa	principal stress tensor
σ_1	MPa	Maximum principal effective stresses
σ_2	MPa	Intermediate principal effective stresses
σ_3	MPa	Minimum principal effective stresses
UCS	MPa	Uniaxial Compressive Strength

Acronyms

Abbreviation	Meaning
A-DITFs	Axial drilling induced tension fractures
BD	Borehole Depth measured along hole from drilling platform
BHTV	Borehole Televiever
BOs	Breakouts
BRGM	Bureau de recherches géologiques et minères (French Geological Survey)
ECRIS	European Cenozoic rift system
E-DITFs	En echelon drilling induced tension fractures
EGS	Engineered Geothermal Systems (or Enhanced Geothermal Systems)
EPS1	Name of a cored borehole of the Soultz geothermal project
FEM	Finite Element Modelling
DITFs	Drilling induced tension fractures
GPIT	General Purpose Inclinometry Tool (Schlumberger tool)

continued on next page

Abbreviation (cont.)	Meaning (cont.)
GPK1, 2, 3 and 4	Names of the deep boreholes of the Soultz geothermal project
HDR	Hot Dry Rock
HFR	Hot Fracture Rock
HWR	Hot Wet Rock
IPCC	Intergovernmental Panel on Climate Change
MD	Measured Depth measured along hole from ground level
MWD	Measurement While Drilling
SPOT	Systeme Probatoire pour l'Observation de la Terre. The French commercial remote-sensing satellite.
TD	Total depth
TVD	True vertical depth
UBI	Ultrasonic Borehole Imager (Schlumberger tool)
URG	Upper Rhine Graben
VSP	Vertical seismic profiling

Abstract

ENHANCED Geothermal Systems (EGS) — initially called Hot Dry Rock (HDR) — is a technology which was developed since the 1970's in order to exploit the heat contained within the low-porosity rocks which underlie large areas of the continents at practically drillable depths. The challenge of this technology is to find the appropriate way of developing flow paths between deep boreholes which permit heat extraction at economic rates. This is usually attempted by performing massive fluids injections which serve to elevate pore pressures, thereby promoting shearing and permeability enhancement of natural fractures within the rock mass. Hence modelling of the permeability-enhancement processes requires quantitative knowledge of the characteristics of the natural fracture population, and the state of stress. The objective of the work presented in this thesis is to improve our understanding of both aspects of the 5 km deep reservoir at the Soultz-sous-Forêts geothermal site (France). The data analysed stem principally from the acoustic televiewer images acquired in the three 5 km deep boreholes of the Soultz site. An unusual feature of the data is that the wells are less than 20 m apart in the granite section down to 2.5 km depth. This allowed the lateral variation in both natural fracture characteristics and stress to be examined. Below 2.5 km, the wells spread apart reaching 700 m at 5 km depth where the natural formation temperature is about 200°C. The intention is to construct a geothermal electricity production plant that will become operational in 2008.

Thousands of natural fractures were identified and analysed on more than 7 km of borehole wall images. An important aspect of the analysis is to find ways to use the fracturing observed at the 30 cm diameter borehole walls for interpreting structures at the reservoir scale (i.e. up to 2 km). Innovative methods were developed that exploited the small spacing of the wells to 2.5 km in order to quantify the spacing and the size of the structures identified in each of the holes. Four major sets of fractures were identified on the basis of orientation. Fractures had mean true sizes of 15 to 40 m diameter. Spacings appeared to follow log-normal laws with arithmetic mean values of 1 to 6 m, although this could be an artefact of selective sampling of what is actually a power law due to the limited resolution of the televiewer. The distribution of fractures along the wells shows distinct clustering, reflecting the intersection of the well with fracture zones composed of an anastomosed network of fractures delimiting shear lenses. Large variations in both the internal structure and the thickness of fracture zones occur over distances of 10 to 20 m. These variations are believed to have a significant influence on the hydraulic behaviour of the zones by channelling the flow. The spacings of the fracture zones range from 40 to 400 m. The size of such

structures cannot be specified with our data set. Microseismic imaging shows they can extend over distances of several hundred metres.

Drilling induced tension fractures (DITFs) occur more or less continuously above 2.2 km, whereas breakouts occur below 3.6 km. This depth-partition, together with hydraulic data from the injections, allows constraints to be placed on the stress state at Soultz down to 5 km depth. The orientation of the maximum horizontal principal stress was found to be at $169^{\circ}\pm 14^{\circ}$. The magnitude of the vertical stress was evaluated by integrating density logs. The magnitude of the minimum principal horizontal stress was estimated from downhole pressure recorded during several massive fluid injections. The magnitude of the maximum principal horizontal stress was constrained using the distinct depth ranges where tensile (i.e. DITFs) and compressive (i.e. breakouts) failure occurred. Extraction of estimates of the far-field stress magnitudes from the DITFs observations required that the profile of maximum cooling of the borehole wall during drilling be specified. This was taken as the temperature at the bit during drilling, and was estimated from measurement-while-drilling data. The constraints on stress from the breakouts required the cooling profile prevailing along the hole at the time of the log be specified, as well as the compressive strength of the rock. The latter was obtained from UCS tests conducted as part of this study. The resulting constraints on SH_{max} magnitude support the conclusion derived from the appearance of both normal and strike-slip fault plane solutions of induced microseismic events that $SH_{max} = 1.0Sv$. The utility of the present results is to place upper and lower bounds on permissible deviations from equality. A by-product of the analysis was the inference that the coefficient in the effective stress law for tensile failure for the Soultz granite must be less than 0.8, and probably significantly less.

Stress heterogeneity was studied by examining the deviation of the orientation of SH_{max} from the mean direction. Stress variations were seen to occur at all scales and follow a self-affine scaling law. Examination of short-wavelength (<50 m) variations of the DITF orientations in the sections where the wells are about 20 m apart shows that they are correlated with natural fractures, but usually not correlated between wells. This suggests that fractures are for the most part not much larger than 40 m in diameter, in agreement with the results of the study of fracture size. Large wavelength variations are also seen and are principally associated with fracture zones. Indeed, the two most prominent large scale perturbations coincide with the two most significant fracture zones intersected by the wells. En-echelon DITFs were often seen to lie sub-parallel to natural fractures. This geometry could be explained if the natural fracture had suffered a large but not a total stress drop, so that one principle stress lies almost normal to its plane. DITFs forming within the zone of stress perturbation about the natural fracture would thus be sub-parallel to it. The natural fractures in question would all be critically stressed under the prevailing linear stress characterisation for the site. This, together with the frequency with which the geometry is seen suggests that the shear stress on the natural fractures was relieved relatively recently, possibly during drilling in response to high wellbore pressure at the drill bit.

Résumé

LA technologie des ‘Enhanced Geothermal Systems’ (EGS, systèmes géothermiques stimulés) — appelée initialement ‘Hot Dry Rock’ (HDR) — a été développée dès les années 1970 afin d’exploiter les vastes réserves de chaleur contenues dans les roches de faible porosité que l’on trouve dans d’importantes portions des masses continentales à une profondeur atteignable par forage. Le défi de cette technologie est de trouver une méthode appropriée pour développer les chemins d’écoulement qui permettront d’extraire la chaleur de manière rentable. Une méthode possible — appelée stimulation hydraulique — consiste à effectuer des injections massives de fluides. Celles-ci ont pour conséquence d’élever la pression interstitielle dans le massif, ce qui favorise le cisaillement des fractures naturelles et permet d’élever leur perméabilité. Par conséquent, la modélisation des processus d’augmentation de la perméabilité nécessite d’acquérir des connaissances quantitatives concernant les caractéristiques de la fracturation naturelle, ainsi que de l’état des contraintes in-situ. L’objectif des recherches présentées dans cette thèse vise à améliorer notre compréhension de ces deux aspects sur le site géothermique de Soultz-sous-Forêts (France). Les principales sources de données pour cette étude sont les imageries acoustiques acquises dans les trois forages profonds du site de Soultz. Une particularité de ces données réside dans le fait que les forages sont distants de moins de 20 m le long de leur section granitique, ceci jusqu’à une profondeur de 2.5 km. Cette configuration est favorable à l’étude des variations latérales de la fracturation naturelle ainsi que celles des contraintes. Au-delà de 2.5 km de profondeur, les forages s’éloignent, atteignant une séparation de 700 m à la profondeur de 5 km, où la température du massif est d’environ 200°C. Le but général du projet est de construire une centrale géothermique pour la production d’électricité, opérationnelle dès 2008.

Plusieurs milliers de fractures naturelles ont été analysées le long de plus de 7 km d’images des parois des forages. Un aspect important de cette analyse est de trouver des méthodes permettant de prendre en compte la fracturation observée sur les parois de forage de 30 cm de diamètre, pour interpréter les structures à l’échelle du réservoir, c.-à-d. pour des tailles allant jusqu’à 2 km. Des méthodes innovantes exploitant la faible séparation des forages dans l’intervalle de profondeur 1.4 km – 2.5 km ont été développées afin de quantifier l’espacement et la taille des structures identifiées dans chaque forage. Quatre principales familles d’orientations des fractures ont été identifiées. Nous avons évalué que la taille moyenne des fractures individuelle se situe entre 15 et 40 m et que leurs espacements vrais suivent une loi log-normale avec une moyenne arithmétique entre 1 et 6 m. Cette distribution log-normale reflète probable-

ment l'échantillonnage sélectif lié à la résolution limitée des imageries de forage sur une distribution originale des espacements qui elle, suit une loi de puissance. Les fractures individuelles ont une organisation en cluster reflétant l'intersection des forages avec des zones de fractures ayant une structure interne suivant le modèle conceptuel de réseau anastomosé. Des variations importantes de l'épaisseur et de la structure interne de ces zones de fractures sont observées sur une distance de seulement 10 à 20 m. Ces variations pourraient jouer un rôle important dans le comportement hydraulique des zones de fractures en favorisant la formation de chenaux. Les espacements des zones de fractures sont d'environ 40 à 400 m. L'extension de telles structures ne peut pas être évaluée sur la base de nos données uniquement. L'étude de la microsismicité montre que ces zones peuvent s'étendre sur des distances de plusieurs centaines de mètres.

Les fractures induites en tension sont observées au-dessus de 2.2 km alors que les élargissements par fracturation et écaillage du forage ('breakouts') apparaissent au-dessous de 3.6 km. Cette répartition en profondeur des différents types de ruptures combinée avec les données recueillies lors des stimulations hydrauliques permet de caractériser l'état des contraintes à Soultz jusqu'à une profondeur de 5 km. La direction de la contrainte horizontale maximale est définie clairement par l'orientation des ruptures des parois des puits et est de $169^\circ \pm 14^\circ$. La magnitude de la contrainte verticale est calculée en intégrant des profils de densité. Les enregistrements de la pression lors d'injections massives de fluides permettent d'estimer la magnitude de la contrainte horizontale minimale. L'analyse de la répartition des ruptures en tension et compression des parois des puits permet de borner la magnitude de la contrainte horizontale maximale. Afin de calculer les magnitudes des contraintes à partir de l'observation des fractures induites en tension, il est préalablement nécessaire de déterminer le refroidissement maximal des parois du forage lors de son percement. Ce dernier est donné par la température au trépan pendant le percement et a été estimée par des mesures en fond de trou lors du forage. Le calcul des contraintes basé sur les 'breakouts' nécessite de connaître le profil de refroidissement lors de l'acquisition des données d'imageries ainsi que la résistance en compression de la roche. Cette dernière a été obtenue par des tests en compression uniaxiale effectués dans le cadre de cette recherche. Les résultats obtenus concernant les magnitudes possibles de SH_{max} sont en accord avec l'observation que les mécanismes au foyer des séismes induits par les stimulations hydrauliques sont de deux types : normaux et décrochants, impliquant que $SH_{max} = 1.0Sv$. L'utilité du résultat présenté ici est de placer des limites concernant les écarts possibles de cette égalité. Un résultat connexe de cette analyse indique que le coefficient dans la loi des contraintes effectives pour la rupture en tension doit être égal ou inférieur à 0.8.

Les hétérogénéités des contraintes ont été étudiées en examinant les écarts à la moyenne de la direction de SH_{max} . Ces variations des contraintes sont observées à toutes les échelles et suivent des lois fractales. L'étude des variations de courte longueur d'onde (<50 m) de l'orientation des fractures induites en tension là où la

distance entre les forages est de 20 m environ montre que ces variations sont généralement bien corrélées aux fractures naturelles, mais pas corrélées entre les forages. Cela suggère que les fractures sont pour la plupart pas plus longue que 40 m, en accord avec l'étude de la taille des fractures naturelles. Des variations de longue longueur d'onde sont également observées et sont principalement associées avec des zones de fractures. En effet, les deux perturbations les plus proéminentes à grande échelle coïncident avec les deux zones de fractures les plus importantes interceptées par les forages. Les fractures induites en échelon sont fréquemment orientées parallèlement aux fractures naturelles. Cette géométrie pourrait s'expliquer si le relâchement des contraintes sur les fractures naturelles est presque total, de telle sorte qu'une composante principale du tenseur des contraintes est presque perpendiculaire au plan de fracture. Les fractures en tension induites dans cette zone de perturbation des contraintes se formeraient alors sub-parallèlement aux fractures naturelles. Sous l'influence des contraintes telles que données par la caractérisation linéaire pour le site, les fractures naturelles en question seraient toutes sous un état de contraintes critique, proche de la limite de rupture. Ceci ainsi que la fréquence à laquelle cette géométrie particulière est observée suggèrent que les contraintes sur les fractures naturelles furent relâchées relativement récemment, possiblement lors du forage, en réponse à une pression élevée au niveau du trépan.

Zusammenfassung

ENHANCED Geothermal Systems (EGS, verbesserte oder stimulierte geothermale Systeme) — zunächst ‘Hot Dry Rock’ (HDR) genannt — ist ein Verfahren, das seit den 70iger Jahren entwickelt wurde, um die Wärme aus dem Gestein der Kontinente durch Bohrungen in erschließbarer Tiefe nutzbar zu machen. Die Herausforderung dieser Technologie liegt darin, eine Möglichkeit zu finden, Fließwege zwischen Bohrungen derart zu entwickeln, die eine Wärmeextraktion aus der Tiefe mit einem ökonomisch vertretbaren Aufwand möglich wird. Eine erfolgversprechende Methode — die sogenannte hydraulische Stimulation — besteht darin, starke Injektionen von Flüssigkeiten in das Gebirge vorzunehmen. Diese führen zu einem Anstieg des Porendruckes im Gestein, was die Scherung von natürlich vorhandenen Klüften vorantreibt und es ermöglicht, ihre Permeabilität zu erhöhen. Die Modellierung dieses Prozesses der hydraulischen Stimulation setzt eine quantitative Kenntnis der Eigenschaften der natürlichen Bruchstrukturen und des in-situ Spannungsfeld voraus. Dies sind auch die Themen der vorliegenden Dissertation, welche im Rahmen des Soultz-sous-Forêts (Frankreich) Geothermie-Projekts im Detail untersucht wurden. In diesem Projekt soll ein geothermisches Elektrizitätswerk erstellt werden, das im Jahr 2008 seinen regulären Betrieb aufnehmen kann.

Die dieser Forschungsarbeit zugrunde liegenden Daten bestehen hauptsächlich aus akustischen Bohrlochwandbildern, die in drei tiefen Bohrlöchern bei Soultz gewonnen wurden. Eine ungewöhnliche Eigenschaft der Daten ist, daß die abgeteufte Bohrungen in einer Tiefe von bis zu 2.5 km in einem Granitabschnitt lateral weniger als 20 m voneinander entfernt sind. Diese Eigenschaft erlaubte es, auch die horizontalen Veränderungen der natürlichen Strukturen sowie des in-situ Spannungsfeldes zu untersuchen. Zwischen 2.5 km und 5 km Tiefe, wo eine Temperatur über 200°C herrscht, verbreitert sich der Abstand der Bohrungen auf bis zu 700 m.

Tausende natürlicher Strukturen sind entlang von mehr als 7 km akustischer Bohrlochwandbilder analysiert worden. Ein wichtiger Aspekt dieser Analyse war es, neue Methoden zu entwickeln, um die im Bohrloch beobachtete Klüftung für die Interpretation der Strukturen im Reservoirmaßstab (d.h. bis zu 2 km) zu nutzen. Hierbei wurden insbesondere der Kluftabstand und die Kluftgrößen in einer Tiefe von 1.4 km – 2.5 km quantitativ untersucht. Basierend auf der Raumstellung wurden vier vorherrschende Kluft-Systeme identifiziert. Diese Klüfte haben eine mittlere wahre Größe zwischen 15 und 40 m und einen Abstand, welcher dem Gesetz einer logarithmischen Normalverteilung folgt. Die mittleren Abstände liegen zwischen 1 bis 6 m. Die logarithmische Normalverteilung der Abstände ist möglicherweise ein Artefakt, wel-

cher auf eine selektive Beprobung einer tatsächlichen Potenzverteilung zurückzuführen ist. Dies steht im Zusammenhang mit der begrenzten Auflösung des akustischen Bohrloch-Televiseurs. Die einzelnen Klüfte bilden Cluster, welche zu Bruchzonen gehören, die aus anastomosierenden Netzwerken von Klüften und intakten Scherlinsen bestehen. Über Distanzen von nur 10 bis 20 m finden grosse Variationen sowohl der internen Struktur wie auch der Mächtigkeit der Bruchzonen statt. Diese Variationen spielen vermutlich für das hydraulische Verhalten der Bruchzonen eine wichtige Rolle, da sie den Fluss kanalisieren. Die Abstände dieser Bruchzonen liegen zwischen 40 und 400 m. Ihre Ausdehnung kann mit dem uns vorliegenden Datensatz nicht ermittelt werden. Mikroseismische Analysen zeigen, dass diese Strukturen eine Ausdehnung von mehreren hundert Metern haben können.

Durch den Bohrvorgang induzierte Zugrisse traten nahezu kontinuierlich oberhalb einer Tiefe von 2.2 km auf, während kompressive Bohrlochrandausbrüche ('breakouts') unterhalb von 3.6 km auftraten. Dieses tiefenabhängige Bruchmuster erlaubt es, zusammen mit hydraulischen Daten von Injektionen, den Spannungszustand bei Soultz bis in eine Tiefe von 5 km zu charakterisieren. Die Richtung der maximalen horizontalen Spannung SH_{max} beträgt $169^\circ \pm 14^\circ$. Der Betrag der vertikalen Spannung S_v wurde durch das Integrieren von Dichte-Logs ermittelt. Druckaufzeichnungen während massiver Fluid-Injektionen ermöglichten es, den Betrag der minimalen horizontalen Spannung Sh_{min} zu ermitteln. Dank der Beobachtung, dass Zugrisse und kompressive Bohrlochrandausbrüche in spezifischen Tiefenbereichen auftreten, konnte der Betrag der maximalen horizontalen Spannung eingegrenzt werden. Die Ableitung des in-situ Spannungsbetrags aus den Beobachtungen der Zugrisse erforderte, daß das Profil der maximalen Abkühlung der Bohrlochwand während des Bohrvorgangs ermittelt wurde. Die minimale Temperatur der Bohrlochwand wurde der Temperatur des Bohrmeißels gleichgesetzt, welche während des Bohrens gemessen wurde. Für die Eingrenzung der in-situ Spannungen aus den kompressiven Bohrlochrandausbrüchen musste das Abkühlungsprofil zur Zeit des Bohrloch-Loggings sowie die Druckfestigkeit des Gesteins ermittelt werden. Letztere wurde aus einaxialen Druckversuchen abgeleitet, die als Teil dieser Studie durchgeführt wurden. Die resultierenden Implikationen für den Betrag der maximalen Horizontalspannung unterstützen die Schlussfolgerungen aus den mikroseismischen Beobachtung, welche Herdflächenlösungen sowohl von Blattverschiebungen wie Abschiebungen ergeben und implizieren, dass die maximale Horizontalspannung der minimalen Horizontalspannung in etwa entspricht ($SH_{max} = 1.0S_v$). Die vorliegenden Resultate lassen sich nutzen, um obere und untere Grenzen für die zulässigen Abweichungen dieser Spannungsbeziehungen festzulegen. Eine weitere Erkenntnis der Analyse war die Folgerung, dass der Koeffizient β_T im Gestein der effektiven Zugspannung kleiner als 0.8 sein muss, und wahrscheinlich sogar wesentlich kleiner als dieser Wert ist.

Spannungs-Heterogenitäten wurde anhand von Abweichungen der lokalen Orientierung von SH_{max} von der mittleren Richtung untersucht. Diese Spannungs-Variationen treten auf verschiedenen Maßstäben auf und folgen selbst-affinen Skal-

ierungs-Gesetzen. Die Beobachtung von Variationen der Zugrissorientierung mit kurzen Wellenlängen ($<50\text{m}$) in den Bohrlochabschnitten mit kleinem Abstand (20 m) zeigt, dass die Orientierung mit jener der natürlichen Klüfte korreliert, aber keine Korrelation zwischen den Bohrlöchern besteht. Dieses legt nahe, dass die Klüfte in den meisten Fällen nicht viel größer als 40 m sind, was in Übereinstimmung mit früheren Studien der Bruchgrößen bei Soultz steht. Variationen großer Wellenlänge ($>50\text{ m}$) sind in unserem Datensatz ebenfalls vorhanden. Diese werden hauptsächlich mit Bruchzonen in Verbindung gebracht. Die zwei wichtigsten großskaligen Variationen der horizontalen Hauptspannungs-Orientierung stimmen mit den zwei bedeutendsten Bruchzonen, die durch die Bohrungen angeschnitten wurden, überein. En-echelon Zugrisse, die durch Bohrvorgänge verursacht wurden, liegen oft sub-parallel zu natürlichen Klüften. Diese Geometrie der Zugrisse könnte dadurch erklärt werden, dass die natürlichen Klüfte einen großen aber nicht vollständigen Spannungsabbau erfahren haben, wodurch eine Hauptspannung fast normal auf die Kluftebene zu stehen kommt. Die Zugrisse, die sich innerhalb der durch diese Spannungsumlagerung beeinflussten Zone um den natürlichen Bruch bilden, würden folglich zu ihm sub-parallel sein. Die Frequenz mit der diese Geometrie beobachtet wurde und die Tatsache, dass alle diese natürlichen Klüfte vermutlich in einem kritischen Spannungszustand sind, weist darauf hin, dass die Spannungsentlastung der natürlichen Klüfte vor verhältnismäßig kurzer Zeit, möglicherweise als Resultat des hohen Bohrlochdrucks am Bohrmeißel, stattgefunden hat.

Acknowledgements

THIS thesis benefited from the support and collaboration of many people who I would like to warmly thank.

Foremost, I would like to thank Dr. Keith Evans who initiated this research project. He has always been very careful in setting the optimal frame for my work and provided thorough supervision with considerable humanism. I am thankful to Dr. Albert Genter for accommodating me in BRGM (Orléans), for sharing his extensive knowledge of the Soultz-sous-Forêts geothermal project and for active involvement with my work during the last three years. I am in debt to Pr. Dr. Simon Löw who welcomed me into his group five years ago and gave me the opportunities to participate in interesting research projects. I also warmly thank Dr. François H. Cornet for bringing his expertise within my thesis examination committee.

This thesis also profited from the help and thoughts of many people outside my supervisory committee. Chrystel Dezayes from BRGM actively worked with me and shared her expertise in borehole log interpretation. The Soultz team is cordially thanked for their help at numerous occasions. Particular thanks are addressed to Dimi Teza, Marion Schindler, Catherine Lanoix and André Gérard who helped me through the drilling reports and Soultz archives. I am thankful to the colleagues of the Swiss Research group on EGSs (DHMA) for sharing ideas. Thanks are due to Erich Pimentel and Thomas Jaggi from IGT-ETH Zürich and Jean-François Mathier and Laurent Gastaldo from LMR-EPF Lausanne who helped with the sample preparation and the performing of the lab tests. I am grateful to the collaborators of geothermal explorers, Florentin Ladner, Markus Haering, Christian Haering and Bob Warrol, for interesting cooperation and for entertainment during long logging nights. During my PhD, I had the opportunity to present my work to many scientists at many different occasions; sometimes fruitful discussions followed such presentations. Among others, Peter Kaiser, Stephen Hickman and David J. Sanderson initiated some interesting discussions and are thanked for that.

I would like to express my gratitude to all my colleagues in the Engineering Geology group for their individual help, for the fruitful scientific discussions and also for the necessary more recreative episodes. Particular thanks are addressed to Frank Lemy who provided assistance in data analysis as well as very friendly discussion — sometimes too late into the night. All (ex-)PhD students, Salina Yong, Heike Willenberg, Lucia Amara, Olivier Masset, Marc Pesendorfer, Freddy Xavier Yugsi Molina, Jürgen Hansmann, David Jaeggi, David Estoppey are warmly thanked for sharing ideas, offices, resources, jokes, worries, good tips, and more. Our office

Acknowledgements

management team, Bettina Roth-Galamb, Bernadette Würsch and Melissa Kündig deserve gratitude for their administrative support. Kathy Kaiser is warmly thanked for helping with the translation of the German Abstract.

I have a special thought for the regretted Martin Burkhard. He brought me to geology and gave to me the initial impulse and motivation to pursue research and to write a PhD thesis.

I am thankful to my Parents and Family who support my education over the years — from my first school day to the completion of this PhD thesis.

Big thanks extended to my wife Myriam for her love and patience.

1 Introduction

1.1 Motivations

THE beginning of the 21st century finds the supply of energy as a major political and societal issue. The recent increase in the price of oil, and speculation about the actual oil world reserves (e.g. *Clarke, 2007; Cochet, 2005; Wingert and Laherrère, 2005*) has served to bring the energy supply issue to the attention of a large public. The debate within Switzerland has been heightened by the question of what to do about the ageing nuclear power plants. Currently these provide 40% of electricity to the Swiss Confederation, the remainder being derived from hydro-electric plants (55%), and conventional thermal plants (slightly less than 5%). Since the fuel for thermal or nuclear plants is not naturally present within Swiss territory, there is an implicit dependence upon the countries that extract oil, gas, coal or uranium.

Another concern related to energy which has enjoyed widespread public exposure of late is the global warming issue. The reality of the global warming and some assessment of its consequences were again recently expressed with a high level of confidence by the Intergovernmental Panel on Climate Change (IPCC) in the Fourth Assessment Report: *Climate Change 2007*. More prosaically, public opinion has perhaps been more impressed by the extreme weather that many areas have experienced in the last few years, sometimes with tragic consequences.

The issues of climate change and energy security together provide essential constraints in defining what types of sustainable energy sources are acceptable for the future: they should be free of CO₂ emissions and not dependent on imported fuel. Geothermal energy meets both these criteria, and has the potential to provide a substantial part of such sustainable energy in the future. Indeed, vast reserves of energy in the form of heat are present within the low-porosity rocks which underlie large areas of the continents at practically drillable depths. The key question then is how can we extract this energy and convert it to high-enthalpy energy like electricity ?

The ‘Hot Dry Rock’ (HDR) concept, which was patented in the USA in the 1970’s (*Potter et al., 1974*), provides a basic plan to extract heat from deep, hot rocks. The original idea was to use the hydrofracture technology developed by the oil and gas industry to link two or more boreholes with a stack of artificial fractures. Hydrofractures — i.e. fresh ‘opening-mode’ fractures — are formed by injecting large volumes of fluid at high rates and pressures. The heat can then be extracted by forcing the water to pass through these fractures from one borehole and producing

the hot water from a second or third borehole.

Since the early years, a great deal of research has been performed into the concept that has led to major revisions of the early ideas, as well as contributing to advances in many fundamental aspects of Earth Science. The revisions to the concept can be briefly illustrated by the semantic evolution of the different names applied to the method, which reflect major advances in our knowledge. The ‘Hot Wet Rock’ (HWR) denomination arose from the realisation that some deep crystalline rock masses can contain significant quantities of water, and may almost be considered natural geothermal aquifers. Given that crystalline rocks composing the basement usually have low porosity and permeability, the question arises “where is this water contained and how does it circulate”? The answer leads us to the next denomination: ‘Hot Fractured Rocks’ (HFR). It has long been recognised that the natural flow paths within the crystalline rocks usually reside in fractures and faults which are created and reactivated during the long tectonic history of the basement rocks in question. Not only the tectonic, but also the hydrothermal history can be long, and include episodes when chemically-active fluids flowed through the rock mass fractures and faults, facilitating rock/water interactions which transform the adjacent rock. The hydrothermally-altered structures can retain significant porosity and permeability, and led *Genter* (1989) to propose a further denomination of HDR systems called ‘Fractured Hydrothermally Altered Geothermal Reservoir’.

The different names that have been proposed reflect the diversity of conditions that can exist within crystalline rock masses in different tectonic settings. Recently, the name ‘Engineered (or Enhanced) Geothermal System’ (EGS) has come into play to describe the collection of different types of reservoir. The name emphasises the overlap with conventional geothermal systems, but indicates the essential difference from the latter is the need to engineer the downhole heat exchanger. Thus, EGS applies not only to systems developed in deep crystalline rocks but also to any geothermal system where the rock is stimulated in order to increase its permeability and therefore the efficiency of the heat extraction.

One way of enhancing the rock mass permeability, a process which is usually called stimulation, is to perform massive fluid injections. Experience at the numerous demonstration projects conducted to date has shown that massive injections of fluid are indeed effective in raising the permeability of rock masses. However, in most if not all cases, the permeability increases appear to be due to the shear failure of natural fractures in response to elevated pore pressure during the injections rather than the driving of new hydrofractures (the latter do not appear to propagate far in fractured crystalline rocks) as the early HDR concept aimed. Shear movement increases permeability because the fracture surfaces are rough and thus dilate upon shearing. In detail, such permeability enhancement processes are very complicated, and are governed by the interaction of the ambient stress field with the natural fractures and faults present in the rock mass.

The fact that the details of the stimulation process are very complicated and not

fully understood has consequences for the development of EGSs inasmuch as it hinders the design of optimal stimulation programs for prescribed geological settings. Optimised design is desirable to permit the target circulation parameters to be attained without inducing excessive micro-seismicity which might disturb the inhabitants in the neighbourhood. This particular problem is currently hindering the progress of several EGS projects.

The motivations of the present thesis is to provide foundation information for understanding the process of permeability enhancement which takes place during reservoir stimulation. Specifically, the thesis presents new constraints on the length characteristics of natural fractures that are present within the Soultz reservoir, and also a comprehensive study of the stress field to 5 km depth. Insights into the interaction between natural fractures and the stress field, which is of fundamental importance for the stimulation process, and also derived from the data.

1.2 Objectives

The primary objective of this PhD thesis was to determine the influence of pre-existing hydrogeological structures on permeability creation/enhancement within the EGS reservoirs. That work should have focussed mainly on the Basel reservoir, including also an important know-how transfer from the Soultz-sous-Forêts to the Basel project. However, a change to the plan was required because of delays in activity and hence data acquisition at the Basel project. Thus thesis plan was reoriented to focus exclusively on data from the Soultz-sous-Forêts project. The three following themes were examined:

1. The characterisation of the natural fracturing in the Soultz-sous-Forêts crystalline basement rocks with particular emphasis on the quantitative assessment of the distribution, orientation and size of the natural fractures and faults.
2. The linear characterisation of the state of stress at Soultz-sous-Forêts. Here the goal is to provide robustly-constrained linearised depth-trends of all attributes of the state of stress to 5 km depth. The emphasis was to use actual data from below 3.5 km rather than extrapolate data trends from above 3.5 km, as done in earlier studies.
3. A study of deviations of stress orientation from the linear trends (i.e. stress heterogeneity). The primary objective was to identify to origin of the implied perturbations to the stress field. This study led naturally to consideration of the interaction of the stress field and natural fractures during drilling.

1.3 Structure of the thesis

The thesis is built around the three objectives listed above, which are covered in Chapters 3, 4 and 5 respectively. These chapters are written in a form that is close to that required for journal publications. The three main chapters are introduced by some foundation studies in Chapter 2 which presents information relevant to the entire thesis, thereby avoiding the need for repetition. Details of aspects covered in the three main chapters that are not intended for publication are presented in the Annexes.

Chapter 2 provides information relevant to establishing the context of the Soultz geothermal project, both motivational (section 2.1) and geological/tectonic (section 2.2). These sections can be omitted by readers who are already familiar with the project. However, section 2.3 will be of interest to all readers since it introduces the borehole image data set that constitutes the basis of the thesis.

2 Foundation Studies

2.1 The Soultz-sous-Forêts Geothermal project

THIS section will briefly summarize the development of the Soultz-sous-Forêts geothermal project. It does not attempt to be an exhaustive review, as other contributions that focus on this issue exist and can be read for complementary information (e.g. *Dezayes et al.*, 2005b). Rather, achievements and some findings directly relevant to the present research work that have been made during the last 20 years at Soultz will be summarised in this section.

The Soultz-sous-Forêts geothermal project was initiated in 1987 and was funded by the European Commission and the energy ministries of France, Germany and United Kingdom. The site of Soultz was chosen because it is located over an intense thermal anomaly known to exist in this area since a long time. Also, the site is located close to the former oil field of Pechelbronn and the local geology was thus well characterised down to 1.4–1.5 km, i.e. the depth of the basement top. A geothermal gradient exceeding 110 °C/km was recorded in oil wells and initially a temperature of 200 °C (the target temperature for EGS) was expected to be encountered at about 2 km depth.

In 1987, when GPK1, the first geothermal exploration well was drilled to 2002 m, the down hole temperature was actually found to be 140°C. Since then, this unexpectedly low temperature has been explained by the combined effect of the presence of convective loop within the upper basement and the thermal insulating properties of the sedimentary cover.

In 1991, an old oil well renamed EPS 1 was deepened with continuous coring in order to precisely characterize the basement rocks. Due to problems in controlling the well trajectory, the total depth of that well is 2227 m instead of the 3200 m planned. Nevertheless 810 m of granite cores was acquired which provide high value scientific information for the project. These cores as well as the short spot cores of GPK1 have been studied by *Genter* (1989); *Genter and Traineau* (1992); *Traineau et al.* (1991) and permits to get a precise knowledge of the upper part of the basement at Soultz concerning the petrology, the type of alterations and their relation with fractures and fracture zones.

Two fundamentally different type of alteration have been described. The first one, referred as the pervasive alteration, is due to a very early alteration event that is probably related to reactions with magmatic fluids. It affects the rock through its

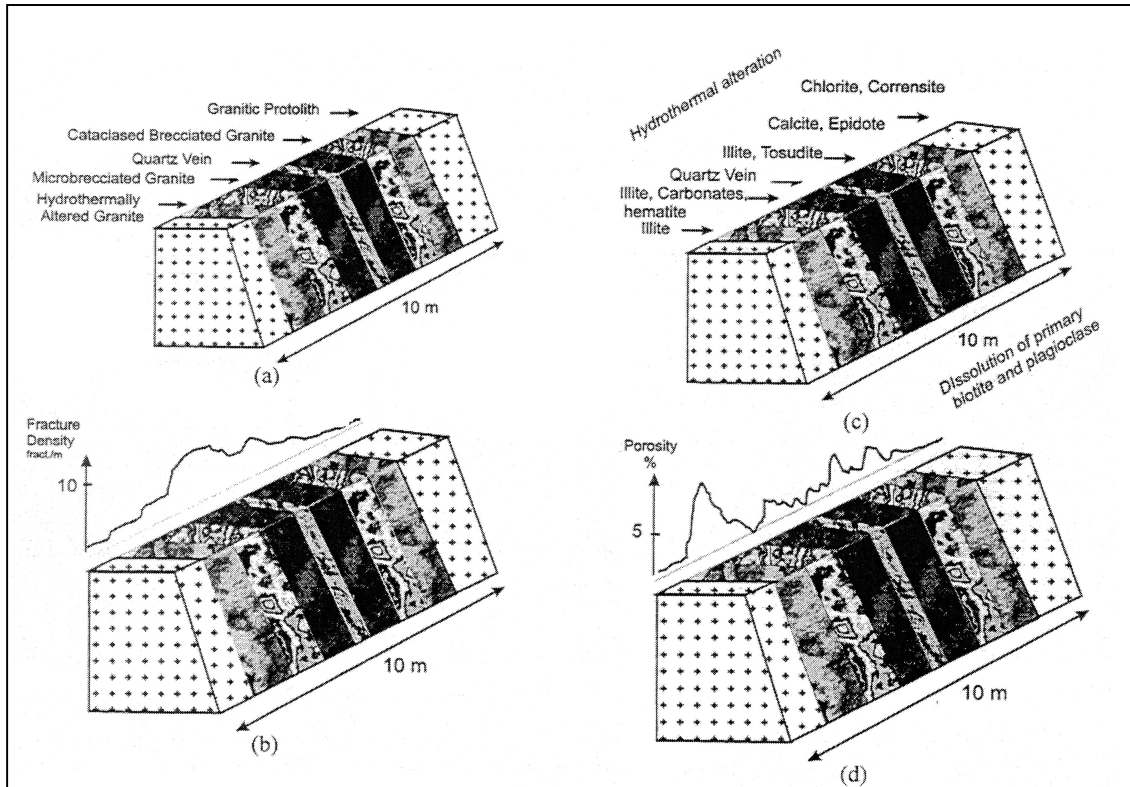


Figure 2.1: Conceptual model of fracture zones in *Genter et al.* (1998). a) Conceptual lithofacies zonation of hydrothermally altered and fractured zone and b) fracture density associated with. c) conceptual spatial hydrothermal alteration sequence of a fractured zone and d) porosity profile associated with.

volume and all of the granite so far explored at the Soultz site presents such alteration. This alteration is characterized by low grade alteration of biotite to chlorite and plagioclase to epidote (saussuritization). K-Feldspars are also affected and become reddish. Rock texture is not modified.

The second type of alteration, vein alteration, is related to hydrothermal fluid circulation within fractures and so, in contrast to the volume impact of the pervasive alteration, it has mainly an effect on fractures surfaces and their vicinity. It is characterized by the illitization of biotite and plagioclases, which usually imparts a yellowish colour to the granite. Fractures which show vein alteration are sealed with quartz (occasionally geodic), calcite, illite, chlorite, sulfides, barite or hematite. The detailed relation of this alteration with the structure of fracture zone has been conceptualised by *Genter et al.* (1998) and is presented in Figure 2.1.

The study of the EPS1 cores was a unique opportunity to get a precise knowledge

of the mineralogy and the petrology of hydrothermalised fractured zones in the Soultz basement as all subsequent wells were drilled mostly in destructive mode with only rare spot cores. For these other wells, the characterisation of the fracture zones and their hydrothermal alteration was based on cuttings description and wireline logs, both of them are more uncertain due to cuttings mixing and non-unique elements of log response interpretation. The concepts built on the EPS1 data set were thus very valuable in the interpretation of cuttings and wireline logs.

But what are the limitations of wireline logs to characterise the fracturing of the Soultz granite ? The study of *Genter et al.* (1997) addressed that question and is of particular relevance for our research. Comparisons of the fracturing seen on EPS1 cores with the images of borehole acoustic televiewer logs (BHTV) have shown that the BHTV is not able to detect fractures thinner than 1 mm. Thus only 17% of the fractures which were seen on cores were imaged by the BHTV. That detection threshold drops to 5% in hydrothermally altered granite compared to 50% within unaltered massive granite. Furthermore, the BHTV was not able to properly characterise the very closely spaced fractures (i.e. with spacing less than 5 mm). However, the orientation distribution of the fractures was correctly sampled since the BHTV distinguished the main fracture sets. The limited resolution of the BHTV introduces bias in the description of the spatial organization of individual fractures. Indeed, the fracture spacing distribution is seen to follow a power law when data come from cores analyses and a log-normal law with data from a BHTV.

After the exploration phases (1987–1991), a second phase was initiated in 1992 by deepening GPK1 down to 3.6 km and continued by drilling a new well, GPK2, down to 3.9 km in 1994/1995. This project phase aimed to develop a reservoir at 3.5–3.8 km, referred as the 'shallow' reservoir. An extensive program of logging, stimulation and circulation was carried out with this borehole doublet which culminated with a four-month closed-loop circulation at rates of about 25 l/s and temperature of 142°C.

During that phase, a detailed analysis (*Evans et al.*, 2005a) of geophysical surveys, wireline and lithologic logs from cuttings showed that fluid percolation under natural conditions occurs mostly if not exclusively in hydrothermalised fractured zones. Moreover, the permeability creation and enhancement achieved by massive injection of water was found to be largely limited to the same hydrothermalised fractured zones. Evidences of shearing of the stimulated fractures was observed and is believed to be the cause of the permeability enhancement. These results indicated that major flow within the rock mass under circulation conditions is likely to be restricted to the hydrothermalised fractured zones. This finding motivated the research developed here in Chapter 3 which aims to characterise the geometry and to quantify the size and distribution of these fractured zones.

Since 1998, the project goal is to develop a 5 km deep reservoir in order to reach the targeted temperature of 200°C. GPK2 was deepened to 5084 m in 1999 and two new deviated wells were drilled to 5 km depth from the same pad: GPK3 in 2002 and GPK4 in 2003/2004. These wells are the primary source of data for this thesis

and more information about them can be found in Section 2.3. These wells have been hydraulically and chemically stimulated in order to develop the 5 km deep reservoir and to achieve targeted injectivity and productivity index. The current aim of the project is the installation of a pilot plant which should start to produce electricity in 2008.

2.2 Geological context and tectonic settings

2.2.1 General morphology of the Rhine Graben

Soultz-sous-Forêts is located within the Upper Rhine Graben (URG), part of the west European rift system (see Figure 2.2) which developed in the Cenozoic times. The URG is about 300 km long, extending from Basel to Frankfurt, and is 30 to 40 km wide. The sedimentary filling of the graben reaches about 3000 m thickness (*Illies*, 1965). The present large elevation difference between the Rhine plain (about 200 m a.s.l.) and the flanking massifs is about 1300m (the highest peak of Black Forest is Felsberg, 1493 m a.s.l, *Tenzer et al.*, 1991). The opening of the URG has been estimated by *Illies* (1972) to be about 4.8 km and the down throw relative to the graben shoulders attains 4500 m. The balanced extensional cross section from *Groschong* (1996), implies an extension of 3.8 km, which correspond to a strain of 6.3% at the top basement level. The calculated detachment depth is 31.2 km which corresponds approximatively to the base of the crust. The deep structure of the graben derived from seismic tomography is presented in *Achauer and Masson* (2002). From comparison between the tomographic images obtained for various rift, they conclude that the URG is more likely a passive rift, where a complex regional stress field and inherited structures play a governing role in its evolution.

The general strike of the URG is NNE. The general aspect of the graben is impressively symmetrical (*Illies*, 1965): both graben borders change in orientation and height concurrently. The Black Forest in the south is symmetrical with the Vosges, followed to the north by Kraichgau and Pfälzburger depression, then by Odenwald and Pfälzerwald highs. Its general cross-sectional structure is also quite symmetric from west to east: the Vosgian fault, the Western Fracture Field, the Western Rhenian fault, the Rhine valley, the Eastern Rhenian fault, the Eastern Fracture Field and the Black Forest fault (see figures 2.3 and 2.4). However in detail this apparent symmetry is less true. This can be seen in the asymmetric sedimentary filling thickness shown in Figure 2.3. North of Strasbourg, the filling is thicker in the eastern part of the graben while south of Strasbourg the reverse is true. This reflects asymmetry in the deep structure of the graben as highlighted by seismic profiles (*Brun et al.*, 1991, 1992; *Mayer et al.*, 1997), possibly owing to extensional movements along a listric shear zone, which appears to merge at depth with a flat-lying detachment in the ductile lower crust (see Figure 2.5). The graben structure and filling is then in

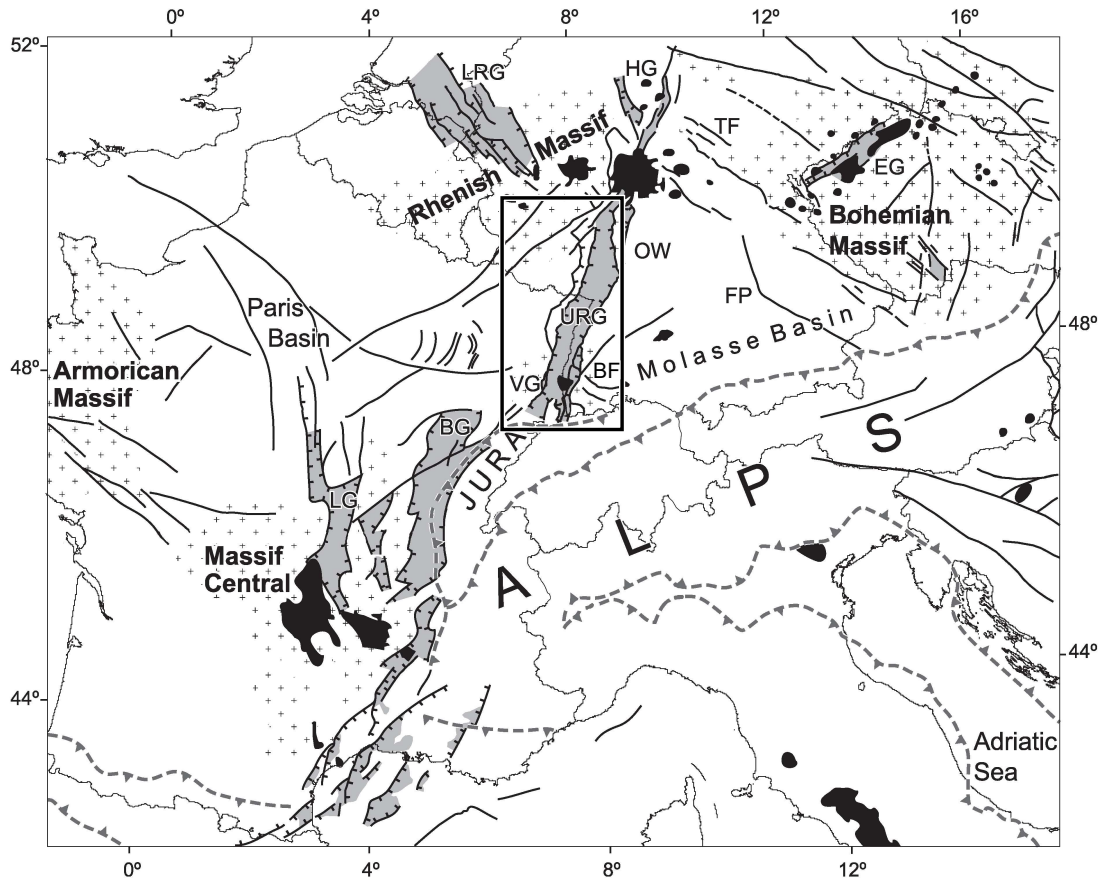


Figure 2.2: West European Rift system after *Dèzes et al.* (2004). The black frame locates Figure 2.4. Black lines show cenozoic fault system, light grey rift related sedimentary basin. Stippled barbed lines: alpine deformation front. BF: Black Forest, BG: Bresse Graben, EG: Eger (Ohre) Graben, FP: Franconian plattform, HG: Hessian Graben, LG: Limagne Graben, LRG: lower Rhine Graben (Roer valley), URG: Upper Rhine Graben, OW: Odenwald, VG: Vosges.

the section from *Brun et al.* dominated by the Western Rhenian Fault with a listric geometry and a throw of about 3000 m.

Soultz is situated close to this Western Rhenian Fault about 4 km from the graben border (see Figure 2.4). At Soultz, the sediment filling is asymmetric, with thicker Cenozoic sediments stacking to the east (see Figure 2.6). The URG is still a tectonically active area, as evidenced by recent seismic activities (e.g. *Bonjer, 1997; Deichmann et al., 2000; Larroque et al., 1987; Lopes Cardozo et al., 2005; Plenefisch and Bonjer, 1997*) and GPS monitoring (*Tesauro et al., 2006*).

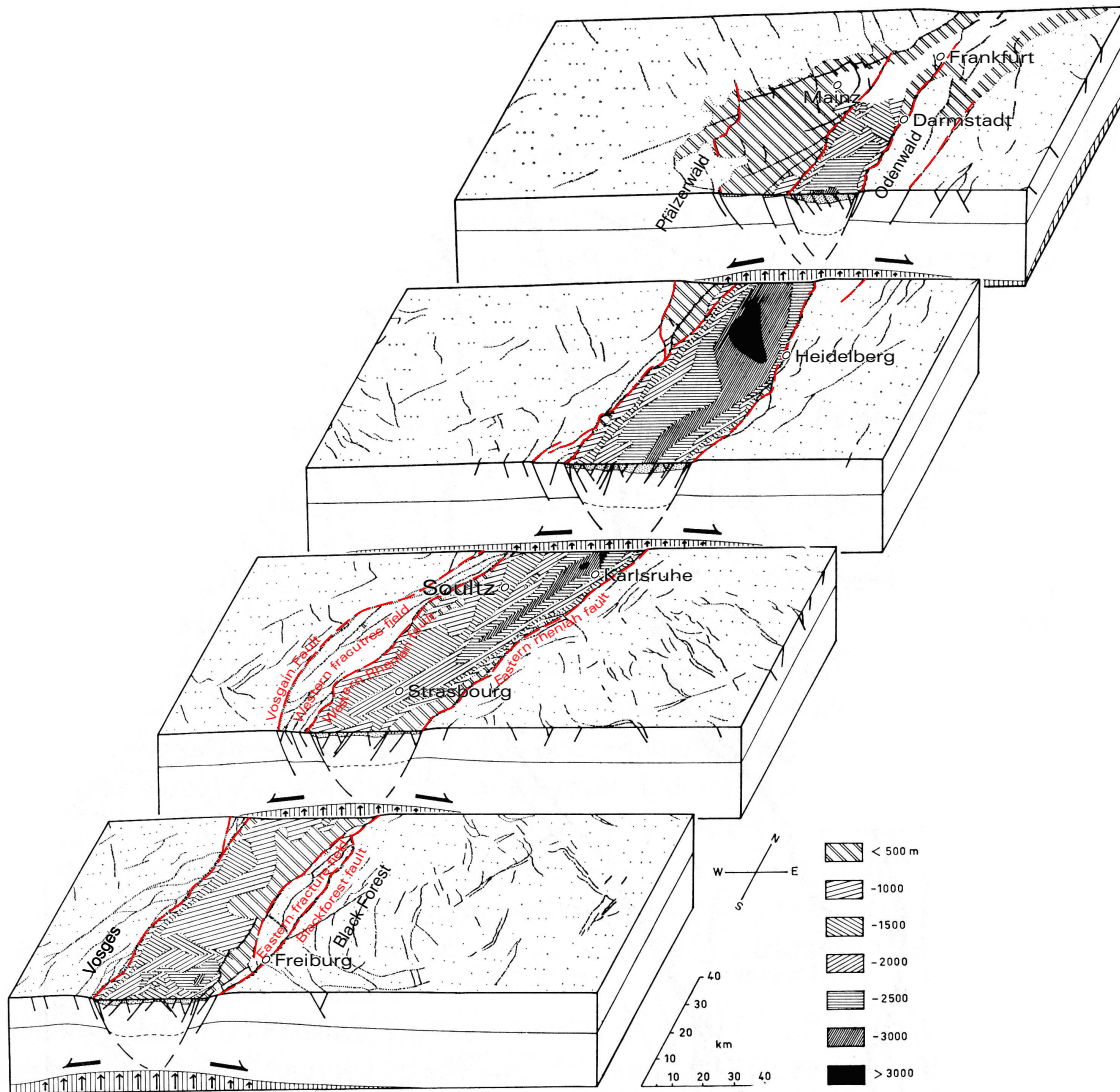


Figure 2.3: Block diagrams of the general rhine graben structure. Various hatching corresponds to the thickness of the Cenozoic fill. Modified after Illies (1972).

2.2.2 Emplacement of the Soultz granite in Visean time

The granites of Soultz are much older than the cenozoic formation of the URG. Two different granites have been encountered in the Soultz wells: a porphyric monzogranite and a fine-grained two-mica granite. *Cocherie et al.* (2004) performed U-Pb dating on the Soultz granites. They obtained an intrusion ages of $334.0 \pm 3.8/-3.5$ Ma for the porphyric granite and a slightly younger or contemporaneous age for the two mica granite (i.e. 327 ± 7 Ma). These ages correspond to Visean time (early

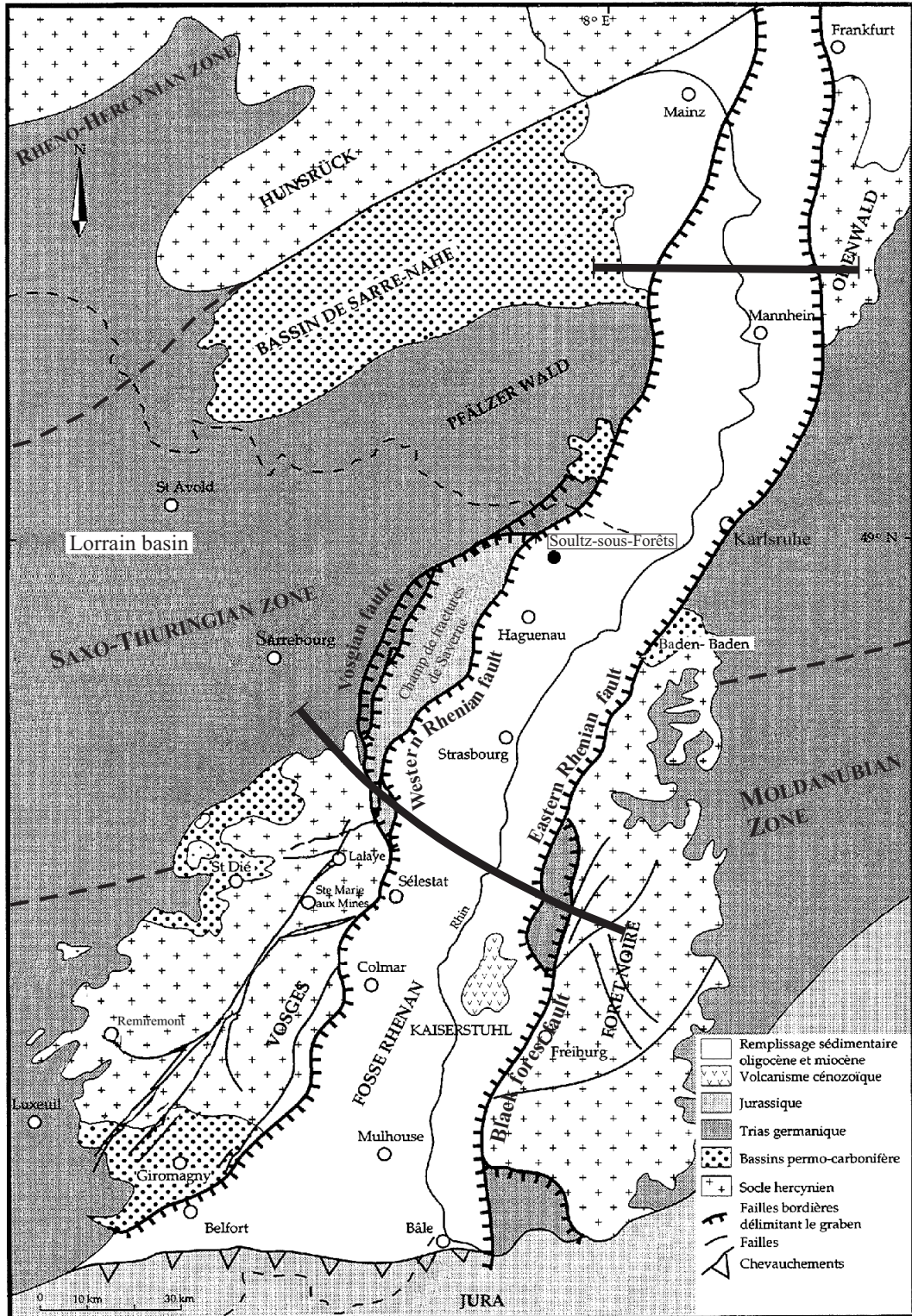


Figure 2.4: Map of the Upper Rhine Graben (after *Dezayes, 1996*). The thick black lines are the traces of the cross-sections of Figure 2.5.

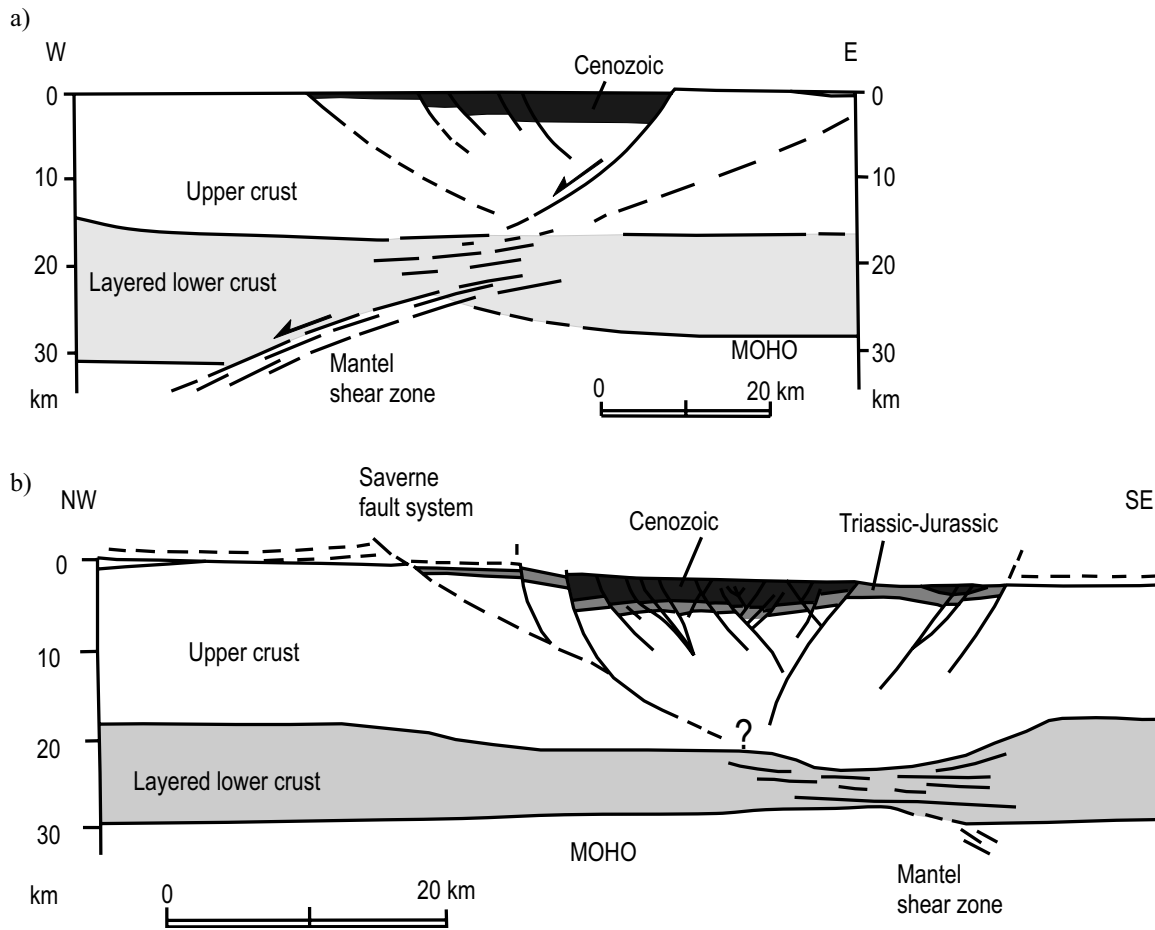


Figure 2.5: Crosssection through the Rhine Graben based on ECORS-DEKORP seismic profile after *Brun et al.* (1992). a) Northern section b) Southern section. The location of the crosssection is shown in Figure 2.4.

Carboniferous). Other dating from *Stussi et al.* (2002) provided similar ages.

Stussi et al. also performed geochemical analyses in order to define the genesis of the porphyric granite. Their results indicate mainly a crustal origin for the magma, involving also a mantle derived component. Crystallisation took place in two stages, one deep-seated (11 to 12 km, 350 MPa, 755–790°C) and a final consolidation stage occurring at about 4.5 to 5.5 km (temperature of 665 to 715°C, pressure of 150 MPa). The production of this magma is probably related to collisional to post-collisional tectonics.

Schulmann et al. (1997) look for crystallographic fabrics in the porphyric granite. Their results show that the Soultz boreholes are located in the central part of a laccolith where vertical shortening and NE-elongation is superimposed in simple shear with a NE-directed stretch, parallel to the elongation of the pluton. This is in agree-

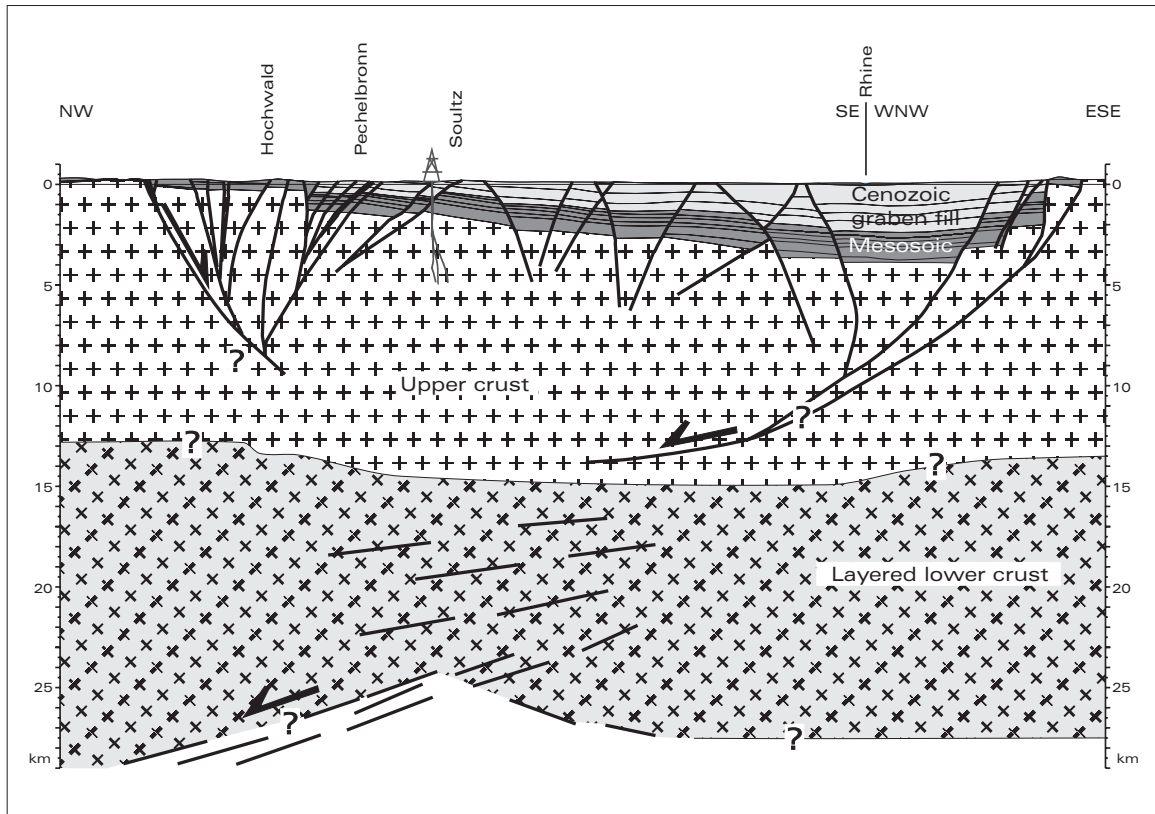


Figure 2.6: Geological cross section through the Rhine Graben at the latitude of Sultz. Modified after *Kappelmeyer et al.* (1991). Interpretation to the lower crust is done by analogy to the cross section of *Brun et al.* (1992) and is highly speculative.

ment with structural studies in the Black Forest, Odenwald and Vosges crystallines where the NE-elongation of plutonic bodies is associated with dominant NE-directed magma emplacement.

2.2.3 Tectonic history of the Sultz granite

The Sultz granite or more generally, the entire current URG area went through a multiphase tectonic history including Hercynian and Alpine orogenesis.

Many publications relate to the tectonic history of the Upper Rhine Graben. Already in 1965, *Illies* (1965) noted that the literature is legion and needs assiduous work to learn what has been published in that field. Since then, even more articles turn up and fortunately also some review papers bringing a synthesis to the various published works. In the following, I will first present the tectonic history as summarized in *Genter* (1989) and extended by *Dezayes* (1996). I used these works primarily

because they are directly related to the Soultz site. These summaries in turn are principally based on work from *Bergerat* (1985); *Schneider* (1984); *Villemain* (1986) (see Figure 2.7). I added to it also some information from *Krohe and Willner* (1995) concerning the Odenwald. Then in the paragraph 2.2.4, I will enlarge this summary to the discussion of the various models proposed for the Cenozoic formation of the Rhine Graben

As the Soultz granite is hidden under an approximately 1.4 km thick sediment suite, knowledge about the tectonic history has to be constructed from analyses of outcropping, neighbouring tectonic units. These are listed in Figure 2.7 and are the Lorraine basin, the Sarre basin, the western periphery of the graben, the middle to southern Vosges and the Odenwald. The locations of these areas are indicated on the map of Figure 2.4. As these zones are remote from the site of Soultz and not always in the same tectonic unit as the Soultz granite, their tectonic histories may well significantly differ from the one experienced by the Soultz granites and some caution has to be taken in using them. For example, granites from the middle and southern Vosges are in the so called Moldanubian zone, whereas Soultz granites are related to the north Vosgean crystalline tectonic unit, itself within the Saxothuringian zone (see Figure 2.8), or more particularly in the mid-german crystalline high (*Tait et al.*, 1997).

The Variscan Belt in Europe resulted from the collision, in Devonian and Carboniferous times, of Laurasia with Gondwana and a number of intervening microplates (*Franke*, 1989). The main orogenic phase is called the Sudetic phase and took place in Upper Viséan to Lower Namurian (i.e. synchronously and slightly after the intrusion of the Soultz granites). This phase has diverse expressions: The northern part of the Sarre basin was under compression, inducing thrust faulting with NE–SW directions (*Villemain*, 1986). In the Middle Vosges, *Schneider* (1984) describes an N–S compression inducing NE–SW sinistral and NW–SE dextral strike-slip faults. The Odenwald crystalline complex underwent a first steep NE–SW sinistral shear, followed by an extensional phase expressed by NNE–SSW trending normal faults dipping to the WNW or the ESE (*Krohe and Willner*, 1995). Extension also developed in the Sarre and Lorraine basins in Westphalian and Stephanian times. It is expressed mostly by N110° to N140° trending normal faults, probably related to the Asturian tectonic phase.

The Saalian phase, a last compression phase within the Variscan orogenesis, induced thrust-folds trending NE–SW as well as dextral E–W and sinistral NW–SE strike-slip faults in the Lorraine and Sarre basin. Then, during the late Permian the Hercynian orogeny ceased. Peneplanation of the mountain ranges occurred. The tectonic activity wound down, characterized by small extensions, first in a N–S to NNE–SSW direction in late Permian and early Trias and then in a E–W direction until end of Jurassic.

The non-diastrophic period ends in the early Tertiary, and in some places during latest Cretaceous, with the onset of volcanic activities. Such activity occurs long

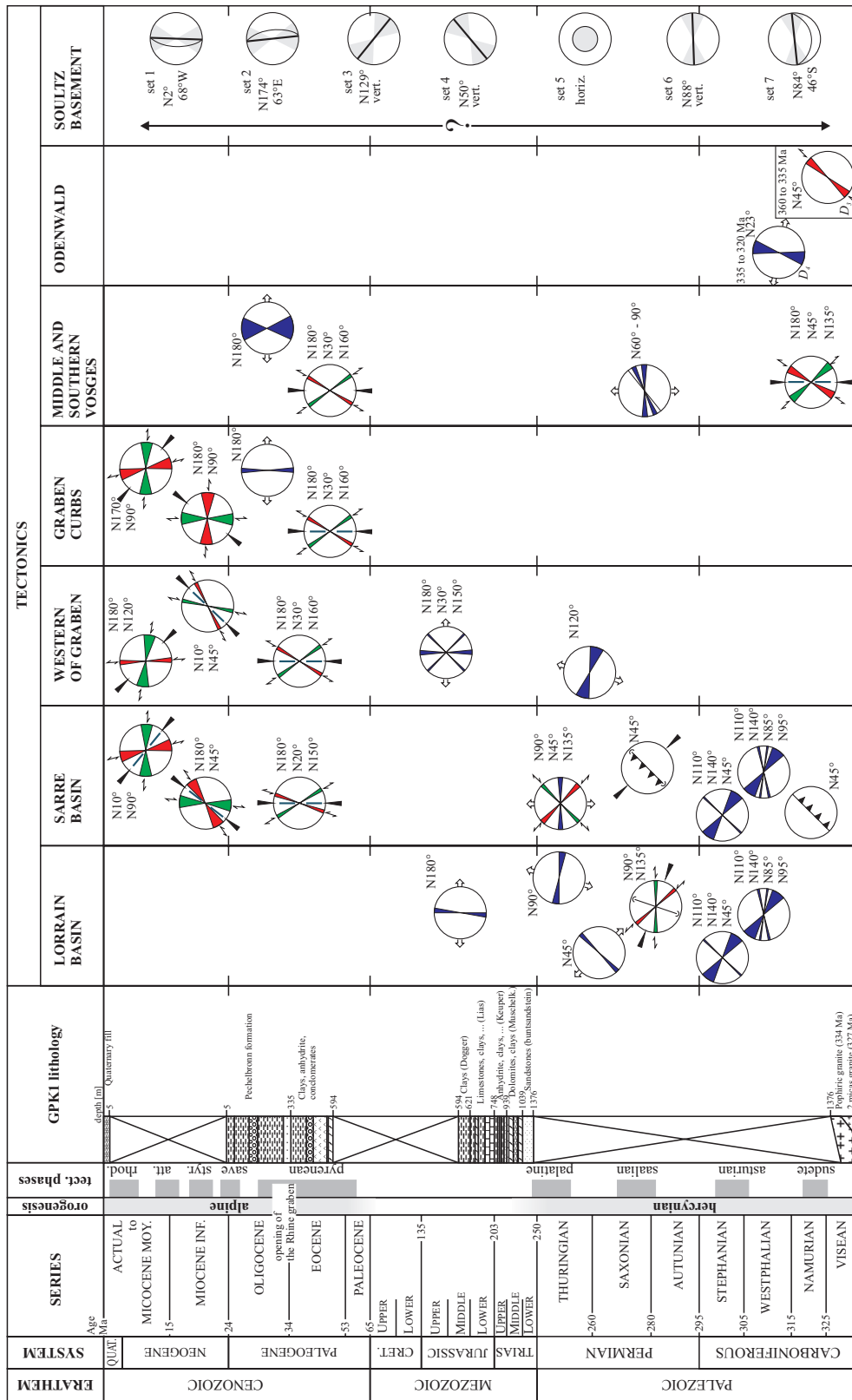
before rifting or graben-like subsidence started. *Bergerat* (1985) and *Villemin* (1986) proposed that the Tertiary tectonic history of the URG occurred on four phases. The analysis from *Dezayes* (1996) of fault/slickenslide data from EPS1 cores supports this scenario for the Soultz granite (Figure 2.9).

The first phase was characterised by N–S compression and took place in middle to late Eocene. It originated from the Alpine and Pyrenean collisions, which reactivated Variscan Permo-carboniferous and Mesozoic crustal scale faults in the URG (*Dèzes et al.*, 2004). At Soultz, *Dezayes* (1996) inverted fault/slickenside measurements on faults in the EPS1 cores for this phase and found a σ_1 direction that was horizontal and oriented N19°E (see Figure 2.9). Strike-slip faults for this phase strike mainly to N50° steeply dipping to the NW and to N150° steeply dipping to the NE.

The second phase was an E–W extension that represents the main rifting stage of graben formation. The extension took place from the end of the Oligocene to that of the Eocene. The transition from the previous phase occurred through an exchange in relative magnitudes of σ_1 and σ_2 without changing the principal stresses directions. This was accompanied by subsidence of the graben with maximum sedimentation in the south section of the graben. The depo-centre moved to the north at later times (see Figure 2.10). This main rifting stage occurred in the context of increased collisional coupling controlled by northerly directed compressional stresses developed within the Pyrenean and Alpine collision zones (*Dèzes et al.*, 2004). This extension is not seen outside of the graben, for example, in the Sarre basin to the west. In the Soultz region, inversion of fault/slickenside data indicates an horizontal N95°E direction for σ_3 (*Dezayes*, 1996). Faults associated to this phase strike about N–S, dipping at 60–70° to the E or W (see Figure 2.9).

In early Miocene, a NE–SW oriented compressive phase took place on Rhine Graben shoulders and surrounding and also in Sarre basin (*Villemin and Bergerat*, 1987). This phase is qualified to be intermediary and its detailed settings is not fully clarified (*Dezayes*, 1996). In middle Burdigalian, while subsidence carried on in the northern part of the URG, the southern part experienced uplift of the Blackforest-Vosges arch. So the maximum sedimentation at that time was located in the northern part of the graben (see Figure 2.10). *Dezayes* (1996) observe this NE–SW compression in the fault/slickenside data from EPS1 cores and found it to be oriented N70°. This event evidenced by NNE–SSW dextral and ENE–WSW sinistral strike-slip faults.

From late Miocene up to the present, the stress regime prevailing in the Rhine Graben is the NW–SE compression that is seen over much of western Europe, that lies north of the Alps and Pyrenees area (e.g. *Ahorner*, 1975; *Illies and Greiner*, 1979; *Muller et al.*, 1997; *Villemin and Bergerat*, 1987, and many others). This stress field reflects a combination of forces related to continued counter clockwise convergence of Africa-Ariabia with Europe and North Atlantic ridge push (*Dèzes et al.*, 2004). Fault/slickensides inversions at Soultz suggest a compression direction of N122° (*Dezayes*, 1996). Faults associated with this phase are N–S striking, very steep sinistral strike-slip faults or E–W striking, north dipping dextral strike-slip faults



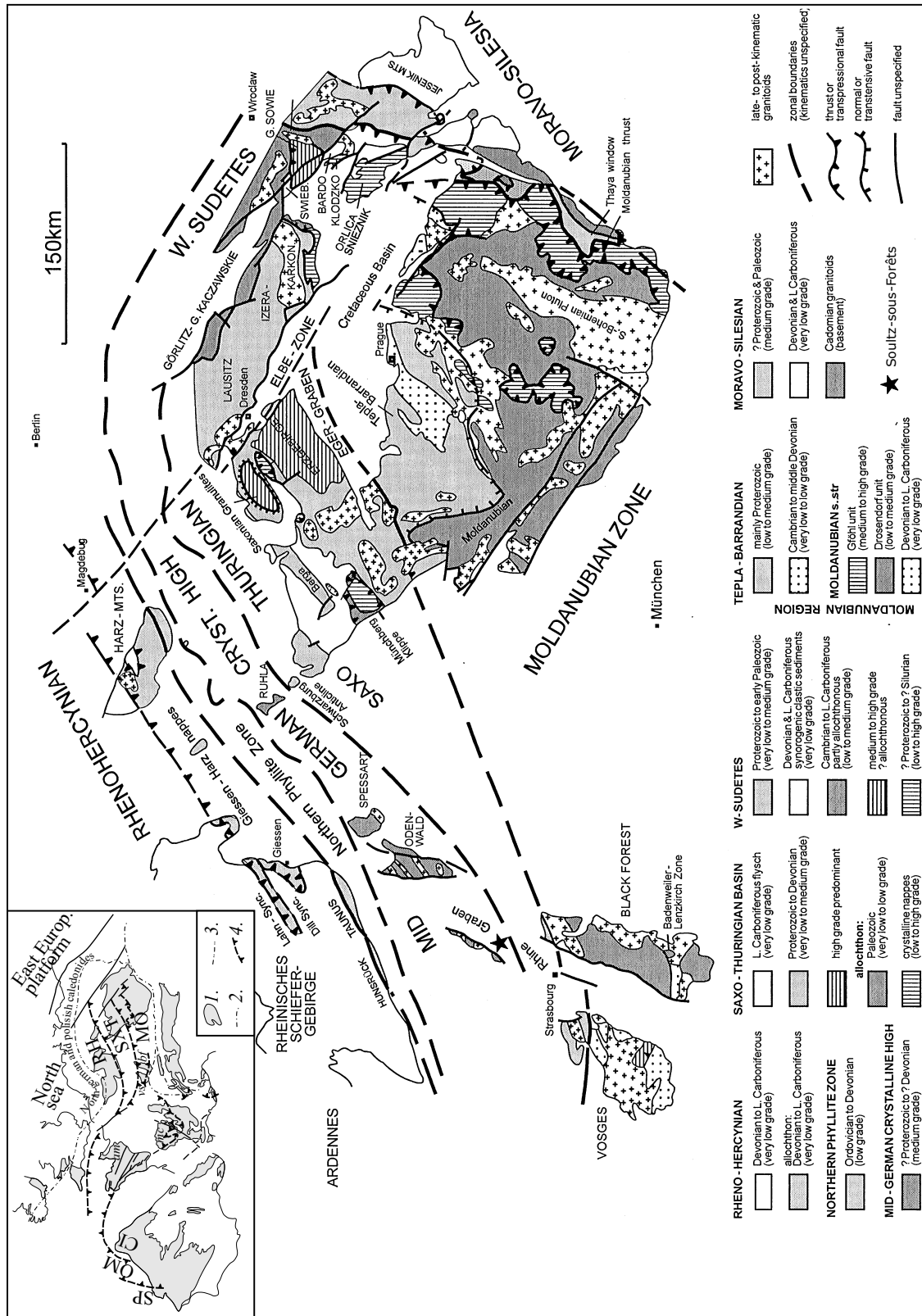
(see Figure 2.9). Note that nowadays, the maximum stress direction in the rock mass around the Soultz boreholes is no longer NW–SE, but N169°, defined without any doubt by borehole breakouts and drilling induced tension fractures directions (*Bérard and Cornet, 2003; Brudy and Zoback, 1999; Cornet and Bérard, 2003; Genter and Tenzer, 1995; Nagel, 1994; Tenzer et al., 1992; Valley and Evans, 2005, 2006a*).

2.2.4 Various tectonic models for the Cenozoic formation of the URG

In the following, I will basically present three models for the Cenozoic formation of the URG as proposed by *Illies (Illies, 1965, 1972; Illies and Greiner, 1979; Illies, 1975)*, *Villemin (Bergerat, 1985, 1987; Villemin, 1986; Villemin and Bergerat, 1987; Villemin et al., 1986)* and *Schumacher (Schumacher, 2002)*. These papers were chosen because they actually focus on the URG, and are thus more applicable to the Soultz area than the also relevant, larger scale reviews given by *Bois (1993; Cloetingh et al. (2005, 2006); Dèzes et al. (2004); Michon et al. (2003); Sissingh (1998, 2003); Ziegler (1992); Ziegler and Dèzes (2005)*. Other models have not been included, for example *Larroque and Laurent (1988)*, because they are focussed on small sub-area of the URG relatively distant from Soultz. The three retained models are not in absolute disagreement and nicely express the successive increase of knowledge with time as these works are published at about fifteen years intervals. Nevertheless, it was found interesting to present all three of them as they are based on various geological methods, for example geomorphologic studies, inversion of fault/slickenslides data or sequence stratigraphy and emphasise various aspects of the Cenozoic formation of the URG.

One key difference in these models is the influence and reactivation of structures inherited from previous tectonic phases, particularly the inheritance received from the Variscan orogenesis. Such reactivation of Variscan structures in Tertiary time is the core of a simplified model for the Rhine Graben formation proposed by *Illies (1965)*.

Figure 2.7: (on page 16) Synthesis of tectonic phases modified after *Genter (1989)*. Lorrain basin, Sarre basin, Western of graben and graben curbs after *Bergerat (1985)* and *Villemin (1986)*. Middle and Southern Vosges after *Schneider (1984)* and Odenwald after *Krohe and Willner (1995)*. In blue normal faults, in red sinistral faults and in green dextral faults. The last column present the fracture sets in the Soultz basement characterised in the present thesis (see Chapter 3).



In the Hercynian basement, the general strike of fold axis and intrusive masses follows a NE direction, oblique to the axis of the current graben. This is also the case for the elongation of the Soultz pluton (*Schulmann et al.*, 1997). However, parallel to and accompanying the young border fault of the graben are zones of blastomylonites, granitic dykes, and shear zones. Most of these lineaments are combined with sinistral strike-slip movement indicators and are possibly related to the Sudete tectonic phase in late Visean (see Figure 2.7). Indeed, the Hercynian mountain range was crossed by a NNE-striking shear element called Mediterranean-Mjoesa-Zone (*Illies*, 1972). Most conspicuous traces of this Hercynian structures are the Oetzberg lineament (Odenwald), the Bühlertal and Schweighof lineaments (Black Forest), and the Sainte-Marie-aux-Mines lineament (Vosges). Therefore, the initial condition for the formation of the Rhine Graben includes the presence of these NNE striking zones of weakness. This led to the simplistic model developed by *Illies* (1965) presented in Figure 2.11, where the inherited Hercynian NNE-striking crustal weakness is reactivated in Cenozoic time during the URG formation.

This simple two-step model is too basic. Particularly, the Cenozoic opening of the graben definitively did not occur in a single movement. Analysis of stylolites and other paleo-stress direction indicators indicate that the maximal principal stress were oriented NNE–SSW to NE–SW in Middle Eocene when the URG began to open (*Illies*, 1975). This orientation differs significantly with the general orientation of σ_1 currently measured in the same area, i.e. about N140°E. *Illies* (1975), as well as *Ahorner* (1975), conclude that a counter clockwise rotation of the stress tensor of about 60° took place between Eocene and present. Based on various chronological and temporal indicators, like swarms of dykes, syn-sedimentary faults, and sedimentary filling thickness, *Illies* was able to propose a timing for this rotation (see Figure 2.12). The three stages presented correspond to three maximum tectonic activity and related subsidence:

- At lower Oligocene with a NE–SW maximum compression.

Figure 2.8: (on page 18) Map of Hercynian structures. The small upper left frame shows a european overview simplified after *Franke* (1989). 1. Variscan Massifs 2. outer limit of alpine deformation 3. outer limit of Variscan 4. major thrusts or sutures. CI : Central Iberian zone ; MO : Moldanubian zone ; OM : Ossa-Morena zone RH : Rheno-Hercynian zone ; SP : South Portuguese zone ; SXT : Saxothuringian zone ; *am* : American Massif ; *bf* : Blackforest ; *mc* : Massif Central ; *vs* : Vosges. Main frame is the map of the tectonostratigraphical terranes in central European segment of the Variscan fold belt after *Tait et al.* (1997). The star localised Soultz-sous-Forêts.

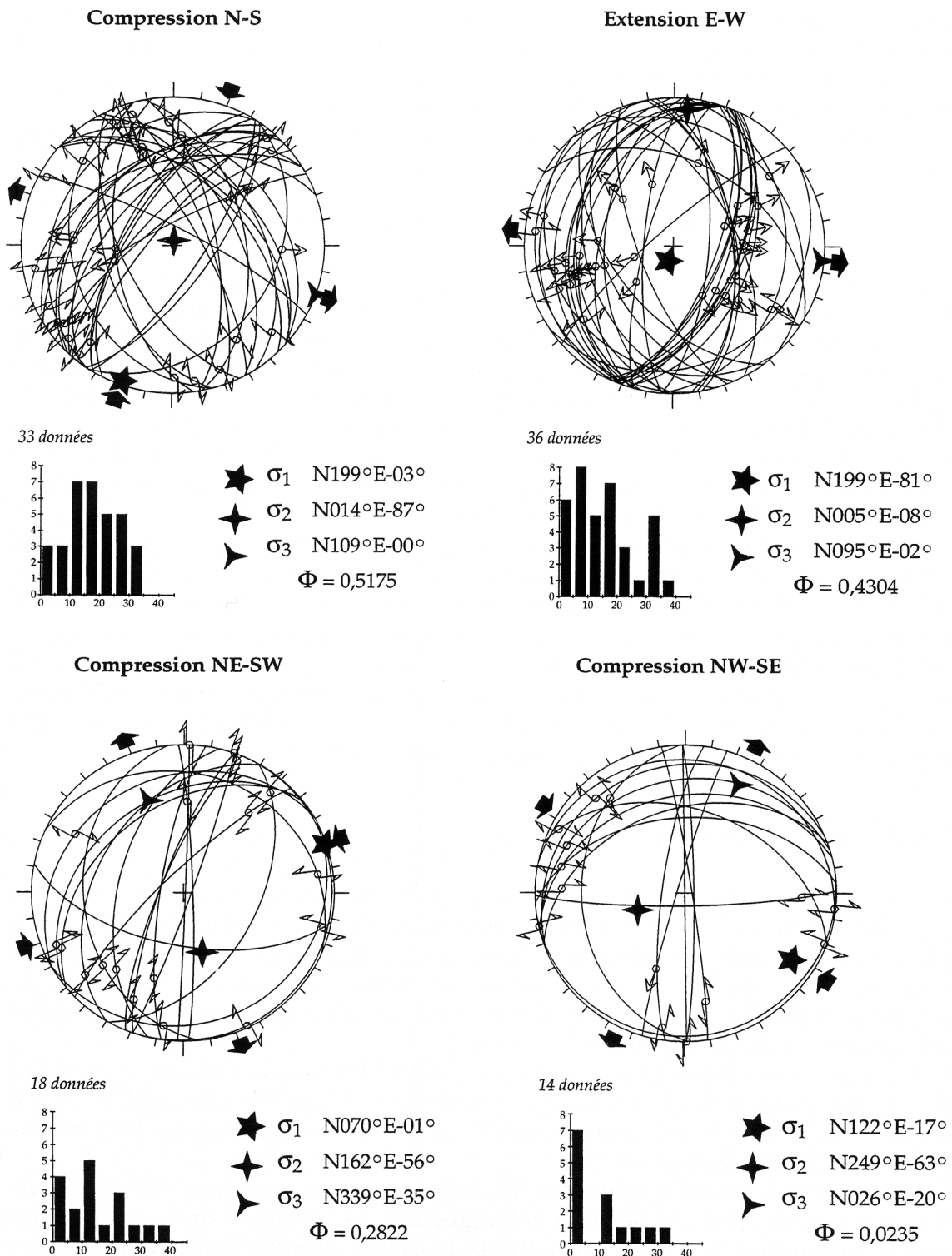


Figure 2.9: Inversion of fault/slickenslide data from EPS1 cores for the four Tertiary tectonic phases. Stereographic projection are equal area, lower hemisphere. After (Dezayes, 1996).

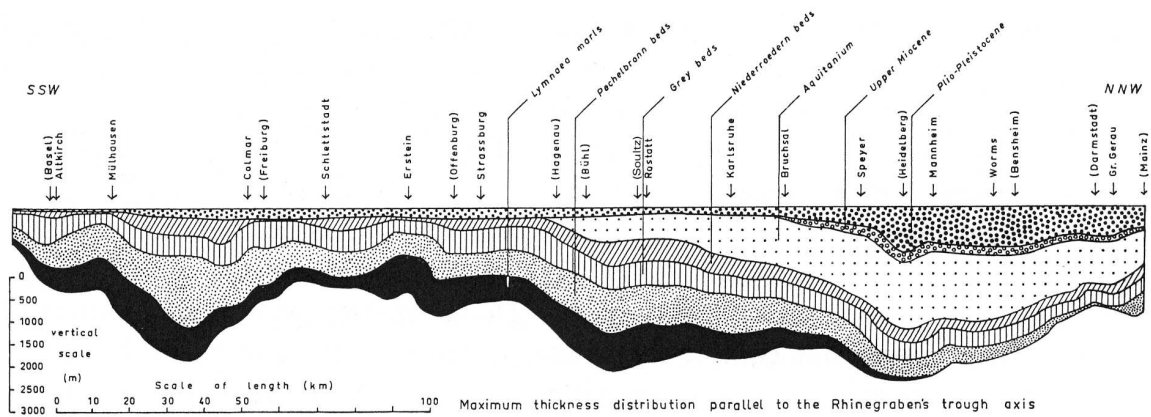


Figure 2.10: Maximum thickness distribution of the sedimentary filling parallel to the Rhine Graben's through axis. After *Illies* (1972).

- At lower Miocene (Aquitanian) with a N–S maximum compression.
- In Pleistocene to present with a NW–SE maximum compression.

The obliquity of the URG with the current state of stress makes the URG a generally sinistral strike-slip structure. Due to its slightly crooked shape, combined movements on the faults induce varying behaviour in different parts of the URG. According to *Illies and Greiner* (1979), the northern and southern parts of the graben are under subsidence while the middle part is uplifting (see Figure 2.13).

The model of *Villemin* (*Bergerat*, 1985; *Villemin*, 1986; *Villemin and Bergerat*, 1987; *Villemin et al.*, 1986) derived a slightly different chronology, with one more phase. Their work is based mainly on the inversion of faults/sliken-slide data. Similar results have been obtained at Soultz from fault/sliken-slide data on the EPS1 cores by *Dezayes* (1996). Their model for the Eocene formation of the Rhine Graben includes four phases:

- A first phase — which arguably took place in late Eocene — is characterized mainly by a conjugate system of N40–50° striking sinistral strike-slip faults and N140–150° striking dextral strike-slip faults. These are frequently associated with sinistral Riedel's fractures striking N10–20° or N–S. The model developed by *Illies* (1965, 1972); *Illies and Greiner* (1979); *Illies* (1975) outlines that these faults may be inherited from Hercynian orogenesis. N–S oriented stylolites and tension fissures also accompanied this phase. The mean stress tensor for this phase, inverted from slickenslides/faults data set, is characterised by a maximum principal stress σ_1 horizontal oriented N–S, and a minimum principal stress σ_3 horizontal oriented E–W.
- At the end of the Eocene and during the Oligocene, maximum subsidence took place in the South of the URG. This corresponds to a second tectonic phase,

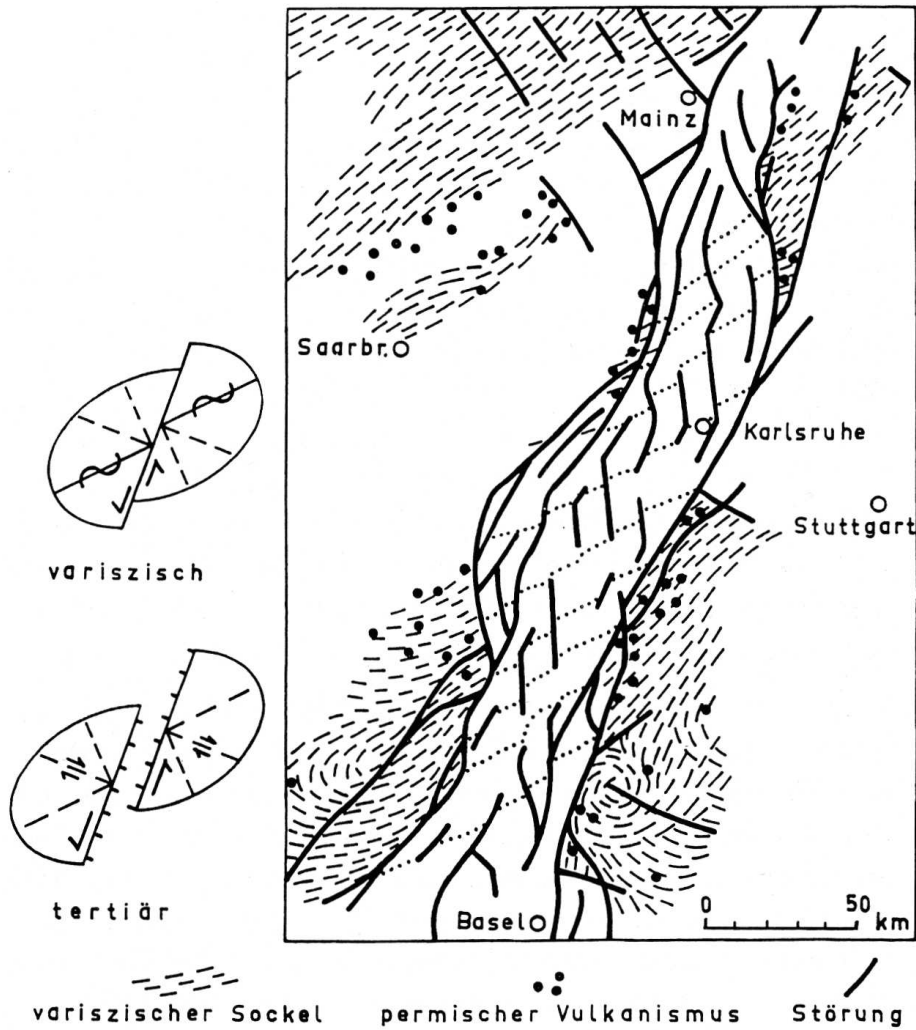


Figure 2.11: Simple model for Rhine Graben formation proposed by Illies (1965). The Cenozoic opening of the graben reactivates a NNE striking crustal weakness inherited from Variscan orogenesis.

where principally N–S to NNE–SSW sinistral strike-slip faults and N–S tension fissures, created during the previous phase, are reactivated in normal faulting. For NNE–SSW faults and even more seriously for some NE–SW or NW–SE faults, a significant strike-slip component is noticeable during that stage. Relays between N–S and NNE–SSW faults are responsible for the zigzagging pattern of the graben borders. The stress state during this phase is characterised by a vertical maximum principal stress and an E–W minimum principal stress. As this stress state is oblique with the general trend of the graben, this produces movements parallel to the graben orientation. Angelier and Bergerat (1983)

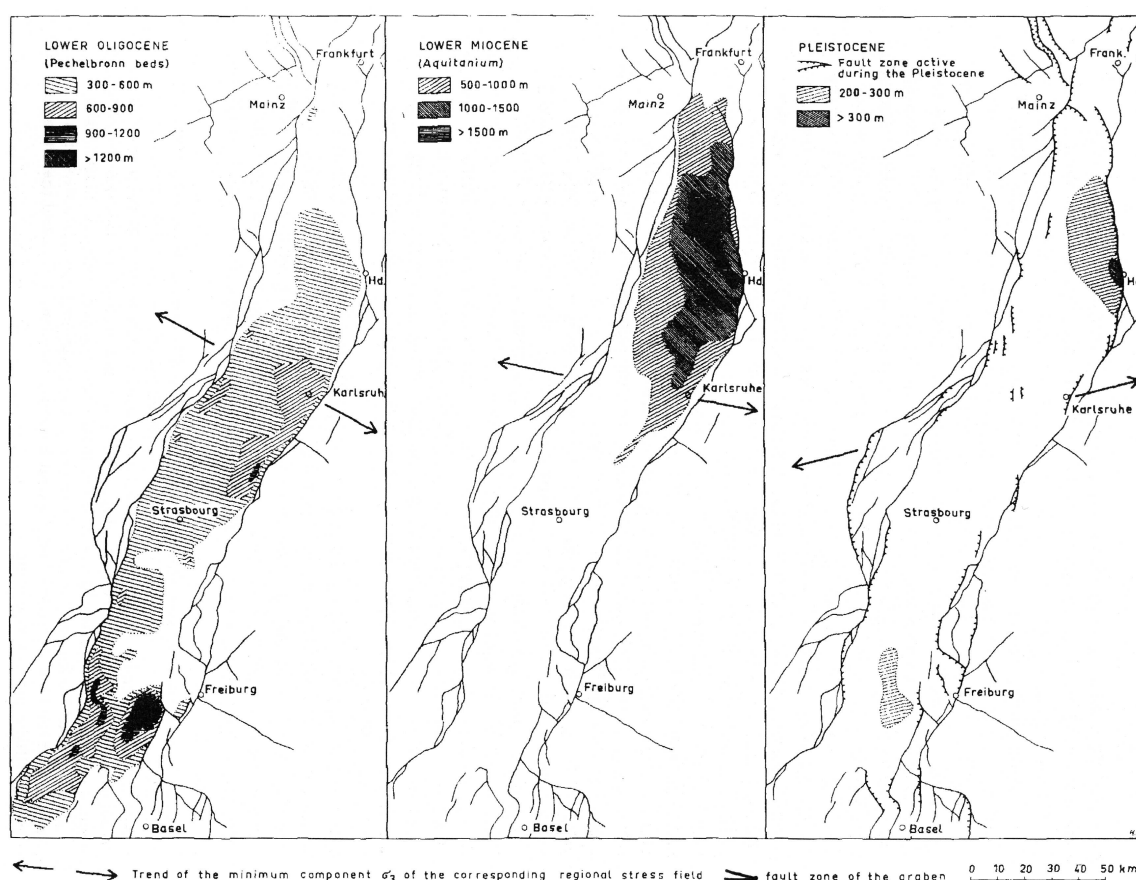


Figure 2.12: Faulting and fault-trough subsidence of the URG and their interdependence with the varying stress condition in the framing plate unit. After Illies (1975).

quantify these parallel movements being 300–400m for each kilometre of extension in the direction perpendicular to the graben. Note that the principal stress directions are the same as during the preceding episode, but the relative magnitude of σ_1 and σ_2 have been exchanged. This permutation explains that contemporaneously, surroundings of the graben remain in a N–S compressive stress field. At that time, the URG is a localised distensive structure within a regional N–S compressive context.

- Posterior to the Oligocene distensive phase, N–S striking faults were reactivated in dextral strike slip movements. They were associated with conjugate N80–120° striking sinistral strike-slip faults as well as the opening of N40–50° striking faults inherited from the Eocene phase. Crystallisation forms on these planes as well as stylolite with the same orientation. The orientation of the principal stresses for this phase is horizontal N40–60° for σ_1 and horizontal N130–150°

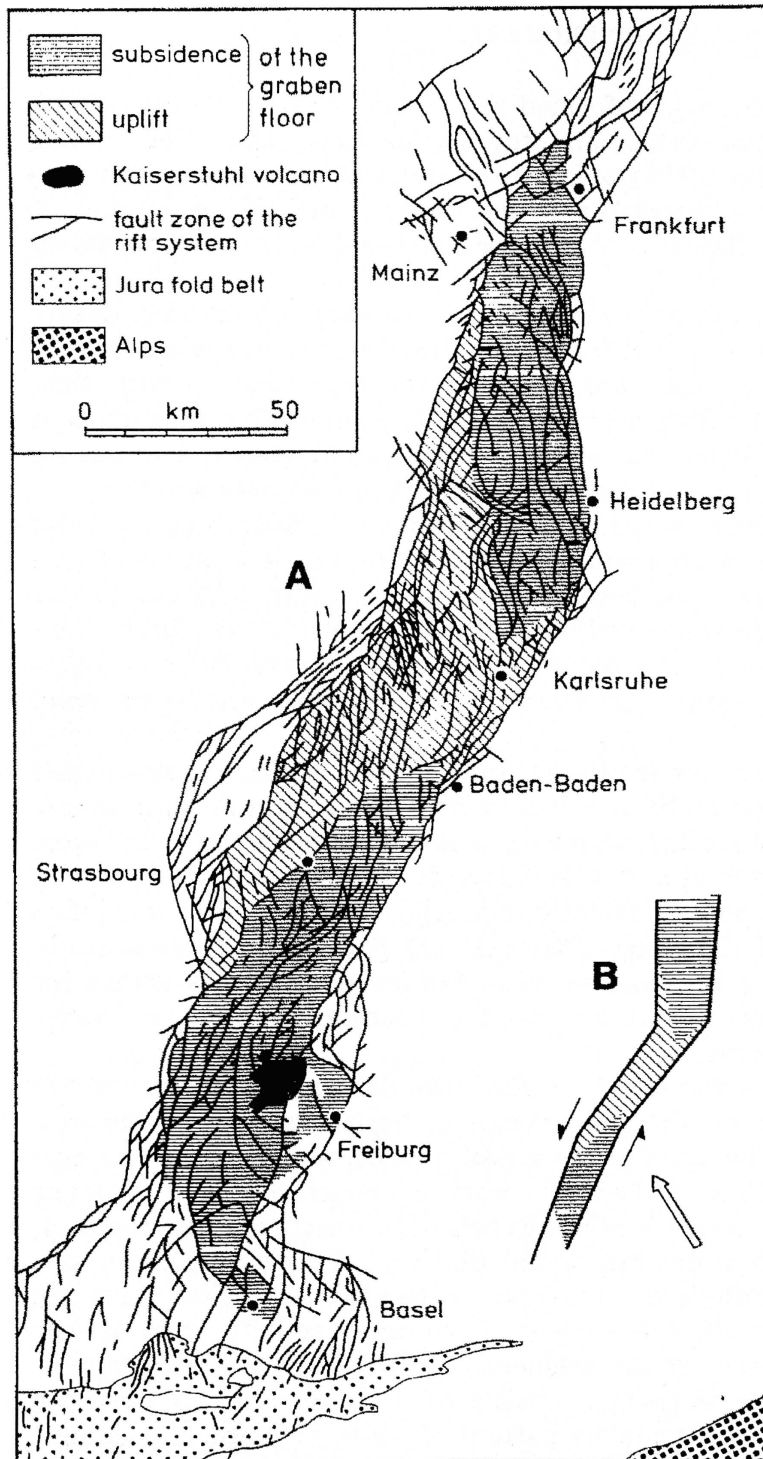


Figure 2.13: Neo-tectonic activity in the Rhine Graben after *Illies and Greiner (1979)*. Due to the obliquity to principal stress direction, the URG behave as a sinistral shear zone. Moreover, the crooked shape of the graben induces different behaviours in the southern and northern parts of the graben comparing to its middle part.

for σ_3 .

- Finally, an ultimate phase which continues today includes a NW–SE maximum compression and a NE–SW minimum compression. Relatively to the previous phase, this implies again a principal stress permutation, but between σ_1 and σ_2 . This state of stress remobilizes N–S striking faults in sinistral strike-slip movements and associated to them are conjugated dextral strike-slip fault oriented N80–120°. These conjugated fault may be inherited from the previous phase.

This tectonic history is schematized in Figure 2.14. Note that the difference between *Illies* (1975) and *Ahorner* (1975), and *Villemin and Bergerat* (1987) is not only that *Villemin and Bergerat* include one more tectonic phase, but the chronology itself is different. The NE–SW compression is placed before the main Oligocene extension in the *Illies* (1975) and *Ahorner* (1975) chronology, however it is placed after the main extension in the *Villemin and Bergerat* (1987) chronology. It is also interesting to note that Hercynian pre-structuring is not required in their model.

On the other hand, pre-structuring plays a dominant role in the model presented by *Schumacher* (2002), for whom the main structural trends of the URG were already established during Paleozoic times. The most prominent trend — often called Erzgebirgian — is the general Hercynian orientation NE to ENE: the major Variscan dislocation zone which delimited the Hercynian tectonic realms strike in that direction (see Figure 2.8). A second very important trend — called Rhenish — is oriented NNE and is related to sinistral strike-slip fault zones associated with Lower Carboniferous to Permian intrusive bodies and dyke swarms (*Cloos*, 1922; *Edel and Weber*, 1995; *Edel et al.*, 2004; *Illies*, 1962; *Rotstein et al.*, 2006). N to NNW (an orientation called Egian) striking Riedel shears are associated to these sinistral shear zones. Dextral fault trending NW (Hercynian) are conspicuous in the surroundings of the URG (*Ziegler*, 1986). Some of them may have acted as dextral Riedel in the late Variscan Orogeny, particularly during Stephanian-Autunian (e.g *Arthaud and Matte*, 1977; *Ziegler and Dèzes*, 2005). Another relevant pre-rift setting is the presence of ENE trending Permo-Carbonifer troughs, which are parallel to the structural grain of the Variscan Orogeny (*Debrand-Passard and Courbouleix*, 1984; *Diebold et al.*, 1991; *Donsimoni*, 1981; *Kneuper*, 1976). In Mesozoic, platform sediments covered the peneplained Variscan basement. The soft tectonic activity of that period did not contribute significantly to the pre-rift structural inventory in the URG area.

Schumacher (2002) describes the rift evolution based on tectono-stratigraphic analysis of the Cenozoic filling of the URG (see Figure 2.15). The proposed tectonic history can be summarized in the four following phases:

- Before Late Eocene, σ_1 were oriented N–S (*Villemin and Bergerat*, 1987). In Middle Eocene, the first Tertiary sediments in the URG were red siderolitic formations and residual clays which documented lateritic and karstic weathering of the Mesozoic platform under a humid tropical climate. They are associated

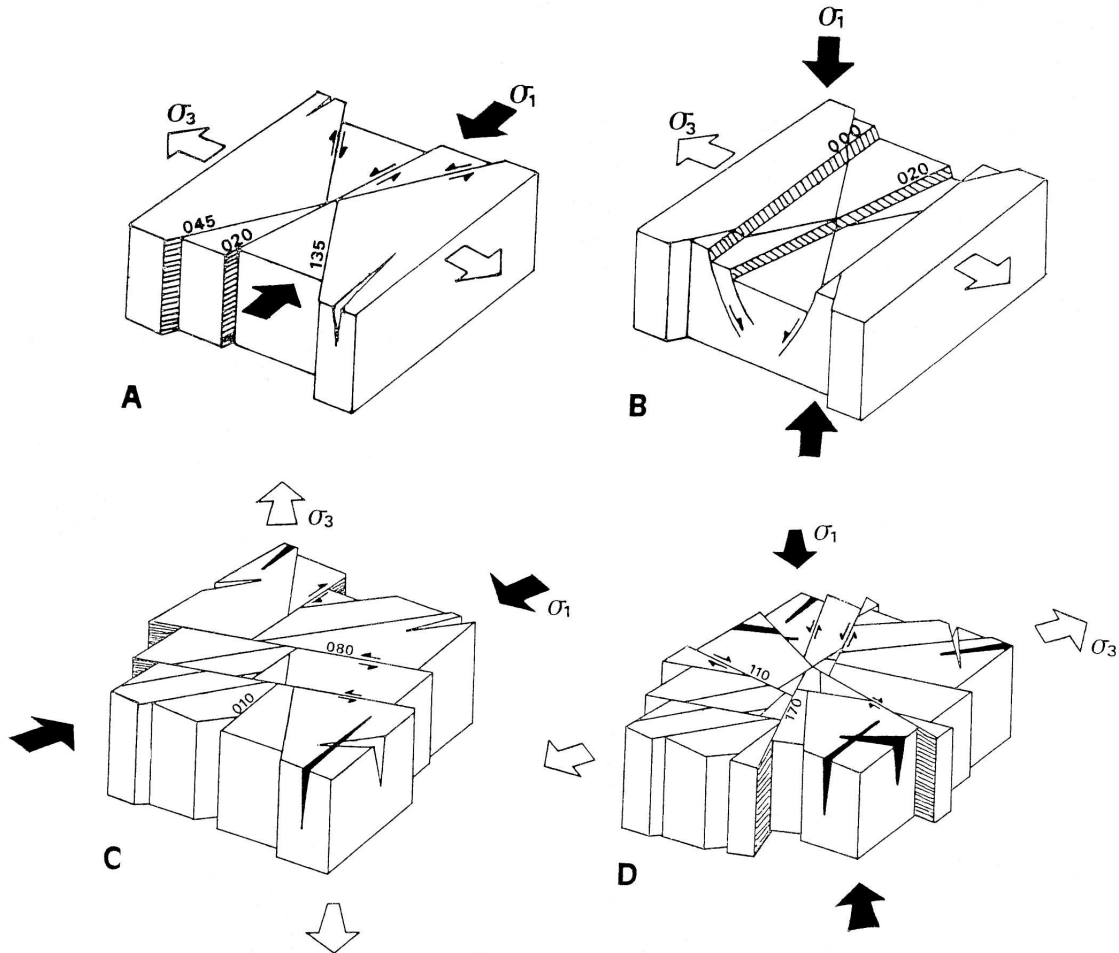


Figure 2.14: Synthetic bloc diagrams of the Cenozoic formation of the URG. A. Eocene N–S compression phase. B. Oligocene E–W extension phase. C. NE–SW compression phase. D. NW–SE compression phase. After *Villemin and Bergerat (1987)*.

and followed by freshwater limestone and swamp deposits which superimposed Late Paleozoic structural depression and prefigured the initial rifting phases of Late Eocene. In Late Eocene, a large subsidence took place in the southern and middle part of the URG, i.e. the Mulhouse and Strasbourg sub-basins (Figure 2.15b). These sub-basins are superimposed on the late paleozoic troughs and highs as previously described. Their depo-centers axis are oriented to the ENE, in obliquity with the later general rift trend. Furthermore, these basins develop where ENE oriented paleozoic troughs intersect NNE striking Rhenish lineaments. *Schumacher (2002)* proposed that these basins were formed in pull-apart like structures, resulting from the sinistral reactivation of the margin of

the Permo-Carboniferous troughs combined with the opening of NNE trending weakness zones. A general ambient stress field with σ_1 oriented NNE–SSW and σ_3 oriented ESE–WNW, i.e. slightly rotated clockwise in comparison to the determination from *Villemin and Bergerat* (1987), is needed to allow such a structural setting to occur. This rotation took place arguably in the Late Eocene. The formation of the initial syn-rift sub-basins of the URG area was then controlled by Permo-Carboniferous inherited crustal discontinuities.

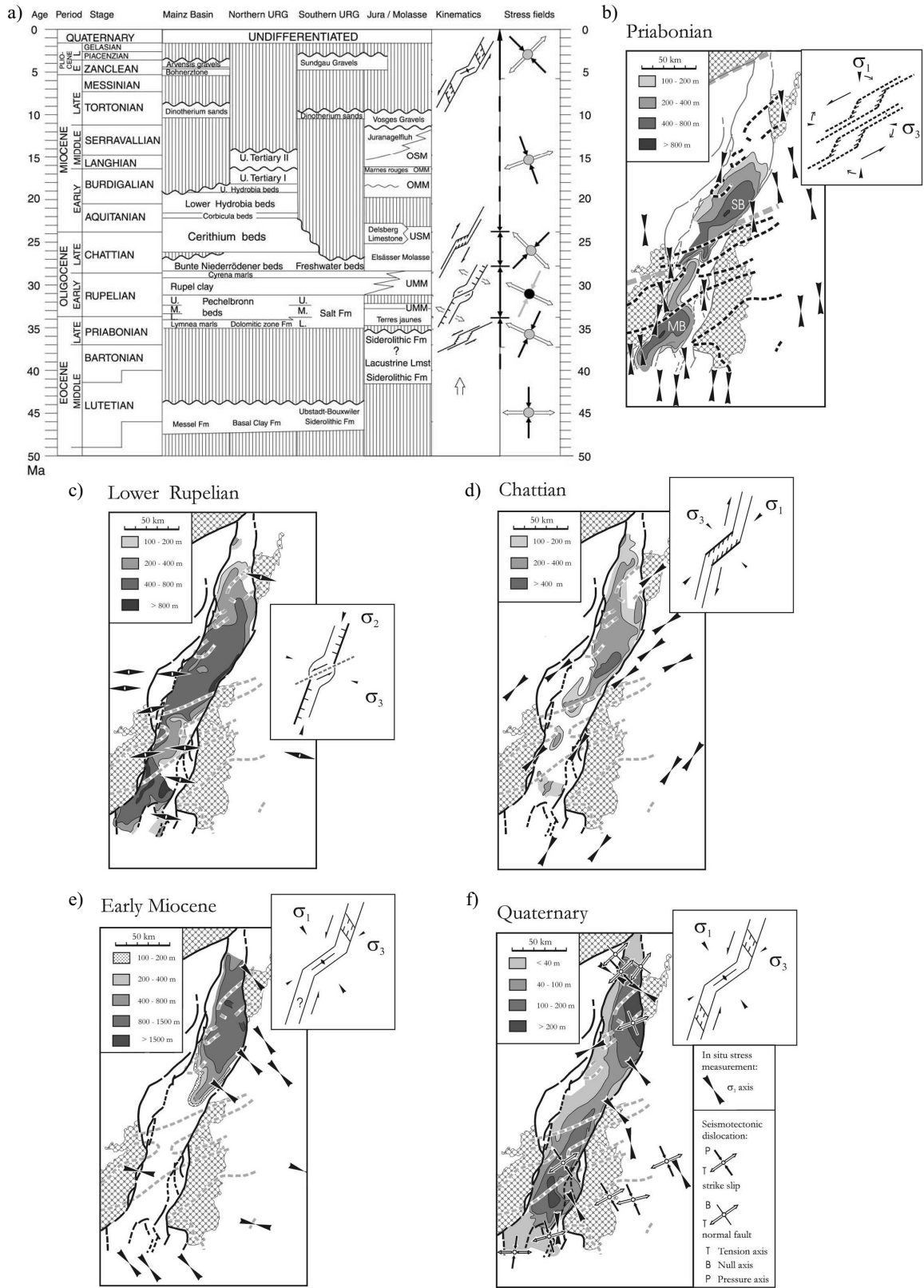
- In Early Oligocene, isopach maps of the lower Rupelian (Figure 2.15c) shows that the depo-centers are located close to the Western Border Fault in the south and close to the Eastern Border Fault in the west. This suggests that the master faults were the western one in the South and the eastern one in the North. The northern margin of the Black Forest High plays the role of a sinistral transfer zone connecting the master faults of the so formed southern and northern half grabens. Global ambient stress in this situation is σ_1 vertical and σ_3 E–W to ESE–WNW, brought by the permutation of σ_1 and σ_3 in comparison to the previous phase (*Villemin and Bergerat*, 1987). This situation persists in Upper Rupelian, but, at that time, a shift of the main depo-center toward the middle graben segment was already evident.
- The positioning of the main depo-center in the middle graben segment, which has a NE orientation, is characteristic of the situation in Late Oligocene (Chat-tian, see Figure 2.15d). This situation is attributed to the reactivation in dextral strike-slip movements of the graben border fault system with the rapidly subsiding central graben segment forming a releasing bend. The ambient state of stress for this phase is a NE compression (σ_1). This situation was introduced by a further clockwise rotation of stress tensor and a permutation between maximum and intermediate principal stress.
- A new tectono-sedimentary regime was established in the early Miocene (Figure 2.15e). At that time the northern part of the URG further subsided, whereas the middle and the southern segments of the Graben started to uplift and were subjected to erosion. This uplift was accompanied with the Kaiserstuhl volcanism and affected the Vosges and Black Forest from which erosion product — Jura Nagelfluh — was shed (*Laubscher*, 2001). This may reflect a northward migration of the external flank of the alpine foreland bulge. On the other hand, localised uplift of the southern margin of the URG may result from transpressional reactivation of the Burgundy Transform Zone under NW–SE orientated compressional stress fields. This new stress setting was initiated in the early Miocene times with the onset of a counterclockwise rotation of σ_1 . This is a different interpretation than the one of *Villemin and Bergerat* (1987) who suggested that this new stress setting was due to another permutation between σ_1 and σ_3 . Regardless of the sequence that sets this state of stress, under these

conditions the URG acted globally as a trans-tensional sinistral strike-slip zone with the formation of a threshold in its middle segment. This general situation has lasted to the present, and the subsidence in the Southern part of the graben has resumed (Figure 2.15f).

As already mentioned, the three presented scenarios have more common than diverging points. In addition to the scenario presented by *Illies*, analyses of fault/strike-slip data outlined by *Villemin and Bergerat* highlight the multiple phases of Cenozoic evolution of the URG, with various states of stress involved in each phase. The synthesis of *Schumacher* refines the studies of *Villemin and Bergerat* by introducing better chronological control from the tectono-stratigraphic analysis. *Schumacher* also placed emphasis on the importance of the Paleozoic pre-structuring, particularly for the early rifting phases. While some diverging points are still unclarified between these scenarios, they do present a clear enough context to assess the tectonic condition that has led to the fracturing of the Soultz granite. Note that the recent publication of *Lopes Cardozo and Behrmann* (2006), analysing newly gathered sets of fault/slickenside data state that the tectonic history of the URG may be less complex than has been presented. Their conclusions bring us back to the *Illies'* (1965) simplified model, i.e. a single phase continuous trans-tensional kinematics in space and time. More realistically, *Behrmann et al.* (2003) also proposed a simpler model based on 3D restoration of fault systems. Their conclusions led to a two-fold evolution of the URG including an early extension oriented N80°E and a subsequent extension oriented N60°E. *Michon and Merle* (2005) also suggested a two-fold history for the URG with a Eocene-Oligocene NW–SE extension followed by a Miocene–Quaternary NE–SW extension. More important is the very active debate that occurs when enlarging the discussion to the evolution of the entire European Cenozoic Rift System (ECRIS). One may refer to *Dèzes et al.* (2004, 2005); *Michon and Merle* (2005); *Michon et al.* (2003); *Ziegler and Dèzes* (2005) for papers on this debate. One main, not fully understood aspect in this debate, is the large scale tectonic history and pattern that caused and drove the formation of the URG.

Figure 2.15: (on page 29) Cenozoic development of the URG after *Schumacher* (2002). a) Stratigraphic table for Cenozoic sediments of the URG and neighbouring region based on *Berger et al.* (2000). For the stress field column, black= σ_1 , gray= σ_2 and white= σ_3 . b), c), d), e) and f), isopach maps for various time span including as inserts a tectono-kinematic interpretations. Arrows for stress measurements are from *Villemin and Bergerat* (1987). Converging black arrow= σ_1 . Diverging black arrow= σ_3 .

2.2 Geological context and tectonic settings



2.3 The 5 km deep borehole image data set at Soultz-sous-Forêts

The primary source of data are acoustic borehole televiewer logs (BHTV) acquired in deep boreholes of Soultz-sous-Forêts geothermal site called GPK2, GPK3 and GPK4. The present section gives information of general interests concerning the characteristics of the deep wells and the logs acquired.

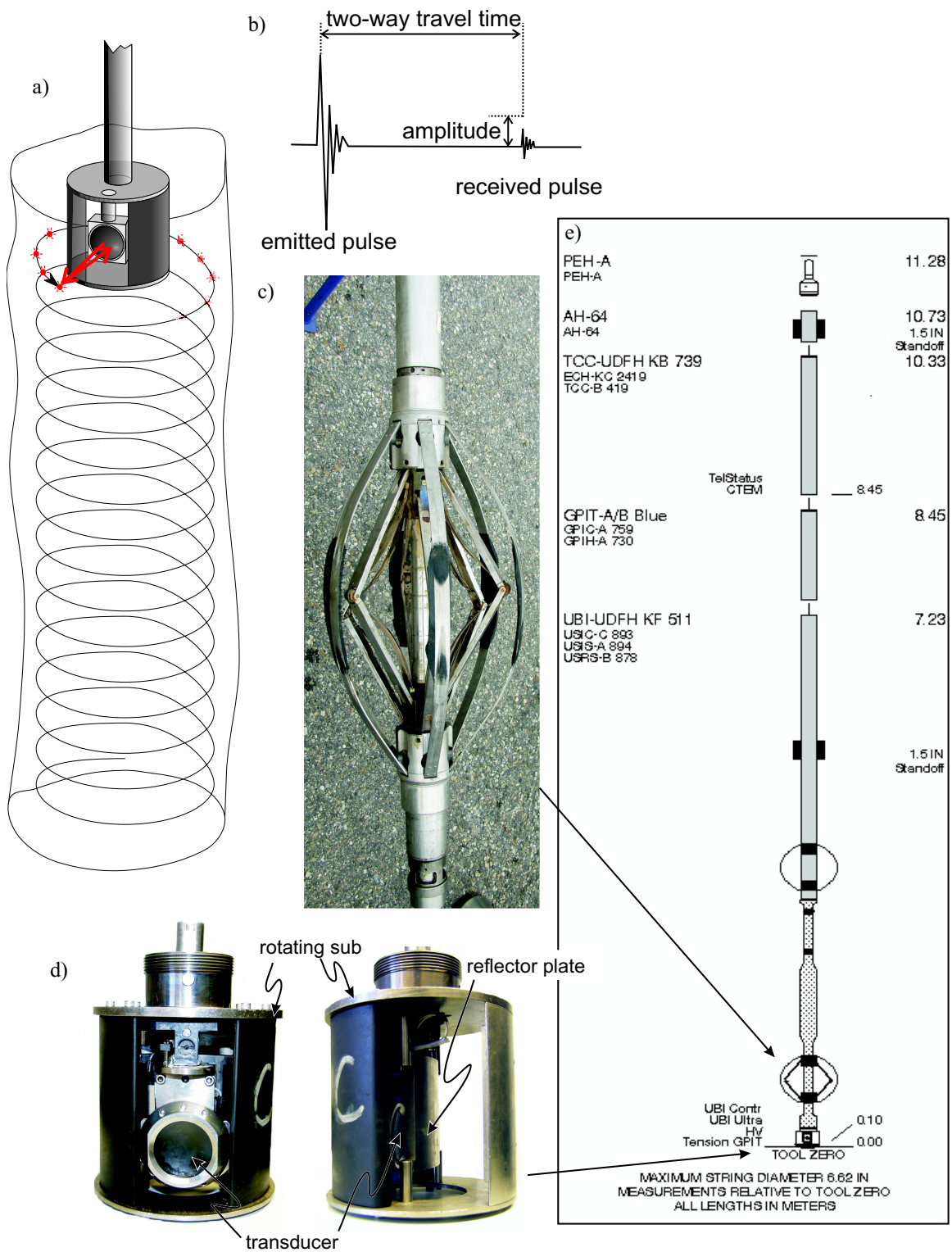
2.3.1 Acoustic imaging measurement principle

The ultrasonic (or acoustic) borehole televiewer was first described by *Zemanek et al.* (1970). The sondes used in the deep boreholes at Soultz are the Schlumberger versions of the tool called the Ultrasonic Borehole Imager (UBI). The master part of the tool used is a 2.5 MHz transducer inserted in a rotating sub (see Figure 2.16d). An important feature of the Schlumberger tool is that the transducer is decentred in the sub so that various sub diameters can be used in order to optimise the transducer–borehole wall distance for various borehole diameters.

A single measurement consists of the emission of an ultrasonic pulse in the direction of the wellbore wall and the recording of its reflection from the borehole wall (Figure 2.16b). Two parameters of the received pulse are evaluated and recorded: the two-way travel time (i.e. the time between emission and reception of the reflected pulse) and the amplitude of the received pulse. The two-way travel time is function of the borehole radius and the wave velocity in the mud filling the borehole. Knowledge of the wave velocity in the mud permits the borehole radius to be estimated. The measurement is repeated 150–250 times as the sub rotates, thereby yielding a very detailed picture of the borehole geometry (Figure 2.17). The received amplitude depends of the borehole fluid attenuation, the acoustic reflectivity of the rock at

Figure 2.16: (on page 31) Description of the UBI tool principle. a) the UBI tool scan the wellbore wall with a spiralling scheme with a distance between two successive spiral loop depending of the logging speed. b) each measurements consist of emitting a ultrasonic pulse in the direction of the wellbore wall and recording the received pulse. The two-way travel time and the amplitude of the received pulse are recorded. c) The image quality is sensitive to tool centralisation. Stiff centralisers are used in order to provide the best centralisation of possible. d) Picture of the master part of a UBI tool, i.e. the rotating sub with the transducer. One the left image, the transducer is in logging position whereas in the right image it is in mud velocity measurement position. e) Sketch of the tool string used in the 8-1/2 inch section of GPK4.

2.3 The 5 km deep borehole image data set at Soultz-sous-Forêts



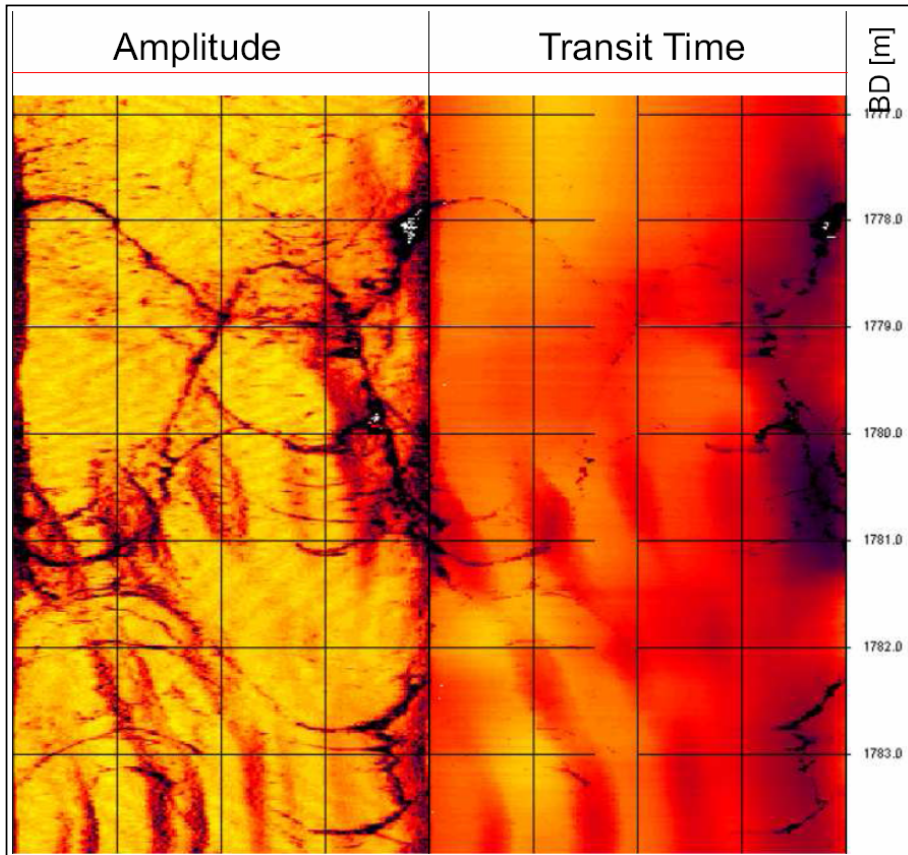


Figure 2.17: Example of UBI images. That example come from GPK4, 1777 – 1784 m BD. Left amplitude image, right two-way travel time image.

wellbore wall, its rugosity which which tends to scatter the energy of the signal, and the perpendicularity of the wellbore wall to the incident beam. Due to these various influences, a unique and unambiguous interpretation of the physical meaning of the received amplitude is often not possible. Nevertheless, the presence of fractures tends to reduce the reflected amplitude because of lower reflectivity and higher rugosity, thereby allowing the fractures to be imaged (Figure 2.17).

Like most geophysical logs, the UBI images are acquired while pulling the sonde out of hole. However, during the trip in hole, the transducer in the UBI sonde is rotated through 180° to look ‘inwards’ towards a reflector plate, thereby allowing the sonde to measure the profile of acoustic velocity velocity in the mud as the sonde run into the hole (Figure 2.16d). These data are afterwards used to transform two-way travel time measurements in true borehole radius.

The 2.5 MHz transducer used in the measurements will produce a spot size of about 0.25” (0.635 cm) in an 8.5” diameter borehole containing water. During logging at the Soultz holes, the sub rotated at 6 revolutions per second, and 180 measurements

per revolution are made, giving an angular resolution of 2° . While pulling the tool out of well, the sonde scans the borehole wall following a spiral as shown in Figure 2.16a. The distance between two successive spiral loops depends of the logging speed, and is 0.508 cm for 2 m/min logging speed, and 1.016 cm for 4 m/min. Since the spot size is 0.635 cm, the measurement swathe for the 2 m/min logging speed completely covers the borehole with a slight overlap, whereas there is a small gap between swathes at 4 m/min.

Due to the high rate of data transmission to the surface, the maximum time window allocated for each measurement is 165 μ s. Thud, if the wellbore walls are too far from the tool, it is possible that the reflected pulse will arrive after this time and the data point will be lost. In such cases it is also possible that late arrivals perturbed the next measurement. Thus, ultrasonic borehole images are difficult to acquire in borehole section with extreme enlargement. For this reason, and also to insure the perpendicularity of the ultrasonic beam with the borehole walls, a good tool centralisation is necessary. Stiff centralisers are thus a very important element of a UBI tool (Figure 2.16c).

In order to permit the orientation of the image, a General Purpose Inclination Tool (GPIT) is included in the tool string (Figure 2.16e). Usually a gamma ray tool is also included in the string in order to permit depth matching with other logs, but unfortunately this was not the case for the GPK3 and GPK4 UBI logs.

2.3.2 Technical information on the 3 deep boreholes

The data analysed in this PhD study stem from the three deep wells GPK2, GPK3 and GPK4 drilled to 5km at the Soultz-sous-Forêts geothermal project site. The granite part of GPK3 and GPK4 were drilled in two sections using two different bit sizes (Figure 2.18). A 12-1/4 inch bit was use down to 4582.8 m MD for GPK3 and down to 4757.3 m MD for GPK4. MD denotes measured depth along hole from ground level, which is at an altitude of 167.9 m (IGN69) for all three boreholes. GPK3 and GPK4 were then extended to total depth with an 8-1/2 inch bit. GPK2 was drilled down to 3880 in 1995 with a 8-1/2 inch drill bit. In 1999, it was deepened to 5057 with a 8-1/2 inch drill bit and from there to 5093 m with a 6 inch core barrel.

All three wells were drilled from the same pad and needed to be deviated in order to build the necessary down hole separation. The well trajectories are presented on Figure 2.19a–c. GPK2 was planned to be about vertical. It finally deviates to the NNW with maximum angle from vertical of 20° at 4500 m. GPK3 and GPK4 are deviated to the SSE with maximum deviation in GPK3 reaching 26° and maximum deviation in GPK4 being 34° .

2.3.3 Description of the images acquired in the deep boreholes of Soutz-sous-Forêts

The GPK3 logs were acquired in two runs with a logging speed that gave a vertical resolution of 1 cm. The first run was acquired on 25th Oct. 2002 in the 12-1/4 inch section, some 5 days after the completion of drilling. This log extends throughout the 12-1/4 inch section from 1439 m MD (the casing shoe of a higher section) to 4532.6 m MD. The images of the lowermost 13.8 m are not oriented. The second log was run on 10th Nov. 2002, some 21 days after the hole had been extended as 8-1/2 inch diameter to TD at 5103 m MD. The log covers the 8-1/2 inch section from the 12-1/4 inch casing shoe at 4558.2 m MD to 5100.8 m MD, with the lowermost 2.6 m not oriented. The images are generally of excellent quality with few logging artefacts. 'Key seats' (see *Lofts and Bourke*, 1999) are visible along the entire inclined 12-1/4 section and some parts of the inclined 8-1/2 section, but they are easily identifiable and affect only a limited part of the borehole circumference. The presence of borehole breakouts, particularly in the lower part of the wells also reduces the visibility of the natural fractures.

The logs in the GPK4 borehole were also acquired in two runs that followed the drilling of the 12-1/4 inch and 8-1/2 inch sections. The log in the 12-1/4 inch was run on 15th Feb. 2004, some 15 hours after drilling, from 1421.3 to 4723.3 m MD. The log in the 8-1/2 inch section was run on 12th Apr. 2004, 18 hours after drilling operations ended, from 4730.3 to 5253.3 m MD. Images suitable for fracture geometry determination were obtained for 1445.3–4720.3 m MD and for 4757.3–5248.3 m MD. Outside these ranges, the logs are run in casing or suffer from acquisition problems.

The logs in GPK2 were acquired on the 2nd of February 1995. Note that Logging conditions were significantly different, including different tools, crew and also a smaller borehole diameter than for GPK3 and GPK4 logs. In 1999, a UBI logging campaign was planned in the lower part of the GPK2 borehole, but due to technical problems, that attempt was largely unsuccessful. Usable images were acquired only between 1433.3 and 3793.3 m MD.

The image quality has been evaluated and classified. Four quality classes have been made that are described in Table 2.1. A detailed evaluation of image quality for all data analysed has been performed and is presented on Figure 2.19d, Table 2.2 and 2.3. The quality of images is generally very good. Only very short sections of images are unusable. These correspond to log extremities, the tops of the logs being run in casing and the last metres of the logs being usually not properly acquired. Few other short sections are characterized as bad quality. These are sections where

Figure 2.18: (on page 35) Technical section of the three deep wells. This schematic view has been put together by the Soutz team.

Table 2.1: UBI image quality classes.

code	designation	usable image width	examples
0	unusable	0%	in casing, log extremities
1	bad quality	0–30%	caves, stick/slip, bit whirling
2	medium	30–70%	key-seat
3	good	$\geq 70\%$	–

more than 70% of the image width is altered. The reasons for such bad quality are various. It may be very unfavourable borehole geometries such as large caves where the reflected ultrasonic pulse cannot be recorded. Other reason may be severe tool stick/slip which cannot be compensated for by the on-board accelerometers. If the drill bit starts to “whirl”, the borehole cross-section will be regular but possibly non circular. Such occurrences are rare in our boreholes, but they will although imply bad borehole image quality if more than 70% of the image width is perturbed. When the borehole is inclined, the wearing of the drill-string on borehole wall will also produce irregular cross-section geometry known as a ‘key seat’. An example of such a feature is presented on Figure 2.20. In such cases about 40% of the width of the UBI images is altered. This will imply a medium quality image, where 30% to 70% of the image width is altered. In GPK3 and GPK4, this occurs when borehole inclination is higher than about 23° (see Figure 2.19c). Good quality images are present everywhere else.

Figure 2.19: (on page 37) a) North-South projection of borehole trajectories. b) West-east projection of borehole trajectories. c) Borehole deviation. d) Borehole images quality. Depth range includes only granitic section.

2.3 The 5 km deep borehole image data set at Soultz-sous-Forêts

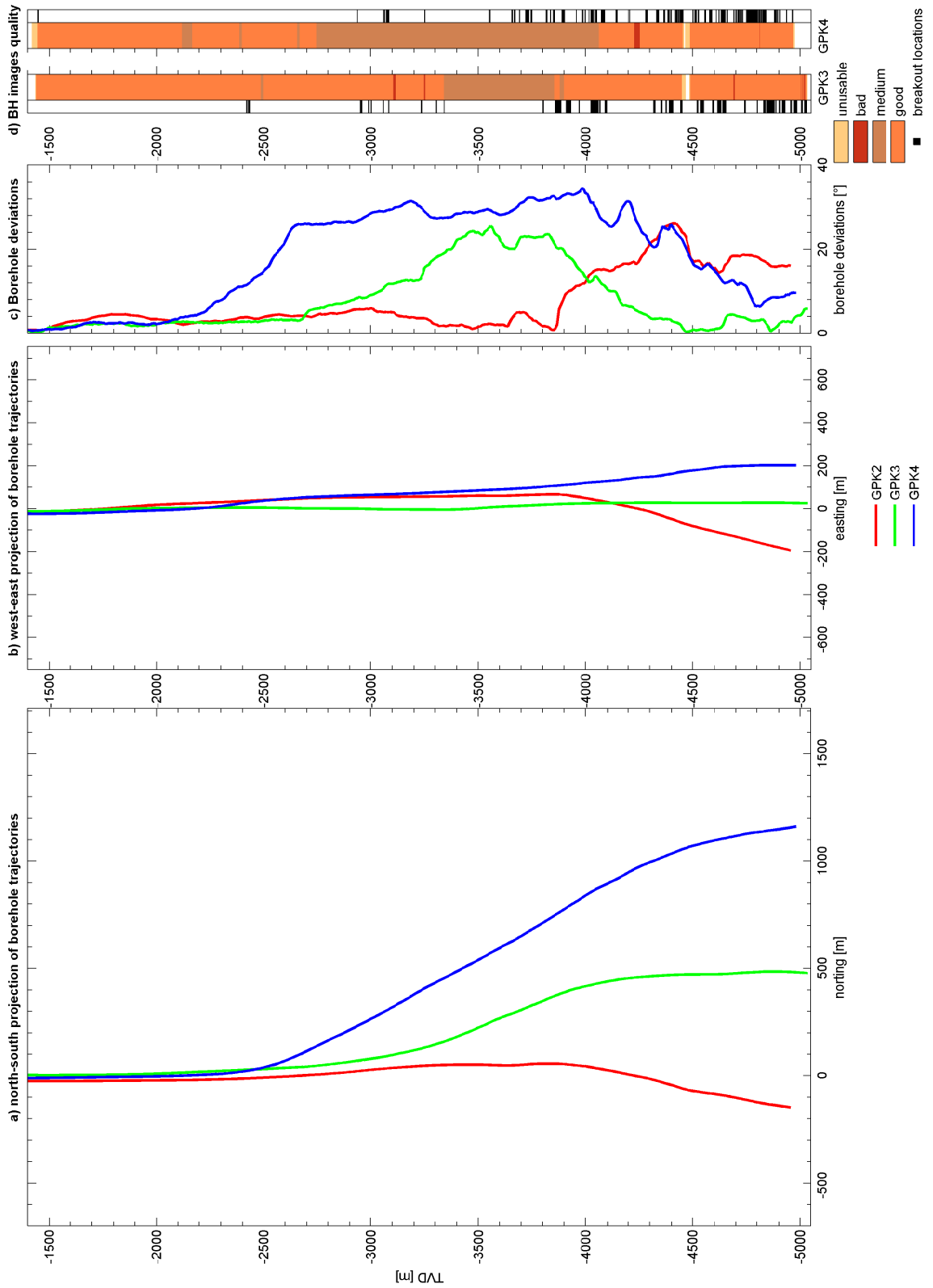


Table 2.2: Image quality in GPK3. 0=unusable, 1=bad, 2=medium, 3=good.

top depth	btm depth	quality
1444.76	1448.2	0
1448.2	2498	3
2498	2514	2
2514	3120	3
3120	3133	1
3133	3335	3
3335	3249	1
3249	3269	3
3269	3275	1
3275	3364	3
3364	3921	2
3921	3950	3
3950	3970	2
3970	4528	3
4528	4541.82	0
4562.71	4567.4	0
4567.4	4769	3
4769	4774	1
4774	5083.9	3
5083.9	5084.2	1
5084.2	5087.3	3
5087.3	5089	1
5089	5093.4	3
5093.4	5097	1
5097	5099	3
5099	5101	1
5101	5107.4	3
5107.4	5110.12	0

Table 2.3: Image quality in GPK4. 0=unusable, 1=bad, 2=medium, 3=good.

top depth	btm depth	quality
1431.3	1455	0
1455	2130	3
2130	2180	2
2180	2400	3
2400	2412	2
2412	2683	3
2683	2694	2
2694	2782	3
2782	4298	2
4298	4486	3
4486	4514	1
4514	4730	3
4730	4733.54	0
4740.87	4767	0
4767	5100	3
5100	5102.14	1
5102.14	5258.4	3
5258.4	5263.13	0

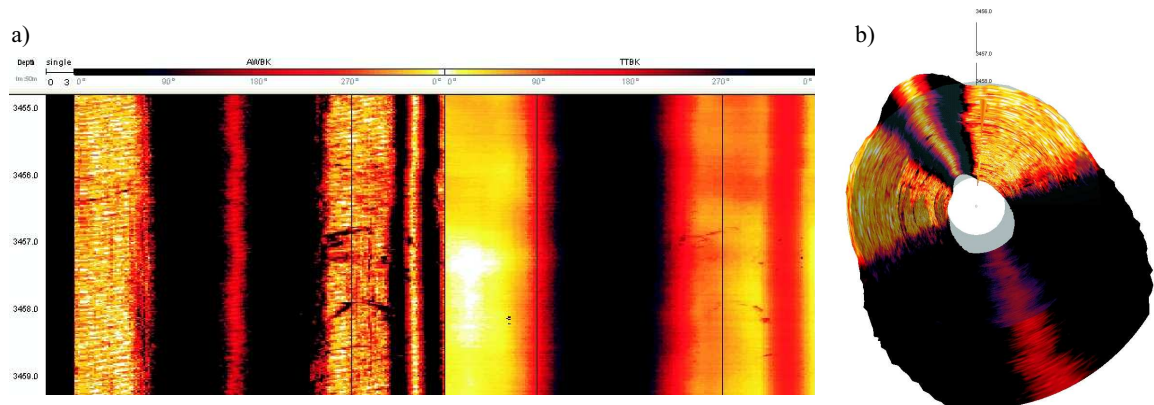


Figure 2.20: Example of key-seat. a) Amplitude (left) and Transit Time (right) image of a key-seat in GPK4 b) Same section in perspective view.

3 Multi-scale fracturing in the Soultz-sous-Forêts basement from borehole images analyses

3.1 Abstract

THREE deep boreholes of the Soultz-sous-Forêts geothermal project penetrate the crystalline basement in order to develop an engineered geothermal reservoir at 5 km depth. This Chapter presents the analysis of more than 7 km of acoustic borehole televiewer logs acquired in the granite sections of these boreholes which permit to characterise more than 4000 individual fractures. One important aspect in that analysis is the scale difference between the size of targeted reservoir, which has a maximum length of 2 km, and the size of investigation which is limited to the wall images of three 30 cm diameter boreholes. The emphasis is then put on developing innovative method which allow, on one hand, to quantify the spacing and the size of the structures, and on the other hand, to characterise natural fracturing at various scale based one borehole data only. Our results permitted to assess that the size of individual fractures observed at wellbore wall are smaller than relevant scale for the reservoir development. However, they are clustered and form fractures zones with spacing in the order of magnitude of a couple of hundreds metres. Cross-hole correlations permitted to describe the architecture and the orientation of these fractures zones, but complementary data (e.g. vertical seismic profiling) will be necessary to constrain the extent of these fractures zones.

3.2 Introduction

Geothermal energy, a CO₂-free energy resource, has been used since Antiquity for bathing and space heating (e.g. *Cataldi et al.*, 1999) and in the last hundred years for electricity generation. However, geothermal exploitations were restricted to singular geological contexts where natural surface geothermal activities are present. Since the 1970s, attempts are made to extend electricity generation, as well as heat production from geothermal energy, by trying to extract the heat from deep and low permeability crystalline rocks (*Duchane*, 1998). The early concept called Hot Dry Rock (HDR) was based on the engineering of man-made hydro-fractures (*Potter et al.*, 1974). The

experiences collected in the last thirty years, made people realise that deep crystalline rocks are usually not dry but contains geothermal brines flowing through an existing natural fracture network and that this natural fracturing will play a prominent role in the reservoir development (e.g. *Gérard et al.*, 1998). Hence, the early HDR concept evolves to the Hot Fractured Rock concept (HFR) or to the more general Engineered (or Enhanced) Geothermal Systems concept (EGS). That terminological evolution reflects the awakening that a good understanding of the natural fracturing system is necessary to permit any successful enhanced geothermal reservoir development (see Chapter 1).

The targeted size of an enhanced geothermal reservoir is in the order of magnitude of some cubic kilometres. At Soultz-sous-Forêts, the extent of microseismicity events generated during stimulation permits to evaluate the size of the 5 km deep reservoir to be about 2 km (NNW–SSE) x 0.7 km (ENE–WSW) x 1.5 km (vertically), i.e. a total of about 2 km³. This reservoir is tapped by three deep boreholes with a horizontal distance at bottom hole of about 700 m (e.g. *Dezayes et al.*, 2005b). The size of the relevant structures which should be considered in the reservoir development ranges, let say for sake of discussion, between a tenth of boreholes' spacing (connecting ten of such structure may potentially form a flow path between the wells) and the reservoir size, i.e. between about 70 m to 2 km. On the other hand, investigation methods like regional tectonic analysis, site geological mapping and geophysical investigations (surface seismic) catch only major faults and cannot resolve structures smaller than 2 km at the depth of the reservoir, i.e. about 5 km depth. A common investigation method in reservoir development is the monitoring of microseismicity during massive fluid injections, but the resolution of that method usually is too low to highlight fault zones and to resolve the details of their architecture. Special treatments of the micro-seismic dataset, for example collapsing (*Evans et al.*, 2005b; *Jones and Steward*, 1997) or multiplet analysis (*Michelet and Toksöz*, 2007; *Moriya et al.*, 2003), permit to get a better insight, but never allow characterising exhaustively fractures zones. At small scale, wellbore logging permits the obtention of a very detailed picture of the fracturing at borehole wall, but with an observation scale reduced to the borehole size, i.e. about 1 m in circumference.

In summary, in the current state of knowledge, there is a lack of information concerning the structures that drain fluids at the reservoir scale. In that context, the present study uses the small scale fracturing imaged at wellbore wall combined with statistical analysis, boreholes correlation, structural analysis, and genetic conceptual models in order to use the wellbore information for characterising the natural fracturing at the reservoir scale.

3.3 Background

Enhanced Geothermal Systems (EGSs) seek to exploit the vast reserves of heat energy that reside within the low-porosity rocks which underlie large areas of the continents at practically drillable depths. The EGS concept is as follows: two or more boreholes are drilled to depths where the temperature of the rock is of commercial interest, and then fluid is circulated around the loop(s) formed by the holes. The fluid heats-up as it passes through the hot rock mass between the boreholes and the heat is extracted at the surface. The problem with this simple scheme lies in the fact that the permeability of deep crystalline rocks is generally too low to allow the requisite flow to pass between the wells and thus, must be enhanced. The engineering of this enhanced-permeability linkage between the wells constitutes the primary challenge of EGS system development, and is the factor that distinguishes them from natural geothermal systems (e.g. *Evans et al.*, 1999).

The Soultz-sous-Forêts EGS project is located in north-eastern France within the Upper Rhine Graben (URG, see Figure 2.4). The Soultz boreholes penetrate the basement rocks at 1.4 km depth. Two different granites form the Soultz basements: a porphyric monzogranite and a fine-grained two-mica granite. These granites went through a complex multiphase tectonic history including Hercynian and alpine orogenesis (refer to Section 2.2). This complex geological history is reflected by the orientations of the current structures forming the URG. A fault traces map of the URG area, presented on Figure 3.1a, permits to get an idea of the orientation of the major structures composing the graben and its vicinity. Three major directions are present. Firstly, a N0°–N20° direction (in red on Figure 3.1), known as Rhenish orientation, corresponds to the normal faults forming the URG. They were formed during the Oligocene opening of the Rhine Graben (*Schumacher*, 2002; *Villemin and Bergerat*, 1987), possibly reactivating an Hercynian structure called Mediterranean-Mjoesa-zone (*Illies*, 1962, 1972, 1975; *Rotstein et al.*, 2006). A second prominent orientation, often called Erzgebirgian (*Cloos*, 1922; *Edel and Weber*, 1995; *Edel et al.*, 2004), is the general Hercynian orientation to the NE to ENE (in green on Figure 3.1). The major Variscan dislocation zones which delimited Hercynian tectonic realm strike in that direction. The third orientation corresponds to NW–SE structures (in blue on Figure 3.1). This orientation is infrequent in *Illies and Greiner* (1979) compilation. It is then in the Cenozoic sediments filling the URG and it is mainly present in the border of the URG in pre-Cenozoic rocks of Figure 3.1. However, in the more recent study of *Villemin and Bergerat* (1987), they state that such NW–SE plane are reactivated in dextral strike-slip movements, as we will expect after their orientation to the current stress field. At a more local scale, the lineament analysis on SPOT images of *Genter* (1989) presents the same dominant orientations, but also some others. Particularly, a N–S to NNW–SSE orientation (in rose on Figure 3.1) is locally important in the Soultz area and the general trend of the microseismicity induced during reservoir stimulation follows such orientation (e.g. *Cornet et al.*, 2007).

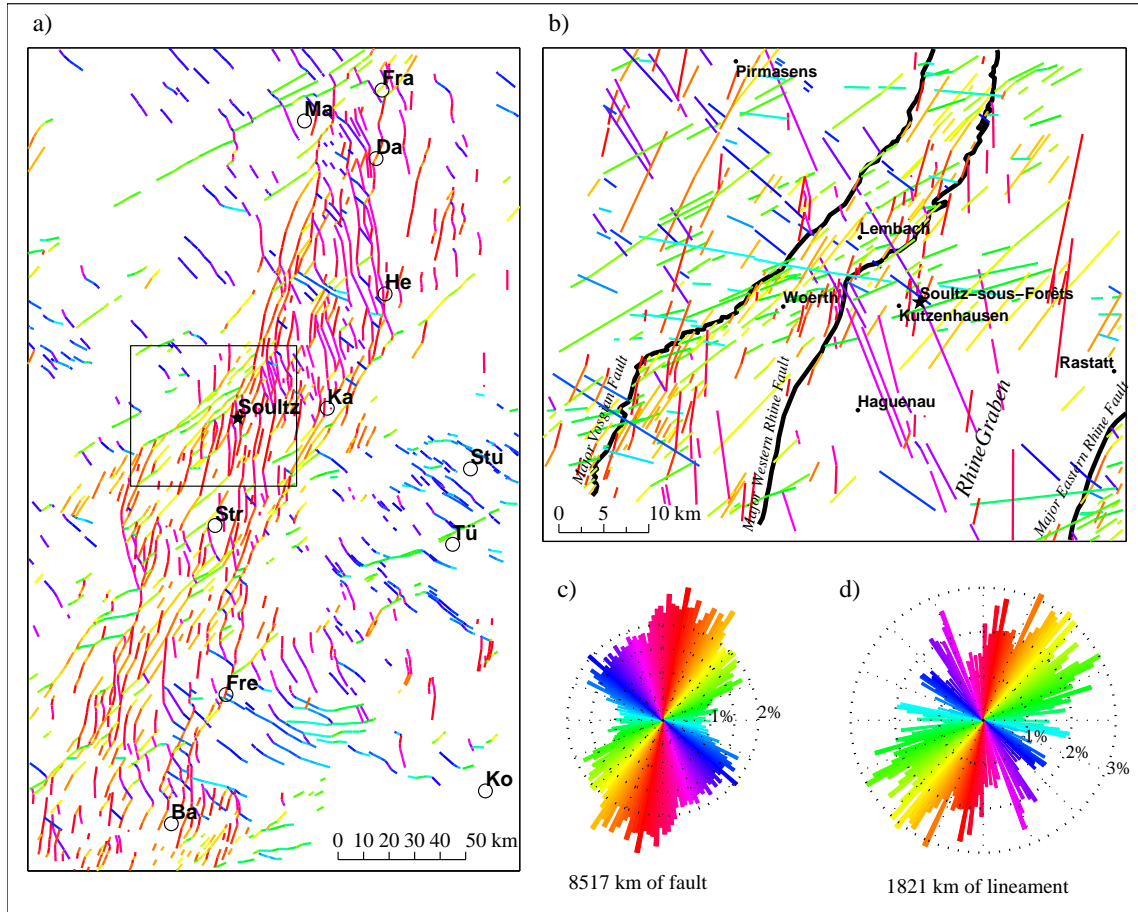


Figure 3.1: a) Fault trace map of the URG. This map is compiled from *Illies* (1972) for the graben border faults and all faults outside the graben and from *Illies and Greiner* (1979) for all faults within the graben. Fault segments have been drawn with various colours after their strike direction. The black box around Soultz corresponds to the location of the map (b). Ba: Basel; Da: Darmstadt; Fra: Frankfurt; Fre: Freiburg; He: Heidelberg; Ka: Karlsruhe; Ko: Konstanz; Ma: Mainz; Str: Strasbourg; Stu: Stuttgart; Tü: Tübingen b) Map of lineament seen on a SPOT image after *Genter* (1989) c) Circular histogram of the fault segments strike directions of faults from map (a) weighted by segment length. d) Circular histogram of the lineaments strike directions of lineament map (b) weighted by segment length.

At the site scale, geological mapping, borehole logs from the Pechelbronn oil field, and surface reflection seismic were used to characterise the major faults system (Menjoz *et al.*, 1989). These data were included by Renard and Courrioux (1994) in the 3-D model presented on Figure 3.2a and c. In this model, all faults have a Rhenish (N-S) strike direction (Figure 3.2b) and are preferentially dipping to the West, i.e. antithetically to the Western Graben border fault. These major faults have a trace length on the regional geologic map of 2 to 20 km and occur with a spacing ranging from about 800 m to 3 km. The block diagram of Figure 3.2c and the stereoplot of Figure 3.2d make it clear that basement top is generally horizontal, but at the top of the Soultz horst, the basement dips slightly to SSE. Deviation of the basement top from horizontality occurs in a E-W direction where it expresses the delimitation of tilted blocks by the faults (half graben or roll-over), but also in the N-S direction possibly permitting strain transfer between relaying normal faults (relay ramp; for normal fault terminology, refer to Peacock *et al.*, 2000). No connecting fault is present in this model in order to accommodate the lateral strain, but such fault may well be present outside the model or pre-existing ENE-WSW or NW-SE striking structures may be reactivated for this purpose.

3.4 Description of the data set

The data analysed in this study stem from the three deep wells GPK2, GPK3 and GPK4 drilled to 5 km at the Soultz-sous-Forêts geothermal site. Information about borehole completion and technical borehole sections can be found in Section 2.3.2 and Figure 2.18. An important feature of the wells is that being drilled from the same pad and deviated only from about 2.2 km depth (see Figure 2.19), the borehole separation is less than 20 m between GPK3 and GPK4 along the upper 800 m of logs in granites.

3.4.1 Ultrasonic borehole images

The principal source of information for this study arises from acoustic borehole televiewer logs. The ultrasonic borehole televiewer images were obtained by a Schlumberger Ultrasonic Borehole Imager (UBI) tool that was run with the ancillary GPIT module which provides sonde positioning and orientation information. Successful UBI logs were run in the entire granite section of both GPK3 and GPK4 to total depth and between 1433.3 and 3793.3 m MD in the borehole GPK2. The UBI tool provides detailed images of the ultrasonic reflectivity of the borehole wall together with borehole geometry, sampled with an angular resolution of 2°. The logging speed is chosen such that a scan is made every 1 cm along the hole. For details on measurement principle, refer to Section 2.3.1 and Luthi (2001). Acquisition and image quality details are given in Section 2.3.3.

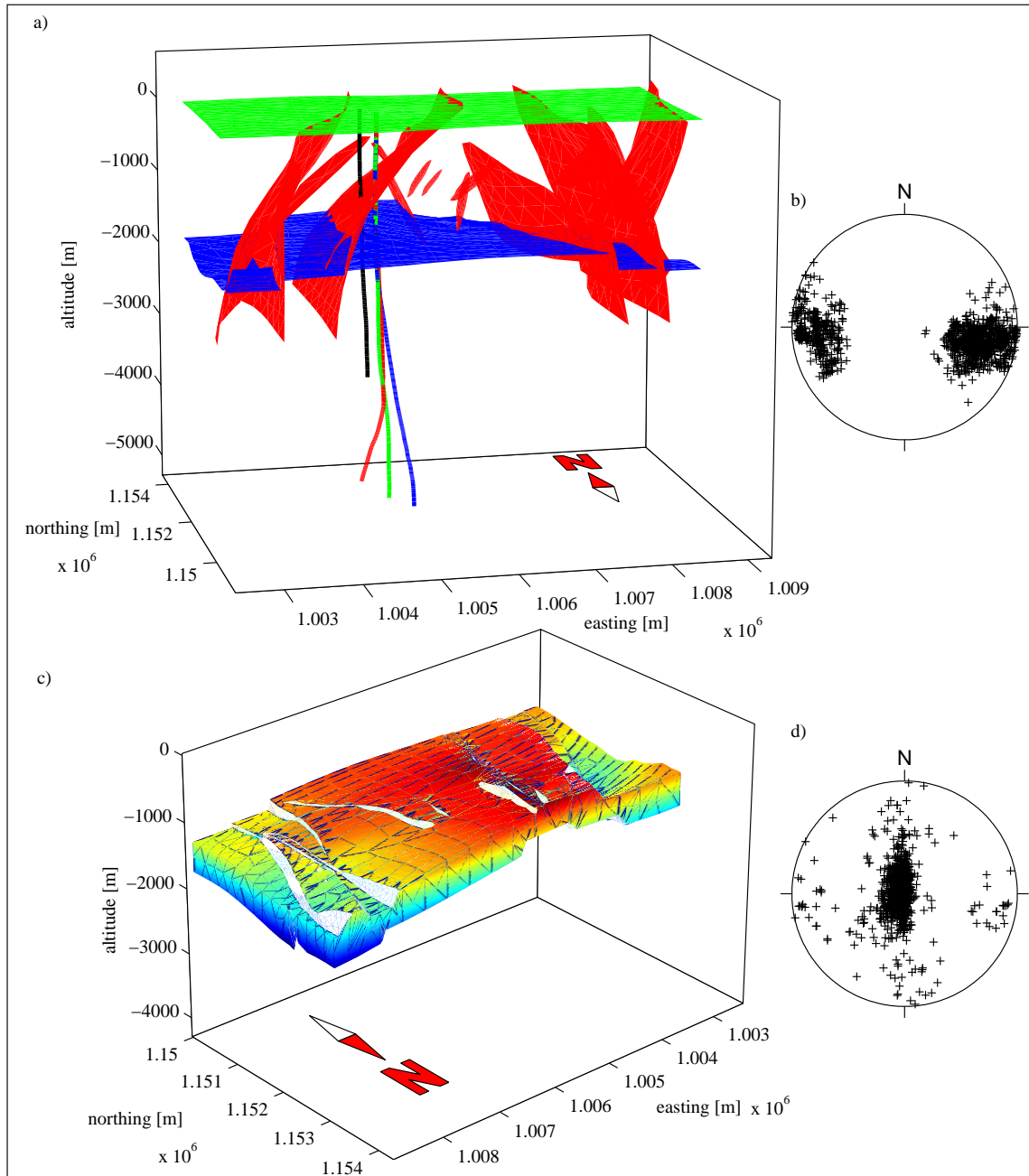


Figure 3.2: a) 3D model of the Soultz-sous-Forêts area. In green: topographical surface; in blue: basement top; in red: faults (after *Renard and Courrioux, 1994*). Boreholes trajectories are also displayed (GPK1: black, GPK2: red, GPK3: green and GPK4: blue) b) Poles of fault planes of the 3D model (lower hemisphere, equal area) c) View of the volume between top Buntsandstein and top basement in the form of a 3D block diagram. Point of view is from Northeast. d) Orientation of the top of the basement (lower hemisphere, equal area). Geographic coordinates are Lambert II coordinates. Altitudes are IGN69 altitudes.

3.4.2 Measurements of fracturing on wellbore images

Fractures have been measured on unwrapped borehole images by manually fitting sinusoids on them using the WellCad software package from ALT. The sensitivity of the method has been evaluated by *Genter et al. (1997)* by comparing fractures determined on cores and on ultrasonic borehole images. Discrete fractures thinner than 1 mm are not properly detected. This is also the case for discrete fractures that are less spaced than 5 mm, which appear only as one single trace. In granite, only about 17% of the fractures detected on cores were seen on borehole images. The sensing of fractures is better in sane granite sections, where approximately 50% of the fractures seen on cores are captured by the BHTV. However, in altered granite section, where the roughness of the borehole wall usually leads to a degradation of the image quality, consequently only 5% of the fractures are recorded.

Natural fractures can be sometimes confused with drilling induced tensile fractures. The latter form where cooling of the borehole wall by circulation of mud during drilling results in a net tangent stress distribution around the hole that is sufficiently tensile at some point to produce failure. The net tangent stress is the sum of a tensile cooling component, which is axially-symmetric, and the natural wellbore stress concentration arising from the ‘far-field’ stresses, which are not necessarily axially-symmetric and may be everywhere compressive. As indicated by their name, such fractures are not present before the borehole is drilled. Their repartition and orientation depend on the current stress condition and on the drilling operations. In the present analysis, special care was taken to distinguish natural and drilling induced fractures. Only the natural fractures are analysed here, the analysis of drilling induced fractures are presented in Chapters 4 and 5.

The apparent dip and dip directions measured on borehole images have been transformed in true dip and dip directions using the borehole azimuth and deviation measurements provided by the ancillary GPIT tool. The accuracy of these measurements is given as $\pm 2^\circ$ in azimuth and in deviation (*Schlumberger, 2002*). Evaluation of repeated logs permits to refine these values for the particular case of Soultz logging condition. Single standard deviations were found to be 1.0° on the azimuth measurement and 0.2° on borehole deviation measurements. On top of this, the inaccuracy of the sinusoidal fitting process has to be considered. Natural fractures being barely perfectly planar and borehole geometry being usually not perfectly circular, the unwrapped fracture trace is usually not a perfect sinusoid. The best fitting process of the sinusoid trace contains some subjectivity which introduced uncertainties. For relatively steep fractures, as they are found in Soultz, that inaccuracy has been evaluated by repeated measurement of the same feature to be about $\pm 2.5^\circ$ for the dip direction and $\pm 0.75^\circ$ for the dip angle.

The importance of each fracture trace has been evaluated using an appropriate fracture typology (see Appendix A for details). A two digit code is attributed to each fracture type. The first digit permits to distinguish between fractures which are

visible on both reflectivity and transit time images (1) and those which are seen on reflectivity image only (2). The second digit estimates the continuity of the fracture traces at borehole wall. The visible length is compared with the full length of the fitted sinusoid and the second digit of the fracture code is attributed as following: 1 = 100%–80%; 3 = 80%–50%; 4 = 50%–0% and 5 for low confidence determination. For example the code ‘23’ will be attributed to a fracture visible only on the reflectivity image with its trace perceptible over more than 50% of the total trace length but less than 80%. Fractures with nearly complete traces on the UBI images, i.e. of type ‘11’ or ‘21’, are believed to be relatively thicker (*Dezayes*, 1996, Figure 18 and 24) and then also possibly longer (e.g. *Kim and Sanderson*, 2005; *Walsh and Watterson*, 1988) than the others and will be referred to as ‘thick fractures’ in this Chapter.

3.5 Analysis of the individual fractures characteristics

In all, 1871 fractures were described on the GPK3 images and 2215 fractures on the GPK4 images. They are all dispatched in the classes defined in the typology presented above. The repartition in the different classes is shown on Figure 3.3a. The repartition in both boreholes is globally the same, so the data from both boreholes are presented together within the same diagram. The dominant type is the type ‘24’ which counts for 42% of the fractures, followed by the type ‘25’ which is about 17% of the fractures. The thick fractures of types ‘11’ and ‘21’ count together for only 12%.

Another aspect to look at is the repartition of fractures with depth. This is represented on Figure 3.3b by the mean of cumulated number of fracture vs. depth curves. Average fracture frequencies are 0.51 fractures per meter for GPK3 and 0.58 fracture per meter in GPK4. Frequencies are variable with depth ranging from a minimum of 0.17 fractures per metre to a maximum of 1.83 fractures per metre. Evidently, very locally frequency may be even lower, e.g. no fractures for a few meters, or substantially higher with one meter containing up to about ten fractures. Also keep in mind the results of *Genter et al.* (1997) that only approximately 50% of the fractures are seen by a BHTV tool when the granite is unaltered and as few as 5% in altered zones. Altered zone may then well be largely under sampled and will not show up as steps on the cumulated number of fracture curves as we may expect if fractures were identified on cores. In a very simplified manner, the cumulated number of fracture curves can be summarized in 5 sections:

- A. a high frequency section, with about 0.9 to 1 fracture per meter, from granite top down to about 1800 mTVD.
- B. a low frequency section, about 0.45 to 0.55 fractures per meter, from 1800 to 2800 mTVD.
- C. a generally high frequency section, with also some very low frequencies, from 2800 to 3400 mTVD.

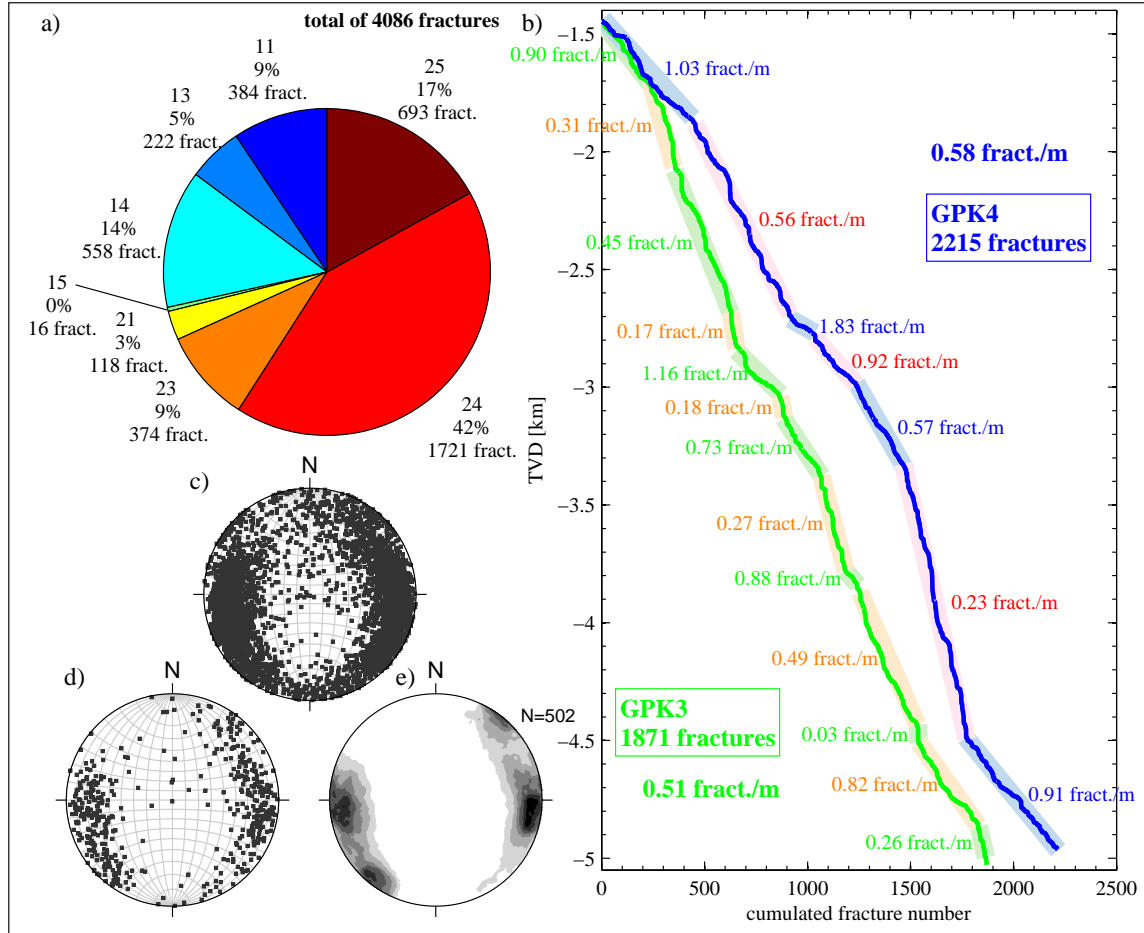


Figure 3.3: Presentation of the entire fracture data set from GPK3 and GPK4. a) Repartition of the fractures in the different types defined by the typology (see text for details). b) Cumulative number of fractures vs. depth. GPK3 is displayed in green and GPK4 in blue. Fractures frequencies are also displayed for various sections. c) Stereographic projection of the poles of all GPK3 and GPK4 fractures (lower hemisphere, equal area). d) poles of fractures of types 11 and 21 (80%–100% of the sinusoidal trace on reflectivity image) of GPK3 and GPK4 (lower hemisphere, equal area). e) Weighted contouring of the fracture density of fracture data presented on d). Weighting is performed for a Terzaghi correction (e.g. *Priest*, 1993, p. 71).

- D. a generally very low frequency section, about 0.25 to 0.45 fracture per meter, from 3400 to 4500 mTVD
- E. a high frequency section, about 0.8 to 0.9 fractures per meter, from 4500 mTVD to the bottom hole.

In detail, there are significant discrepancies within this simplified scheme. Particularly, the very bottom section of GPK3 from 4850 mTVD has a low frequency of about 0.26 fractures per meter. Also, the first high frequency section (A) lasts deeper in GPK4 than GPK3, and the first low frequency section (B) lasts deeper in GPK3 than GPK4. These two differences are responsible for the slightly higher average frequency in GPK4 than GPK3. Note that the discrepancies in the upper part of the well (above 2500 m) are surprising as the boreholes are only about 20 m apart. In this upper part, the cumulative fracture curve are different mainly in between 1850 and 2050 m. Is the intersection with a major fractures zone at about 2000 m (see description later in section 3.6) and its lateral heterogeneity responsible for these discrepancies ? This remains uncertain.

Figure 3.3c presents the orientation of the poles of all GPK3 and GPK4 fractures on a stereographic projection. The dominant orientation is N–S striking, with fractures dipping to the west or to the east. Dip angles are generally higher than 50°. These results are in agreement with previous study made on the dataset of the 3.6 km deep reservoir (*Dezayes, 1996; Genter and Traineau, 1992; Tenzer et al., 1991, 1992*).

Looking at all fracture simultaneously, i.e. at fractures along borehole length of about 7 km, as in Figure 3.3c evidently do not permit to isolate clear sets. Figures 3.3d and 3.3e present plots of a subset of the data. This subset contains only the ‘thick fractures’, i.e. fractures of type ‘11’ and ‘21’. The presence of directions other than N–S striking fractures suggest that if these orientations are rather rare, they nevertheless exist and cannot be attributed to uncertain determination. The contouring of this data set, including a Terzaghi correction to compensate sampling bias arising from the sampling line orientation (*Priest, 1993*), presented on Figure 3.3e permit to isolate three maximum of fracture poles density. Two of them correspond to N–S striking fractures dipping steeply to the East or to the West. The third maximum corresponds to sub-vertical fractures striking NW–SE.

3.5.1 Clustering of the fracture data to derive orientation sets

In order to permit rigorous clustering of the fracture set one has to consider a shorter borehole section in order to avoid the overlapping of various structural domains. The fractures were treated borehole by borehole and using a 75 m long moving window shifted by 25 m steps along the borehole’s depth. This way, two successive windows had a 50 m overlap which ensures coherent processing over the entire borehole length. For each window, a preliminary clustering was performed using the fully automatic

algorithm described in *Priest* (1993, p. 76–87). That preliminary set repartition was then refined using the same 75 m moving window with an expert-supervised method. This method coupled a k-means clustering algorithm, i.e. an iterative algorithm that minimizes the sum of distances from each object to its cluster centroid over all clusters (e.g. *Seber*, 2004), adapted for spherical data with interactive manual control.

In all, seven sets were isolated. The first fourth sets were the dominating sets. Set 1 and 2 strike N–S and dip to the West or to the East respectively (Figure 3.4). Together they contain more than 60% of the fractures (Figure 3.5). Their orientations correspond to the Rhenish orientation already described at graben and site scale. Set 3 is sub-vertical, striking NW–SE, an orientation also apparent at larger scales (Figure 3.1 in blue). Set 4 is also sub-vertical and strikes NE–SW, parallel to the Hercynian large scale structures (Figure 3.1 in green). Together, the first four sets include 95% of all described fractures. The remaining 5% includes three secondary sets: set 5 to 7. All sets contain more than 15% of indisputable fractures (type ‘11’, ‘13’, ‘21’, or ‘23’).

The repartition along depth of the fractures of the different sets is presented on the East-West projection of Figure 3.6a. The four major Sets (1 to 4) are present along the entire length of each borehole, whereas Sets 5 to 7 occur at specific locations. Set 5 which is sub-horizontal, occurs mostly above 2.5 km and also between 3.2 and 3.8 km. *Genter and Traineau* (1996); *Genter et al.* (1991) have already described such sub-horizontal fractures on the GPK1 dataset and attributes them to sheeting joints (*Martel*, 2006; *Twidale*, 1973) which formed during the post-hercynian erosion. If this interpretation holds for the fractures located close to the current basement top, it is unlikely to be also true for fractures located at more than 2 km depths from the paleo-surface. The genesis of these deeply located sub-horizontal fractures is unknown. Set 6, a sub-vertical E–W striking fracture set, occurs mostly below 4 km depths as does also Set 7, another E–W striking set, but dipping at about 45° to the South.

Figure 3.6b to d shows the repartitions of the four dominant sets versus depth. The proportions between Set 1 and 2 (Figure 3.6c) are globally equal except above 1835 m where Set 2 (east dipping) is clearly dominating and below 4600 m where Set 1 (west dipping) is more present. The repartition between Set 3 and 4 (Figure 3.6d) is usually less well balanced, one set or the other is totally dominant or disappears entirely for a given section.

Abutting relations between the four main Sets were studied by analysing the singular locations where the borehole cuts two fractures at their intersection. In all, 124 such intersections of the four major sets were found along the entire granitic section of both boreholes. For each of these intersections, the abutting relations were described and a confidence index from ‘high’ to ‘very low’ was attributed to each characterisation. The result of this analysis is presented in Table 3.1. Interactions between Sets 1 and set 2 show than in about two third of the cases, Set 1 is abutting on Set 2. Interactions between Set 1 and 3 show in most of the case that Set 1 is

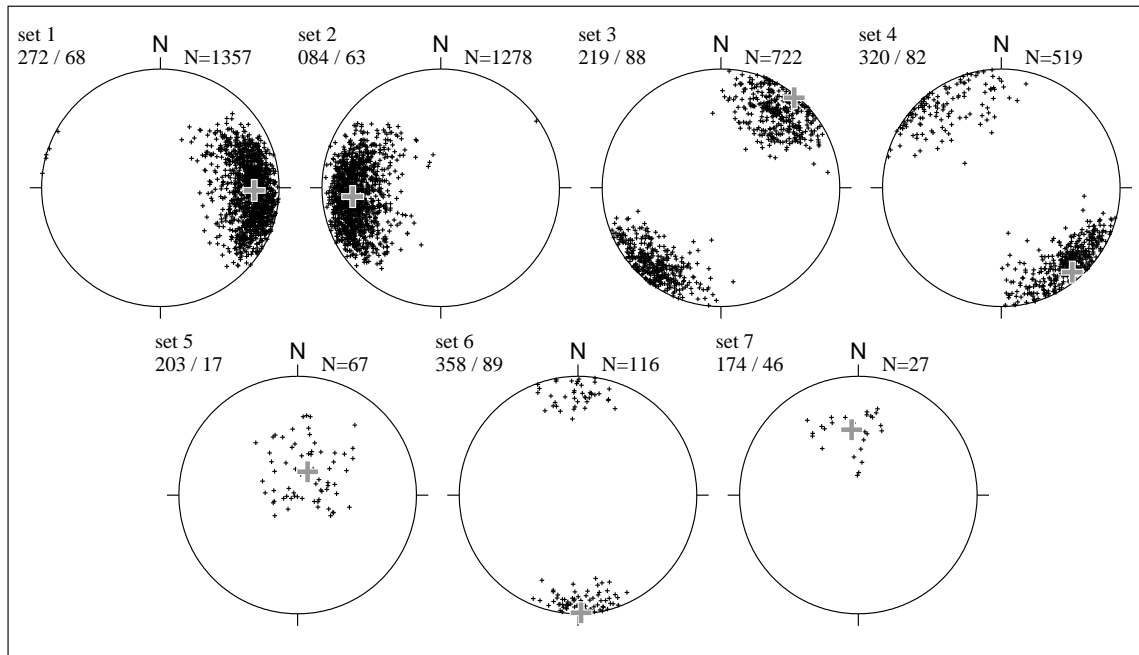


Figure 3.4: Result of the clustering process performed on the fracture data of Figure 3.3c. Poles of fracture for all seven isolated sets are presented in stereographic projection (lower hemisphere, equal area). The mean orientation is displayed next to the set label and with a thick grey cross on the stereographic projection.

abutting against Set 3. Set 4 is most of the time abutting against Set 1. Set 3 and 4 are abutting against Set 2, and Set 4 against Set 3. In summary, the less abutting, or most persistent set, is Set 2, followed by Set 3 Set 1, and finally Set 4. Note that as the genesis mechanisms of these fractures are not known, these abutting relations cannot be used as chronological markers. Indeed the mode of formation of the new fracture, and especially the healing conditions of the crossed old fracture, will influence the final abutting relations. In the case of joints, i.e. Mode I fractures, younger joints will usually stop on older ones, if these last are open and not healed. Contrarily, for faults, i.e. shear fractures with detectable throw, younger faults will displace older ones, and so older faults will be in abutting relation on younger faults.

3.5.2 Spacing distributions

For fracture sets 1 to 4, true spacings have been computed. This was done by projecting the borehole length between two subsequent fractures in the mean normal direction of the fracture set.

Note that when considering true spacing this way, the effective total sampling

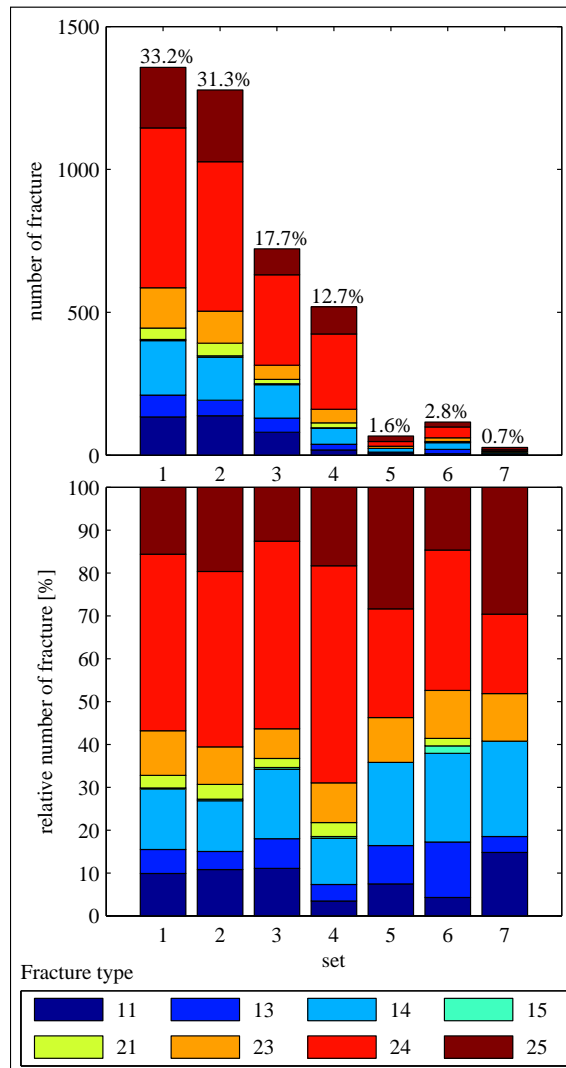


Figure 3.5: Repartition of the sets and their type. See text for discussion.

length is reduced compared to the length measured along boreholes. The effective sampling length is like projecting the logged borehole section in the direction normal to the fracture planes. This can be computed simply by summing all true spacings for a given set in a given borehole. These lengths are: Set 1: 1398 m (GPK3) and 1554 m (GPK4); Set 2: 1493 m (GPK3) and 1539 m (GPK4); Set 3: 321 m (GPK3) and 764 m (GPK4); and Set 4: 908 m (GPK3) and 1452 m (GPK4). Remember that Set 3, as it is unfavourably oriented relative to the borehole trajectory, has a quite short effective sampling length.

Statistical descriptive parameters and distributions for true spacing are presented in Table 3.2 and in Figure 3.7. Mean true spacing for Set 1 is 2.30 m in GPK3 and 2.08

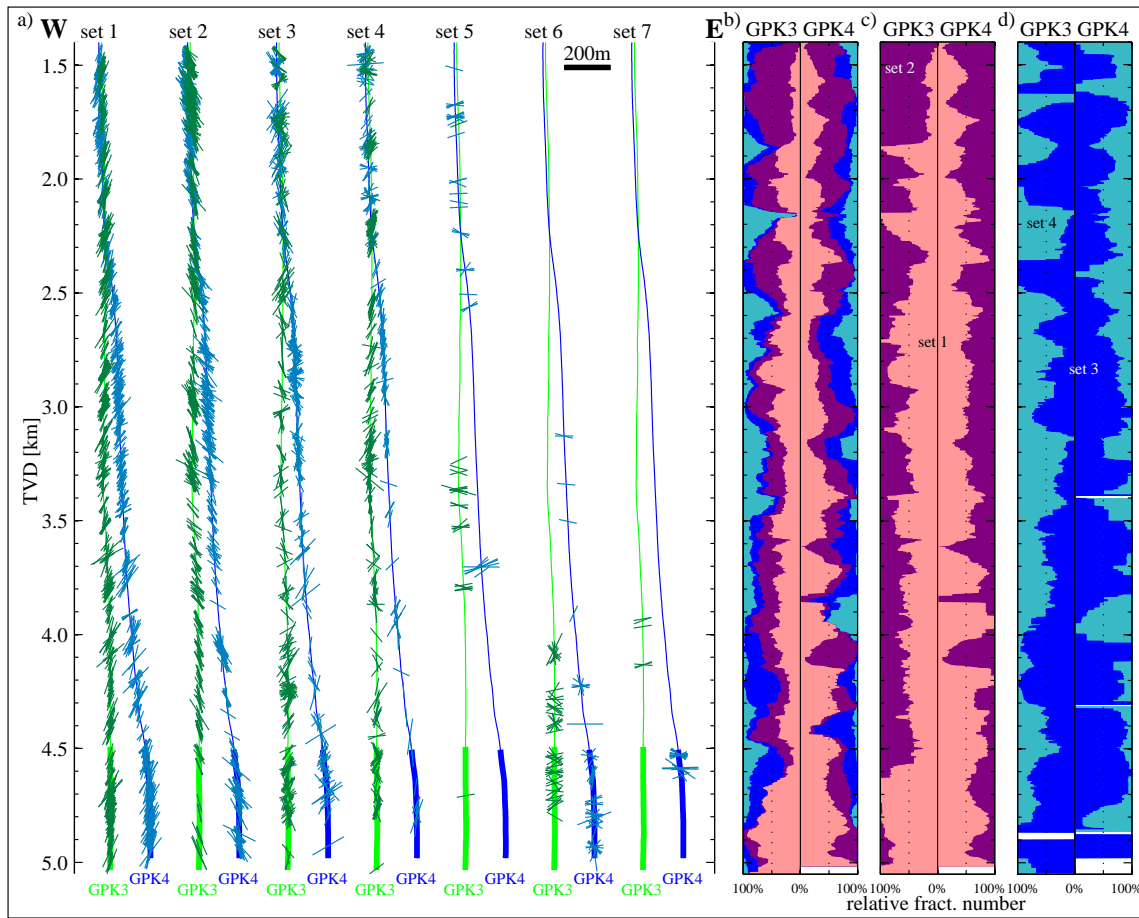


Figure 3.6: Repartition of fracture sets versus depth. a) West-East projection of the GPK3 (green) and GPK4 (blue) borehole trajectories and apparent dip of the fractures for each set. Thick lines correspond to open sections. b) proportion between Set 1 (rose), Set 2 (violet), Set 3 (blue) and Set 4 (cyan) versus depth. c) proportion between Sets 1 and 2 versus depth. d) proportion between Sets 3 and 4 versus depth. Computations of the set proportions are done using a 100 m long sliding window.

m in GPK4 with standard deviations of 4.21 m and 4.95 m respectively. Coefficient of variation ($CV = \sigma/\mu$) is 1.83 for GPK3 and 2.38 for GPK4. Mean spacing, standard deviation and CV for Set 2 are slightly higher than for set 1. Set 3 has spacing of 1.04 m in GPK3 and 1.86 m in GPK4 which is the least spaced set. Keep in mind that this set is also the least favourably oriented relative to the borehole trajectory. CV for Set 3 is 2.21 in GPK3 and significantly higher in GPK4, i.e. 2.91. Mean spacing of Set 4 is significantly higher: 3.16 m and 6.31 m respectively. It is also accompanied by larger standard deviations, which implies a CV of 1.99 and 2.67.

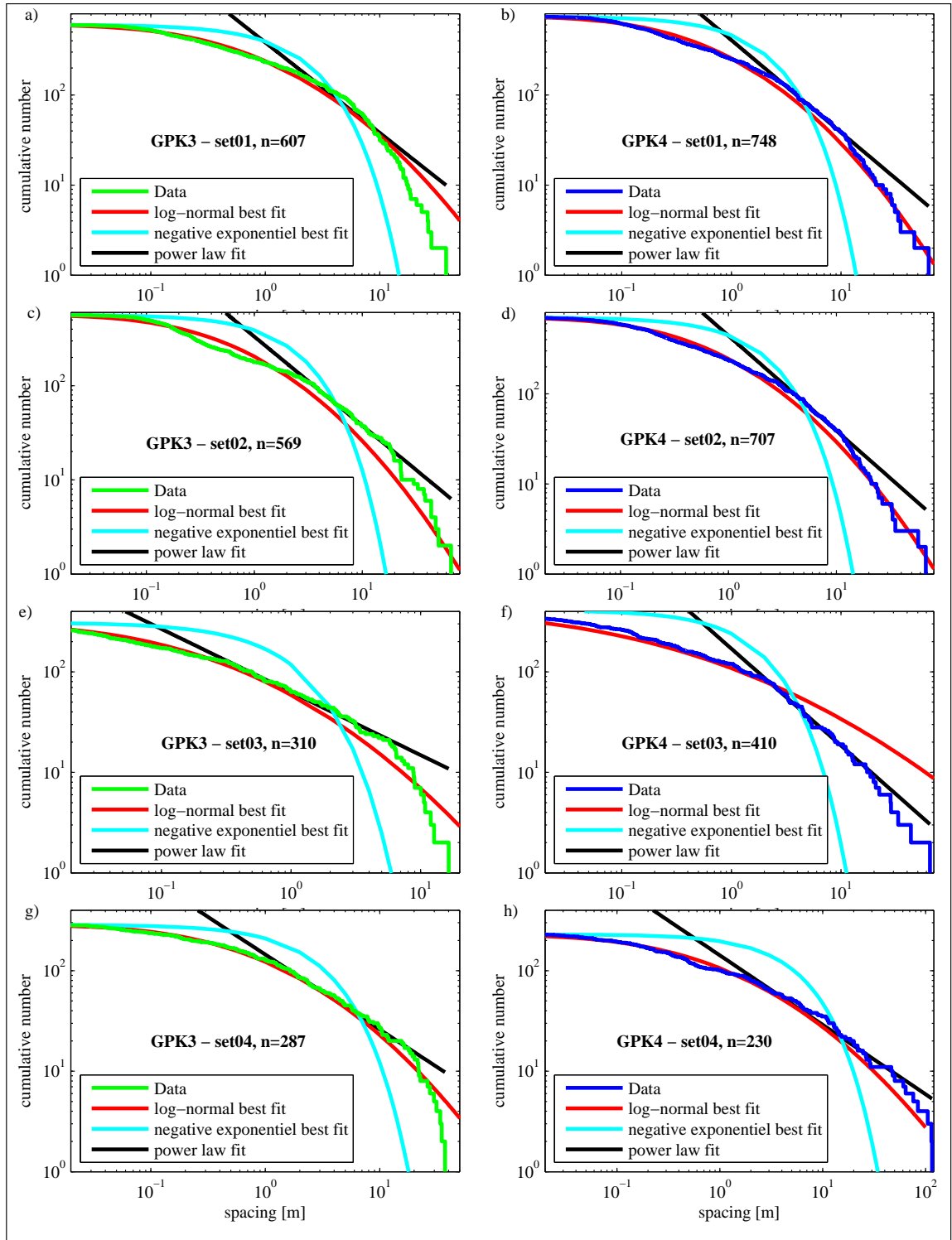


Figure 3.7: Spacing distribution for the four major sets. See text for details.

Table 3.1: Abutting relations between the four major set.

		all set 2 stop on set 1 set 1 stop on set 2					
intersections set 1 – set 2	all	57	24	42%	33	58%	set 2 is more persistant than set 1
	only sure	17	6	35%	11	65%	
		all set 3 stop on set 1 set 1 stop on set 3					
intersections set 1 – set 3	all	21	2	10%	19	90%	set 3 is more persistant than set 1
	only sure	3	1	33%	2	67%	
		all set 4 stop on set 1 set 1 stop on set 4					
intersections set 1 – set 4	all	10	8	80%	2	20%	set 1 is more persistant than set 4
	only sure	2	2	100%	0	0%	
		all set 3 stop on set 2 set 2 stop on set 3					
intersections set 2 – set 3	all	19	11	58%	8	42%	set 2 is more persistant than set 3
	only sure	3	3	100%	0	0%	
		all set 4 stop on set 2 set 2 stop on set 4					
intersections set 2 – set 4	all	10	8	80%	2	20%	set 2 is more persistant than set 4
	only sure	2	2	100%	0	0%	
		all set 4 stop on set 3 set 3 stop on set 4					
intersections set 3 – set 4	all	7	4	57%	3	43%	set 3 is more persistant than set 4
	only sure	1	1	100%	0	0%	

**general persistence result
set 2 > set 3 > set 1 > set 4**

Concerning the fitting of statistical distributions, negative exponential distributions are never in agreement with the data sets, which is clearly visible on the plots of Figure 3.7 and which has also been evaluated with a χ^2 Goodness of Fit test. Log-normal distributions usually agree quite well with the data, always with a CV significantly higher than 1 ($\sigma > \mu$). This indicates a clustering of the fracture population (Gillespie *et al.*, 2001). Comparisons between fractures identified on cores and fractures seen on BHTV images show that if on BHTV spacing-distribution usually agree well with a log-normal law, spacing datasets from cores for the same borehole sections will follow a power law over more than two decades (Genter *et al.*, 1997). This is due to the selective sensing of the BHTV tool which does not see a significant portion of the fracture population. Indeed, small spacing will be neglected because some fractures are not seen on BHTV images, but also some large spacing will not be recorded due to the limited sampling length (Bonnet *et al.*, 2001; Einstein and Baecher, 1983; Segall and Pollard, 1983). Adjusting power laws on fracture the spacing-distributions of Figure 3.7 between 1 to 5 m leads to fractal numbers (D) close to 1, i.e. similar to the ones obtained on cores (Genter *et al.*, 1997). However

Table 3.2: Spacing statistics and distribution of the four major fracture sets.

	GPK3 set1	GPK4 set1	GPK3 set2	GPK4 set2
descriptive statistical parameters				
mean μ	2.3	2.08	2.62	2.18
standard deviation σ	4.21	4.95	6.66	5.31
maximum spacing	38.15	63.00	66.83	67.55
minimum spacing	0.00	0.00	0.00	0.00
coefficient of variation CV	1.83	2.38	2.54	2.44
best fit parameters				
log-normal ν, ϱ^a	-0.49, 1.78	-0.69, 1.70	-0.63, 1.73	-0.68, 1.72
exponential μ^b	2.3	2.08	2.62	2.18
power law D, i^c	1.00, 376	1.03, 350	0.95, 468	1.06, 323

	GPK3 set3	GPK4 set3	GPK3 set4	GPK4 set4
descriptive statistical parameters				
mean μ	1.04	1.86	3.16	6.31
standard deviation σ	2.29	5.42	6.28	16.87
maximum spacing	16.46	64.61	37.28	115.41
minimum spacing	0.00	0.00	0.00	0.00
coefficient of variation CV	2.21	2.91	1.99	2.67
best fit parameters				
log-normal ν, ϱ^a	-1.79, 2.04	-1.90, 3.03	-0.35, 1.89	-0.21, 2.13
exponential μ^b	1.04	1.86	3.16	6.31
power law D, i^c	0.63, 733	0.97, 205	0.75, 789	0.69, 1301

^a log-normal law with parameters corresponding to the mean and standard deviation of the corresponding normal distribution and defined by: $y = f(s | \nu, \varrho) = \frac{1}{x\varrho\sqrt{2\pi}} \exp\left(\frac{-(\ln(x)-\nu)^2}{2\varrho^2}\right)$

^b exponential law is expressed by: $y = f(x|\mu) = \frac{1}{\mu} \exp\left(-\frac{x}{\mu}\right)$

^c power law is expressed by : $y = f(x|D) \propto x^{-D}$. i is the maximum theoretical spacing and it is computed by extrapolating the power law line to its intersection with the origin abscise.

In these three expressions x is for spacing.

in this case, given that the distributions are actually not fractals and the linear fits are valid over less than one decade, interpreting the intercept with the origin abscise (i) as the maximum theoretical spacing is meaningless.

3.5.3 Variogram analysis on fracture spacing

Classical statistic and theoretical distribution fitting, as presented above, are not sufficient to define joint spatial correlations. Geostatistics was introduced in fracture spacing analysis to deal with this particular aspect (e.g. *Chilès, 1988; Miller, 1979; Villaescusa and Brown, 1990*). Figure 3.8 presents variograms for the Soultz fracture spacing data with respect to distance, as presented in *Villaescusa and Brown (1990)*, i.e. using the following equation to compute them:

$$\gamma(h) = \frac{1}{2n} \sum_{i=1}^n [z(x_i) - z(x_i + h)]^2 \quad (3.1)$$

where z is the studied variable, n the number of observation couples, h the distance between two measurements, for example between $z(x_i)$ and $z(x_i + h)$ where x_i and $x_i + h$ is the spatial localisation of the measurements. γ is computed for successively increasing values of h in order to build the complete experimental variograms. Experimental variograms have been smoothed using a moving average filter in order to highlight the trends (black lines on Figure 3.8). Information on interpretations of fracture spacing variograms are presented in Appendix B.

For Set 1, in both boreholes, there is a nugget value of about one half of the entire sample variance, which indicates that there is some correlation in fracture spacing. This can be interpreted to reflect fracture clustering. Range is 90 m for GPK3 and 150 m for GPK4. This gives an estimate of the distance of influence of the correlation; if clusters exist their inter-distance should be at least 90–150 m.

For the set 2, the nugget value is again significantly lower than the entire sample variance which may be interpreted to be a result of fracture clustering. Since, the range is 110 m in GPK3 and 200 m in GPK4, the inter-cluster distance will be at least 220–400 m. In GPK3, values clearly oscillate about the sill value with a wavelength of 280 m over two complete cycles. This particular experimental variogram may well be approximated by a modified hole-effect model (*Miller, 1979*), which indicates spatial periodicity for the occurrence of zones containing similar spacing. This also indicates an inter-cluster distance of about 280 m.

3.5.4 Fracture correlations

Trajectories of the Soultz deep boreholes are very appropriate to try to perform fracture cross-hole correlations. Indeed, for the first kilometer of granite section, borehole GPK3 and GPK4 have a horizontal distance of less than 30 m. At 1919 m

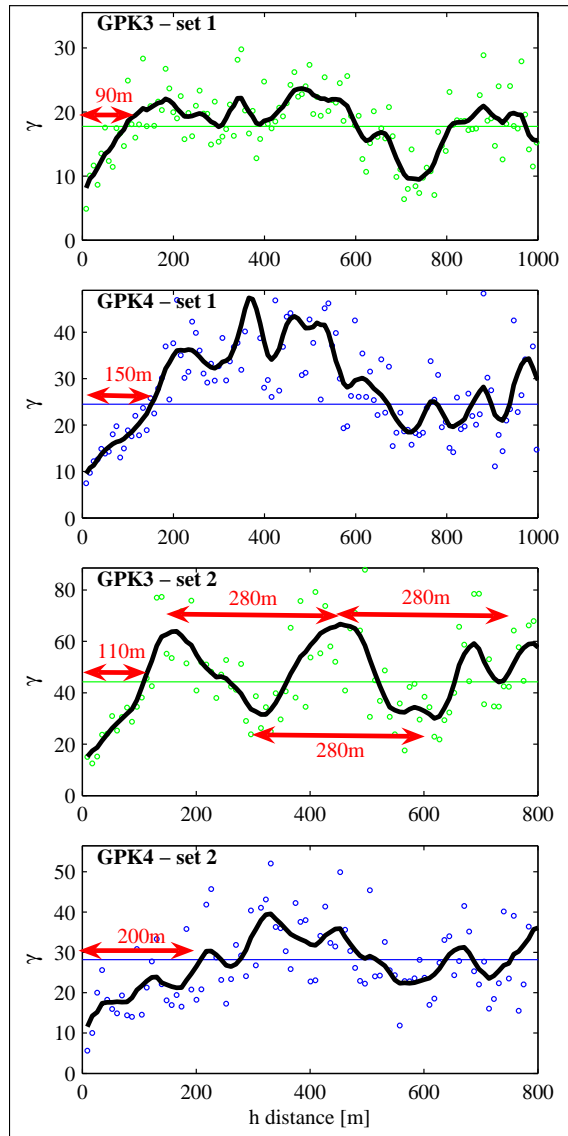


Figure 3.8: Variograms for fracture spacing with respect to distance for Set 1 and Set 2. Points correspond to the calculated experimental variogram. Black lines smooth the experimental variogram with a moving average in order to highlight the data trends. The horizontal line in blue or green corresponds to the variance of the entire sample, i.e. the expected sill value.

TVD, horizontal distance reaches a minimum of 12.6 m. At the top of the granite, distance is about 15.2 m. From 1920 m this horizontal distance begins to increase and reaches 36.4 at 2500 m TVD and 705 m at bottom holes. The third borehole, GPK2, is also located relatively close to the other boreholes in the upper part of the basement, although not as close as in the GPK3–4 case, and the opportunity of including it in the correlation analysis has been evaluated. Unfortunately, the image quality of GPK2 is far less good than the one of GPK3 and GPK4, resulting in an inhomogeneous fracture database. For this reason, it is preferred to not include GPK2 in this analysis.

In the correlation process, each fracture was considered to be perfectly planar. The uncertainties of borehole trajectories and fracture orientation, as described in Section 3.4.2 (i.e. $\pm 2.5^\circ$ on azimuth and $\pm 0.75^\circ$ on dip angle), were used in this process to permit the computation of an index of the probability that the two candidate fractures are co-planar. Practically, this is done by considering the fracture location and orientation to be random variables, and by computing the probability of coplanarity of fracture couples using Monte Carlo simulations. Details and examples of this method are presented in Appendix C.

One has to keep in mind that, because in this analysis the fractures are considered to be perfectly planar, significantly undulating fractures are excluded from the analysis result. The uncertainty in azimuth and dip angle considered here will correspond to a change of depth of intersection of about ± 1 m for a fracture dipping at 60° and a borehole distance of 20 m. This will allow the inclusion to some degree of slightly undulating fractures. To be more precise, the output of the analysis does not include the significantly undulating fractures if they exist, but only relatively planar sections of these fractures. Thus, when we will later on quantify the size of the fractures, we will actually quantify the size of relatively planar sections of fractures and not quantify the size of the entire fracture if such fracture are significantly undulating.

Combining the analysis of the 1871 fractures of GPK3 with the 2215 fractures of GPK4 permits us to test 4'144'265 (1871×2215) fracture couples. Evidently, most of the couples have a very low index of probability to be co-planar. Choosing an appropriate threshold for the index of probability to validate correlation allowed the isolation of 101 correlated fractures couples. The locations of these correlated fracture couples along boreholes GPK3 and GPK4 are presented in Figure 3.9a.

Type and set of correlated fractures are presented in Figure 3.9 b) to i). In absolute number (Figure 3.9b and c), the dominant type is the type '24'. This was also true for all fractures (see Figure 3.3a). It is more informative to look at the relative number of correlated fractures for each type (Figure 3.9d and e). In this view, except for 3 correlated fractures of type '14' in GPK3, the dominant type is the type '21', where approximately 30% of the fractures are correlated. In GPK4, the three best correlated types are also the strongly developed features on borehole images (type '11', '21', '23'). Other correlated types are types '14', '24' and '25' that are, in general, also the most prevalent types (see Figure 3.3a). As these types

3.5 Analysis of the individual fractures characteristics

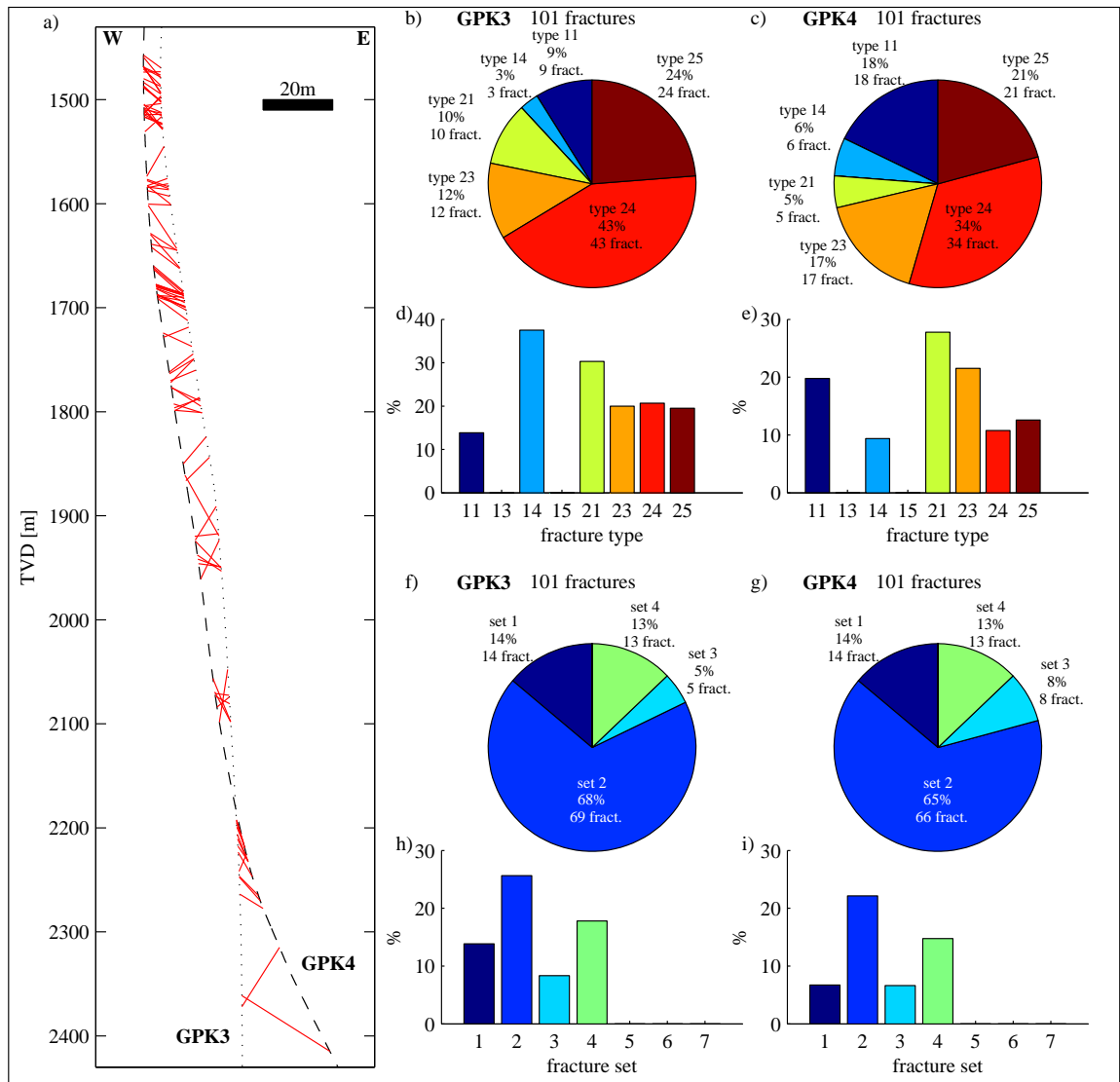


Figure 3.9: a) Borehole projection in a W-E cross section with link between the locations of the 101 correlated fracture couples. Note that depth scale and horizontal scale are not identical. b) types of the correlated fractures in GPK3. c) types of the correlated fractures in GPK4. d) proportion of correlated fractures for each fracture type in GPK3. e) proportion of correlated fractures for each fracture type in GPK4. f) set of the correlated fractures in GPK3. g) set of the correlated fractures in GPK4. h) proportion of correlated fractures for each fracture set in GPK3 in the borehole depth range 1400–2383 m, i.e. where the boreholes are close enough to permit correlation. i) proportion of correlated fractures for each fracture set in GPK4 in the borehole depth range 1400–2428 m, i.e. where the boreholes are close enough to permit correlation.

are very common, the probability to get reasonably well aligned fractures by chance that are actually not the same geological structure is higher. Thus, it cannot be excluded with this data set that some of the correlated fractures correspond to such occurrences. In GPK3, the correlation of fracture of the types ‘14’, ‘24’ and ‘25’ are as good the correlation of fractures of the types ‘11’ and ‘23’.

Concerning the sets, the most correlated set is Set 2 (N–S striking, east dipping) both in absolute and relative number. In the borehole depth range 1400–2400 m, where borehole inter-distance permits correlation, about 25% of this set is correlated. The next best correlated set is Set 4. Other correlated sets are Sets 1 and 3, with less than 14% of correlated fractures in GPK3, and less than 7% in GPK4. This is a good indicator that east dipping structures have a higher persistence than others, at least in the upper part of the granite, i.e. about from 1400 to 2400 m.

3.5.5 Fracture size

The dataset of correlated fractures permits the evaluation of the size of fractures. A first approach is purely deterministic: one can state that a correlated fracture is at least as big as the distance between boreholes in the correlated fracture plane. On the other hand, an upper bound for fracture size cannot be estimated. Size of uncorrelated fractures cannot be estimated at all. Indeed, it cannot be excluded that a fracture that crosses only one borehole has a very big extent, but in a direction opposite to the second borehole.

One aspect related to fracture size is the fracture shape. From our two boreholes data set, this aspect cannot be solved at all. For the sake of simplicity, we will consider penny shape fracture geometry. With this hypothesis, fracture size can simply be described by the fracture radius r . This simple hypothesis is probably acceptable when considering fractures growing in an isotropic granite (*Bankwitz, 1965, 1966*). For the interpretation of the following results, this undemonstrated initial hypothesis has to be kept in mind.

The inter-borehole half distances in the correlated fracture planes are presented in Figure 3.10. It corresponds to a lower bound for the radius of these fractures. For these 101 correlated fractures, this minimum radius ranges from 6.4 to 30.3 m, the average being about 10 m. Note that this minimum is not controlled by fracture size, but by the borehole trajectories.

A probabilistic approach gives more precise constraints on fracture size. Let us first consider the simple 2D case presented in Figure 3.11. We will express fracture radius r as function of the distance between boreholes in the fracture plane d with the following formula:

$$r = k \cdot d \tag{3.2}$$

k is a factor of proportionality between r and d . k is always bigger than 0. In this first simple theoretical approach, we will consider that all fractures have the same

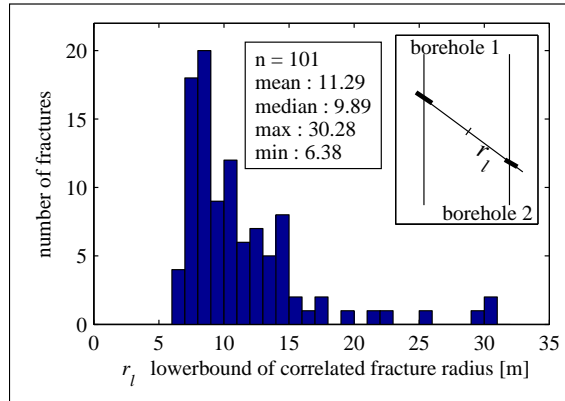


Figure 3.10: Half inter-borehole distance within the plane of the 101 correlated fractures couples, i.e. lower bound for the radius of these fractures.

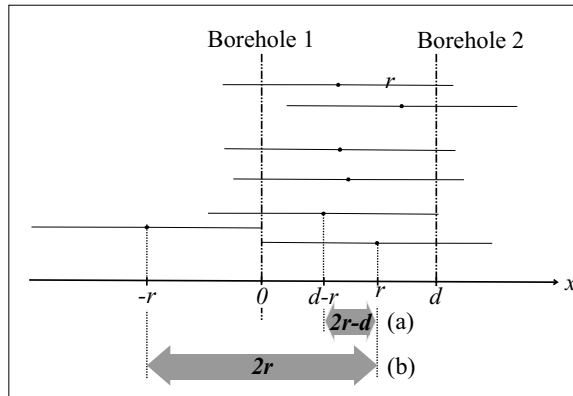


Figure 3.11: Simple 2d scheme for probabilistic fracture length estimation.

radius r . Let us compute the probability p that a fracture observed in borehole 1 crosses borehole 2. If the fracture radius is smaller than half of d ($k < 0.5$) then the probability that this fracture, seen in one borehole, crosses the other borehole is zero (the fracture is too short):

$$p = 0 \text{ for } k < 0.5 \quad (3.3)$$

If a fracture has a radius higher or equal to one half of d ($k \geq 0.5$), this fracture, seen in one borehole, has some chance to cross the other borehole. It depends on the relative position of the fracture center to both boreholes. A fracture, visible in borehole 1, will obligatory have its center in a $2r$ interval around borehole 1 (Figure 3.11b). However, a fracture visible in both boreholes will have its center in a $2r - d$ interval only (Figure 3.11a). Considering that fracture center repartition is uniformly random, for a fixed d , the probability that intersection of both boreholes occurs is

given by:

$$p = \frac{2r - d}{2r} \text{ for } k \gtrsim 0.5 \quad (3.4)$$

Combining equations (3.2) and (3.4), the probability that intersection of both boreholes occurs can be expressed as a function of k only:

$$p = 1 - \frac{1}{2k} \text{ for } k \gtrsim 0.5 \quad (3.5)$$

This computation contains two major simplifications: 1) a 2D geometry is considered whereas the problem is 3-dimensional, 2) a constant fracture size is considered. Using Monte Carlo simulations, the relation linking the probability p with the factor of proportionality k as in equation (3.5) was numerically evaluated for the 3-dimensional problem considering penny shape fractures with lengths following an exponential negative distribution. The exponential negative distribution was chosen for the sake of simplicity. Indeed, such distribution is defined by a single parameter ($\mu = \sigma$). However, we have no way to control what is the actual distribution of fracture length.

In order to extract fracture length information, equation (3.5), or more precisely its equivalent considering 3-dimensions and exponential fracture lengths distribution, is solved for k . Using an estimate of p permits to compute k and to constrain fracture size. An estimate of p is obtained by comparing N_c , the correlated number of fracture within a certain range of d , with N_a , the total number of fractures within the same range of d :

$$\text{probability of intersection of both holes: } p \cong p_e = \frac{N_c}{N_a} \quad (3.6)$$

The results of this analysis are presented in Figure 3.12. The upper frame of this figure shows the number of correlated fractures (N_c) relative to all fractures (N_a) in classes of d of 5 m intervals which permits computing the estimate of the probability that a fracture cross both boreholes p_e for each classes. For each class, equation (3.5) is solved for k using the estimated probability p_e . Finally, r is computed by multiplying, for each class, k by the center value of the class, d (equation 3.2). Computed mean radius are presented in Figure 3.12b and range from 8 to 22 m with an average of 15 m. In an ideal world, the mean radius should be independent from the in plane borehole separation. The variations that we observe in the computed mean radius reflect the limitation of our fracture model, i.e. perfect penny shaped fractures with size following an exponential distribution.

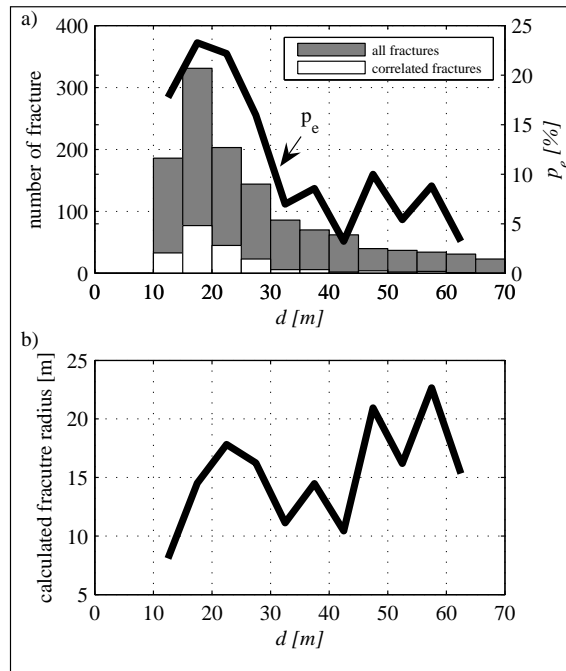


Figure 3.12: Computation of fracture radius. a) From the ratio of the number of correlated fractures over all fractures, p_e is computed. b) From p_e a mean fracture radius for an exponential distribution is calculated.

3.6 Analysis of the fractures zones from wellbore images

Fractures zones are usually understood to be zones of one to several metres in thickness with a large number of persistent fractures belonging often, but not necessary, to the same set. At Soultz-sous-Forêts, fractures zones in the basement have been first described on cores where they are not only characterised by high fracture density but also by the presence of hydrothermal alteration (*Genter et al.*, 1998, see also Chapter 2). These fractures zones carried and possibly still currently carry fluid flow. Moreover, the permeability creation and enhancement achieved by massive injection of water was found to be limited to these hydrothermalised fractured zones (*Evans et al.*, 2005a) and we believed that they play a salient role in the reservoir behaviour.

As the deep boreholes of Soultz are mostly if not entirely not cored, alternative methods to identify and to describe fractures zones have been envisaged. These include integrated study of cuttings and wireline logging, i.e. spectral gamma ray and acoustic televiewer. Due to the selective sampling involved in fracturing description from acoustic BHTV (*Genter et al.*, 1997) the original fractures zone definition proposed above has to be extended in order to permit exhaustive identification of

Table 3.3: Description of the six type of fractures zone.

<i>Type 1</i>	Acoustic image alteration without any thick fracture trace.
<i>Type 2</i>	Single thick fracture.
<i>Type 3</i>	Single thick fracture with image alteration.
<i>Type 4</i>	Cluster of thick fractures without image alteration.
<i>Type 5</i>	Cluster of thick fractures with image alteration.
<i>Type 6</i>	Enlarged borehole section resulting in very poor UBI image but possibly reflecting an intersection with a major fractures zone.

fractures zones along the wells.

In order to clarify the situation, we propose to classify fractures zones identified on acoustic BHTV in six different types (see Figure 3.13 and Table 3.3). Fracture zones of type 1 are characterized by clear acoustic image alteration but without any thick fracture trace. Some fractures zones are characterized by virtually a single thick fracture without other indices on the images (type 2), but more often this single fracture is also accompanied by some trace of alteration (type 3). For these three first types it is sometimes difficult to decide if this single fracture or alteration zone has really to be considered as fractures zones *sensus stricto*. Any doubts disappear when thick fractures occur in cluster as for type 4 (without clear alteration) or type 5 (with clear alteration). Sometimes, when the borehole intercepts a strongly developed fractures zone, the spalling of the borehole wall is so strong that it results in highly enlarged borehole sections. UBI tools do not perform well in these enlarged borehole sections (see Section 2.3.1) and usually individual fractures can hardly be isolated (type 6), however such section should not be neglected, as they may be intersections of major structures with the wellbore.

One key question concerning these fractures zones is to characterise their orientation from borehole images. The internal structure, i.e. the geometric relations of the individual fractures building the zone and the orientation of the zone itself, is unknown. It is not possible to use the fractures composing them to derive *a priori* a general orientation for the zone. Borehole cross-correlations of fractures zones give some insight into the fractures zones internal architecture in the Soultz granite.

Between 1400 and 2200 m depth, 16 fractures zones were isolated and correlated between boreholes GPK2, GPK3 and GPK4. The intersection of a given fractures zone with all three boreholes forms three points in space, from which the general orientation of the fractures zone can be computed. Comparing this general orientation with the fracture composing the fractures zone permits us to better understand the fractures zone architecture.

Sometimes the components (i.e. the individual fractures) of the fractures zone

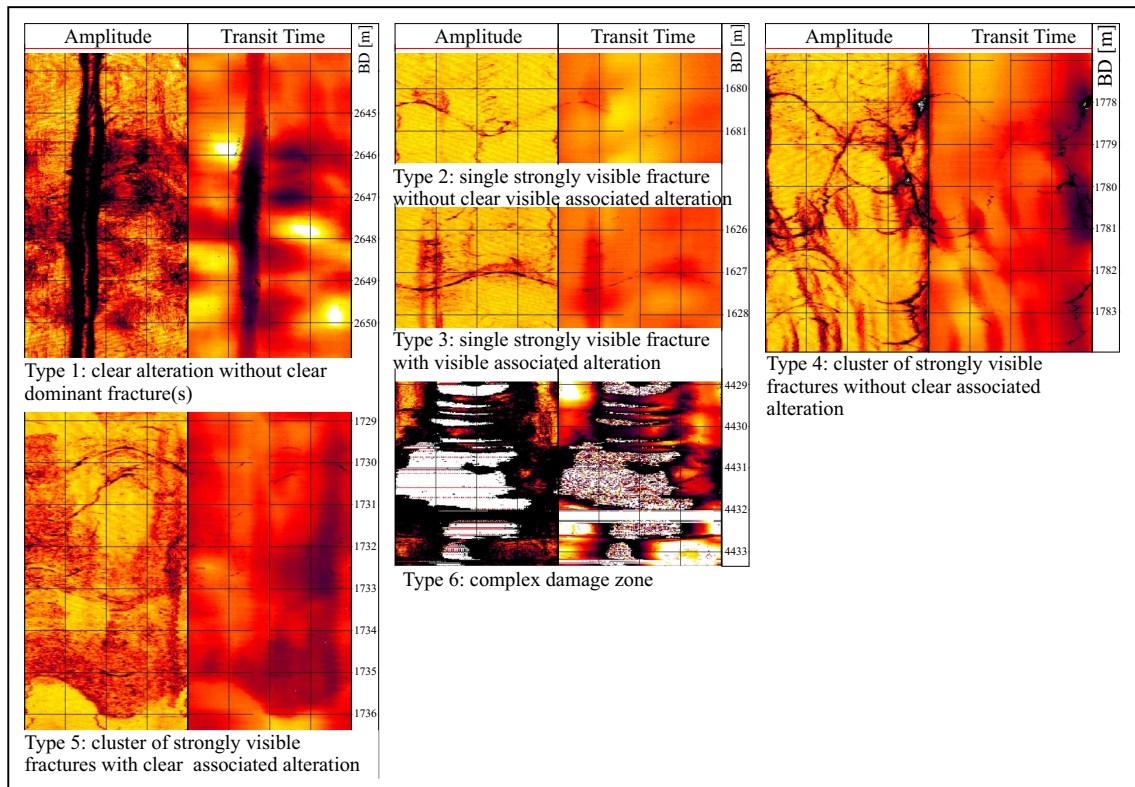


Figure 3.13: Examples for the sixth different types of fractures zones.

have all the same orientation (see for example fractures zone number 6 in Figure 3.14). In such case, the fractures zone itself follows the same orientation that its components. When more than one orientation is present in the fractures zone's components (see for example fractures zone 11 in Figure 3.14), the general orientation of the fractures zone is found to be about the same than one present orientation, usually the one containing the thickest fracture. The variability within a fractures zone from one borehole to the next is usually quite strong. Over the couple of tens of meters between the intersections of a fractures zone with one borehole to the next, significant changes in thickness and architecture usually occur.

All these elements made us think that the adequate conceptual model for fractures zones internal structure is that they are built of anastomosed fracture networks with through going thick fractures delimiting shear lenses. This geometry corresponds to the most developed stage of Riedel type shear zones, as presented for example in *Naylor et al.* (1986). Note that this formation model of shear zone is debated and other evolution model could produce similar final geometry (e.g. *Kim et al.*, 2003; *Martel*, 1990). The analysis of the borehole images of Soultz-sous-Forêts does not provide a complete enough dataset to further develop this debate.

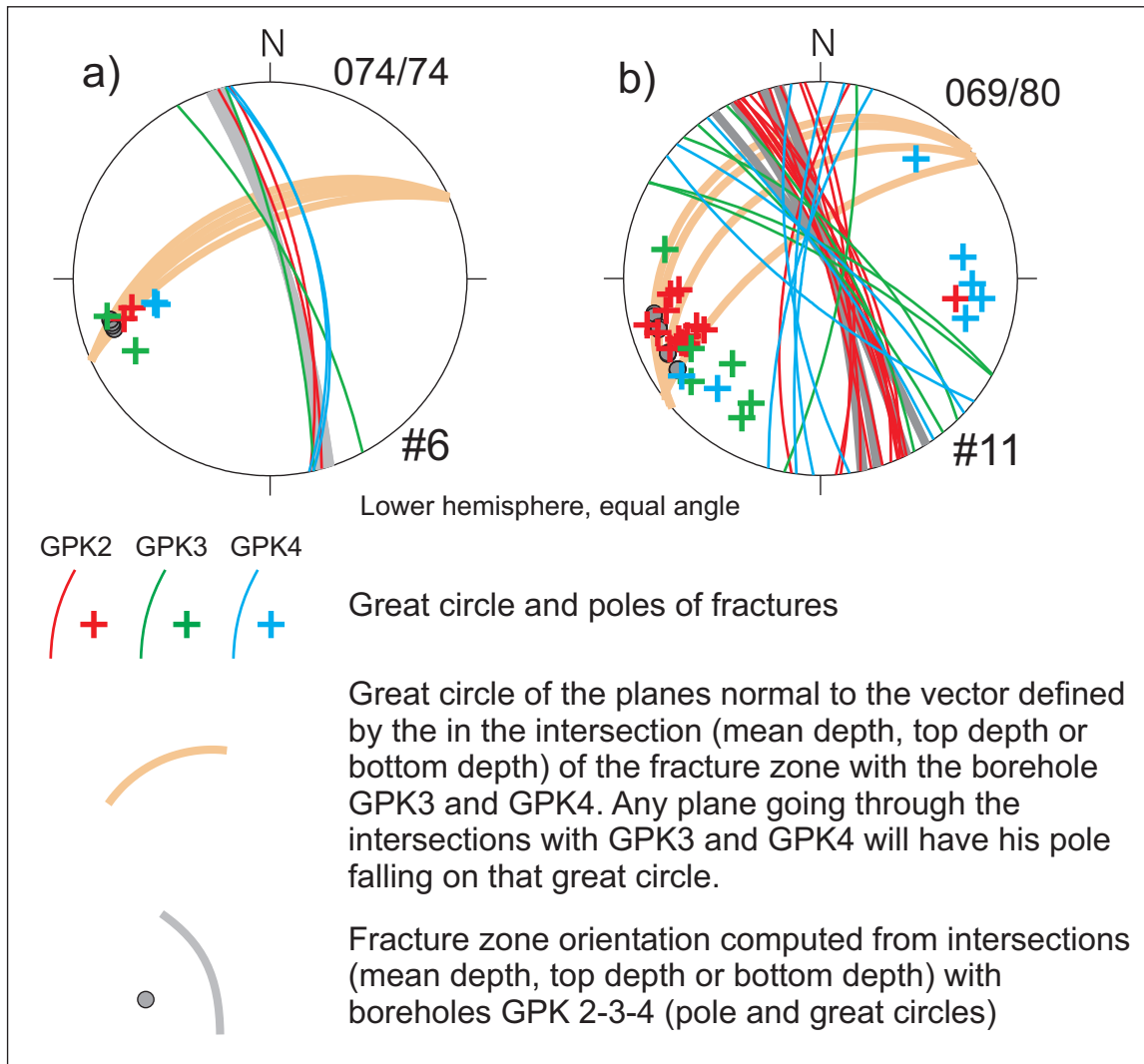


Figure 3.14: Two examples of correlated fractures zone and their constituting fractures. The orientation of the fractures zone (in gray) is computed from the intersections with the three boreholes GPK2-3-4 (3 points in space) and is compared with the orientation of the constituting fractures. The orange planes consider only the intersection with GPK3 and GPK4 (2 points in space) and represent the plan normal to a all possible planes going through the intersection of the fractures zone with these two boreholes. a) fractures zone number 6 oriented 074/74. All constituting fractures have the same orientation than the zone. b) fractures zone number 11 oriented 069/80. The constituting fractures are separated in two distinct orientation, one being similar to the orientation of the zone, the other being oblique.

3.6 Analysis of the fractures zones from wellbore images

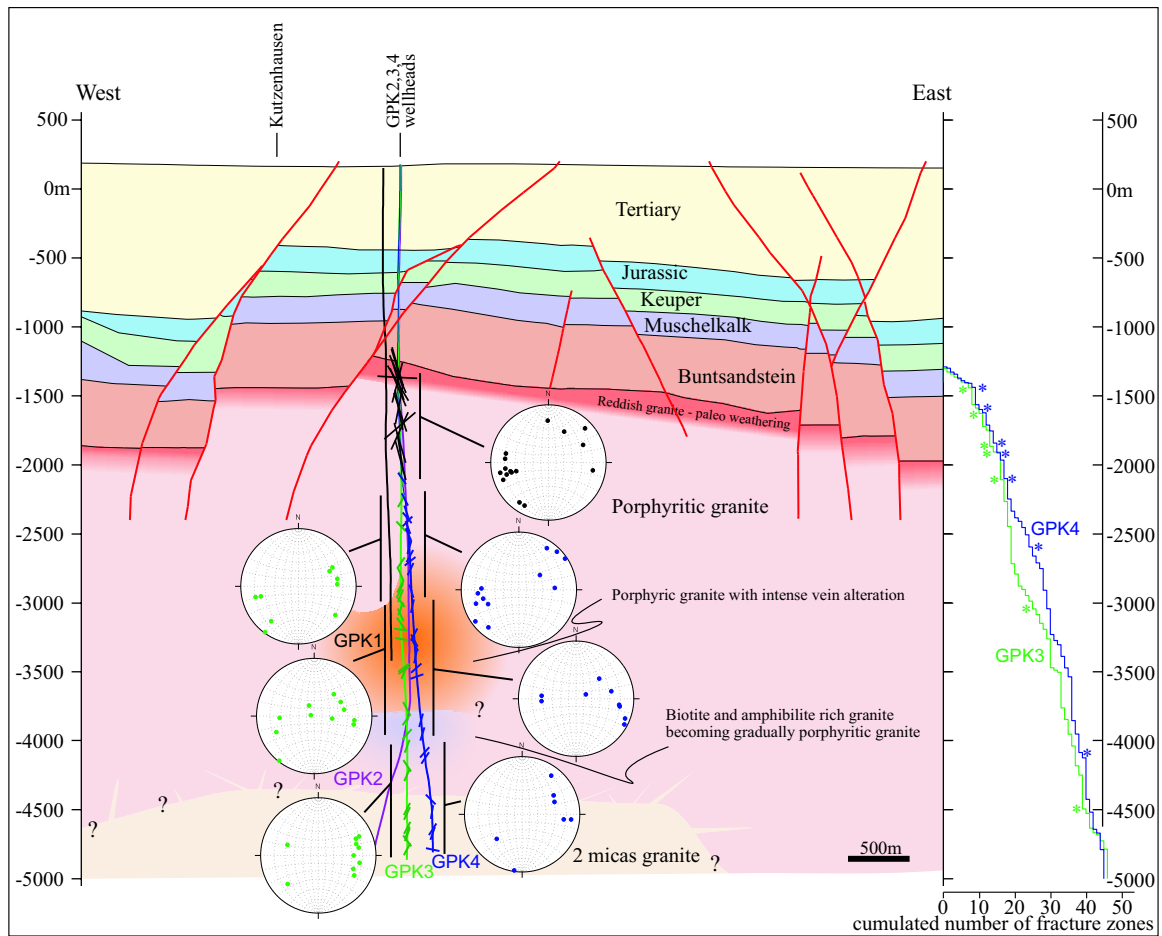


Figure 3.15: Location and orientation of the fractures zones on a W–E cross-section. The right frame present the cumulative number of fractures zones vs. depth. The depth of flowing fractures zones is indicated by asterisks.

The position and the general orientation of the 16 correlated fractures zones are displayed in black in the cross-section of Figure 3.15 and listed in Figure 3.4. Nine of the sixteen fractures zones are east dipping. They have orientation similar to the fracture Set 2 described above. A predominance of this orientation was already highlighted in the upper section by the analysis of the individual fracture characteristics (see Figure 3.6). The other seven fractures zones have various orientations mostly about vertical NW–SE striking, comparable to the orientation of fracture Set 3, which is the second dominant set according to the analysis of fracture abutting relations described here over. Only one zone is west dipping, an orientation similar to the fracture Set 1. There is no NE–SW striking fractures zone.

Below 2200 m, fractures zones were also tracked in GPK3 and GPK4, but due to the increasing distance between the boreholes it was not possible to correlate

Table 3.4: List of correlated fractures zone in the upper part of boreholes GPK2, GPK3 and GPK4.

#	GPK2 BH depth		GPK3 BH depth		GPK4 BH depth		orientation	
	<i>top [m]</i>	<i>btm [m]</i>	<i>top [m]</i>	<i>btm [m]</i>	<i>top [m]</i>	<i>btm [m]</i>	<i>dip direc.</i>	<i>dip [°]</i>
1	1515	1517	1478	1480	1468	1470	82	74
2	1507	1509	1504	1506	1477	1479	102	74
3	1460	1465	1541	1543	1505	1507	179	72
4	1554	1558	1513	1527	1514	1528	75	67
5	-	-	-	-	1534	1564	-	-
6	1688	1691	1577	1581	1567	1569	74	74
7	1551	1553	1548	1565	1582	1585	280	76
8	1595	1597	1584	1586	1586	1589	75	60
9	1657	1675	1602	1638	1606	1628	77	68
10	1657	1675	1732	1749	1721	1763	227	82
11	2033	2044	1791	1821	1771	1784	69	80
12	1986	1989	1761	1772	1799	1802	29	81
13	1840	1852	1899	1901	1889	1891	207	62
14	1868	1873	1925	1929	1931	1933	243	68
15	2116	2131	2041	2047	2014	2027	95	74
16	2297	2299	2078	2093	2085	2099	78	81
17	2341	2344	2078	2093	2141	2149	36	81

them. Indeed, planar extrapolation of fractures zone is not valid over long distance as the fractures zone are not necessary planar and the uncertainty of the intersections become to large to allow definitive correlations between wells. A general orientation at the well intersection was attributed to these lower fractures zones, following the here over described rule, i.e. the general orientation of the zone follow the orientation of its major fracture. At total number of 47 fractures zones are described in GPK3 (including the 17 fractures zones above 2200 m) and 45 fractures zones in GPK4 (also including the 17 fractures zones above 2200 m).

Locations and orientations of fractures zones are also presented in Figure 3.15, in green for GPK3 and blue for GPK4. The predominance of east dipping fractures zones in the upper part of the granite was already highlighted. Below 2200 m and down to 4 km, west and east dipping fractures zones are better balanced. Below 4 km west dipping fractures zone are dominating.

The vertical distance between two subsequent fractures zones is in average 80 m, with minimum and maximum values ranging from 5 to about 300 m. Note that this distance is not a true spacing since the fractures zones have not all the same orientation. If they were parallel and dipping at about 60°, as the majority do, the

mean true spacing would be about 40 m ($80 \cdot \cos(60^\circ)$). Sorting fractures zones in sets of fractures zones with similar orientation has not been considered, but considering similar distributions for the fractures zone like for the individual fractures sets, i.e. that an specific set will contain 10-30% of the fractures zone, the mean true spacing within one set of fractures zone should range between 120 (40 m/30%) and 400 m (40 m/10%), in relatively good agreement with the indication from the variogram analysis presented above.

One aspect that borehole wall images do not provide is the ability to characterise which fractures zone are carrying flowing water. In order to get some insight into this aspect, the location of fractures zones is displayed in Figure 3.16 with temperature logs run about three months after drilling completion. Permeable fractures zones will be more deeply cooled during drilling operations and present anomalies on the post drilling temperature profile. If run under adequate conditions, temperature logs can be very informative and allow a very precise determination of the flowing fractures (see e.g. *Evans et al.*, 2005a). In our case, months after drilling, the anomalies are smeared and we do not expect such precise indications, as well as not an exhaustive listing of flowing fractures zones. Nevertheless, seven temperature anomalies were seen in each borehole, and all of them were clearly related to a fractures zone determined on borehole images. Moreover, the four anomalies which were corresponding to correlated fractures zones (above 2200 m), were consistently indicating flow in the same fractures zone on both GPK3 and GPK4 boreholes.

Depth locations of flowing fractures zones are highlighted by asterisks in Figure 3.15 and Figure 3.16. On the seven fractures zones which present temperature anomalies, five are situated in the upper part of the borehole. These five fractures zones are all East dipping. The other fractures zone located deeper in boreholes are all West dipping. As we are not sure to have an exhaustive listing of flowing fractures zones, that dataset cannot be used to estimate mean spacing between flowing fractures zones.

With the presented data, it is not possible to further sort the fractures zones for their hydraulic importance. However, it noteworthy to mention that in within the zones presenting temperature anomalies, two of them particularly impacted the drilling operations. One was intersected in GPK2 at 2110 m TVD during the initial drilling of the well in 1995, and resulted in total loss of circulation fluid. No cuttings were obtained from the well during the subsequent drilling to 3876 m because they were swept into the fractures zone along with the drilling fluid. The zone was eventually plugged with 23 m³ of cement during the extension of GPK2 to 5000 m in 1999. This zone cut GPK3 at 2030 m TVD and GPK4 at 2005 m TVD and we estimated its orientation to be 095/74. Another important fractures zone is penetrated by GPK3 at 4697 m TVD. It produces total mud loss during drilling (*Hettkamp et al.*, 2004) and flow logs have shown that this zone accounts for more than 70% of the outflow in the GPK3 open hole section (*Tischner et al.*, 2007).

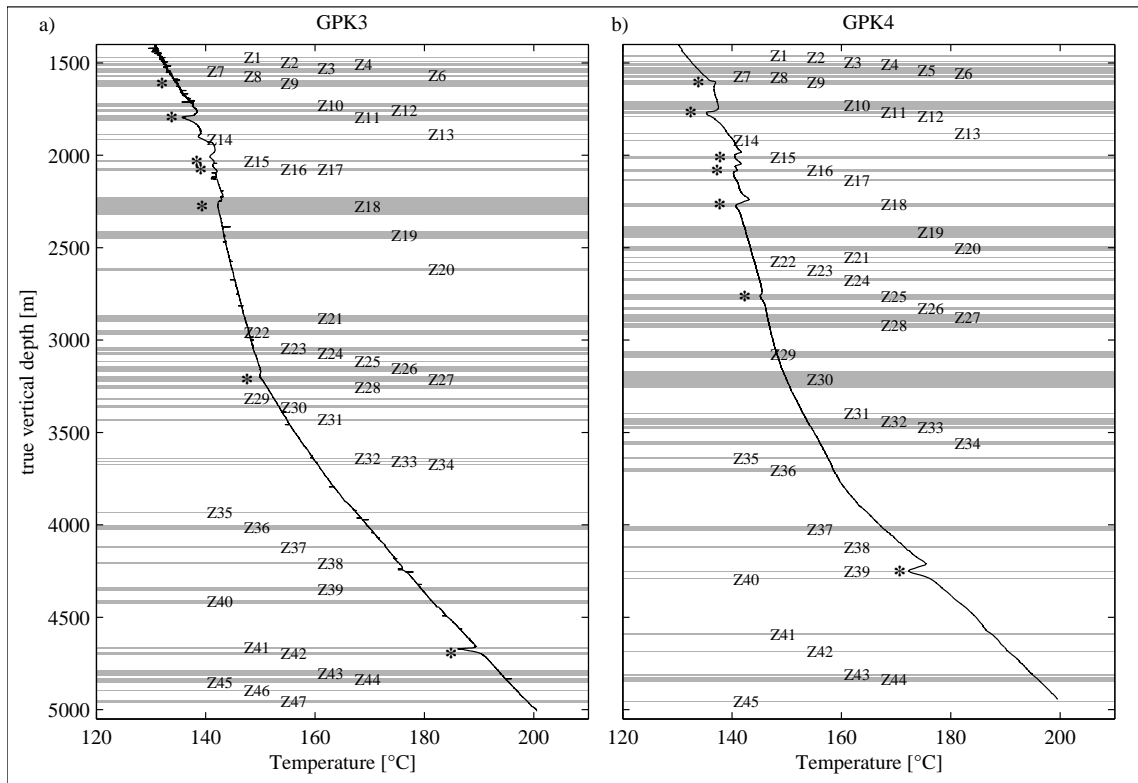


Figure 3.16: Temperature logs about 3 months after drilling in GPK3 (a) and GPK4 (b) compared to fractures zones locations. Asterisks denote fractures zones associated with temperature perturbations.

3.7 Synthesis

The fracturing of the basement of the Upper Rhine Graben during its long tectonic history generated discontinuities at various scales. The analyses presented above permitted us to define several of these structures and allowed us to quantify their characteristic size. Figure 3.17 present these results in a synthetic manner.

On the upper end of the size scale, the Upper Rhine Graben, a major structure through Central Europe, is 300 km long, 30 to 40 km wide and affects the entire thickness of the continental crust. It is itself a segment of the European Cenozoic Rift System which extends over a distance of some 1100 km (*Dèzes et al.*, 2004). The border faults of this graben accommodate large strain with down throw reaching about 4.5 km.

The inner architecture of the Upper Rhine Graben is made of tilted blocks delimited by major faults. These faults are brought in evidence by geological mapping in sediments and geophysical investigations. Their length range from about 2 km to 20 km. Examples of such faults in the Soultz area are the Pechelbronn fault,

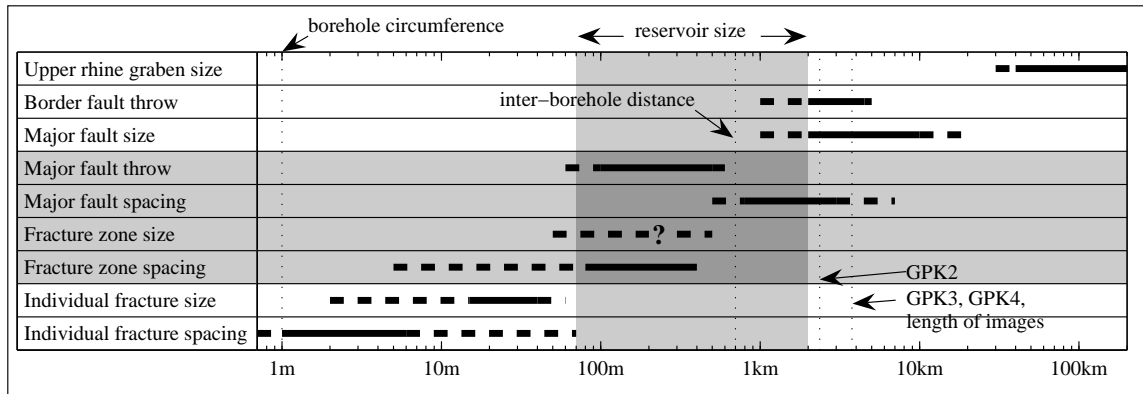


Figure 3.17: Synthesis of the size of the various structures crossing the Upper Rhine Graben basement. In grey are highlighted the relevant size for the reservoir development and the relevant structure which correspond to that size.

the Surbourg-Kutzenhausen fault or the Hermerswiller-Soultz fault. They built local horst and graben systems, with down throws ranging from about 100 to 500 m. The spacing of such structures ranges from about 800 m to 3 km or even more.

Detailed analysis of the fracturing at borehole walls, appropriate statistical analyses, and borehole cross-correlations permit us to highlight structures at an intermediate scale that we call fractures zones. These fractures zones occur with a spacing ranging from about 40 to 400 m and sometimes less. Their extent cannot be reliably constrained with the available data, but we make the rough estimate that they are about 50 m to a maximum of maybe 500 m long. Additional data from micro-seismic monitoring or VSP could possibly give some more constraints on the size of these fractures zones as these methods are not restricted to the borehole vicinity.

Borehole wall images permit the description of thousands of fractures with mean spacing of 1 to 6 m. Spacing distribution follows log-normal laws with clustering of the fractures which reflects the occurrence of the fractures zones mentioned above. Due to sampling bias, power law distributions cannot be excluded and even maybe be most probable, considering previous studies on cores (*Genter et al., 1997*). The size of the fractures was evaluated, considering them to be perfectly planar and penny shaped, by studying borehole cross-correlations. Mean fracture size was evaluated to be about 15 m to 40 m. With borehole data only, the fracture lengths distribution cannot be evaluated and an exponential negative distribution was used in the fracture lengths computation.

For the development of a geothermal reservoir, the relevant structures are clearly, due to their size and spacing, the fractures zones. Major faults may also play a role in the reservoir behaviour, but due to their spacing only one or two of these structures will cross a potential reservoir. They may function as a dominant drain within the

reservoir and producing short cuts which would not permit to build an efficient heat exchanger. At lower scale, single fractures may not have enough connectivity to carry significant flow rates, except within fractures zones.

The characterisation of fractures zones then becomes a key issue in the reservoir development. Unfortunately, major uncertainties remain concerning the exact geometry of these fractures zones. Their length is not constrained, but we believed that it is long enough to build connections between boreholes assuming the relay of a limited numbers of these structures. Spacings are small enough to permit multiple flow paths between boreholes and to efficiently exchange heat with the rock mass. The orientation of these fractures zones were estimated at borehole wall and seem to be similar to the orientation of the small scale fractures and large scale fault, i.e. N–S striking dipping at about 60° to the west or to the east, sub-vertical striking NW–SE or sub-vertical striking ENE–WSW. East dipping fractures zones dominate in the upper part of the basement while West dipping structures dominate at the level of the deep reservoir. The internal architecture of fractures zones seems to correspond to the conceptual model of anastomosed network of fractures delimiting shear lenses. More important is the observed high heterogeneity of the architecture of fractures zones with major change in width and structure over 10 to 20 m. Such heterogeneities may play a major role in the hydraulic behaviour of the fractures zones by channelling the flow in better developed fractures zone sections. This may explain the fact that only a limited number of fractures zones show clear permeability at the borehole wall.

More effort should be done to characterise fractures zones, particularly their extent and geometry within the reservoir. This last aspect cannot be solved with borehole data, only and other methods which permit to investigate the volume between boreholes should be used. Presently, a VSP (Vertical Seismic Profile) survey is performed on the Soultz site which is expected to refine the results presented here. Micro-seismic monitoring bring also some insight on the possible size of these fractures zones, when they become seismically active during stimulation injections (e.g. *Evans et al.*, 2005b).

3.8 Conclusions

Various tectonic structures with various sizes cross the basement under the geothermal site of Soultz-sous-Forêts. The detailed analysis of the fracturing permits to characterise and quantify the size of these structures. Results are following:

1. Individual observable fractures on acoustic BHTV have mean size ranging between 15 and 40 m and mean spacing between 1 to 6 m. Spacing distribution follows a log-normal law but this probably reflect sampling bias on a original power law distribution. Four major fracture orientation sets were found. About 60% of the fractures strike N–S and dip about 60% to the East or to the West. East dipping fractures are dominant in the upper part of the basement while

West dipping fractures dominate at reservoir depth, i.e. about 5 km depth. The two other major sets are sub-vertical, striking NW–SE and ENE–WSW.

2. Individual fractures cluster to form fractures zones with spacing ranging from about 40 to 400 m. Their extension cannot be reliably constrained with the available data, but we estimate that they are about 50 m to 500 m long. Their orientations seem to include the major direction seen for individual fracture sets. Uncertainties subsist concerning their internal architecture, but it seems to correspond to the conceptual model of anastomosed network of fractures delimiting shear lenses. This includes also major variations in both internal structure and width over distances of 10 to 20 m. These variations are suspected to play an important role in the hydraulic behaviour of the fractures zones by channelling the flow.
3. Major faults have lengths of about 2 km to 20 km and spacing of about 800 m to 3 km or even more.

Due to their size and spacing, the most relevant structures on which a geothermal reservoir can be developed are the fractures zones. The available data, i.e. principally the borehole images, have a scale of investigation limited to the borehole circumference which is about 1 m and do not permit the further characterisation of the extent and the geometry of fractures zones within the reservoir volume. Alternative method like for example VSP will be used to refine the results presented here.

4 State of stress in granite at Soultz-sous-Forêts to 5 km depth from wellbore failure and hydraulic measurements

4.1 Abstract

OBSERVATIONS of breakouts and drilling-induced tension fractures (DITFs) in two 5 km deep boreholes of the European Enhanced Geothermal Project of Soultz-sous-Forêts, France, have been combined with the analysis of pressure data from stimulation tests in all 3 deep wells to obtain a description of the state of stress in the granite down to 5 km depth. The orientation of the maximum horizontal stress, SH_{max} , in the 5 km deep reservoir is found to be $N169^{\circ}E \pm 14^{\circ}$, in accord with previous results from the 3.5 km reservoir. Estimates of minimum principal horizontal stress (Sh_{min}) in the deep reservoir were obtained by taking Sh_{min} as given by the pressure at the casing shoe during stimulation injections in the holes, all of which show evidence of jacking. The resulting Sh_{min} profile was consistent with the extrapolation of that defined in the shallow reservoir. Bounds on the profile of SH_{max} for the depth range 1400–5000 m were obtained from the observation that DITFs occurred primarily above 2.2 km, whereas breakouts occurred almost exclusively below 3.6 km. The analysis of the conditions for each type of wellbore failure to occur, or not occur as the case may be, used laboratory-derived values for UCS , and drilling-related cooling stress estimates obtained from temperature sensors inside the logging sondes, and also MWD estimates of mud temperature inside the drill bit. The resulting bounds limit SH_{max} to the range $0.7-1.2 \cdot Sv$ in the lower reservoir below 3.6 km, although the absence of breakouts near 3.5 km limits SH_{max} to be less than $1.0Sv$. The results per se do not impose tight constraints on the magnitude of SH_{max} , and the best working hypothesis remains $SH_{max} = 1.0Sv$, as imposed by the observation of strike-slip and normal fault plane solutions. A corollary of the analysis is that the coefficient in the effective stress law for tensile failure is less than 0.8, possibly significantly so. SH_{max} estimates were also computed from measurements of the width and depth of the breakouts using two recently applied formulae, and the results compared with the strict bounds obtained from the presence

or absence of failure. Neither yielded an improvement on the bounds. However, it is clear that variations in the width of breakouts occur that are systematic and probably reflect stress heterogeneity.

4.2 Introduction

The setting of reliable constraints on some or all attributes of the state of stress is necessary to take informed engineering decisions in many practical rock mechanics problems, such as in deep mining, tunnelling, borehole stability analysis and reservoir enhancement in both the petroleum or geothermal industries. The latter constitutes the context of the present study where stress information is needed to model the behaviour of the crystalline rock mass at the European Enhanced Geothermal System (EGS) project located at Soultz-sous-Forêts in the Rhine Graben. Stress is important for the development of EGSs because it is a primary factor influencing the reservoir response to the massive stimulation injections that are commonly performed to enhance the permeability of the rock mass within the reservoir.

Unfortunately, stress characterisation of a rock mass is a difficult and expensive task, particularly with regard to constraint of the magnitude of the maximum horizontal stress, SH_{max} . At Soultz, numerous studies have constrained attributes of the stress tensor to 3.5 km, although published estimates of the magnitude of SH_{max} remain controversial. No studies have critically analysed relatively recent data obtained below 3.6 km to directly constrain the stress state in the deeper reservoir to 5 km. In this paper we analyse ultrasonic borehole televiewer data run in two of the three 5 km deep wells at the site, together with hydraulic data obtained during the stimulation injections performed in the deep reservoir to extend the data-constrained stress characterisation of the shallow reservoir to 5 km, including the magnitude of SH_{max} . This paper is concerned with defining the linear depth trends of the various stress attributes, the so-called linear stress characterisation that is useful for modelling. Deviations of the stress attributes from the linear depth trends, referred to as stress heterogeneities, are described in Chapter 5.

The stress constraints arise principally from analysis of breakouts and drilling-induced tension fractures (DITFs) seen of the ultrasonic borehole wall images of the wells. It is well established that these features constitute one of the best indicators of the orientation of the principal horizontal stresses. However, since they represent stress-induced failure of the wellbore, a careful analysis of the conditions of their formation allows constraints to be placed upon stress magnitudes. To obtain unique, relatively well-constrained values for each of the two principal horizontal stress magnitudes essentially requires that one be independently specified. Thus we analyse downhole pressure data from stimulation injections to estimate the magnitude of Sh_{min} , and use this in the analysis of wellbore failure to constrain the magnitude of SH_{max} . These results are evidently of importance for the Soultz geothermal project,

but they also touch on issues of more general interest, particularly with regard to the mechanics of wellbore failure. Thus, the results should be of interest for anyone interested in rock mass stress characterisation.

4.3 Background

The Soultz-sous-Forêts EGS project is located in north-eastern France within the Upper Rhine Graben (URG). The URG is a NNE trending graben, part of the European Cenozoic Rift System (e.g. *Dèzes et al.*, 2004). The formation of the URG was initiated in middle Eocene. Fault slip analysis suggests four distinct tectonic phases in the Cenozoic history of that structure with various principal paleo-stress orientations (e.g. *Schumacher*, 2002; *Villemin and Bergerat*, 1985). Presently, the large scale tectonic regime of the Rhine Graben is under the influence of the combination of the mid-Atlantic ridge-push with the Europe/Africa collision with maximum compression oriented about NW–SE (*Brereton et al.*, 1991; *Müller et al.*, 1992; *Villemin and Bergerat*, 1985).

At the Soultz site, the basement is covered by about 1.4 km of Mesozoic and Cenozoic graben fill (Figure 4.1). The first borehole of the project called GPK1 was drilled in 1987 down to 2 km (e.g. *Dezayes et al.*, 2005b). In 1992, that borehole was extended to 3.6 km depth and stimulated with massive fluid injections. In 1995, a second hole, GPK2, was drilled to 3876 m and stimulated in order to form a duplet with the 400 m distant GPK1. The ‘shallow’ reservoir between the wells at 2.8–3.5 km depth was circulated in 1997 at 24 l/s for 4 months. In 1999, GPK2 was deepened to 5 km depth and two new partially-deviated boreholes, GPK3 and GPK4, were drilled in order to develop a ‘deep’ reservoir at 5 km depth.

4.3.1 Previous knowledge of the stress state at Soultz

Prior to this study, knowledge of the stress state in the 5 km deep reservoir at Soultz-sous-Forêts was largely based upon extrapolation of the characterisation defined for the shallower reservoir to 3.5 km depth. Although this reservoir has been extensively studied, some questions remain, principally with regard to the magnitude of SH_{max} . It is commonly assumed at Soultz and elsewhere that one principal stress is vertical. The presence of inclined DITFs along some vertical borehole section provides a fairly clear indication that this is not always the case, at least locally (see also Chapter 5). However, the balance of evidence shows that when averaged over scales greater than 100 m, one principal stress is vertical. This justifies the assumption that the magnitude of S_v is equal to the integrated overburden.

The orientation of the horizontal principal stresses have been studied by several authors, mostly using breakouts and DITFs seen on the logs run in the shallow reservoir down to about 3.5 km (*Tenzer et al.*, 1991). *Tenzer et al.* (1992) identified axial

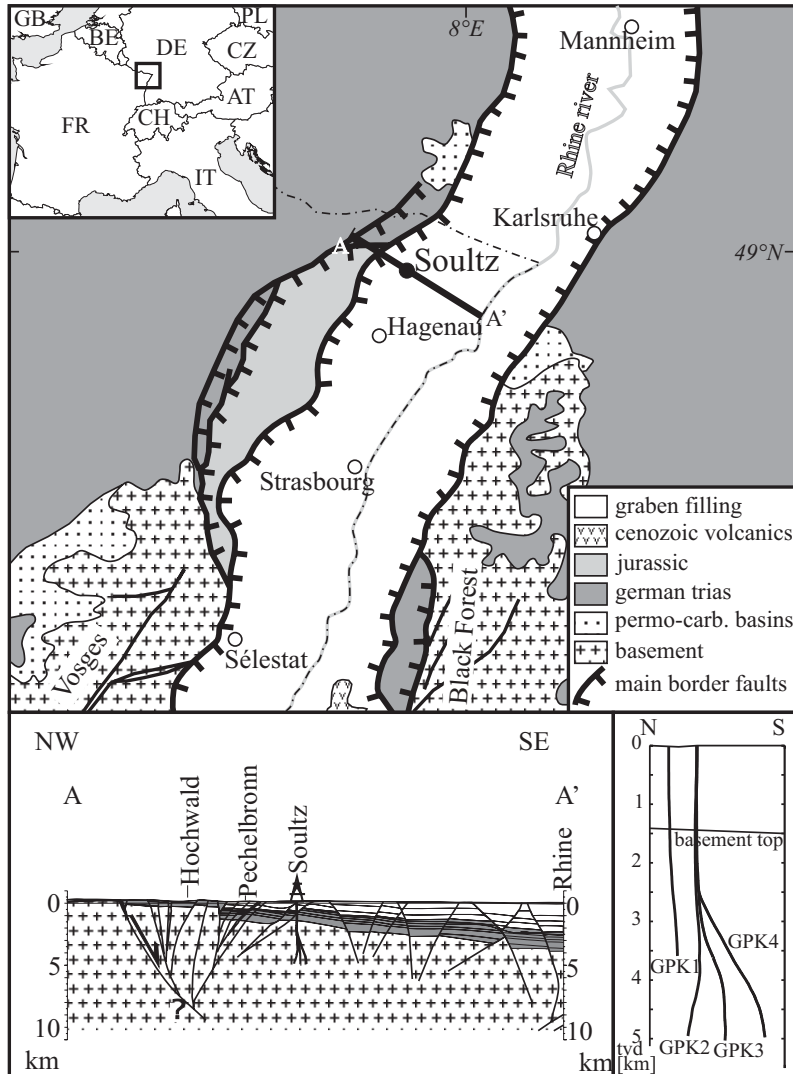


Figure 4.1: Location of the Soutz EGS test site close to the western border fault of the Upper Rhine Graben (after *Dezayes, 1996*). The lower left frame shows a geological cross section through the test site along A–A' (modified after *Kappelmeyer et al., 1991*). The trajectories of the four principal boreholes at the Soutz site, GPK1, 2, 3 and 4, is shown in north-south cross-section in the lower-right frame. At Soutz, the boreholes penetrates the basement at a depth of approximately 1400 m, within a local Horst structure.

tension fractures in ultrasonic televiewer records from GPK1 in the depth range 1450–2000 m and concluded that SH_{max} was oriented $N169^\circ \pm 11^\circ E$. Nagel (1994) picked axial DITFs on an FMI logs run in GPK1 between 2000 and 3590 m and obtained a mean orientation of SH_{max} of $N181^\circ \pm 22^\circ E$. Brudy and Zoback (1999) extended Nagel’s analysis to include en-echelon DITFs and found they indicated the same orientation as the axial DITFs. Bérard and Cornet (2003), identified compression-induced breakouts in GPK1 in the depth range 3050–3450 m that implied an SH_{max} orientation of $N5^\circ \pm 7^\circ E$. Genter and Tenzer (1995) identified vertical DITFs in GPK2 in the depth range 1420–3880 m and found they indicated an orientation for SH_{max} of $N175^\circ \pm 17^\circ E$. These studies collectively provide an extraordinarily well-defined indication that the orientation of SH_{max} in the basement above 3800 m is essentially N–S. This is at odds with the SH_{max} orientation estimates obtained from inversion of focal mechanisms (Cuenot *et al.*, 2005, 2006; Helm, 1996; Plenefisch and Bonjer, 1997) which suggest a more NW–SE orientation. Cornet *et al.* (2007) proposed that this discrepancy reflects a kind of sampling bias arising from the tendency of microseismic events to occur within fault zones where stresses are locally perturbed.

The general trends of the magnitudes of the principal stresses with depth are usually found to be reasonably well represented by linear relations, even if it is clear that heterogeneities may induce local deviations from these linear trends. Estimates of Sh_{min} at four depths between 2 and 3.5 km suggest that this is true in the Soultz shallow reservoir, at least for Sh_{min} , although the details of the linear fit to the data are important. Various linear characterisations of stress magnitude have been proposed for the Soultz site based on observations in the shallow reservoir to 3.5 km. The linear characterisation most often reported in the literature (e.g. Baria *et al.*, 1995) is due to Heinemann-Glutsch (1994), although it is usually mistakenly ascribed to Klee and Rummel (1993). Almost all recent studies of the deeper reservoir assume that this stress characterisation can be extrapolated to 5 km depth. This characterisation predicts a switch in maximum stress orientation from vertical to horizontal at 3 km depth. Some support for such a transition comes from the focal mechanisms of seismic events that tend to become increasingly strike-slip with increasing depth, although rigorous inversion indicates that it occurs nearer 4.5 km (Cuenot *et al.*, 2005, 2006). The inversion results, however, must be treated with considerable caution as the shape factors obtained from the inversions are inconsistent with the approximate equality of SH_{max} and S_v indicated by the transition in faulting style. The observations on which the earlier stress characterisations are based may be summarised as follows.

The magnitude of the vertical stress is generally taken as the integrated overburden as estimated from density logs or density measurements on core samples. A further refinement of this approach will be given later.

The magnitude of Sh_{min} is constrained by five small-volume hydraulic tests on pre-existing fractures in the depth range 1450–1990 m (Rummel and Baumgärtner, 1991), and a further four tests on induced hydrofractures in the depth range 2190–

3510 m (Klee and Rummel, 1993). These data were fitted by Heinemann-Glutsch (1994) to produce her Sh_{min} profile. Evans (2005) fitted the same data but without the lowermost point at 3508 m, which probably derives from a test conducted within a zone of perturbed stress. Cornet and Bérard (2003) discounted all small volume tests and claimed that a better Sh_{min} estimate was given by the maximum pressures of large-volume, relatively high-rate injections where the jacking pressure is reached. In such cases they proposed that the maximum pressure at the top of the injection interval equals Sh_{min} at that depth.

The only direct SH_{max} magnitude estimates stem from the hydrofracture test data interpreted using the ‘re-opening method’ (Klee and Rummel, 1993). Several authors have shown that this method yields invalid SH_{max} estimates for tests conducted in deep holes (Ito et al., 1999; Rutqvist et al., 2000), and hence both Cornet and Bérard (2003) and Evans (2005) discounted them. A more robust constraint on SH_{max} stems from the observation that focal mechanisms show a mix of normal and strike slip faulting (Cuenot et al., 2006), suggesting that SH_{max} is not greatly different from S_v . Both Cornet and Bérard (2003) and Evans (2005) adopt this equality as a working hypothesis. An extreme lower bound on SH_{max} is that it must be greater than Sh_{min} by definition. An upper bound on SH_{max} is obtained by assuming that the strength of fractured rock masses is limited by the strength of optimally oriented fractures (Brace and Kohlstedt, 1980). The worldwide crustal stress dataset supports this assumption and indicates an upper limit on rock mass strength is given by a Coulomb friction criterion with a friction coefficient of 1.0 and zero cohesion. Evans (2005) showed that this constraint imposes an upper limit on SH_{max} of $1.21S_v$. Further constraints on SH_{max} magnitude will be set by the analysis of wellbore failure presented in the following sections.

4.4 Description of the data set

The data analysed in this study stem from the three deep wells, GPK2, GPK3 and GPK4, drilled to 5 km true vertical depth (TVD) at the Soultz-sous-Forêts geothermal project site. The principal source of information are high-quality acoustic borehole televiewer (UBI) logs run in the entire granite sections of GPK3 and GPK4, which furnish a detailed picture of the borehole geometry as well as an image of acoustic reflectivity of the borehole wall. Such data allow stress-induced wellbore failure to be quantified, thereby imposing constraints on the causal stress state. A UBI log was also run in GPK2 but the image quality was relatively poor. Thus, we focus on the data from the other two wells. In addition to the UBI data, hydraulic data obtained during the stimulation injections of all three wells have been analysed to independently constrain Sh_{min} .

The granite sections of both GPK3 and GPK4 were drilled in two sections using two different bit sizes. A 12-1/4 inch bit was used down to 4582.8 m MD for GPK3

and down to 4757.3 m MD for GPK4. (MD denotes measured depth along hole from ground level, which is at an altitude of 167.9 m (IGN69) for all three boreholes.) GPK3 and GPK4 were then drilled to total depth with an 8-1/2 inch bit. Both holes are moderately inclined in their central section. The deviation of GPK3 from verticality exceeds 15° between 3257 m and 4037 m MD and reaches a maximum of 26° (Figure 4.3a). That for GPK4 exceeds 15° in the depth range 2490–4740 m MD and reaches a maximum deviation of 34° (Figure 4.4a).

4.4.1 Ultrasonic borehole images

The acoustic borehole televiewer images were obtained using a Schlumberger Ultrasonic Borehole Imager (UBI) tool run with the ancillary GPIT module which provides sonde positioning and orientation information. The latter also includes two on-board temperature sensors that provide a measure of borehole temperature at the time the logs were run, which was shortly after the completion of drilling. Successful UBI logs were run in the entire granite section of both GPK3 and GPK4 to total depth. The UBI tool provides detailed images of ultrasonic reflectivity and borehole centre-to-wall distance with an angular resolution of 2°. The logging speed was chosen so that a scan was made every 1 cm along hole. For details of the measurement principle see *Luthi (2001)*.

The GPK3 logs were acquired in two runs (see Table 4.1). The first run was acquired on 25th Oct. 2002 in the 12-1/4 inch section, some 5 days after the completion of drilling. This log extends throughout the 12-1/4 inch section from 1439 m MD (the casing shoe of a higher section) to 4532.6 m MD. The images of the lowermost 13.8 m are not oriented. The second log was run on 10th Nov. 2002, some 21 days after the hole had been extended as 8-1/2 inch diameter to TD at 5103 m MD. The log covers the 8-1/2 inch section from the 12-1/4 inch casing shoe at 4558.2 m MD to 5100.8 m MD, with the lowermost 2.6 m not oriented. The images are generally of good quality with few logging artefacts. ‘Key seats’ (see *Lofts and Bourke, 1999*) are visible along the entire inclined 12-1/4 section and some parts of the inclined 8-1/2 section, but they are easily identifiable and affect only a limited part of the borehole circumference.

The logs in the GPK4 borehole were also acquired in two runs that followed the drilling of the 12-1/4 inch and 8-1/2 inch sections. The log in the 12-1/4 inch was run on 15th Feb. 2004, some 15 hours after drilling, from 1421.3 to 4723.3 m MD. The log in the 8-1/2 inch section was run on 12th Apr. 2004, some 18 hours after drilling operations ended, from 4730.3 to 5253.3 m MD. Images suitable for fracture geometry determination were obtained for 1445.3–4720.3 m MD and for 4757.3–5248.3 m MD. Outside these ranges, the logs are run in casing or suffer from acquisition problems.

Table 4.1: Summary of UBI logging in GPK3 and GPK4

borehole	logging date	time after drilling completion	depth [m MD]
12-1/4 section			
GPK3	25th Oct. 2002	5 days	1439 – 4532.6 m
GPK4	15th Feb. 2004	15 hours	1421.3 – 4723.3 m
8-1/2 section			
GPK3	10th Nov. 2002	21 days	4558.2 – 5100.8 m
GPK4	12th Apr. 2004	18 hours	4730.3 – 4253.3 m

4.4.2 Description of wellbore failure

Breakouts or drilling-induced tension fractures occur when the local value of tangent compression or tension respectively at the borehole wall exceeds the rock strength. Breakouts are typically manifest as pairs of diametrically-opposite spall zones that extend along the borehole axis (Figure 4.2a and b). In the simple case of a vertical borehole penetrating a rock mass in which one principal stress is vertical, breakouts, if they occur, indicate the orientation of the Sh_{min} (Bell and Gough, 1979).

Drilling induced tension fractures (DITFs) form where cooling of the borehole wall by circulation of mud during drilling results in a net tangent stress distribution about the hole that is sufficiently tensile at some point to produce failure. The net tangent stress is the sum of a tensile cooling component, which is axially-symmetric, and the natural wellbore stress concentration arising from the 'far-field' stresses, which is usually not axially-symmetric and may be everywhere compressive. In the case of a vertical borehole penetrating a medium in which one principal stress is also vertical, the least compressive value of the circumferential stress variation about the borehole due to the far field stresses occurs in the direction of SH_{max} . Thus, it is in this direction that the greatest net tension develops during cooling and a pair of diametrically-opposite DITFs form. If the borehole axis is aligned with a principal stress, the fractures will be axial, hereafter denoted as A-DITFs (Figure 4.2c and d). However, in the case where the borehole axis is not aligned with a principal axis, the criterion for tensile failure might still be met but then the DITFs will tend to form as a stack of en-echelon induced fractures, hereafter denoted as E-DITFs (Figure 4.2e and f). The relationship between the induced fracture geometry and the in-situ stress orientations and magnitudes in this case is not as simple as in the aligned case (Peška and Zoback, 1995).

The stress-controlled wellbore failure features were identified and described as follows. First, borehole intervals affected by either breakouts (BOs), axial drilling induced tension fractures (A-DITFs) or 'en-echelon' drilling induced tension fractures (E-DITFs) were identified. Then, for breakouts and A-DITFs, the mean orientations of the features were determined over successive 0.5 m depth windows. For E-DITFs,

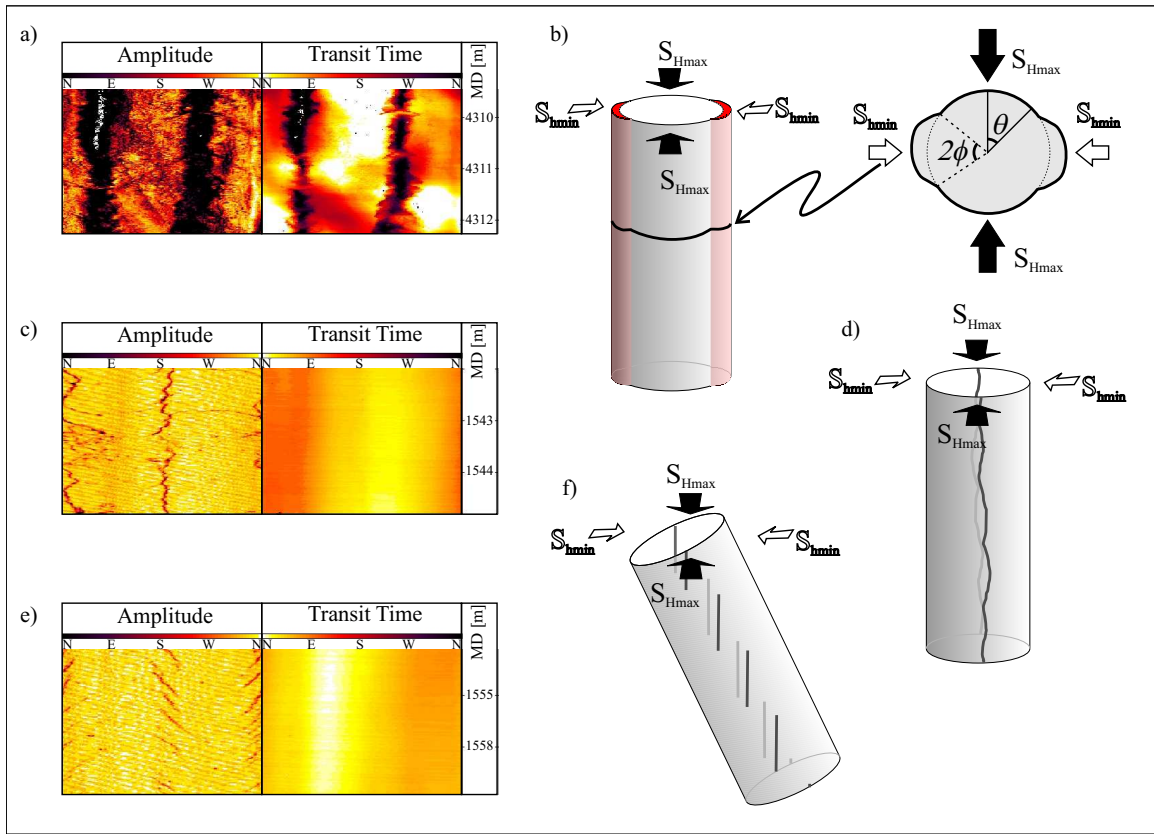


Figure 4.2: Examples of stress induced wellbore failure of a vertical borehole. a) breakouts on UBI images. b) sketch of a borehole section affected by breakouts showing the relationship with maximum and minimum principal horizontal stresses, S_{Hmax} and S_{Hmin} . θ is the angle around wellbore measured from the S_{Hmax} direction. 2ϕ is the breakout angular width. c) axial drilling induced tension fractures (A-DITFs) on UBI images. d) sketch of a borehole affected by A-DITFs. e) 'en-echelon' drilling induced tension fractures (E-DITFs) on UBI images. f) sketch of a borehole affected by E-DITFs. All UBI images are from the borehole GPK4.

the orientation (strike) of the best-fitting plane for each fracture in each pair was chosen (i.e. two strike determinations for each en-echelon pair). In all cases, the confidence of the identification was recorded by assigning an index ranging between 1 and 3, corresponding to low and high confidence respectively.

Similar counts of features were obtained for both boreholes. About 10% of the logged borehole lengths were affected by breakouts, 10% by A-DITFs, and 7% by E-DITFs. The orientation distributions with depth of the breakouts and DITFs in GPK3 are shown in Figure 4.3. The corresponding plot for GPK4 is given in Figure 4.4.

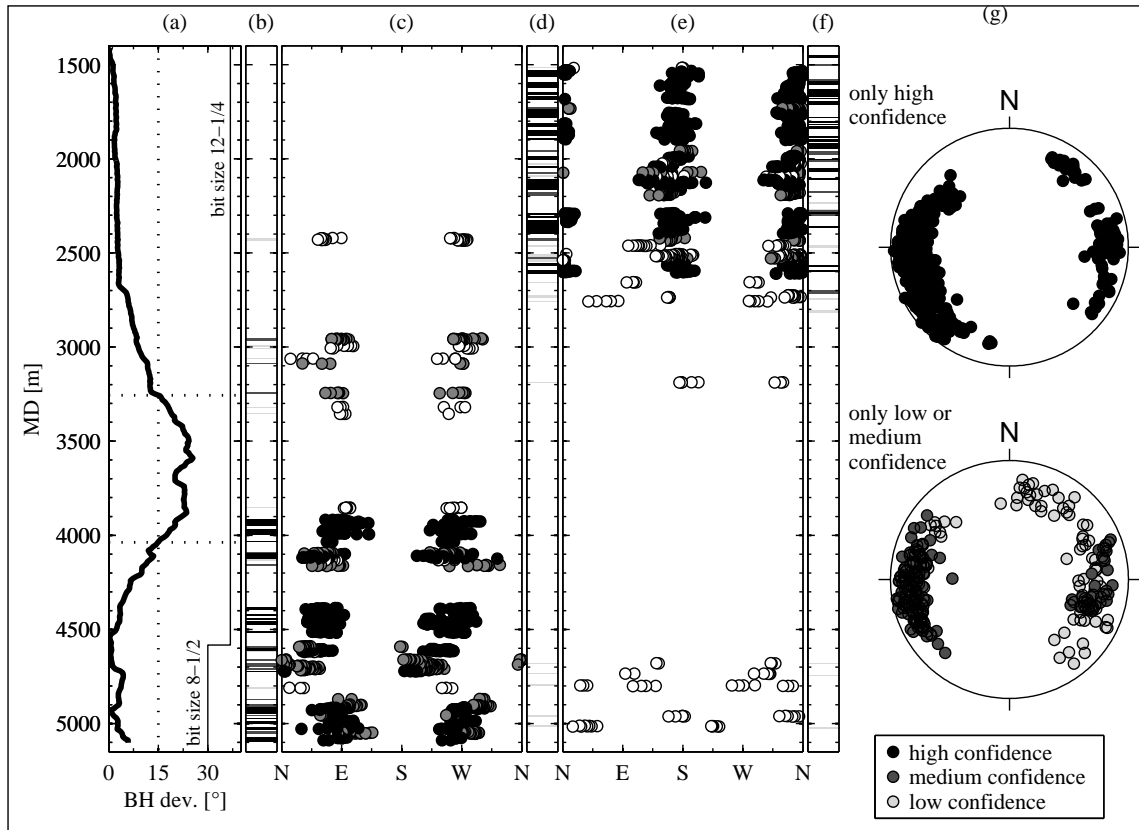


Figure 4.3: Summary of wellbore failure observations in the borehole GPK3. a) Borehole deviation from verticality and borehole nominal diameter b) Location of identified breakout intervals. c) Breakout orientation. Filled black, grey and white circles denote high, medium, and low confidence identifications respectively. d) Location of identified A-DITF intervals. e) A-DITF strike directions. f) Location of identified E-DITF intervals. g) Stereographic projections of poles to the E-DITF planes (lower hemisphere, equal area).

4.5 Interpretation of the wellbore failure observations to constrain the stress state

4.5.1 Principal stress orientation

It is evident that there is a depth-partition in the style of failure, with DITFs occurring predominantly in the upper parts of the holes whereas breakouts predominate below. Both A-DITFs and E-DITFs occur in similar numbers in the upper vertical sections, indicating that one principal stress is sometimes locally vertical, and sometimes inclined from vertical. However, the E-DITFs are always fairly steep and deviate both

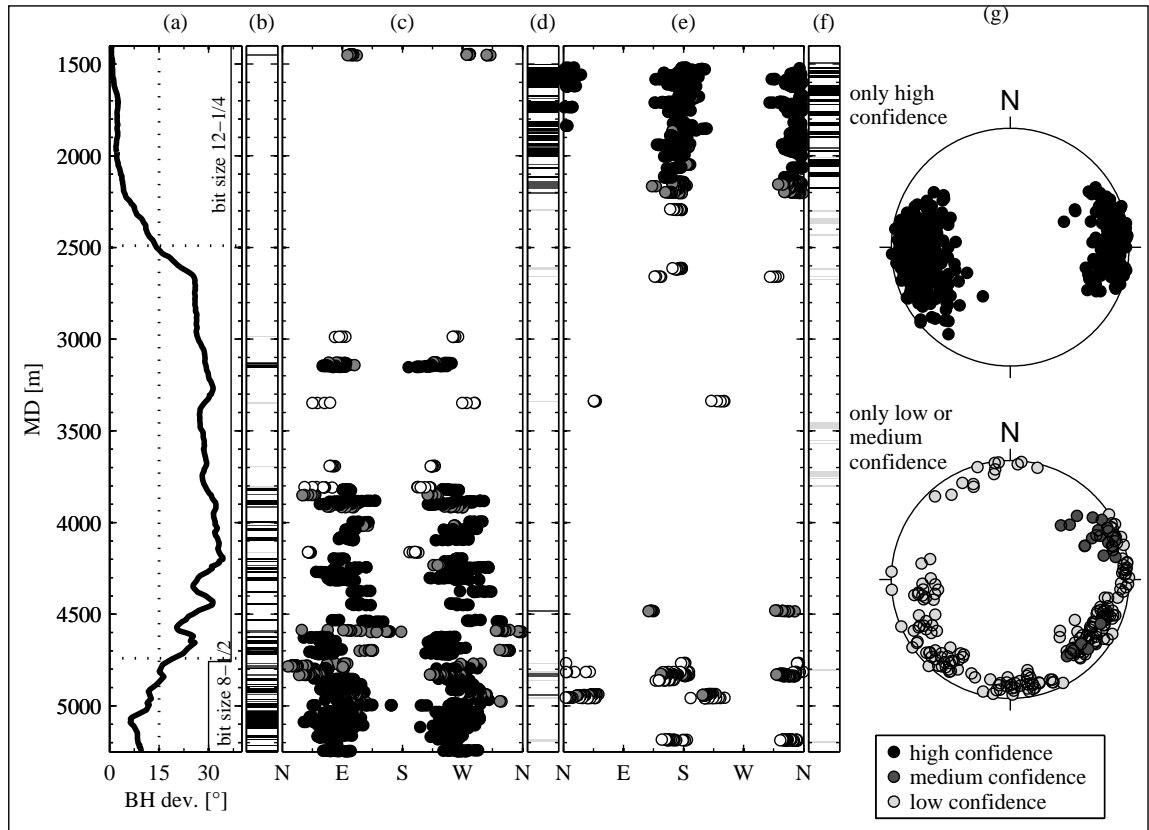


Figure 4.4: Summary of wellbore failure observations in the borehole GPK4. See Figure 4.3 caption for explanation.

to the east and to the west so that their mean orientation is about vertical. This suggests that one principal stress is, on average, vertical, with localised deviations from verticality indicating zones of stress heterogeneity. Thus, for the stress characterisation we take one principle stress as vertical, leaving only the direction of the maximum horizontal stress has to be ascertained to fully characterise principal stress orientation.

For the vertical borehole sections, the wellbore failure features provide a direct measure of the horizontal stress orientations: the breakouts denote the Sh_{min} -orientation, and the DITFs the SH_{max} -orientation. For the purpose of the analysis we consider borehole sections that lie within 15° of vertical as being essentially vertical. This excludes from the analysis the section 3257–4037 m MD for GPK3, and 2490–4740 m MD for GPK4. As noted earlier, breakouts dominate in the lower vertical sections of both wells and DITFs in the upper sections. To maintain rigour we analyse the A-DITFs and E-DITFs separately.

Numerous A-DITFs are found in the vertical section of GPK3 above 3257m MD,

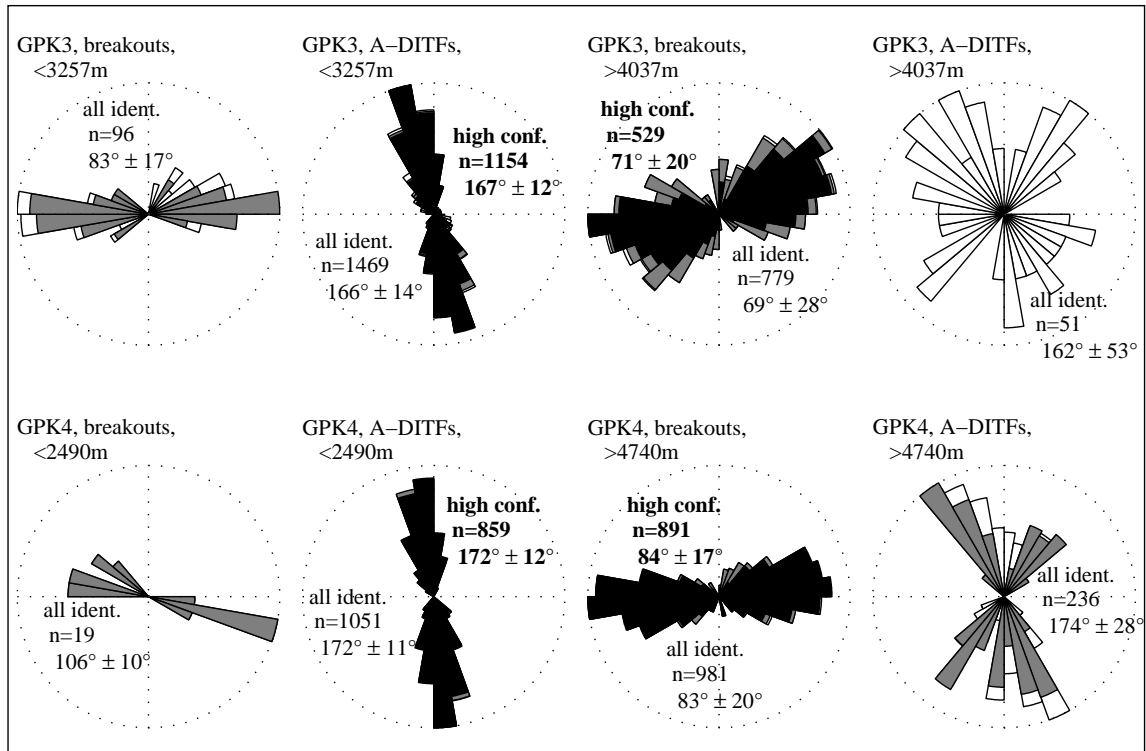


Figure 4.5: Circular histograms of breakout and A-DITF orientations along sub-vertical sections of GPK3 and GPK4. Sectors filled with black denotes high confidence data; grey denotes medium confidence data, and white is for low confidence data. The circular mean direction and single standard deviation are given.

with only a few medium- to low-confidence identifications of breakouts. The high-confidence A-DITFs show a preferred orientation in this section of $167^\circ \pm 12^\circ$ (see histogram of Figure 4.5b), a result that does not significantly change by including medium- and low-confidence estimates. The orientation of the medium- and low-confidence breakouts in this upper, vertical section is found to be $83^\circ \pm 17^\circ$ (Figure 4.5a), which is approximately 90° rotated from the mean A-DITF orientation, as would be expected if the identifications were correct. This indicates that some, albeit few, breakouts do indeed occur above 3257 m MD in GPK3. In contrast, the lower sub-vertical section of the borehole, below 4037 m MD, is dominated by numerous breakouts with only a few low-confidence A-DITFs present. The high confidence breakouts have an orientation of $71^\circ \pm 20^\circ$. The A-DITFs have no clear preferred orientation and are in part due to the stress perturbation associated with a major structure that cuts the hole (Chapter 5), although some are possibly erroneous identifications.

A similar distribution of wellbore failure features is seen in GPK4. Many A-DITFs are found in the upper sub-vertical part above 2490 m MD, whereas only one medium confidence breakout is present. High confidence A-DITFs for this upper section show a clear preferential orientation of $172^\circ \pm 12^\circ$. Below 4740 m MD, breakouts dominate with a few medium-to-low confidence A-DITFs. The high-quality breakouts have a strong preferred orientation of $84^\circ \pm 17^\circ$ (see histogram in Figure 4.5g). The medium-to-low confidence A-DITFs are oriented $174^\circ \pm 28^\circ$, and are thus 90° from the breakouts. This suggests that at least some of the identified A-DITFs are real.

SHmax-orientation estimates obtained from the mean direction of the high-quality A-DITFs in the upper sub-vertical sections of GPK3 ($167^\circ \pm 12^\circ$) and GPK4 ($172^\circ \pm 12^\circ$) are consistent with the results of previous analyses from the wells in the shallow reservoir ($0^\circ \pm 20^\circ$). In the lower sub-vertical sections of GPK3 & 4, the high-quality breakout identifications indicate a *SHmax*-orientation for the deeper reservoir of $162^\circ \pm 20^\circ$ and $174^\circ \pm 17^\circ$ respectively, which is not significantly different from the *SHmax*-orientation in the shallow reservoir. Taking an average of all estimates from GPK3 and GPK4 by weighting each value by the length of borehole considered in the study yields a mean orientation for *SHmax* at the Soultz site from 1.4 km to 5 km depth of $169^\circ \pm 14^\circ$.

As mentioned above, the presence of E-DITFs along sub-vertical borehole sections indicates localised deviation from verticality of one principal stress implying stress heterogeneity. The mean strike of the E-DITFs is $172^\circ \pm 23^\circ$ in GPK3 and $176^\circ \pm 15^\circ$ in GPK4. As these values are not significantly different from the mean strike of the A-DITFs, this suggests that where E-DITFs occur, for example along a steeply inclined borehole, this mean strike can be taken as a reliable indicator of the maximum horizontal stress direction.

4.5.2 Natural formation pressure

The natural formation pressure is required for computations that involve effective stresses. The value used here is based on the analysis of downhole pressure recorded in isolated intervals to 3.5 km given in *Evans et al.* (1992) and is:

$$Pp \text{ [MPa]} = 0.9 + 9.8z \text{ [km]} \quad (4.1)$$

4.5.3 Vertical stress magnitude

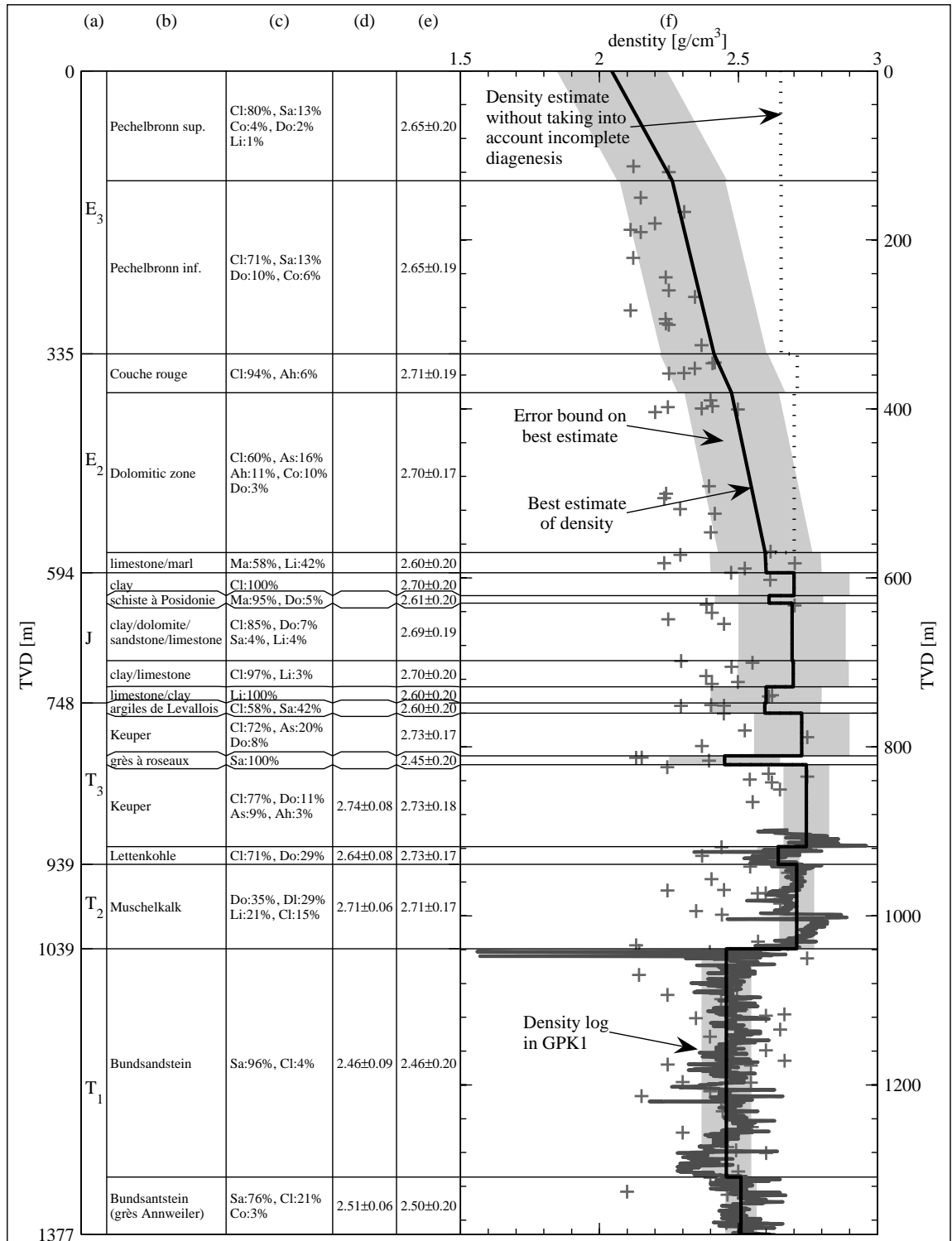
Since the evidence indicates that on average one principal stress is vertical, its magnitude can be taken as the integrated overburden. Ideally, the latter can be estimated from gamma-gamma bulk density logs. A series of three such Schlumberger density logs have been run in the borehole GPK1 which together span the depth range 898 m to 3563 m. No other density logs have been run on the site, so the primary problem

concerning Sv estimation lies in estimating the bulk density profile above and below this depth range.

Figure 4.6 summarises the estimation of the density within the sedimentary section (i.e. down to 1377 m). For each litho-stratigraphic unit, the mean density and corresponding error bound was estimated by considering the weighted average of the density of the unit's lithological constituents (Figure 4.6e). The validity of this procedure can be checked for the lowermost sedimentary units by comparing with the mean density obtained from a gamma-gamma log that is available for the depth range 898–1377 m (Figure 4.6d). The latter shows that significant density variations occur between units, the sandstones of the Buntsandstein being significantly lighter than the limestones and dolomites of the Muschelkalk and the marls of the Keuper. The density estimates from lithological constituents are in excellent agreement with the mean density from the wireline logs, the only exception being the Lettenkohle where the lithology-derived estimate exceeds the mean from the log by 0.1 g/cm^3 , although the discrepancy lies within the confidence limits of the estimates. This provides a basis to use the lithology-derived estimates of density for Jurassic and older litho-stratigraphic units in the depth range 594–898 m. However, at shallower depth, the approach appears to overestimate density. The evidence stems from a compilation of density logs run in boreholes in the Alsace region (*Corpel and Debeglia, 1994*). The

Figure 4.6: (on page 91) Estimation of the density profile for the sedimentary section using the lithological profile of GPK1 given by *Kappelmeyer et al. (1991)*. a) Chronostratigraphy where T_1 is early Triassic, T_2 is middle Triassic, T_3 is late Triassic, J is Jurassic, E_2 is Eocene, E_3 is Oligocene. b) Lithostratigraphy. c) Lithological constituents of each litho-stratigraphic unit (see 'e' for key). d) Mean and single standard deviation of density derived from GPK1 density logs if run in the unit. e) Mean and standard deviation of density obtained from the weighted average of lithological constituents. The densities (gm/cm^3) assumed for the latter are as follows: Co is conglomerate (2.3 ± 0.2), Sa is sandstone (2.45 ± 0.2), Cl is clay/silty clay/shale (2.7 ± 0.2), Ma is sandy marls (2.6 ± 0.2), Li is limestone (2.6 ± 0.2), Do is dolomite (2.8 ± 0.1), Dl is dolomitic limestone (2.7 ± 0.2), Ah is anhydrite (2.9 ± 0.1), As is anhydritic shale (2.8 ± 0.1). f) Estimated density profiles for the sedimentary section. The dotted line denotes the density profile obtained from consideration of the lithological constituents and the solid line is the profile after correction for increasing porosity at shallower depth. The grey band denotes the estimated error. The wireline log is shown between 898 and 1377 m. The crosses denote data values from a compilation of density profile from boreholes in the Alsace region (*Corpel and Debeglia, 1994*).

4.5 Interpretation of the wellbore failure observations to constrain the stress state



1377

data are plotted as crosses in Figure 4.6f. The scatter is large, primarily because the data were sorted by depth rather than lithology, and thus many datapoints are ascribed to the wrong units. Thus, only general trends can be taken as valid. In the Jurassic and older units below 594 m, the lithology-derived estimates lie near the upper range of scatter of the compiled estimates. However, in the overlying Cenozoic sediments, the discrepancy becomes much more significant, the compiled estimates indicating a progressive reduction in density towards 2 gm/cm³ with shallower depth, in contrast to the lithology-derived estimates which remain relatively stable near 2.6–2.7 gm/cm³ (Figure 4.6f). This might reasonably be explained as reflecting higher porosity due to incomplete compaction and diagenesis of these relatively young sediments, processes not considered in the lithology-derived estimates. In view of this, the lithology-derived profile was progressively deviated in the Cenozoic sediments above 594 m towards a value of 2.0 g/cm³ in order to mimic the reduction of density suggested by the data of *Corpel and Debeglia* (1994). The result leads to a mean density for the entire sedimentary section of 2.50±0.14 g/cm³. The magnitude of the vertical stress at the top of the basement (1377m) is thus 33.81±1.94 MPa.

Within the granite, wireline density logs down to 3.6 km give a mean density of 2.6±0.1 g/cm³. Comparison of the measured density of a core sample taken in GPK1 at 3524 m with the values registered on the density log in the vicinity showed good agreement, the log values being at most 0.015 g/cm³ too low. Thus we regard the estimates from the density log as valid. Note that the mean density of the granite obtained from wireline logs is slightly lower than that obtained from core measurements because it includes the effects of relatively low densities in altered zones. Below 3.6 km, there is no published information on the density of the granite, and thus we use the value of 2.6±0.1 g/cm³ that is valid for the granite above. This assumption becomes particularly questionable below about 4500 m TVD where petrological studies indicate a change in the composition of the granite (*Dezayes et al.*, 2005a).

Drawing these considerations together, we conclude that the currently available data indicate a vertical stress profile for the granite given by:

$$Sv[\text{MPa}] = -1.30 + 25.50z[\text{km}] \text{ with a standard error equal to } \pm (0.98z[\text{km}] + 0.6) \quad (4.2)$$

The uncertainty on Sv magnitude at the basement top of ±1.9 MPa thus increases to ±5.5 MPa at 5 km.

4.5.4 Minimum horizontal stress magnitude

For the deep reservoir, no formal, hydraulic stress tests have been conducted below 3.5 km from which the magnitude of Sh_{min} could be estimated. Thus, we follow *Cornet and Bérard* (2003) and assume that the maximum pressure attained during the stimulation injections provides a direct measure of Sh_{min} at the depth of the

Table 4.2: Maximum pressures recorded at the casing shoe during the stimulation injections of the three deep wells. The data denote the pressures prevailing at the end of injection stages with different flow rates.

Borehole	Injection test ID	Depth of casing shoe [m TVD from ground]	Max. pressure at casing shoe [MPa]	Flow rate at max. pressure [l/s]
GPK2	00JUN30	4402	55.4	31
GPK2	00JUN30	4402	56.9	50
GPK3	03MAY27	4488	60.8	50
GPK3	03MAY27	4488	61.5	70
GPK3	03MAY27	4488	61.2	50
GPK4	04SEP13	4489	62.1	30
GPK4	04SEP13	4489	61.7	40

casing shoe. This approach must be considered as tentative since it assumes the following conditions are met:

1. The maximum pressure attained during the test is controlled by jacking and not shearing.
2. Near-wellbore pressure drops (i.e. entrance losses) due to the focussing of flow are negligible.
3. The minimum stress prevailing at the time of maximum pressure reflects the ambient stress and is not elevated by poro-elastic effects.

These conditions appear to have been met for the large injections into the shallower reservoirs at 2.0 and 3.0 km, since the suggested Sh_{min} profile of *Cornet and Bérard* (2003), which is based on maximum pressures during large volume injections, does not differ greatly from that determined from the small-volume injections. Violation of assumption 1 would result in underestimation of the ambient minimum stress, whereas 2 and 3 would result in overestimates. The data describing the maximum pressures inferred at the casing shoe during stimulation injections of the three wells of the 5 km reservoir are listed in Table 4.2 and are plotted in Figure 4.7. Only estimates derived from down hole pressure measurements are listed. It is evident that all data show pressure-limiting behaviour. The three data points from the 03May27 stimulation of GPK3 are from a sequence when the flow rate was stepped from 50 l/s to 70 l/s for 2 hours and then back to 50 l/s. The small, reversible changes in pressure that accompanied the flow rate steps indicates that jacking was occurring, as required for the Sh_{min} estimation procedure to be valid.

The resulting estimates of Sh_{min} are plotted as a function of depth in Figure 4.7, together with estimates from small-volume tests. In fitting the data with a linear

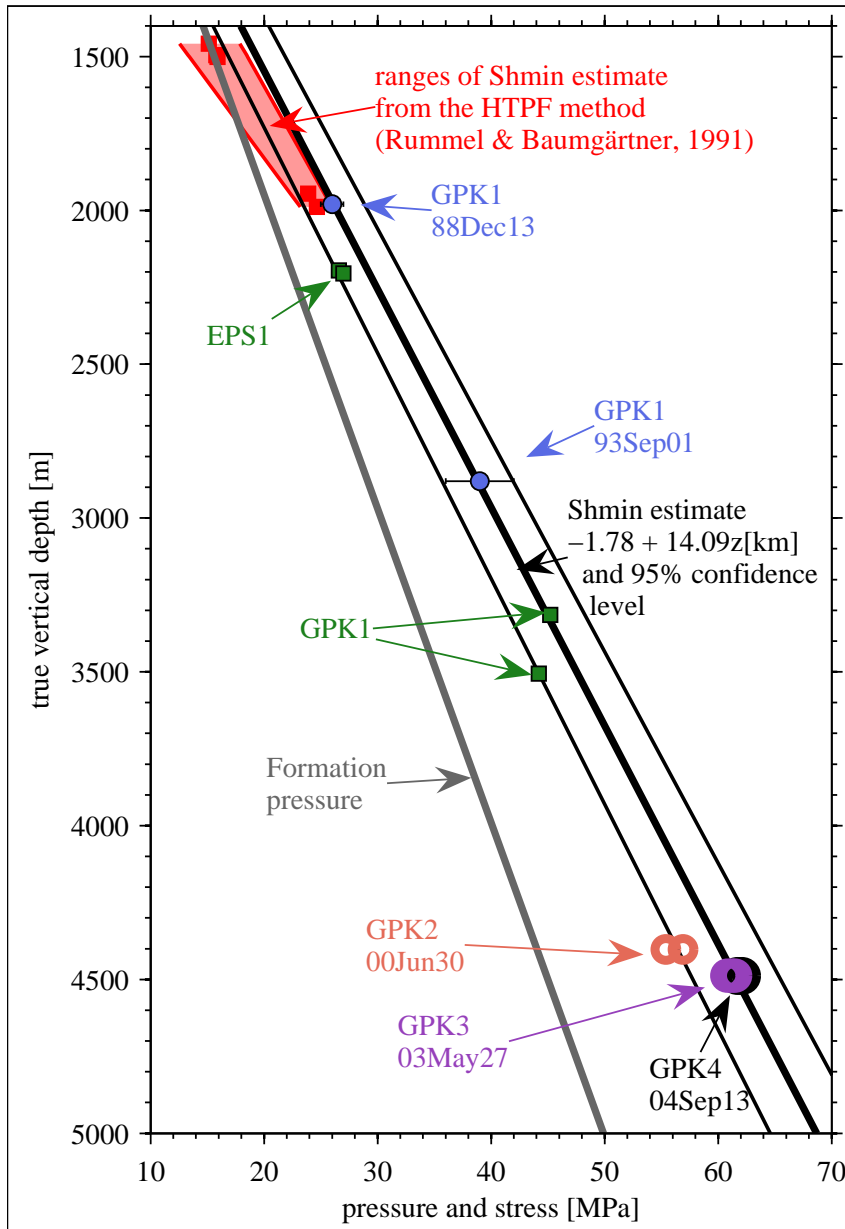


Figure 4.7: Estimates of Sh_{min} from small-volume injection tests (squares) and large-volume injection tests (circles). The well ID and, for the large volume injections only, the test number are indicated. The best-fitting linear trend to these data and the 95% confidence limits are denoted by the thick-black and thin-black lines. See text for details.

trend, we used only estimates obtained from large-volume injection tests because these are less sensitive to local stress heterogeneities. The $Shmin$ estimates fall closely on a linear trend, with the exception of the data points for GPK2 which are too low by about 4 MPa. It is noteworthy that pressure was continuing to slowly increase at the end of this stimulation (Weidler *et al.*, 2002). This can be interpreted as indicating that the jacking pressure was not reached, although other explanations are possible. Because of this complexity, the GPK2 injection pressures were excluded from the fitting process. The resulting best-fit linear trend obtained from the casing-shoe injection pressures of the two GPK1 injections, the GPK3 and 4 injections is given by:

$$Shmin[\text{MPa}] = -1.78 + 14.09z[\text{km}] \text{ with an uncertainty of } \pm (0.45z [\text{km}] + 1.82) \quad (4.3)$$

The uncertainty level is derived from the 95% confidence bounds on the linear best fit process, and is ± 2.5 MPa at 1400 m depth and ± 4.1 MPa at 5 km depth. This profile is very similar to that proposed largely on the basis of data from the shallow reservoir to 3.6 km in earlier studies (Cornet and Bérard, 2003; Cornet *et al.*, 2007).

4.5.5 Maximum horizontal principal stress magnitude

As noted earlier, there are currently no reliable constraints on $SHmax$, save for the observation that induced seismic events show both strike-slip and normal fault plane solutions. In this section we derive constraints on $SHmax$ magnitude imposed by the pattern of wellbore failure. Specifically, tensile failure in the form of DITFs is seen to dominate at shallow depth, and compressive failure in the form of breakouts below (see Figure 4.3 and 4.4). This pattern of failure, coupled with the independently known estimates of $Shmin$, impose useful constraints on $SHmax$.

Since the UBI logs from which the breakouts and DITFs were identified were run before any injections had been conducted, the failure must have occurred either during drilling or shortly afterwards. The hydro-mechanical situation at the advancing hole face, is very complex because of the effects of stress re-orientation ahead of the face (Ito *et al.*, 1998), mechanical stress due to the weight on the bit, as well as possible overpressuring from fluid expelled from the nozzle of the bit to remove the cuttings. Thermal stresses due to cooling tend to inhibit breakout formation directly at the drill bit. Thus, for breakouts it is acceptable to neglect the complex near-face stress state and to consider what occurs at least one borehole diameter above the drill bit. Here, the total stresses about a wellbore can be considered to result from the superposition of four components: 1) the stress concentration developed around an empty wellbore due to the far-field stresses applied to the medium with uniform pore pressure; 2) the stresses generated by the wellbore fluid pressure; 3) the stresses

arising from a perturbation of pore pressure about the well, and 4) the stresses arising from a perturbation of temperature about the well. Components 1 and 2 are always present. They represent the tangent stresses prevailing long after drilling, when the well has reached thermal and hydraulic equilibrium with the surroundings. In contrast, the conditions during drilling include the perturbing stress components 3 and 4 activated in tension by the cooling and overpressuring effects of the drilling mud. The overpressure is believed to be small for the holes in question, at least away from the complex zone at the drill bit (see Chapter 5, Section 5.5.5.2), since the annulus pressure was maintained at near-hydrostatic conditions. Hence overpressure will be neglected. The conditions prevailing shortly after the completion of drilling, when the UBI logs were run, are similar to those during drilling with the exception that some warming of the cooled wellbore has taken place. Thus, the tension associated with component 4 will be reduced somewhat from the tensile maximum during drilling.

In the case of a vertical borehole, the total hoop stress (compression taken as positive) at the borehole wall including component 1, 2 and 4 is given by:

$$S_{\theta\theta} = Shmin + SHmax - 2(SHmax - Shmin) \cos 2\theta - P_w + S_{\Delta T} \quad (4.4)$$

where θ is the angle around borehole measured from the $SHmax$ direction (Figure 4.2b), P_w is the well bore fluid pressure which will be taken as equal to Pp (equation 4.1) in our analysis, and $S_{\Delta T}$ is the stress arising from the thermal perturbation of the wellbore wall. $S_{\theta\theta}$ has a minimum value of $S_{\theta\theta}^{\min} = 3Shmin - SHmax - Pp + S_{\Delta T}$ at $\theta = 0^\circ$ and 180° , where DITFs may form, and a maximum value of $S_{\theta\theta}^{\max} = 3SHmax - Shmin - Pp + S_{\Delta T}$ at $\theta = 90^\circ$ and 270° , where breakouts may form.

If the borehole is not aligned with a principal stress axis, there is no direct analytic formulation for $S_{\theta\theta}$, $S_{\theta\theta}^{\min}$ and $S_{\theta\theta}^{\max}$, although they can be computed using the method described for example in *Peška and Zoback (1995)* (presented also in Appendix D). Since the Soultz boreholes are deviated, we used this latter method to compute $S_{\theta\theta}$, $S_{\theta\theta}^{\min}$ and $S_{\theta\theta}^{\max}$. Note that equation (4.4) assumes that linear elasticity is valid. This is a commonly accepted simplification, even though laboratory simulations of wellbore failure show some non-elastic behaviour (*Haimson and Herrick, 1989*).

To conduct the analysis of DITFs we require estimates for the maximum cooling of the boreholes from which the thermal stress can be obtained, whilst for breakouts and DITFs we require compressive and tensile failure criteria respectively. In the following we describe the estimation of these parameters.

4.5.5.1 Estimation of thermal stress component

The thermal stress $S_{\Delta T}$, is a key component for the formation of DITFs, and can be estimated using the relation given by *Stephens and Voight (1982)*. Specifically, the hoop stress at the borehole wall produced by cooling by an amount ΔT ($\Delta T < 0^\circ\text{C}$)

is:

$$S_{\Delta T} = \frac{\alpha_o E \Delta T}{1 - \nu} \quad (4.5)$$

Here, α_o is the coefficient of thermal expansion, E is the Young's modulus, and ν is the Poisson's ratio. The coefficient of thermal expansion was derived from the mineralogical composition of the rock and was found to be $8 \pm 2 \cdot 10^{-6} \text{ K}^{-1}$. Young's Modulus will be taken equal to $54.0 \pm 2.0 \text{ GPa}$, the static value obtained from uniaxial compression tests on unaltered Soultz granite (Appendix E). No reliable measurements of the static Poisson's ratio for the Soultz granite are available. Measured p- and s-wave velocities indicate a dynamic Poisson's ratio close to 0.25. However, static values are usually smaller than dynamic. Thus, we will consider Poisson's ratio values ranging between 0.2 and 0.25.

The key problem in the analysis of DITFs is to estimate the most negative value that ΔT ever reaches at each depth throughout the entire drilling operation. We will refer to this as the profile of minimum temperature. A commonly-used approach to this problem is to compare temperature logs acquired a short time after the end of circulation with logs acquired some months after the end of circulation. However, as noted by *Brudy and Zoback (1999)* and *Bérard and Cornet (2003)*, the radial thermal gradient around the well is high at the end of drilling. Hence, non-negligible heating of the wellbore can take place during the few hours or days between the end of the circulation and the first temperature log acquisition. *Bérard and Cornet (2003)* used an analytic model of conductive heat flow to estimate the heating that took place between the end of drilling of GPK2 and the a temperature log run some 3 days later. They found that up to 45% of the net temperature drawdown from equilibrium was recovered by the time the log was run. However, a basic flaw in these approaches arises from the fact that the temperature of the borehole wall at the end of drilling is usually not the coolest temperature ever reached. Indeed, consideration of typical temperature profiles in the annulus during drilling (e.g. *Kabir et al., 1996*), shows that the maximum temperature of the mud during forward circulation of a well (i.e. down the drill pipe and up the annulus) is not at hole bottom, but higher up in the well. Thus, for a given depth, the coolest temperature that the borehole wall will experience is when the drill bit passes this depth. As drilling advances, the temperature of the borehole wall at that depth will increase, heated by the ascending drilling mud coming from the deeper and hotter borehole section. The only exception to this occurs for low geothermal gradients coupled with vigorous mud circulation. Thus, the post-circulation profile provides only an upper bound to the minimum temperature profile. *Bérard and Cornet (2003)* in their analysis of GPK2 data neglected this, and found that the tangential stress at the borehole wall computed from equation 4.5 using their estimate of the post-circulation temperature profile was not sufficient to produce the observed extent of tensile failure. They explained this by proposing an additional component of tensile stress arising from the thermoelastic mismatch

of the mineralogical constituents in the granite. Although strong grain-scale stresses are likely to be produced by cooling of poly-crystalline materials such as the Soultz granite, and will generate microcracking that will reduce the tensile strength of the rock, it is not clear that they will produce an additional macroscopic stress component to augment that in equation 4.5 (i.e. one that is coherent on scales greater than the grain scale). An alternative explanation is that the cooling profile they used underestimates the true maximum-cooling profile.

The best way of estimating the coolest temperature ever experienced by the borehole walls is to use measurements of temperature of the mud at the drill bit conducted during drilling (i.e. ‘measurement-while-drilling’ or MWD). Such data were not available in the case of GPK2. However, intermittent MWD mud temperature data are available for GPK4, and we have used these in our analyses. To summarise the approach we use, we shall assume that the borehole wall and mud are in thermal equilibrium. We will also assume that the depth of penetration of the cooling wave is unimportant for the initiation of DITFs, although it will control their depth of extent. The temperature profile along the borehole during drilling is very complicated owing primarily to heat transfer between the down-going fluid in the drill string, the up-going fluid in the annulus, and the surrounding rock mass. It is also complicated by the discontinuous nature of drilling operations, with periods of mud circulation during drilling interspersed with periods where the well is left to stand during bit changes. Nevertheless, the general shape of the temperature profile during drilling is well known (e.g. *Charlez, 1997; Kabir et al., 1996*), at least for normal geothermal gradients, and implies that the coolest mud temperature ever felt by the borehole wall at a given depth occurs just when the drilling bit reaches that depth. As noted earlier, after this time, the mud flowing past the point will be warmer than at drilling as it flows up the annulus from below. Thus a lower bound on the ‘minimum temperature’ profile is placed by mud temperature measurements at the drill bit obtained from the MWD system. This system measures the temperature of the mud in the drilling string just before it emerges from the drill bit nozzle and thus constitutes a lower bound for the coolest temperature ever seen by the rock at the depth of the measurement. An upper bound for the coolest temperature ever seen by the borehole wall would be given by a temperature log run just after drilling completion. Unfortunately such a log was not acquired in either GPK3 or GPK4. However, temperature profiles were recorded by two sensors within the GPIT sondes of the wireline logs run just after drilling. These data are not ‘guaranteed’ temperature measurements since they are the output of two sensors used in the temperature compensation of the magnetometers and accelerometers. Since the sensors are not in direct contact with the wellbore fluid, some inertia in the thermal equilibrium between sensor and mud is present. The fact that these sensors recorded relatively high frequency temperature variations along the boreholes indicate that the inertia effects are not large, and that these data provide a reasonable measure of the wellbore mud temperature just after drilling.

Figure 4.8a shows the profile of borehole mud temperature of GPK4 recorded

within the GPIT sonde of spectral gamma logs run 12 hours and 18 hours after the end of drilling of the 12-1/4 inch and 8-1/2 inch sections respectively. This can be compared with a temperature log run 3 months after drilling, which closely approximates the natural temperature profile. Evidently, at the time of the post-drilling logs, the borehole remained cooled by 35-40°C in the 12-1/4 inch section and 25-30°C in the 8-1/2 inch section. Maximum cooling will actually be greater than this since the post-drilling profile is an upper bound to the profile of maximum-cooling (note that even a log run immediately upon the termination of drilling would only be an upper bound for the latter, except near the hole bottom, because of warming of higher sections of the hole by up-flowing drill mud in the annulus). The spot measurements of temperature from the MWD system are indicated in Figure 4.8a by the diamonds. Under normal circumstances, these constitute lower bounds on the maximum-cooling profile. Above 3 km in the 12-1/4 inch section and within the 8-1/2 inch section, the values lie below the post-drilling temperature profile, as expected. However, below 3 km in the 12-1/4 inch section, the MDW temperature estimates are about the same and occasionally exceed the post-drilling log profile. Whilst this would be understandable near the hole bottom, it is perhaps surprising that it extends over 1 km. We take the lower bound on the maximum-cooling profile for the lowermost 1 km of the 12-1/4 inch section as given by the few MWD temperature measurements that are lower than the post drilling log. Although this leads to an uncertainty in the maximum cooling profile that appears unrealistically small in this section, the available evidence suggests that it is not greatly so. This issue illustrates the complexity of the drilling temperature history. This complexity is unfortunately not fully documented by the drillers and so it is very difficult to find explanations for each single data point. In any case, the control on the maximum cooling profile for GPK4 can be considered to be reasonably good.

The bounding profiles of maximum-cooling are shown in Figure 4.8b. The amount of cooling in GPK4 is always more than 20°C, and may reach up to 65°C at some depths. The implied bounding profiles of hoop stress induced at the borehole wall are shown in Figure 4.8c. These were calculated from equation (5) using the thermo-elastic parameter values and their uncertainties given earlier. The extreme estimates of thermally-induced hoop stress range from -8 MPa to -48 MPa. The mean value ranges from -17.1 MPa at 3160 m TVD to -31.3 MPa at 2235 m TVD.

For well GPK3, the temperature data set is less complete. Only five MWD temperature measurements were recorded by the drillers and no temperature channel was included in the Schlumberger spectral gamma log. For these reasons we were not able to place reliable constraints on the thermal stress of GPK3, and hence GPK3 data will not be included in the following analyses.

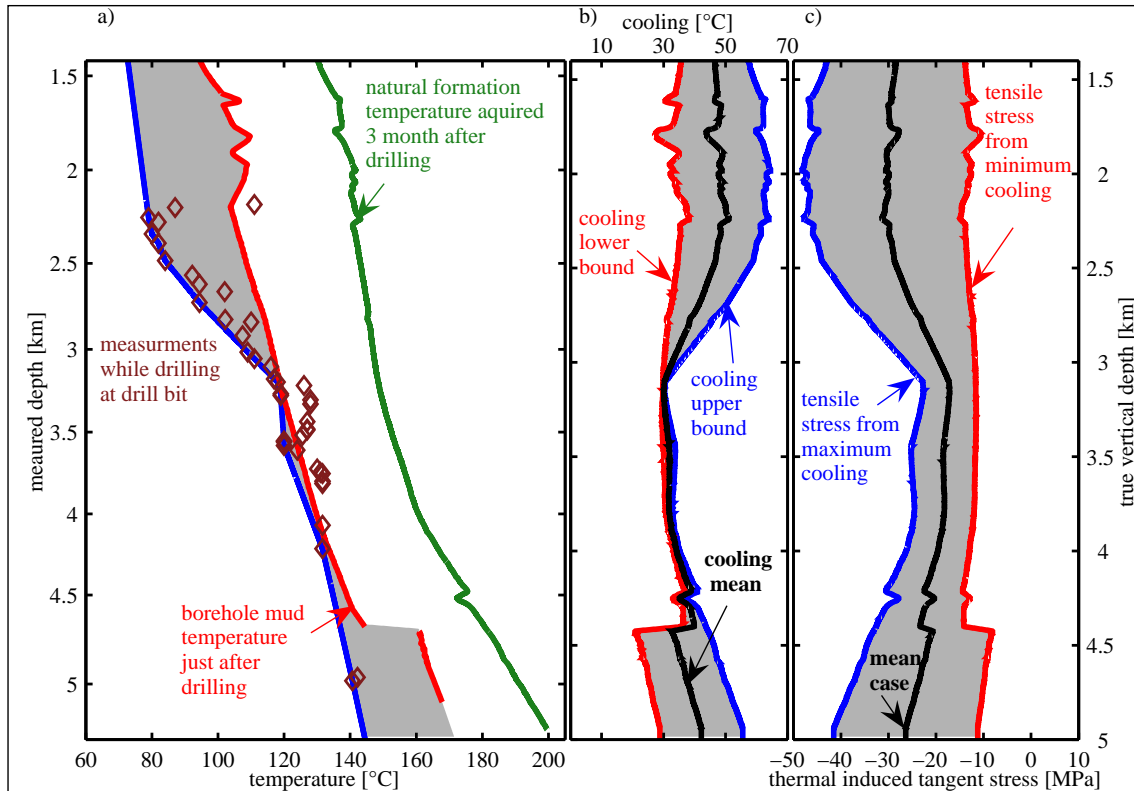


Figure 4.8: a) Estimates of the temperature profile in GPK4 prevailing shortly after drilling and after 3 months. The diamonds denote point-measurements of the temperature of the mud within the bit during drilling obtained with a MWD system. The grey area denotes the range of estimates of the coolest temperature that occurred during the drilling operations. b) Corresponding range of values of maximum-cooling of the borehole wall. c) Implied range of estimates for the thermally-induced hoop stress. Tensile stress for maximum cooling is computed with $\alpha_o = 10 \cdot 10^{-6}$, $E = 56$ GPa and $\nu = 0.25$. Tensile stress for minimum cooling is computed with $\alpha_o = 6 \cdot 10^{-6}$, $E = 52$ GPa and $\nu = 0.2$.

4.5.5.2 Strength criteria and effective stress

Analysis of the breakouts requires a compressive strength criterion. Uniaxial compressive tests were conducted on ten samples of unaltered Soultz granite, and yielded values of UCS ranging from 100 to 130 MPa (*Valley and Evans, 2006b*, and Appendix E). *Schäfer (1990)* conducted triaxial compressive strength tests on unaltered samples of Soultz granite at a confining pressure of 40 MPa and obtained a significantly higher value of 477 ± 52 MPa. Several authors (*Al-Ajmi and Zimmermann, 2006*; *Haimson, 2007*; *Haimson and Chang, 2005*; *Wiebols and Cook, 1968*) have pro-

posed failure criteria that attempt to take into account the triaxial stress state at the borehole wall, although there is currently no consensus as to which is the most appropriate. We assume the appropriate strength is given directly by the *UCS*. Although it is true that higher strength estimates would have been obtained had the tests been conducted under the confined conditions that prevail at the borehole wall, there are other issues that should be born in mind when considering whether laboratory values of strength derived from tests on cores extracted from considerable depth are representative of *in-situ* strengths. Firstly, there is the question of microcracking induced by stress relief when the core pieces are removed from *in-situ*. *Martin and Stimpson* (1994) show that the *UCS* of Lac du Bonnet granite reduced from about 210 MPa for samples collected at shallow depth to about 150 MPa for samples collected at a depth of about 400 m where the maximum principal *in-situ* stress was estimated to be about 55 MPa. The Soultz samples tested in uniaxial compression were extracted at depths ranging from 1600 to 2000 m where the vertical stress range from 40 to 50 MPa (from equation 4.2). However, both cores and the borehole wall at the depth of removal have experienced complex stress paths during drilling. Whilst these paths are not identical, both involve stress relief to some extent, and both will result in damage and strength reduction in comparison to that of *in-situ* rock remote from the wellbore. Thus, the reduction in strength of the core samples mimics that of the borehole wall to some degree. A second consideration is that stress corrosion cracking will serve to reduce the strength of the borehole wall on timescales that are long compared to the laboratory tests (*Diederichs et al.*, 2004). This weakening of the wall rock will be promoted by the high in-situ temperature and the reactive nature of the pore fluid. Thus, there are competing effects that make it is difficult to decide whether the *UCS* measured in the laboratory is generally higher or lower than the strength of the rock at the borehole wall under in-situ conditions. In view of this uncertainty, we take the measured *UCS* values as providing a reasonable measure of the compressive strength of the borehole wall. The resulting compressive failure criterion used for the breakout analysis is,

$$\sigma_{\theta\theta}^{\max} = S_{\theta\theta}^{\max} - \beta_c Pp = UCS \quad (4.6)$$

This criterion incorporates an effective stress law for compressive failure with a coefficient $\beta_c = 1.0$, as found by *Brace and Martin* (1968) to be valid even for very low-porosity crystalline rocks.

The analysis of DITFs requires a tensile failure criterion. No laboratory measurements of the tensile strength of Soultz granite are available. A review of the literature suggests values for intact granite specimens of the order of 10–20 MPa can be anticipated (e.g. *Segall and Pollard*, 1983). However, *in-situ* values will be less than this — perhaps as low as a few MPa — owing to drilling induced borehole wall damage and microcrack growth assisted by the reaction of the poly-crystalline material to cooling (*Bérard and Cornet*, 2003). Indeed, many practitioners adopt a value

of zero for tensile strength when considering similar borehole stability problems (e.g. *Brudy and Zoback, 1993*). In view of this, tensile strength, T , will be considered to range between 0 and 5 MPa. There is considerable uncertainty regarding the value of the coefficient in the effective stress law for tensile failure that is appropriate for low-porosity crystalline rocks. Laboratory studies generally indicate a value of unity (*Jaeger, 1963; Jaeger and Cooke, 1963; Schmitt and Zoback, 1992*). Nevertheless, several practitioners routinely assume a coefficient of zero when analysing breakdown pressures in hydrofracture tests conducted in low porosity rocks (e.g. *Rummel, 1987*), and it is clear that the coefficient must be zero for vanishingly small porosity rocks. In hydrofracture stress tests interpreted classically using the breakdown pressure, the difference in the estimates of SH_{max} obtained with coefficients of 0.0 and 1.0 is equal to the pore pressure, and this is sufficiently large at great depth to severely compromise the utility of the estimates. There is thus considerable importance to understanding the effective stress law in low porosity rocks. Since the porosity measured on the Soultz core samples is typically 0.3% (*Geraud et al., 2005; Surma and Geraud, 2003*), we will allow the coefficient in the effective stress law for tensile failure to range between 0.0 and 1.0 in our analysis. Thus, the failure criterion in tension in our analysis is:

$$\sigma_{\theta\theta}^{\min} = S_{\theta\theta}^{\min} - \beta_T Pp = -T \quad (4.7)$$

where $0.0 < \beta_T < 1.0$.

4.5.5.3 Constraints on maximum horizontal principal stress magnitude imposed by wellbore failure

The compressive and tensile failure criteria of equations (4.6) and (4.7) place bounds on the value of $S_{\theta\theta}^{\max}$ and $S_{\theta\theta}^{\min}$. This, in turn, places bounds on SH_{max} from equation (4.4), since Sh_{min} , $S_{\Delta T}$, and P_w are known independently. Broadly speaking, borehole sections showing the presence of compressive or tensile failure place lower bounds on SH_{max} magnitude, while those without compressive or tensile failure place upper bounds. The resulting constraints on SH_{max} obtained from the wellbore failure analysis are represented by the four bold solid lines in Figure 4.9. The light lines denote contours of fractions of the vertical stress and are presented for reference.

At shallow depth, the upper limit on SH_{max} is set by the absence of breakouts (curve A). A strict upper limit is obtained assuming the maximum value of compressive strength (i.e. $UCS = 130$ MPa), and a minimum cooling stress profile of Figure 4.8c (note: this was derived using the actual temperature profile prevailing at the time of the logs when the presence or absence of breakouts was determined). Above 2.5 km the upper limit exceeds $1.15S_v$ but is less than this below 2.5 km, declining steadily to $0.95S_v$ at 3.6 km where breakouts begin to occur more or less continuously. This upper-bound curve does not apply to a short, isolated section of wellbore with

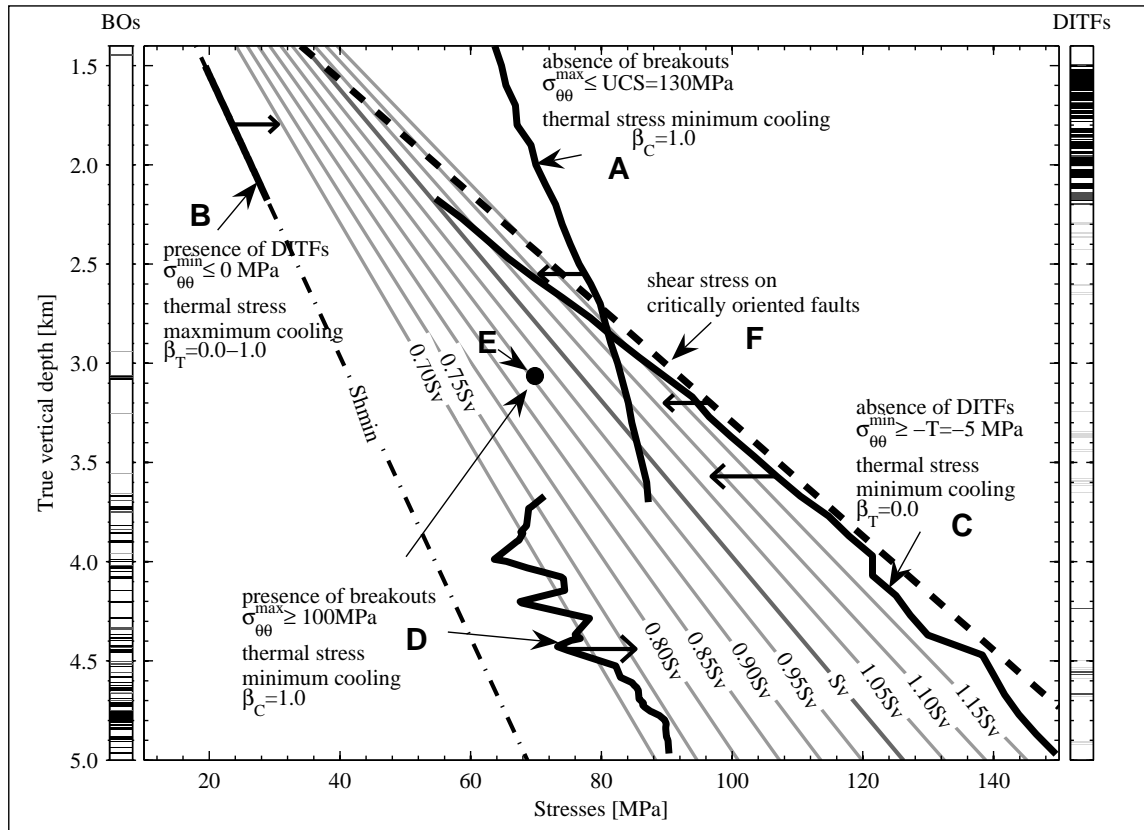


Figure 4.9: Constraints on SH_{max} magnitude placed by the presence or absence of DITFs and breakouts in GPK4. The arrow on the bounds indicates whether they are upper or lower limits. Contours of SH_{max} given as various fractions of Sv are shown to provide a reference background. Conservative values were used for all parameters used in deriving the bounds so as to yield absolute limits. The distributions of breakouts and DITFs along the well are shown at left and right respectively. See text for details.

breakouts at 3100 m which is interpreted as reflecting a zone of perturbed stress.

The lower limit on SH_{max} at shallow depth is given by the logical constraint that SH_{max} must be greater than Sh_{min} (Curve B). Although in principle the presence of DITFs along the hole section imposes constraints on SH_{max} , the adoption of the maximum cooling stress profile yields a constraint that is less than Sh_{min} for all values of the coefficient in the effective stress law for tensile failure. Thus, at shallow depth, the maximum cooling stress is sufficient to produce tensile failure regardless of the value of SH_{max} .

The relatively sudden disappearance of DITFs at 2.3 km depth and their essentially continued absence below imposes an upper bound on SH_{max} (Curve C). To

be conservative, this bound assumes a maximum value for tensile strength of 5 MPa, the minimum-cooling thermal stress profile, and a value for β_T of 0.0. The effect of using a larger value for β_T is to translate the bound to lower $SHmax$ values, as will be discussed later. If the initial hypothesis we made that DITFs form under hydrostatic conditions were not true (i.e. that an additional wellbore pressure, ΔP_w , participates in the formation of DITFs), then taking the upper bound would also translate to lower $SHmax$ values. Thus even if that initial hypothesis was violated, our proposed upper bound would stay an absolute upper bound. At 2.3 km depth, $SHmax$ is constrained to be less than $1.05Sv$. This strict upper limit increases with depth, although it is always less than $1.20Sv$.

The presence of numerous breakouts at depth imposes a lower limit on the value of $SHmax$ below 3600 m (Curve D). This lower bound was computed assuming a minimum compressive strength of 100 MPa, a minimum-cooling thermal stress, and a value of β_c equal to 1.0. The lower bound on $SHmax$ between depths 3.6 and 5.0 km ranges erratically between $0.65Sv$ and $0.75Sv$. As noted earlier, a group of clear but isolated breakouts is seen at about 3100 m TVD. Taken on face value, these would require that $SHmax$ be at least $0.9Sv$ at this depth (Point E). However, the isolated nature of this group suggests they are due to a local stress perturbation, and that breakouts forming under the larger-scale depth trend occur predominantly below 3.6 km TVD.

In summary, the most useful constraints that wellbore failure observations impose on $SHmax$ relate to the upper bound. $SHmax$ must be less than $1.0Sv$ at 2.2 km, less than $1.15Sv$ at 2.8 km, less than $0.95Sv$ at 3.6 km, and less than $1.15Sv$ at 5 km. The corresponding lower bounds require $SHmax$ to be greater than $0.8Sv$ at about 3.5 km and greater than $0.75Sv$ at 5 km.

The resulting upper bounds on $SHmax$ are consistent with the proposed limits on shear stress imposed by the strength of the Earth's crust. A variety of data suggests that strength is limited by the frictional strength of geological discontinuities that are pervasive in almost all rock masses (*Brace and Kohlstedt, 1980; Zoback and Healy, 1984*). Whilst it is clear that some types of sub-planar, geological discontinuities, such as fully-healed fractures, can have strengths that exceed that given by a Coulomb friction law with $\mu = 1.0$ (e.g. *Evans, 2005*), fractures that retain significant porosity and are not healed are likely to conform to this strength limit. For a rock mass whose strength is governed by a Coulomb friction criterion with a friction coefficient of μ , the ratio between the maximum and the minimum effective principal stresses must satisfy (e.g. *Jaeger et al., 2007*):

$$\frac{S_1 - P_p}{S_3 - P_p} \leq \left[\sqrt{\mu^2 + 1} + \mu \right]^2 \quad (4.8)$$

The upper bound on $SHmax$ imposed by this relation for $S_1 = SHmax$, $S_3 = Shmin$ and $\mu = 1.0$ is shown by the dashed line (Curve F) in Figure 4.9. It is

everywhere greater than the upper bound on $SHmax$ from wellbore failure.

Collectively, the results per se do not impose very tight constraints on the magnitude of $SHmax$ and the best working hypothesis remains that proposed by earlier studies (e.g. *Evans, 2005*): that $SHmax = 1.0Sv$. This stems from the observation that micro-earthquake focal mechanisms show both strike-slip and normal faulting mechanism. The results presented quantify the maximum permissible deviation from that equality. For the lower reservoir (i.e. deeper than 3.6 km), $SHmax$ must lie in the range 0.7–1.2 Sv . Expressed as a function of the true vertical depth this gives:

$$SHmax[\text{MPa}] = -1.30 + 25.50z[\text{km}] \quad (4.9)$$

with error bounds equal to $+(5.10z[\text{km}] - 0.26) / -(7.65z[\text{km}] - 0.39)$

4.6 Additional Results

4.6.1 Constraints on the effective stress law for tensile failure

The observed pattern of wellbore failure also imposes constraints on the value of the coefficient β_T in the effective stress law for tensile failure. Figure 4.10 shows depth profiles of minimum effective tangent stress $\sigma_{\theta\theta}^{min}$ for various values of β_T . All computations assume a minimum-cooling thermal stress, and $SHmax = 0.7Sv$, which is the smallest value allowable. The vertical band denotes the threshold for tensile failure to occur. It is evident that a value of $\beta_T = 1.0$ predicts tensile failure along the entire borehole length, which is not in accord with the observed distribution of tensile failure (Figure 4.10a). Adopting more severe cooling profiles, or higher values of $SHmax$, both of which are realistic, serves to reduce the upper bound on β_T still further. Thus, the wellbore failure observations suggest that β_T must be less than or equal to 0.8.

A similar constraint is imposed by the absence of DITFs below 2.2 km which sets the upper limit on $SHmax$ shown in Figure 4.9 (Curve C). This upper limit curve was derived assuming the minimum-cooling thermal stress profile and a value for β_T of 0.0. The effect on the $SHmax$ upper limit curve of using higher β_T values is shown in Figure 4.11. Values of β_T in excess of 0.8 produce an upper limit on $SHmax$ which violates the lower limit profile (Curve D) obtained from the observed breakouts above 4.3 km. If the lower limit is taken as $SHmax = Sv$, which is the best working hypothesis based on the observation of both strike-slip and normal fault focal mechanisms, then β_T cannot be greater than 0.3. Thus, the well bore tensile failure observations, together with the balance of evidence regarding the stress state at Soultz suggest that the coefficient in the effective stress law for tensile failure is significantly less than 1.0 for the Soultz granite.

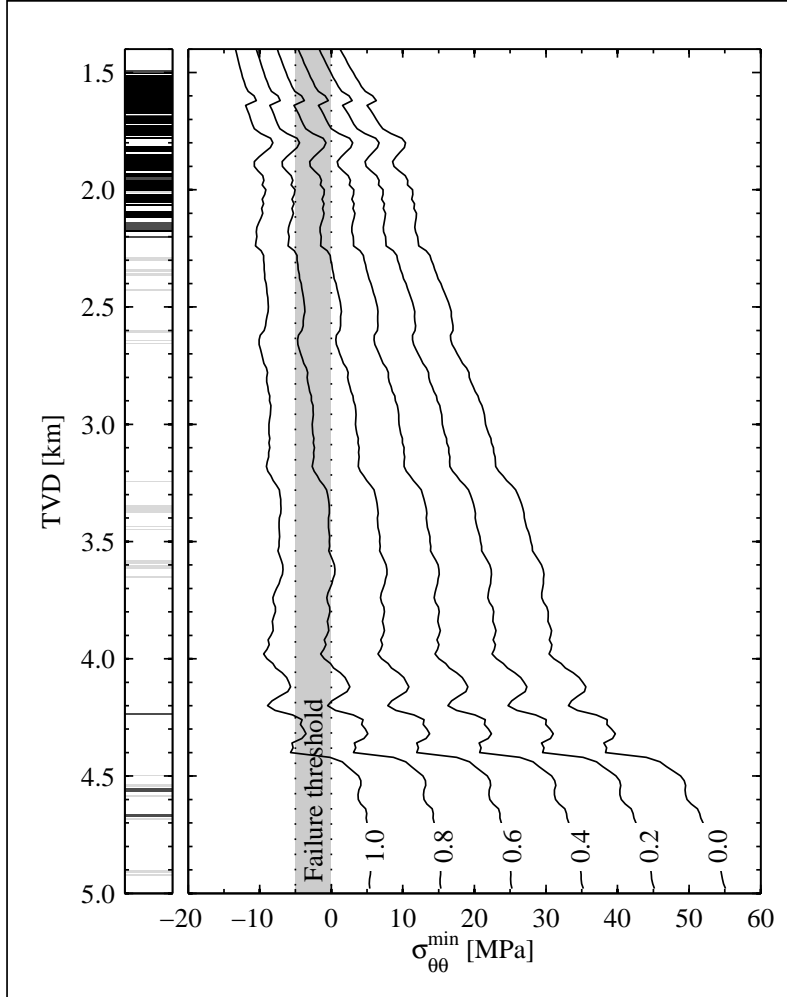


Figure 4.10: Effect of varying the coefficient of the effective stress for tensile failure, β_T , on the profile of minimum tangent effective stress, $\sigma_{\theta\theta}^{min}$. The profiles of Pp , Sv , and $Shmin$ were taken as given by equations (4.1), (4.2) and (4.3) respectively, and $SHmax$ was taken as equal to $0.7Sv$, which is the lower bound value. The thermal stress was derived using the minimum cooling temperature profile. At left is the distribution of DITFs in the well. DITFs are expected to form when $\sigma_{\theta\theta}^{min}$ becomes less than the tensile strength. Values of β_T greater than 0.8 lead to failure extending much deeper than observed.

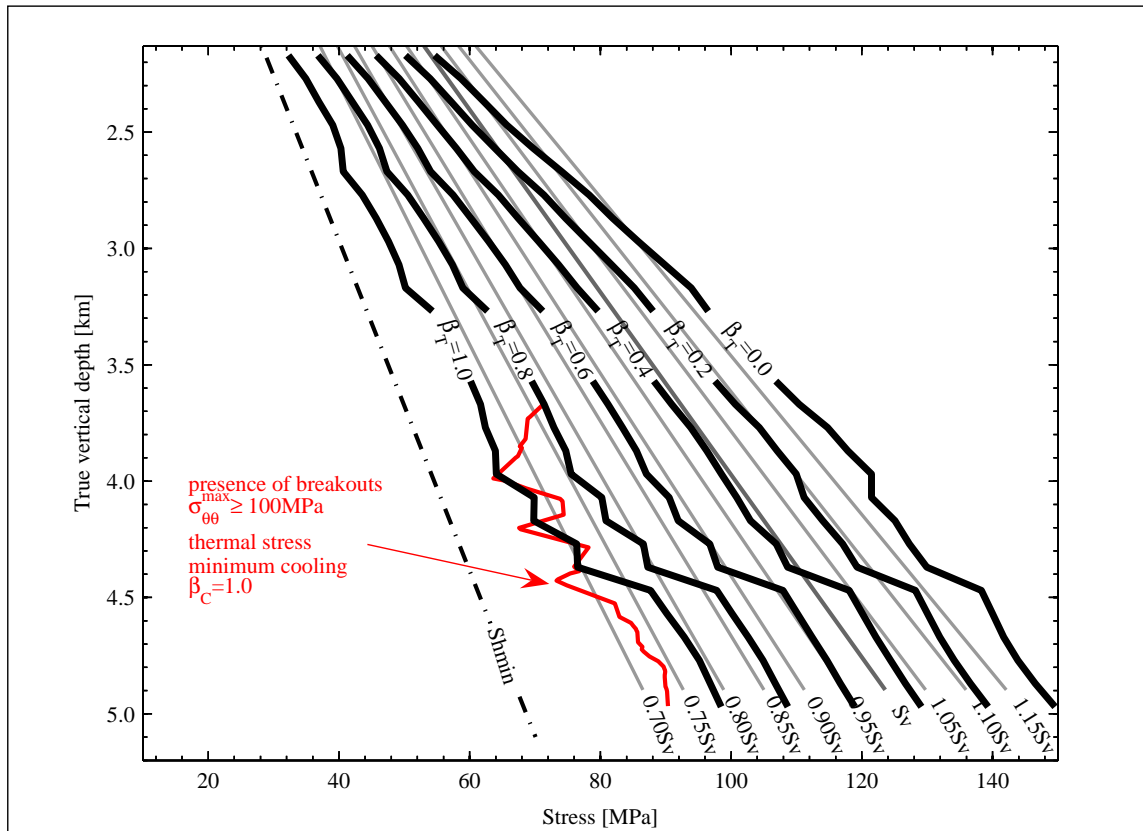


Figure 4.11: Effect of varying the coefficient of the effective stress for tensile failure, β_T , on the upper bound on $SHmax$ imposed by the absence of DITFs in the lower part of the hole. The profiles of Pp , Sv , and $Shmin$ were taken as given by equations (4.1), (4.2) and (4.3) respectively, and the minimum cooling temperature profile was used. The lower bound on $SHmax$ set by the observation of breakouts is violated for values of β_T greater than 0.8. Indeed, if $SHmax$ is taken equal to Sv , as suggested by the earthquake focal mechanisms, then the maximum value for β_T is 0.3.

4.6.2 Evaluation of breakout geometry as a stress indicator

There have been numerous investigations over the past 20 years into the possibility of extracting exact information about the magnitude of $SHmax$ from the geometry of the breakouts in cross-section. Two attributes of geometry are commonly proposed: the depth of breakouts and the width of breakouts, the former expressed as a fraction of borehole diameter. In this section we examine the depth and width of the breakouts formed in the granite section of GPK4, and evaluate whether the proposed estimation procedures yield estimates of $SHmax$ that are consistent with the bounds derived in

the earlier sections.

One of the earliest studies of the mechanics of breakouts was that by *Zoback et al.* (1985) who derived relations between the far-field stress ratio and the depth and width of failure based on a Mohr-Coulomb failure criterion. Laboratory simulations of breakout formation in various rock types by *Haimson* and co-workers provided a test for the predictions of theory and offered insight into the failure mechanism involved. *Haimson and Herrick* (1986, 1989) conducted tests on Indiana and Alabama limestones (grainstones with very uniform texture and grade) and found linear relationships between SH_{max} magnitudes and breakout depth and width that were not in agreement with the prediction of *Zoback et al.* (1985) failure criterion. Examination of thin sections of tested samples shown that for such a limestone, the failure mechanism was intra- and inter- granular tensile cracking, in contrast to the shear (compression) failure criterion used by *Zoback et al.* (1985). Experiments on weak limestones (Cordova cream), however, showed breakouts initiating as shear microcracks which then propagated into the rock along high shear stress trajectories (*Haimson and Song*, 1993). Breakouts in Westerly granite were seen to develop from intra- and trans- granular extensile microcracks that were densely spaced and sub-parallel to the direction of SH_{max} (*Song and Haimson*, 1997). The progressive coalescence of these cracks formed rock flakes that eventually spalled, forming the breakout. Within well cemented sandstone (*Haimson and Kovacich*, 2003; *Haimson and Lee*, 2004; *Song and Haimson*, 1997) breakouts initiated through the development of clusters of intra-granular extensile microcracks sub-parallel to SH_{max} which extended through coalescence and rotation toward the borehole wall. Despite the diversity of breakout formation mechanisms in different rock types, the final shape of the breakouts is usually V-shaped or dog-eared, although the depths and widths are not necessarily the same. An exception are breakouts forming in medium- to high porosity sandstone such as the St. Peter sandstone where very narrow breakouts were seen to extend relatively large distances into the rock (*Haimson and Lee*, 2004). The mechanism underpinning this geometry appears to involve the formation of compaction bands within which grains are dislodged and removed by circulating drilling fluids.

The laboratory results demonstrates that the mechanisms underlying the formation of breakouts is complex and highly dependent of the type of rock involved. Although the final shape of the breakouts tends to be similar, it is far from clear that a unique relation between the depth and width of the breakouts and the in-situ stress magnitudes that produce them exists.

Numerous models have been developed in order to assess the breakouts shape and compute SH_{max} magnitudes. The method by *Zoback et al.* (1985) is based on shear failure criteria and is not obviously appropriate for the Soultz granite where failure is likely to occur through the coalescence of tensile cracks. *Barton and Zoback* (1988) used a strength-of-materials approach to the compute breakout width as a function of SH_{max} by calculating the arc width where circumferential stress magnitude remained

less than some prescribed threshold, taken as the *UCS*. This method is independent of the mechanism of failure, and will be applied to the case of Soultz, as discussed in Section 4.6.2.2.

Others have developed more complex approaches requiring numerical solutions. *Shen et al.* (2002) used a fracture propagation numerical code (FRACOD^{2D}) based upon linear-elastic fracture mechanics in order to study the formation of breakouts. This model includes both tensile (mode I), shear (mode II), and mixed mode (mode I+II) fracture propagation. They modelled the various fracture initiation and propagation mechanisms seen in the laboratory simulations of breakout formation, and found that breakouts eventually developed in shear, regardless of whether initiation involved shear or tensile cracks. *Klerk* (2000) developed a model for quasi-brittle materials in compression and tensile stress fields. The model included explicit coupling between compressive and tensile strength degradation allowing the realisation of discrete fracturing in purely compressive stress fields a situation relevant for formation of breakouts. He was able to reproduce breakouts formed by shear failure as well as breakouts initiated by tensile cracking. He determines that the critical parameters that decide what mechanism will dominate in the breakouts formation is the relative difference between peak and residual strength.

All these models neglect the influence of the complex stress path occurring below the progressing borehole bottom on the breakout geometry. *Read et al.* (1995) observed and modelled asymmetric breakouts formed in a tunnel advancing obliquely to the principal stress directions. *Ito et al.* (1998) examined the formation of breakouts at the borehole bottom with relatively shallow extent. He found that breakouts were predicted to occur preferentially on one side of the borehole, and have an orientation approximately perpendicular to the orientation of standard breakouts, contrary to that observed.

Another aspect of breakout formation that potentially impacts the accuracy of *SHmax* estimates from breakout shape is the question of the time dependency of their formation (*Cuss et al.*, 2003). Aside from the effect of stress-corrosion cracking on the progressive reduction of compressive strength, breakout formation will be moderated by the progressive warming of the borehole after drilling which will give rise to a progressive increase in compressive hoop stress at the wellbore wall with time.

4.6.2.1 Depth of failure

The depth of failure is considered by many authors (e.g. *Zoback et al.*, 2003) to be an unreliable indicator because once a breakout has formed, the stress concentration around the wellbore is such that it will tend to deepen with time. Thus, at the time of logging, which is commonly shortly after drilling, breakouts may not have reached their final depth, leading to inconsistent results. However, *Diederichs et al.* (2004) (referring to results given in *Kaiser et al.*, 1995) published an empirical relation which related the maximum attainable stress induced depth of failure to the ratio (maximum

effective tangent stress)/ UCS :

$$\frac{d_f}{a} = 0.49 + 1.25 \frac{\sigma_{\theta\theta}^{\max}}{UCS} \pm 0.1 \quad (4.10)$$

Here d_f , the maximum radius of the breakout, is normalized by a , the nominal borehole radius. This empirical relation is based on data from observations of the failure of shallow tunnels (*Kaiser et al.*, 1995). The relation was developed for the practical issue of predicting the amount of possible enlargement of tunnel sections rather than stress measurement per se. As such, it pertains to situations where a final breakout depth has been reached, and will be expected to overestimate breakout depth where breakout formation is ongoing at the time of measurement. It is of interest to examine the degree to which the measured breakout depths in GPK4 conform to the predictions of this relation, although it will be necessary to correct for the presence of a thermal stress since the well was still warming up when the UBI logs were run.

Figure 4.12a plots the ratio of maximum to minimum borehole radii as a function of maximum effective circumferential stress at the borehole wall normalised by UCS . The solid line denotes the prediction from equation 4.10 and the dashed lines are the corresponding uncertainties. Also plotted are data points obtained by measuring the ellipticity of sections of GPK4 both with and without breakouts. The ratio $\frac{d_f}{a}$ was computed by dividing the maximum by the minimum borehole diameter obtained at 15 cm intervals from a Schlumberger 6-arm caliper log. The UCS was taken as 115 MPa. The maximum circumferential effective stress $\sigma_{\theta\theta}^{\max}$ was computed using the linear trends of Sv , $Shmin$ and Pp given by the equations (4.1) to (4.3) together with the assumption that $SHmax = Sv$. The thermal stress prevailing at the time of the logging is also included in the computation by using the minimum-cooling thermal stress profile shown in Figure 4.8c.

It can be seen from Figure 4.12a that the depth of failure in GPK4 is always significantly less than the maximum depth of failure predicted by equation (4.10). One explanation for this discrepancy may arise from our measurement of UCS . As discussed earlier, it is likely that our UCS measurements are affected by stress relief due to the large sampling depth. This would mean they probably underestimate the UCS of the material in-situ, although they might still be reasonable estimates for the compressive strength of the borehole wall, since that material has also suffered damage from mechanical and thermal effects. The situation is not clear. In view of this it is of interest to replot Figure 4.12a using a UCS of 185 MPa, a value which the literature suggests is more in accord with expectations for an undamaged, coarse grain granite (e.g. *Hoek and Brown*, 1997). The fit of the extrema of the data to the trend predicted by equation (4.10) is now somewhat better. This improvement can be taken as a tentative indication that the laboratory values of UCS may indeed underestimate the compressive strength of the borehole wall. However, the vast majority of data points remain discrepant. Thus it is concluded that the depth of breakouts in GPK4

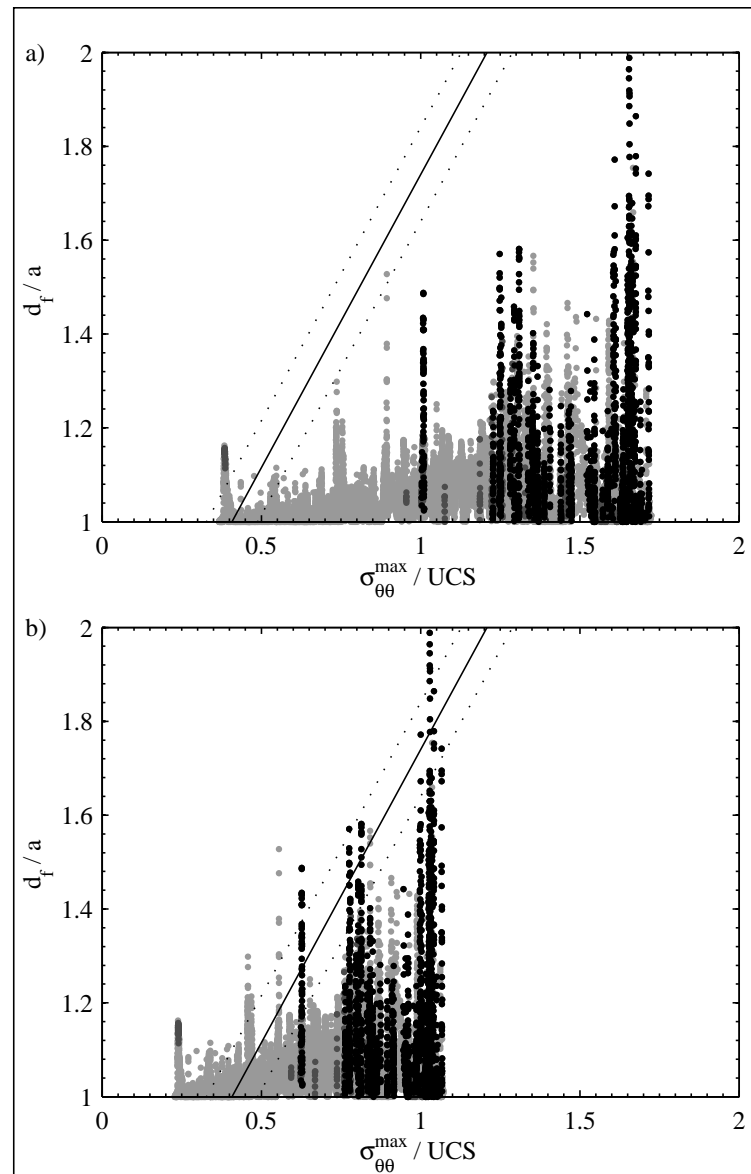


Figure 4.12: a) Plot of the ratio of maximum to minimum borehole radius versus maximum effective tangent stress normalized by the measured mean UCS of 115 MPa. The light grey points are from borehole sections not affected by breakouts, medium grey are from sections affected by low to medium confidence breakouts, and black points denote high confidence breakouts. The lines denote the enlargement predicted from equation (4.10), which is empirically derived from tunnel observations. The values of Pp , Sv , and $Shmin$ used to compute $\sigma_{\theta\theta}^{\max}$ are from equation (4.1) to (4.3) respectively, and $SHmax$ is taken equal to Sv . This computation uses the solution for inclined borehole and includes thermal stress for minimum cooling b) Same as a) but with the value of UCS used in the normalisation increased to 185 MPa to produce a better fit.

at the time of logging are not consistent with the predictions of equations (4.4). There are several factors that might account for the discrepancy. Firstly, time-dependent failure processes (e.g. *Cuss et al.*, 2003) may slow breakout development sufficiently that they had not reached their final depth at the time the caliper logs were run shortly after the completion of drilling of each borehole section. Secondly, the hole was still warming when the log was run and thus a thermal stress component is present which will tend to suppress breakout formation. However, by including the thermal stress at the time of logging in the computation we should have compensated for that effect. Thirdly, scale effects have been seen to influence breakout geometry in laboratory experiments (*Haimson and Herrick*, 1989; *Rajmeny et al.*, 2004), and so it is questionable whether empirical relations derived from tunnel failure should apply to boreholes almost two orders of magnitude smaller.

4.6.2.2 Width of failure

Breakout width has been applied by several authors to derive constraints on SH_{max} (see section 4.3). A relation between SH_{max} magnitude and breakouts width was given by *Barton and Zoback* (1988) by solving equations (4.4) and (4.6) at the borehole wall (i.e. calculating the sector width at the borehole wall where the effective hoop stress exceeds a specified compressive strength). Since at Soultz the boreholes were still warming up after drilling when the breakout observations were made, a thermal stress component will still be present that must be accounted for in the analysis. Thus, we modified Barton's equation to include a thermal stress term, $S_{\Delta T}$, giving:

$$SH_{max} = \frac{UCS + 2Pp - S_{\Delta T} - Sh_{min} [1 - 2 \cos(2\phi)]}{1 + 2 \cos(2\phi)} \quad (4.11)$$

where ϕ is the half breakout width (Figure 4.2b). Inherent in this equation are the assumptions that that the coefficient in the effective stress law for compressive failure $\beta_c = 1.0$ and borehole fluid pressure P_w is equal to pore pressure Pp . The relation is valid for $0^\circ < \phi < 60^\circ$ if $(UCS + 2Pp - S_{\Delta T}) > 2Sh_{min}$, and $60^\circ < \phi < 90^\circ$ if $(UCS + 2Pp - S_{\Delta T}) < 2Sh_{min}$.

The sensitivity of breakout width, 2ϕ , to the ratio of SH_{max}/Sh_{min} predicted by this equation is illustrated in Figure 4.13 where breakout width is plotted against the normalised axi-symmetric stress/strength term, $(UCS + 2Pp - S_{\Delta T})/Sh_{min}$, for different values of SH_{max}/Sh_{min} . It can be seen that for $(UCS + 2Pp - S_{\Delta T})/Sh_{min}$ values greater than 2.0, breakout width becomes increasingly insensitive to the value of SH_{max}/Sh_{min} as 2ϕ increases, and approaches a limiting value at $2\phi = 120^\circ$. This increasing insensitivity of breakout width on SH_{max} is illustrated in Table 4.3 which plots values of SH_{max}/Sh_{min} for a series of breakout angles at three different values of $(UCS + 2Pp - S_{\Delta T})/Sh_{min}$. Two points are of note. Firstly, accurate SH_{max} estimation from breakout width using equation 4.11 is critically

Table 4.3: Analysis of the sensitivity of $SHmax$ magnitude to the breakouts width. See text for details.

$\frac{(UCS+2Pp-S_{\Delta T})}{Shmin}$	$\frac{SHmax}{Shmin}$					
	$\phi = 20^\circ$	$\phi = 40^\circ$	$\phi = 60^\circ$	$\phi = 80^\circ$	$\phi = 100^\circ$	$\phi = 110^\circ$
2.2	1.069	1.079	1.1	1.15	1.31	1.63
3.2	1.417	1.474	1.6	1.89	2.84	4.78
4.2	1.764	1.869	2.1	2.63	4.37	7.96

dependent upon the accurate estimation of the term $(UCS + 2Pp - S_{\Delta T})/Shmin$. Secondly, large breakout widths impose weaker constraints on $SHmax$ than small widths, particularly for smaller values of $(UCS + 2Pp - S_{\Delta T})/Shmin$ (i.e. less than 4). A further point of note applies to the assumption inherent in equation 4.11 that the stress distribution around the borehole during breakout width development is that for a circular hole. *Barton and Zoback* argue that breakouts, when they begin to form, immediately assume their final width according to the prevailing stress field and then deepen. However, in situations where the borehole wall has been significantly cooled during drilling, breakouts will form or at least continue to develop during the warming phase when the hoop stress becomes more compressive due to the disappearance of the thermal stress. Equation 4.11 would predict that breakout width would increase during this period, although the stress field would in general not be that for a circular hole owing to the existence of the breakout.

At 3.6 km depth at Soultz, where breakouts begin to occur, the ratio $(UCS + 2Pp - S_{\Delta T})/Shmin$ lies in the range 3.8–4.4, whereas at 5 km it is 3.1–3.5. These values were computed assuming a UCS between 100 and 130 MPa and the minimum cooling thermal stress profile of Figure 4.8c. Referring to Table 4.3 and Figure 4.13, such values suggest the following: 1) breakout width (2ϕ) should never exceed 120° , and 2) breakout width should be reasonably sensitive to $SHmax$ magnitude.

To test relation 4.11, the width of breakouts seen on UBI images from GPK4 was measured every 15 cm. These measurements are displayed on the Figure 4.14c. Most widths are less than 120° , with 90% in the range 40° – 97° , although two short sections of borehole centred at depths of about 3840 and 3770 m have wider breakouts. The scatter of the data is quite large and no trend of increasing width with depth is evident. Such a trend is expected since the difference in the two principal horizontal stresses undoubtedly increases with depth.

The magnitude of $SHmax$ inferred from the width measurements considering UCS between 100 and 130 MPa, pore pressure Pp given by equation (4.1), Sv given by equation (4.2), $Shmin$ given by equation (4.3) and the minimum-cooling thermal stress profile as shown in Figure 4.14c. Note that because the well is significantly deviated above 4.5 km, the solution for a deviated well was used to compute the stress around the well (*Peška and Zoback, 1995*). Evidently, the scatter in the breakout

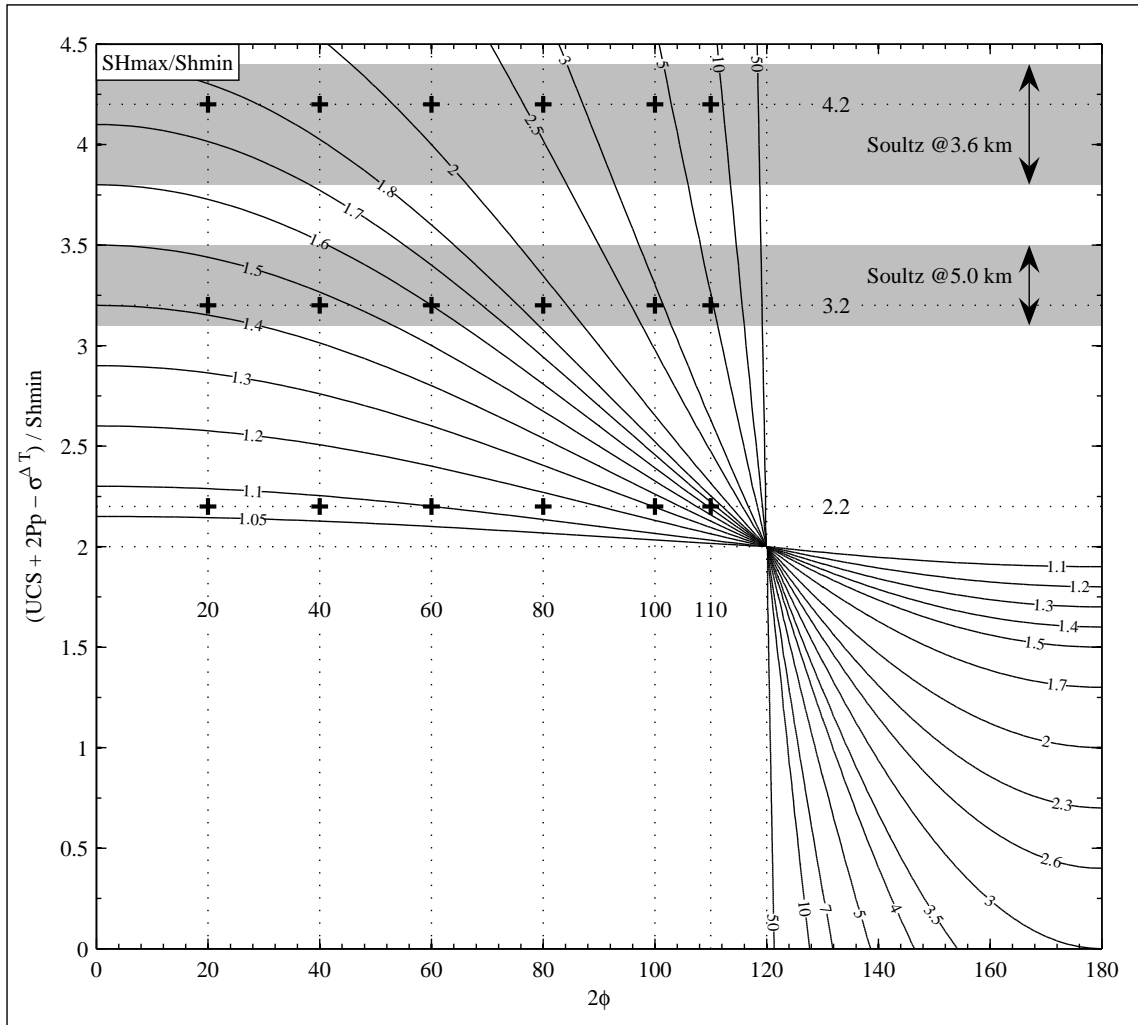


Figure 4.13: Analysis of the sensitivity of SH_{max} magnitude to the breakouts width (2ϕ) predicted from equation (4.11). The contours denote breakout angular width as a function of the term $(UCS + 2Pp - S_{\Delta T})/Sh_{min}$, for values of SH_{max}/Sh_{min} . Values of SH_{max}/Sh_{min} evaluated at the cross symbols which span the range of values of interest to the GPK4 observations are listed in Table 4.3. See text for details.

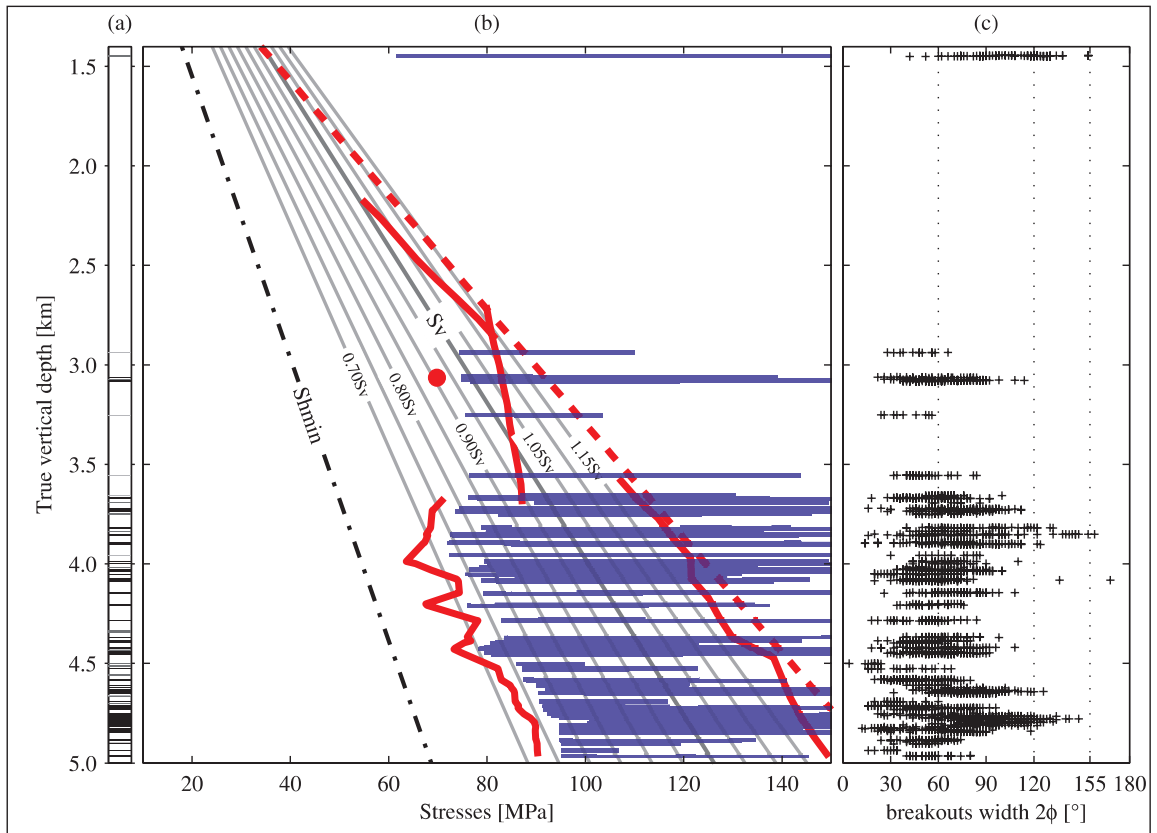


Figure 4.14: Results of the analysis of breakouts width using equation (4.11). The distribution of breakouts in GPK4 is shown at left and their measured angular width at right. The centre frame shows the range of SH_{max} values derived from the observed breakout widths using the adequate solution for an inclined well, assuming P_p , S_v and Sh_{min} given by equations (4.1), (4.2) and (4.3) respectively, a UCS ranging between 100 and 130 MPa, and the minimum cooling stress profile. The broad red lines denote the absolute limits of SH_{max} from the general analysis of wellbore failure. The wide variation in the SH_{max} estimates primarily stems from the scatter in the breakout width estimates.

width data results in a large range of values for the SH_{max} magnitude estimates, although the uncertainty in UCS also contributes. The lower limits of the SH_{max} estimates lie on or slightly above the lower bound set by the presence of the breakouts, which is appropriate given that the same failure law underpins both estimates. The upper limits of the SH_{max} estimates, however, are much more variable, and often significantly exceed the upper bounds imposed by the absence of DITFs and the proposed shear strength limit of the crust given by a Coulomb friction criterion with $\mu = 1.0$.

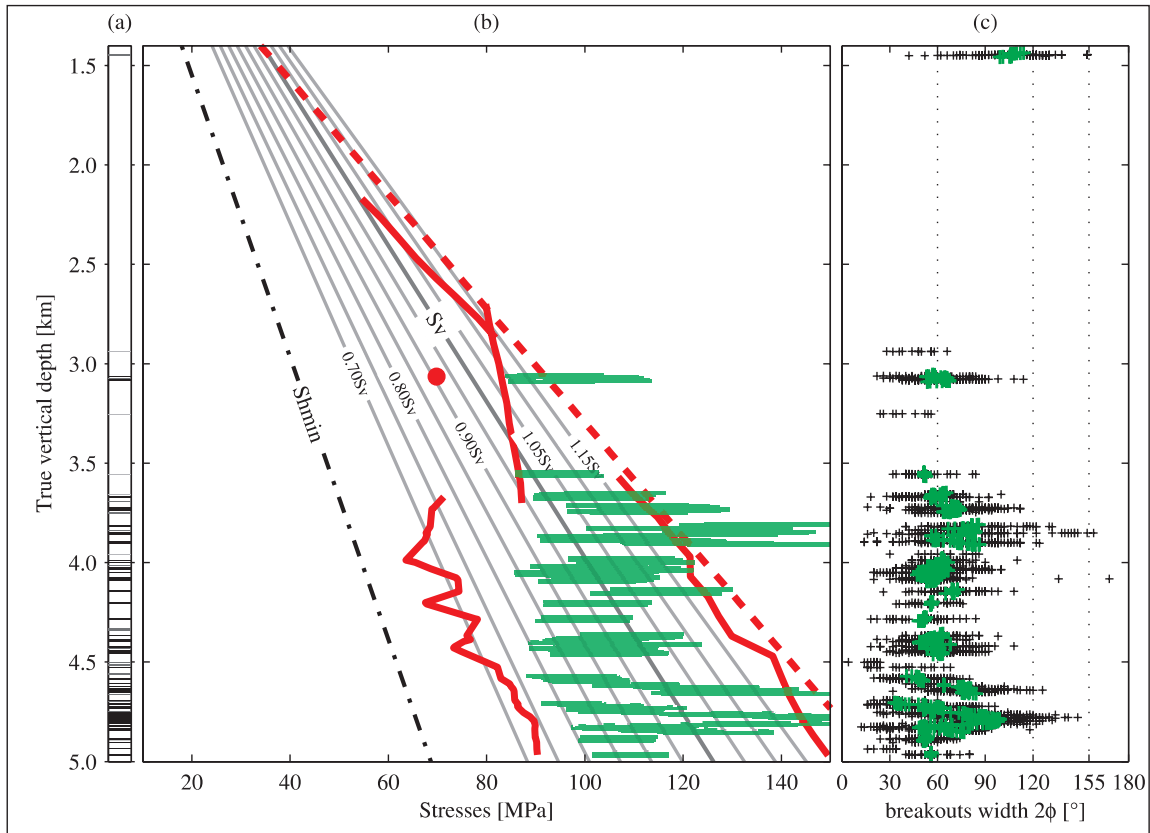


Figure 4.15: Same as Figure 4.14 but showing results after smoothing the breakout width distribution with a 20 m moving window (boxcar) filter.

Part of the apparent scatter probably reflects real variations in the stress magnitude reflecting stress heterogeneity. In Chapter 5 it is shown that the orientation of the principal stress varies significantly over borehole lengths of tens of metres and more, and that this is associated with fractures. Stable estimates of stress orientation that are indicative of the average stress orientation within the rock mass are obtained by averaging. It is reasonable to suppose that stress magnitudes vary similarly, and that point-estimates of stress magnitude such as represented by those derived from breakout width, must be averaged to obtain estimates that are representative for larger scales. Figure 4.15 shows the results of applying a 20 m moving average filter to the 15 cm sampled data. In the averaging, width estimates for each member of a breakout pair are treated as individual datapoints, and windows which contain fewer than 25 data points are discarded. The scatter is now much reduced, with most values lying within the absolute bounds from wellbore failure, although in several places, large excursions resulting from exceptionally large breakout widths continue to exceed the upper bound.

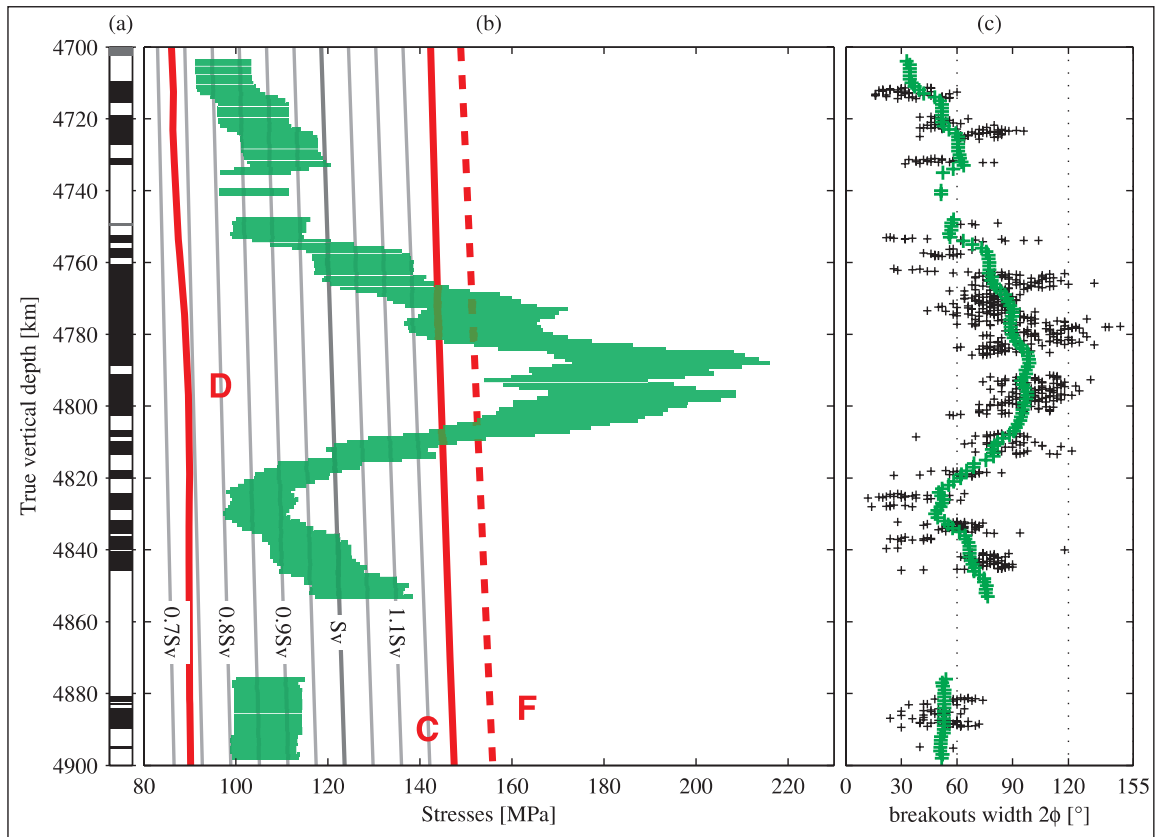


Figure 4.16: Expanded view of Figure 4.15 in a region where relatively large breakout widths that lead to unacceptably high estimates of SH_{max} are observed. The large excursion reflects a systematic change in breakout width over an 80 m section of wellbore. Systematic changes in breakout width are observed to occur on scales greater than a few tens of metres. Variations at scales less than 10 m, are predominantly random and typically amount to $\pm 20^\circ$.

To clarify the nature of the breakout width variations, an expanded view of a section near the hole bottom that contains a large excursion is shown in Figure 4.16. Variations in the breakout width estimates on a local scale of metres are generally random, scattering within $\pm 20^\circ$ of the mean. However, at scales larger than several tens of metres, systematic changes in width occur. The anomalously high estimates of SH_{max} between 4750 and 4850 m reflect one such extreme systematic increase in breakouts width that occurs over scale of a 70 m. Quite possibly this is related to stress heterogeneity, although no clear correlation with large-scale variations in the orientation of breakouts can be found (Chapter 5).

Regarding the validity of the smoothed SH_{max} estimates obtained from breakout width (Figure 4.15), the present data cannot be considered a definitive test since

the absolute bounds on $SHmax$ are too broad. Aside from issues about the validity of the theoretical framework for the present context, such as the stress distribution about the borehole remaining that for a vertical hole during breakout growth, there are many parameters besides breakout width that must be estimated to obtain an $SHmax$ estimate (i.e. all parameters in the term $(UCS+2Pp-S_{\Delta T})/Shmin$). What is clear from the present study is that breakout width appears to vary both randomly and systematically. Thus, smoothing is essential to obtain $SHmax$ estimates that are useful on scales of interest to engineering.

4.7 Conclusions

Observations of breakouts and drilling induced tension fractures formed in two of the three 5 km depth boreholes of the European Enhanced Geothermal System Project at Soultz-sous-Forêts were analysed together with hydraulic data from stimulation injection tests to place constraints on stress to 5 km depth. It is well established that breakouts and DITFs constitute one of the best indicators of the orientation of the principal horizontal stresses. However, when combined with independent estimates of the magnitude of $Shmin$ from the hydraulic tests, the wellbore failure data place constraints on the magnitude of $SHmax$, a stress attribute that is poorly constrained at Soultz, even in the shallow reservoir. The results suggest the following constraints on the various stress attributes:

1. The presence of en-echelon DITFs indicates local deviations from verticality of one principal stress axis. However, on average, these are vertical, suggesting that one principal stress can be taken, on average, to be vertical. This justifies the estimation of vertical stress magnitude as being equal to the integrated overburden load.
2. The orientation of $SHmax$ was estimated from the azimuthal distributions of breakouts and axial DITFs between 1.4 and 5.0 km. Taken together, these indicate an $SHmax$ orientation of $169^{\circ}\pm 14^{\circ}$, consistent with that found for the depth range 2.8-3.6 km. Thus, there is no evidence for a change in $SHmax$ orientation with depth.
3. The magnitude of Sv was taken equal to the integrated density profile. The latter was estimated between zero and 898 m depth from regional density log surveys and lithology density estimates, between 898 m and 3600 m from gamma-gamma density logs run in well GPK1 at the site, and below 3600 m by taking the mean value from that logs run in the granite section above 3600 m. The results indicate a vertical stress profile for the granite described by (equation 4.2):

$$Sv[\text{MPa}] = -1.30+25.50z[\text{km}] \text{ with a standard error equal to } \pm(0.98z[\text{km}]+0.6)$$

4. The $Shmin$ magnitude profile was estimated from the maximum pressures attained at the top of the injection intervals for all large-volume, high-rate injection tests conducted in boreholes that penetrate the shallow (to 3600 m) as well as the deep (to 5000 m) reservoirs. In most tests, the top of the injection interval is the casing shoe. This $Shmin$ -estimator was found to give results in accord with classic hydrofracture stress tests conducted in the shallow reservoir. The pressure data for tests in the deep reservoir invariably showed pressure-limiting behaviour, which in most cases could be attributed to jacking, as required for the estimator to be valid. Six estimates of $Shmin$ at the depths between 2000 and 4489 m TVD were obtained that were well-fit by the following linear trend (equation 4.3):

$$Shmin[\text{MPa}] = -1.78 + 14.09z[\text{km}] \text{ with an uncertainty of } \pm(0.45z [\text{km}] + 1.82)$$

5. Bounds on the magnitude of $SHmax$ were obtained from the depth distributions of breakouts and drilling-induced tension fractures imaged by acoustic televiewer logs. The approach was promoted by the relatively distinct partitioning of the two types of wellbore failure, DITFs occurring almost exclusively above 2.2 km, and breakouts below 3.6 km. The presence or absence of each type of failure placed bounds on the tangent stress at the wellbore wall, which in turn placed bounds on $SHmax$ and $Shmin$. The data were analysed using linear elastic equations appropriate for vertical or inclined boreholes. The maximum thermal stress component required to analyse DITFs was estimated from point temperature measurements conducted in the bit (MWD data) during drilling and also a profile of temperature recorded with the logging sondes shortly after drilling. The latter also allowed the thermal stress needed for the analysis of breakouts to be calculated. Compressive strength was taken from a series of UCS tests conducted on core, whilst tensile strength was taken as lying in the range 0–5 MPa. The coefficient of the effective stress law for compressive failure was taken as 1, whereas that for tensile failure was allowed to range between 0 and 1. The resulting bounds limit $SHmax$ to the range 0.7–1.2 in the lower reservoir below 3.6 km. Immediately above, at 3.5 km, the absence of breakouts limits $SHmax$ to be slightly less than $1.0Sv$. Above this, the upper limit increases steadily to $1.12Sv$ at 2.8 km before reversing trend to decrease to $1.0Sv$ at 2.2 km. The results per se do not impose tight constraints on the magnitude of $SHmax$. The best working hypothesis for the $SHmax$ magnitude profile remains that proposed in earlier studies of $SHmax = 1.0Sv$. This stems from the observation that both strike-slip and normal faulting earthquakes occur within the rock mass during stimulation. Since this is a qualitative result, it is difficult to assign an uncertainty to the equality. The utility of the present results is

to place upper and lower bounds on permissible deviations from equality. For the lower reservoir, i.e. below 3.6 km these bounds are expressed in function of depth by (equation 4.9):

$$SHmax[\text{MPa}] = -1.30 + 25.50z[\text{km}]$$

with error bounds equal to $+(5.10z[\text{km}] - 0.26) / -(7.65z[\text{km}] - 0.39)$

6. The results indicate that the coefficient in the effective stress law for tensile failure cannot exceed 0.8, and most likely is significantly smaller. The upper bound on $SHmax$ below 3.8 km was derived assuming a value for the coefficient of 0.0. Adopting larger values in the computations moves the upper bound on $SHmax$ to lower values. A value of 0.4 would result in an upper bound given approximately by $SHmax = 1.0Sv$.
7. The width and depth of breakouts, which occurred below 3.8 km, were measured to evaluate whether they were consistent with the predictions of two formulae that have been proposed for $SHmax$ estimation. The stress state was taken as that derived in this study with $SHmax = 1.0Sv$. Corrections were made to the formulae to account for the fact that stress conditions about the wellbore were still evolving (i.e. becoming more compressive) at the time the logs were run due to the wellbore heating up from its cooled state at the end of drilling. The observed depth of the breakouts was compared with the predictions of an empirical formula that related tunnel ellipticity to maximum effective hoop stress normalised by UCS . The results suggested that the UCS of the Soultz core samples taken from 2000 m were possibly lower than in-situ values owing to stress-relief microcracking. But, even allowing for this, the conformance of the observations with the predictions of the formula was poor. Breakout width was evaluated against the predictions of a relation given by *Barton and Zoback* (1988). The resulting estimates of $SHmax$ were found to have large scatter, although the estimates for the most part lay within the bounds placed by the aforementioned wellbore failure constraints with some excursions to unacceptably higher $SHmax$ values. The scatter in $SHmax$ estimates largely reflects the variation in breakout width, which had a random component of $\pm 20^\circ$. However, systematic deviations in breakout width occur on scales of several tens of meters which may reflect stress heterogeneity. Smoothing of the breakout width profile using a 20 m moving window boxcar filter resulted in more usefully constrained $SHmax$ estimates, although the accuracy of the estimates remains open to question, not least because the occasional excursions to unacceptably high $SHmax$ values remain.

5 Stress heterogeneities in the Soultz granite inferred from analysis of wellbore failure to 5 km depth

5.1 Abstract

STRESS heterogeneity is thought to play an important role in many aspects of crustal mechanics, including the influencing of the space-time distribution and scaling of earthquakes, and the reaction of rock masses to massive fluid injection such as at HDR sites. Despite this importance, too little is known about the magnitudes and spatial variations of stress in the crust, primarily because heterogeneity is so difficult to measure. Breakouts and drilling-induced tension fractures (DITFs) observed in boreholes offer one of the best direct methods of studying stress heterogeneity since they provide perhaps the best indication of the orientation of the principal stresses. Such features are observed on acoustic borehole televiewer logs run in two boreholes, GPK3 and GPK4, that penetrate granite between 1.4 km and 5 km depth at the Soultz geothermal site. Collectively, they indicate a mean orientation for the maximum horizontal principal stress (SH_{max}) at the site of $N169^{\circ}\pm 14^{\circ}$. However, significant systematic variations in the orientation of the breakouts and DITFs from their respective means are recognised, which reflect the heterogeneity of the stress field along the trajectory of the holes. In this paper we describe these variations and attempt to explain them. A novel feature of these data is that the holes are separated by only 20 m between 1400 m and 2400 m where DITFs cover 55% of the borehole lengths, thus allowing the lateral coherence of the variations to be examined.

The variations are seen to occur at all scales, from relatively abrupt changes over a couple of metres, to gradual variations over scales of several hundred metres. Deviations in SH_{max} orientation from the mean in excess of 90° occasionally occur. The variations follow a power law scaling with an index close to -2.0 , indicating self-affine behaviour where variations appear progressively ‘rougher’ at shorter scales. Two large long-wavelength (>100 m) variations seen at 2.0 and 4.7 km correlate with the two most prominent fracture zones penetrated by the wells. The uppermost of these occurs where the wells are separated by only 20 m, and is only partly correlated between wells, indicating high spatial gradients in stress about the perturbing fracture zone. Short wavelength variations in orientation occur more or less continuously and

are usually associated with natural fractures, as are pauses in wellbore failure, and terminations of DITFs or their transformation from one sort to another, such as axial (A-DITFs) to en-echelon (E-DITFs). Little coherence is seen for short-wavelength variations between wells. Almost all fractures associated with stress perturbations are ‘critically stressed’ under the linear stress characterisation of the site. E-DITFs are often seen to form parallel to natural fractures, which typically dip at 50–70°. The parallel geometry suggests partial relaxation of shear stress from near critical level on the associated natural fractures, and can be explained as due to slip induced by momentary pressurisation as they are penetrated by the drill bit. Low shear stress levels on at least some of the fractures may also be pre-existing.

5.2 Introduction

Analysis of stress induced wellbore failure is a powerful tool to characterise the state of stress (e.g. *Bell and Gough, 1979; Zoback et al., 2003*). In rocks without strong strength anisotropy, the failure is controlled by the variation in tangent stress that develops around the wellbore circumference when the maximum stresses in the plane normal to the wellbore are not equal. Failure may be compressional where the tangent stresses reach a maximum, producing breakouts, or tensile where they reach a minimum, giving rise to so-called drilling-induced tension fractures (hereafter referred to as DITFs). Wellbore failure occurs in the 5 km deep wells at Soultz-sous-Forêts, with DITFs dominating above 3 km and breakouts below 3.5 km. The data have been analysed by *Valley and Evans (2007)* and more completely in Chapter 4 of this thesis to obtain the linear depth trends of the attributes of the stress tensor at Soultz, as needed for site stress characterisation. That study ignored the small and medium scale deviations from the large-scale trends. Such perturbations are commonly called stress heterogeneities, and they are believed to play a significant role in earthquake complexity (e.g. *Shaw, 2004; Zöller et al., 2005*), faulting mechanism (e.g. *Faulkner et al., 2006*), errors in the stress estimates obtained from inversion of earthquake focal mechanism (e.g. *Cornet and Jianmin, 1995; Cuenot et al., 2006; Scotti and Cornet, 1994*) and reservoir stimulation (e.g. *Cornet et al., 1992*).

Despite their perceived importance, stress heterogeneities are difficult to reliably identify, let alone quantify. Stress-induced wellbore failure in deep holes offers perhaps the best opportunity to study the spatial variability of stress. In this paper we present results of an analysis of deviations for the linear stress trends in the Soultz wells to 5 km as expressed through the breakouts and DITFs. A novel aspect of the data is that the two wells that serve as the data source are separated by only 15–30 m over the depth range 1.5–2.5 km. Thus, the lateral variation of the stress perturbations as well as the vertical can be examined. Possible stress perturbing mechanisms which may explain these variations are discussed.

5.3 Background

The effect of gravity is such that stress magnitudes usually increase with depth. Commonly, the increase at a particular locality is seen to be reasonably well approximated by linear trends for the magnitude of the two horizontal and the vertical principal stresses, the latter being equal to the integrated overburden, and a constant orientation for the horizontal principal stresses. This description is referred to as the stress characterisation of a site, and its estimation through measurement is an important task in developing EGSs (Engineered Geothermal Systems). Throughout this chapter, stress variations or perturbations shall be taken to mean deviations in stress from this simple linear description.

There is good reason to believe that stress variations should occur on all scales. At the largest scale, geodynamic processes give rise to changes at scales that are large compared to lithospheric thickness, the so-called first and second order patterns of lithospheric stress variation (*M.L. Zoback, 1992*). The first-order stress provinces are large regions which have a rather uniform stress orientation and largely common stress regime (i.e. normal, strike-slip or thrust). The likely sources of these broad-scale stress fields are related to plate tectonic driving forces (e.g. *Zoback et al., 1989*). For example, for Western Europe, the first-order stress field has a NW–SE orientation for the maximal horizontal stress with a predominant strike-slip regime. The source of this first-order stress field is probably the combination of the mid-Atlantic ridge-push with the Europe/Africa collision (e.g. *Müller et al., 1992*).

Large-scale (compared to lithospheric thickness) deviations from the stress uniformity of the first-order stress provinces are called second-order stress patterns. They constitute very broad scale stress heterogeneities and are controlled by geodynamic processes like lithosphere flexure, buoyancy forces, lithospheric thinning or thickening, lateral density or strength contrast or glacial rebound (e.g. *Zoback and Zoback, 2001*).

At a higher order, stress perturbations are also expected to occur at tectonic plate boundaries, as for example within active orogens due to plate indentation, topography increase and across tectonic units with different geological history (e.g. *Kastrup et al., 2004*).

At a still smaller scale, the stress is influenced by the local structures. The internal structure of the Rhine Graben is made of blocks bounded by major faults. For the Soultz area, *Hosni (1997)* attempted to model the evolution of stresses within the Rhine Graben to the contemporary stress state by building a block model representative of the local geology and geometry of the major faults and applying four successive stress state corresponding to four successive Tertiary tectonic phases derived by *Villemin and Bergerat (1985)* (see also Section 2.2.4). The stresses within the model were then perturbed by the movements on the faults.

The perturbation of stress around faults that slip in earthquakes is also demonstrated by the success of the Coulomb stress concept in predicting aftershock distri-

butions (*Harris*, 1998). This perturbation occurs on scales of the order of the length of slip, and so, since earthquakes occur on all scales, perturbations of stress can be expected on all scales. However, the magnitude of the variations in stress that can build up as a consequence of the repeated action of stress-perturbing mechanisms is tempered by the limited strength of the fractured and faulted crust. For example, a stress perturbation generated by slip on a fault can be partly relaxed by post-seismic slip on secondary fractures and faults, of which aftershocks are a manifestation. Thus, the processes at work are complicated, and our understanding of the degree of stress variability that typically prevails within the crust (if one can generalise), is poor.

The limited state of knowledge has important implications for the development of EGS projects, because it bears on the issue of whether the state of stress at a prospective EGS site will be essentially the same as at a site say ten kilometres distant where stress has been characterised. In this regard it is important to note that the N–S orientation of maximal horizontal principal stress at Soultz (e.g. see Chapter 4) is significantly different to the regional orientation of NW–SE (*Muller et al.*, 1997). It is thus relevant to quantify the deviations in the state of stress from the simple linear characterisation, and understand their origin. Another implication is related to the modelling and prediction of stimulation processes. Indeed, one basic input for most if not all numerical simulations of reservoirs is the initial state of stress. The uniform state of stress provided by the linear site characterisation reflects only partially the actual *in-situ* conditions. The introduction of stress heterogeneities into the initial stress conditions of the models would bring the simulations closer to reality and thus may give some improvement of the quality of the model predictions. This is particularly true for models that seek to simulate induced microearthquake frequency-moment distributions.

One of the most detailed analyses of variations of breakout orientation and their implications for stress heterogeneity comes from the Cajon Pass research borehole (*Shamir*, 1990). Heterogeneity was seen to be pervasive, occurring at various scales. No correlation with lithologic variations, borehole deviation and trend, drill bit penetration rate or changes in rock texture were found. However, in several cases, perturbations occurred in the vicinity of local faults. Three ways in which stress perturbations can develop at faults have been proposed in the literature:

1. The stress perturbation is due to slip on faults that occurs before drilling and is thus pre-existing.
2. The stress perturbation is due to slip on faults that occurs during drilling. The slip may be initiated by the local modification of the stress field at the advancing hole bottom (*Ito et al.*, 1998) or around the wellbore, or through changes in pore pressure related to the circulation of drilling mud.
3. The stress perturbation is due to changes in elastic parameters within the damaged zone of a fault. Such changes are capable of producing significant stress

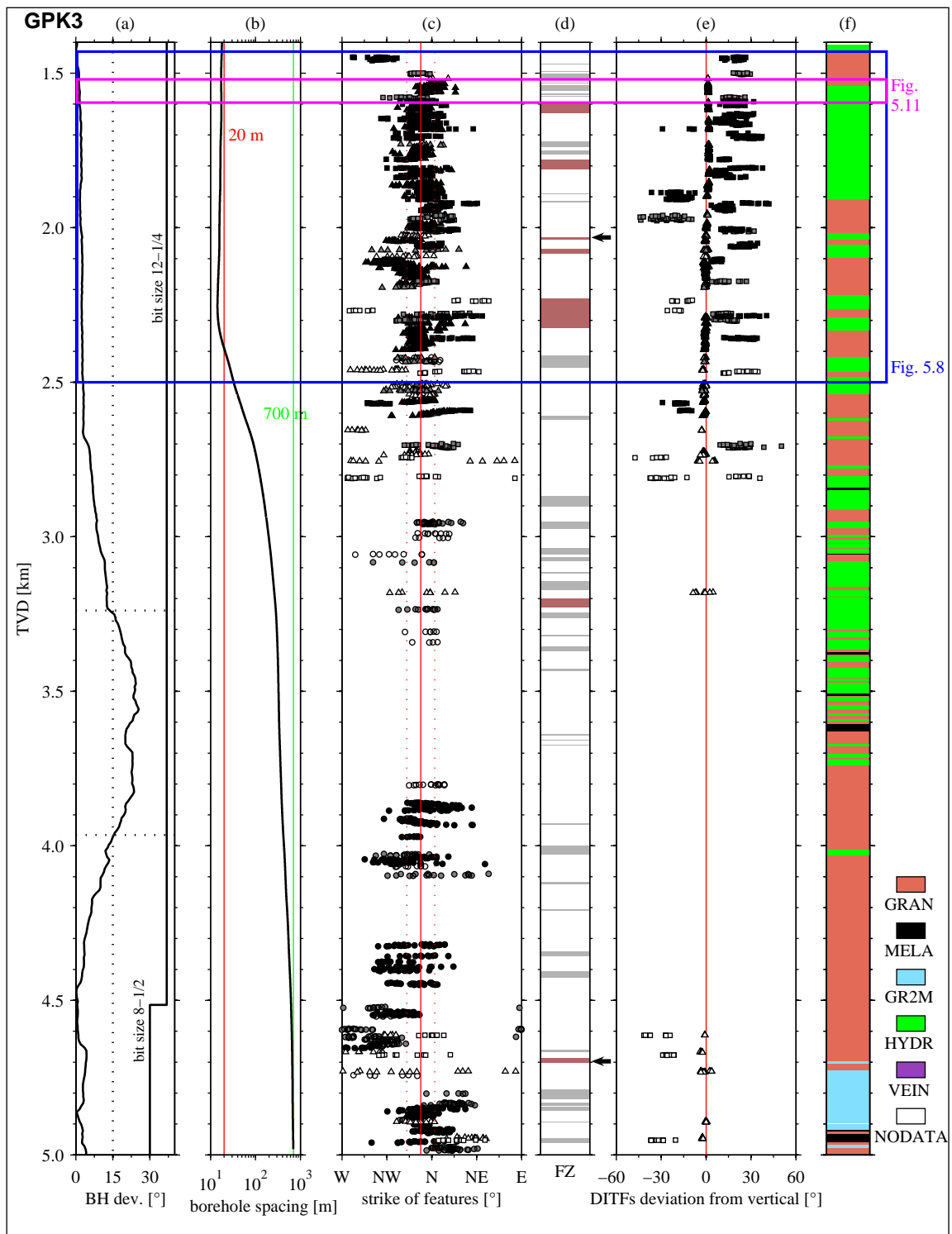
rotations (*Faulkner et al.*, 2006; *Rice*, 1992).

For the Cajon Pass well, *Shamir* (1990) found that deviations in breakout orientation along sections of the hole where they were more-or-less continuous followed a power law between wavelengths of 10 cm and 10 m with indexes ranging from -2.28 to -1.38 . Since natural fractures were also found to follow a power law distribution, *Shamir* concluded that the fault-related stress perturbations were largely a consequence of mechanism (1) and hence were pre-existing, since if mechanism (2) was dominant, one should expect to see a breakdown in the power-law for high frequencies.

Shamir (1990); *Shamir and Zoback* (1992) modelled the expected changes in breakout orientation on faults of known dip by calculating the stress field generated by prescribed slip on the fault and superposing this on the large-scale stress field. There are many degrees of freedom in the exercise with regard to specifying the geometry of slip (i.e. direction, magnitude distribution, and the boundaries). Only the simplest geometries were considered: slip occurred on a square dislocation surface centred on the wellbore, and the slip direction was taken parallel to the maximum shear stress resolved on the plane that arose from the far-field stresses alone. The assumption that the borehole cuts the fault in the centre of the patch is a simplification with significant consequences as it is expected that the stress perturbation is particularly strong at fault tips. Nested dislocation surfaces were used to simulate slip distributions of given constant stress drop, and the resulting stress field computed with dislocation theory codes (*Dunbar*, 1984; *Erickson*, 1987).

The simulations were able to reproduce the key features of the perturbed breakout patterns in the Cajon Pass well, such as the length scale and magnitude of the perturbation in breakout orientation and their occasional disappearance in the fault vicinity, for reasonable slip values. *Shamir* (1990) considered a slip surface with a size of 53 m dipping at 45° centrally penetrated by a vertical borehole, and found the predominant wavelength of the breakout perturbations was similar to the slip surface size. The perturbation of the maximum tangent stress magnitude at the borehole wall, which governs breakout formation, depended on the size of the stress drop relative to the magnitude of the far field stresses, and could increase or decrease, thereby accounting for the sudden appearance or disappearance of breakouts in the fault vicinity.

Subsequently, several other studies (*Barton and Zoback*, 1994; *Hickman et al.*, 2000) have applied the method to attempt to reproduce observed patterns of borehole failure. *Barton and Zoback* (1994) modelled breakout perturbations associated with faults in boreholes at several different locations within various stress regime and found that near total stress drop was needed in some cases to explain the observations.



5.4 Presentation of the data

The data analysed in this study stem from two of the three deep boreholes drilled to 5km in granite at the Soultz-sous-Forêts geothermal project site where the granite top lies at 1400 m. The main sources of information are UBI (ultrasonic borehole imager) images collected in these boreholes.

The background details of the data are given in Section 2.3, so only some key aspects will be summarised here. The UBI data were acquired in two holes GPK3 and GPK4 which were drilled from the same pad. Both are sub-vertical in the upper 2–3 km, and penetrate granite at 1.4 km, which means their separation in the uppermost kilometre of granite to 2.4 km is less than 20 m (Figure 5.1b). Below 2.5 km, the wells deviate from vertical to build up separation before returning to sub-vertical in the lowermost 500 m (Figure 5.1a/5.2a). The granite sections in both wells were drilled with a 12-1/4 inch bit to 4514 m TVD (GPK3) and 4489 m TVD (GPK4), and then with 8-1/2 inch to total depth (Figure 5.1a/5.2a). The UBI logs in each well were run after completing each section, about a month apart. The wells were drilled one year apart. The same UBI sonde was used for both sections of each well but different sondes were used for each well.

Wellbore failure was identified from both the travel-time (i.e. borehole geometry) and acoustic reflectivity images. Breakouts are typically manifest as pairs of diametrically-opposite spall zones that extend along the borehole axis. They occur where the maximum tangent stress acting at the borehole wall exceeds the compressive strength of the rock. In the simple case of a vertical borehole penetrating a rock

Figure 5.1: (on page 126) Summary of stress induced wellbore failure data for the borehole GPK3. Note that depth is given as true vertical depth (TVD) and not measured depth along hole. a) borehole deviation from vertical and bit size. b) horizontal separation of the boreholes plotted on a logarithmic scale. c) azimuth of A-DITFs (squares), E-DITFs (triangles) and breakouts (circles) with the latter rotated anticlockwise through 90°. The mean azimuth of SH_{max} and its standard deviation from all indicators in both GPK3 and 4 is denoted by the vertical red line ($N169^\circ \pm 14^\circ$). d) location and thickness of fracture zones that intersect the well. Brown bands indicate the zones with evidence of permeability. The black arrows point to two fracture zones which impacted the drilling operations. e) deviation from vertical of high-quality en-echelon DITF identifications. Positive values denote dip to the east. f) simplified profile of lithology showing granite types GRAN: standard granite, MELA: biotite rich or xenolith-rich granite, GR2M: fine grained 2-mica granite, HYDR: hydrothermalised granite, VEIN: quartz vein (*Dezayes et al.*, 2003).

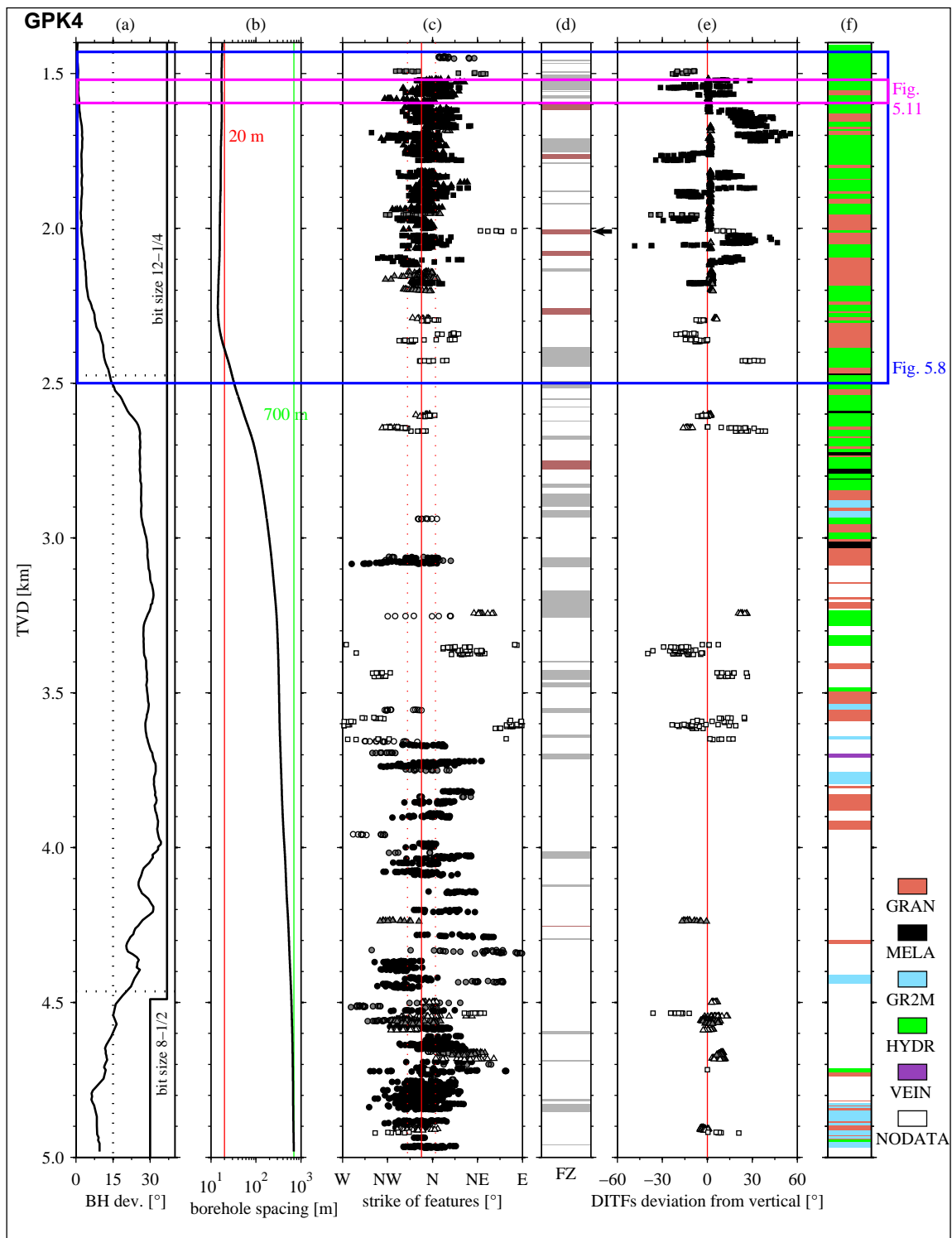


Figure 5.2: As Figure 5.1 but for GPK4. f) simplified lithology is modified after *Dezares et al. (2005a)*

mass in which one principal stress is vertical, this maximum occurs in the direction of the minimum principle horizontal stress, Sh_{min} (Bell and Gough, 1979).

DITFs are identified primarily on acoustic reflectivity images where they show as thin, often ragged fracture traces that may be either axial or en-echelon. DITFs seen on UBI images from the 3.6 km deep well GPK1 do not show on Azimuthal Resistivity Imager (ARI) logs, indicating they do not penetrate deeply. DITFs occur when the tangent stress at the borehole wall becomes sufficiently tensile to produce tensile failure. Although, in principle, the minimum tangent stress produced by far-field stresses can be tensile, it is usually the cooling stress component arising from the circulation of cool drilling fluids that is decisive in driving the minimum tangent stress to negative values and producing tensile fracturing. However, the cooling stress is axi-symmetric, and so the location of the tensile fracture is governed by the far-field principal stress orientations. In the case of a vertical borehole penetrating a medium in which one principal stress is also vertical, the least compressive tangent stress at the borehole wall is horizontal and occurs in the direction of SH_{max} . This results in a pair of diametrically-opposite DITFs, which hereafter are denoted by A-DITFs. However, if the borehole axis is not aligned with a principal axis and the criterion for tensile failure is met, the least compressive tangent stress at the borehole wall will in general be inclined to the borehole circumference. In this case, tensile failure will occur as a stack of slightly-overlapping en-echelon tensile fractures, which hereafter are denoted by E-DITFs. The relationship between the induced fracture geometry and the in-situ stress attributes (i.e. orientations and magnitudes) in this case is not as simple as in the aligned case (e.g. Peška and Zoback, 1995, or refer to Appendix D).

The procedure employed in this study for describing the wellbore failure observations is as follows. First, intervals affected by breakouts, A-DITFs, or E-DITFs were identified. Then, for breakouts and A-DITFs, the mean azimuth of the two limbs of the features was determined for successive 0.5 m depth windows. For E-DITFs, the best-fitting plane to each member of each fracture pair was found and the strike and dip of the plane noted. Typically, this led to one sample every 0.5 to 1.0 m. In all cases, the confidence of the identification was quantified by assigning an index ranging between 1 and 3, corresponding to low and high confidence respectively.

5.5 Analysis of variability of stress induced failure orientation

5.5.1 General variability in the orientation of stress indicators

The orientation distributions of breakouts and DITFs in each borehole are shown in Figure 5.3. The stereographic plot of poles of the DITFs indicates a wide range of fracture strikes, although the rose diagram of Figure 5.3b makes clear that the

vast majority of DITFs lie within 20° of the mean orientation with outliers being relatively few in number. A 5° discrepancy in mean orientation of the DITFs in the two boreholes is evident, and a 10° discrepancy in the same sense for breakouts 5.3c. Given that the horizontal distance between boreholes is less than 35 m for the section where most of the DITFs occur (1400 m to 2500 m depth), so that essentially the same rock volume is sampled, the discrepancy must be due either to stress variations occurring over relatively short horizontal distances or to some systematic error in the logging process. The former explanation seems most improbable, given that the observations span a depth range of 3.5 km. The UBI logs are oriented by coupling the sonde to a GPIT (General Purpose Inclinator Tool) sonde. Different GPIT sondes were used in GPK3 and GPK4 (see section 5.4), but the same sonde was used for both sections of each well. Thus, calibration error is a possible explanation.

The modal peaks of the breakout distributions, which are shown in Figure 5.3c rotated through 90° to permit direct comparison with the DITFs, are essentially identical to means of the DITF populations for the same hole. The distributions of the strikes of breakouts show greater scatter than the DITFs. This is at least partly due to the angular width that breakouts span which makes the determination of their representative orientation more uncertain than for DITFs. A slight asymmetry of the breakout distribution is also visible for each borehole but particularly for GPK3 data: the distribution is slightly overbalanced in an anti-clockwise sense about the mode of the distribution, which is approximately aligned with the DITFs strike directions. This may reflect a bimodal distribution with a main mode at 168° and a weak secondary mode at about 150° . Such a deviation may be associated with the reported counter-clockwise bias in the orientation distribution of hydro-thermally altered shear structures compared to the mean orientation of all fractures (*Evans et al.*, 2005a, Fig. 3). The same explanation was used by *Bérard* (2003) (see also *Cornet et al.*, 2007, Fig. 5) to interpret a bimodal distribution seen in the orientation of wellbore failure in GPK2, although in that case the described features were ‘thermal breakouts’ — borehole elongation in the SHmax direction — a proposed new type of wellbore failure.

With very few exceptions, deviations from verticality of E-DITFs are less than 30° (Figure 5.3a). Non-vertical DITFs dip preferentially to the east. In that respect, they mimic natural fractures which show a similar preference in the upper section of the wells (*Valley et al.*, 2007, and also Chapter 3).

A-DITFs and E-DITFs are clearly distinguished in Figure 5.3a, the former lying around the margin of the stereoplot, and the latter lying inside. E-DITFs with small deviation from axial are rare or absent, indicating that a critical deviation of the ‘vertical’ principal stress from alignment with the borehole axis is required before DITFs form in the en-echelon mode. This behaviour has been predicted theoretically (*Ito et al.*, 2001). Neighbouring tensile fractures developing only a few degrees out of alignment with the borehole axis will tend to interact and link to form an axial fracture, albeit a ragged one. At some misalignment, the interaction will be insuf-

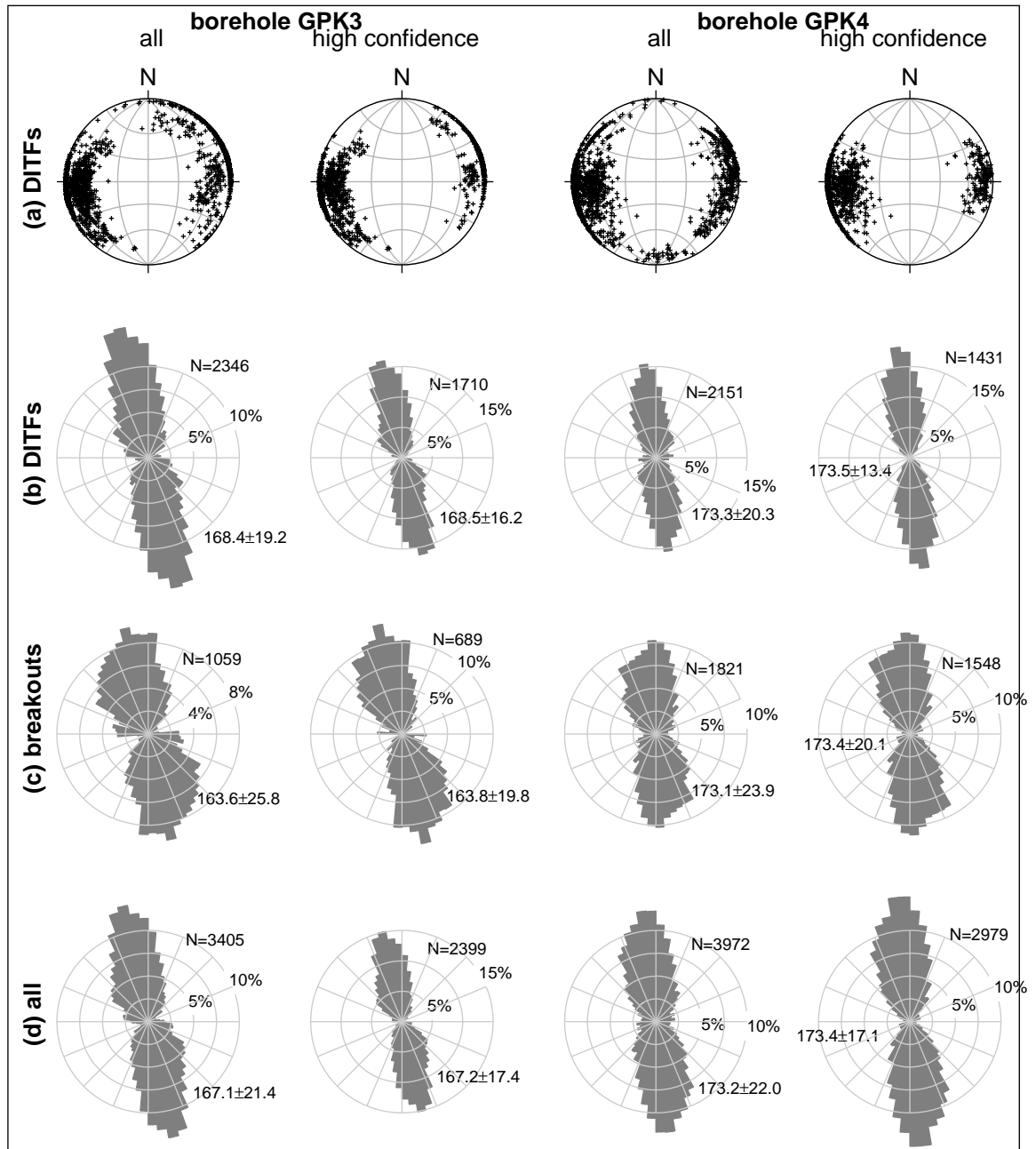


Figure 5.3: Orientation of stress induced wellbore failure in GPK3 and GPK4. a) Stereographic plot of poles to DITF planes (equal area, lower hemisphere). b) Distribution of strikes of DITFs. c) Distribution of the orientation of borehole breakouts rotated through 90° to facilitate direct comparison with the DITFs. d) strike orientation of all features together. Here also, 90° has been added to the breakouts directions. For all circular histograms, N is the number of data point and the circular mean and single standard deviation are also displayed.

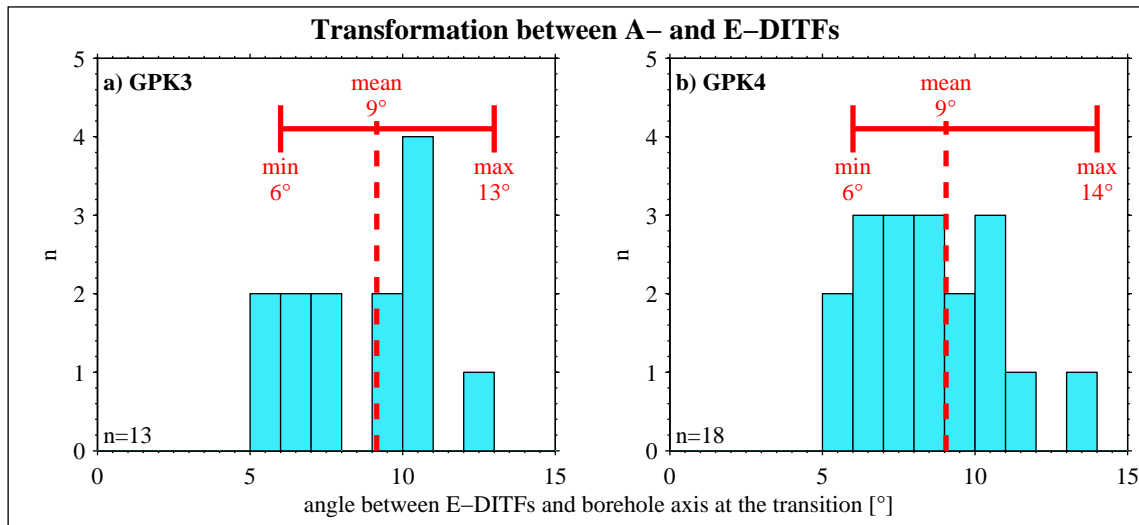


Figure 5.4: Histogram of the angle between E-DITFs and the borehole axis at the transition between A-DITFs and E-DITFs seen in a) GPK3 and b) GPK4.

efficient for linkage to occur, resulting in en-echelon fractures. In order to determine this critical misalignment, cases where A-DITFs transform to E-DITFs in the GPK3 and GPK4 data were examined. Figure 5.4 shows the histogram of angles measured between E-DITFs and the well bore axis at the transitions between E-DITFs and A-DITFs. These angles provide an indication of the maximum angles for linkage to occur, and range from 6° to 14° with a mean of 9° for both boreholes.

This linkage angle will influence our ability to detect deviations from one principal stress from verticality. Therefore, we will digress and examine this aspect in some details before returning to the theme of stress heterogeneity in Section 5.5.3.

5.5.2 Deviation of one principal stress from verticality and E-DITFs linkage

Ito et al. (2001) developed a theoretical framework for computing the critical angle at which DITFs begin to link. The linkage criterion was approximated by relations applicable to fractures interacting within an infinite elastic medium, and did not take account of the wellbore. The analysis considered only far-field stresses and wellbore pressure, and did not include thermal stress.

It is of interest to determine whether *Ito et al.*'s model predictions are consistent with the GPK3 and 4 observations. The analysis was conducted for a depth of 2 km where both wells are vertical. The stress magnitudes were taken as those given by the linear characterisation in Chapter 4: $S_v = SH_{max} = 49.7$ MPa, $Sh_{min} = 26.4$ MPa and $P_p = 20.5$ MPa. Vertical stress was assumed to deviate from true verticality

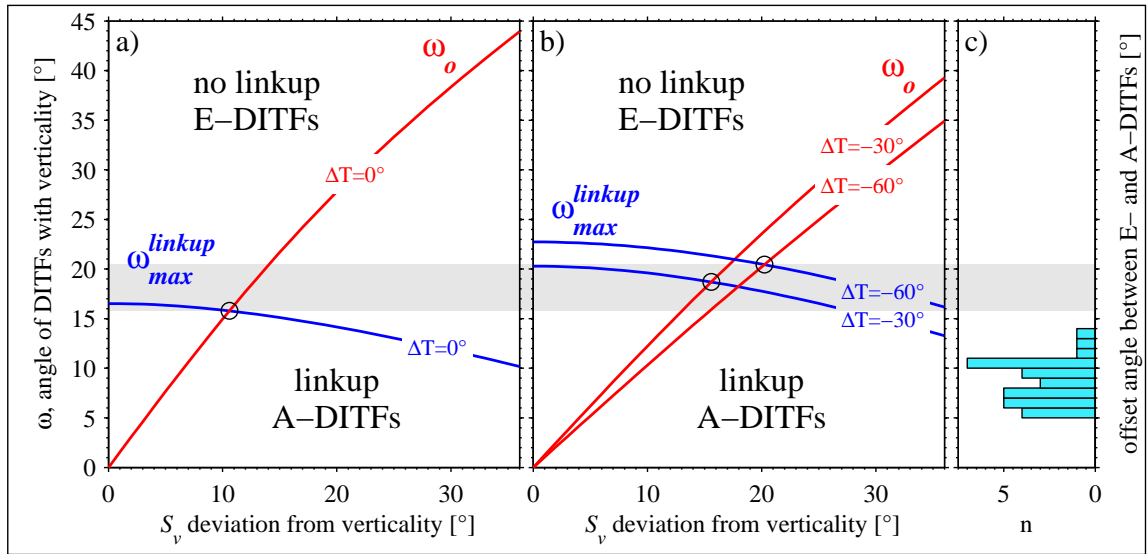


Figure 5.5: Comparison of the maximum deviation from vertical that a A-DITF can have before linkage is no longer possible and E-DITFs form. a) Prediction from the theory given by *Ito et al.* (2001) computed using the stress and wellbore conditions appropriate for GPK3 and 4 at 2 km depth but excluding thermal stress. The red curve denotes the deviation from horizontal (ω) of the minimum tangent stress at the wellbore wall as a function of S_v deviation from verticality. The blue curve denotes the linkage threshold computed from the theory of *Ito et al.* (2001). Intersection gives the maximum value of ω for linkage to occur. b) Similar to a) but including thermal stresses generated by cooling of 30°C and 60°C. The linkage criterion was modified to include thermal stress. c) Histogram of observed inclinations of E-DITFs at the transition from A-DITFs (see also Figure 5.4). These angles are smaller than the transition angles predicted in b).

resulting in a minimum tangent stress at the wellbore that is inclined from horizontal by an angle, ω . If the effective minimum tangent stress, σ_t becomes sufficiently negative, a tensile fracture will form at an angle ω from the borehole axis. Figure 5.5a shows the variation of ω with the deviation of S_v from vertical obtained from the relations of *Peška and Zoback* (1995) (see also Appendix D). The intersection of this curve with that computed by Ito's link-up criterion gives the predicted maximum angle of ω for linkage, and is 16°. This case is presented for illustration only, because the neglect of thermal leads to an effective tangent stress at the borehole wall that is compressive for the given stress conditions and an effective stress law with a coefficient of 0.0. Hence no DITFs would form.

To rectify the situation and make the analysis conform to the conditions in GPK3 and 4, a thermal stress appropriate for a cooling of 30–60°C was included in the

calculation. This range of temperatures denote the bounds on cooling at 2 km set by the analysis of temperature measurements described in Chapter 4 (see Figure 4.8b). Figure 5.5b shows the variation of ω with Sv deviation from vertical predicted from *Peška and Zoback's* relations (1995) that now include a wellbore cooling component of 30°C and 60°C. In this calculation, Young's modulus was taken as 54 GPa, Poisson's ratio as 0.225, and the linear expansion coefficient as $8 \cdot 10^{-6} \text{ K}^{-1}$. These values give negative σ_t values for both temperature and thus DITFs are likely to form. To determine whether they would link, Ito et al's critical link-up equation was modified to include a thermal stress component. The modified equation is given by:

$$\omega_{max}^{linkup} = \sin^{-1} \left[\left(\frac{\sigma_{para} - \sigma_{norm}}{P_w - \sigma_{norm}} \right)^{-0.72} \right] \quad (5.1)$$

where σ_{para} and σ_{norm} are the effective stresses resolved parallel and normal to the forming DITFs respectively. Both are computed using *Peška and Zoback's* relations modified to include the thermal stress. P_w is the well bore fluid pressure which is taken as equal to Pp .

The predicted maximum ω angles for linkage to occur correspond to the intersection of the linkage curve predicted from this equation with the corresponding curve of ω as a function of deviation of Sv . The predicted range of critical angles of 18–20° is slightly greater than the case without thermal stress. The range of critical angles inferred from A-DITF to E-DITF transitions in GPK3 and 4 are shown in Figure 5.5c, and are significantly less than those predicted from Equation 5.1. Thus, we conclude that the model proposed by *Ito et al.* (2001), modified to include thermal stress is not in agreement with borehole failure observations in Soultz boreholes GPK3 and GPK4.

5.5.3 Variability with depth of the stress orientation indicators

The depth profiles of the orientation of breakouts and DITFs are shown in Figure 5.1b and 5.2b for GPK3 and GPK4 respectively. DITFs occur almost exclusively above 3.0 km, whereas only breakouts are confidently identified below 3.7 km. This partitioning of the different modes of failure reflects the depth trends of stress magnitude, as discussed by *Valley and Evans* (2007) and in Chapter 4. Here we are interested only in the variation in the orientation of the horizontal principal stresses that the two indicators imply. The variation of the orientations of the breakouts and DITFs about the mean for the site is shown in Figures 5.6a and 5.7a for GPK3 and 4 respectively. The nature of the variations is made clearer in the expanded views over selected depth windows in Figures 5.6c/d and 5.7c/d. Evidently, depth sections where the indicators have a stable orientation are rare: in most cases, the continuous sections of breakouts or DITFs show locally-progressive rotation in one direction or the other. These local rotations appear as streaks in the compressed-depth profiles in Figures 5.1c and 5.2c.

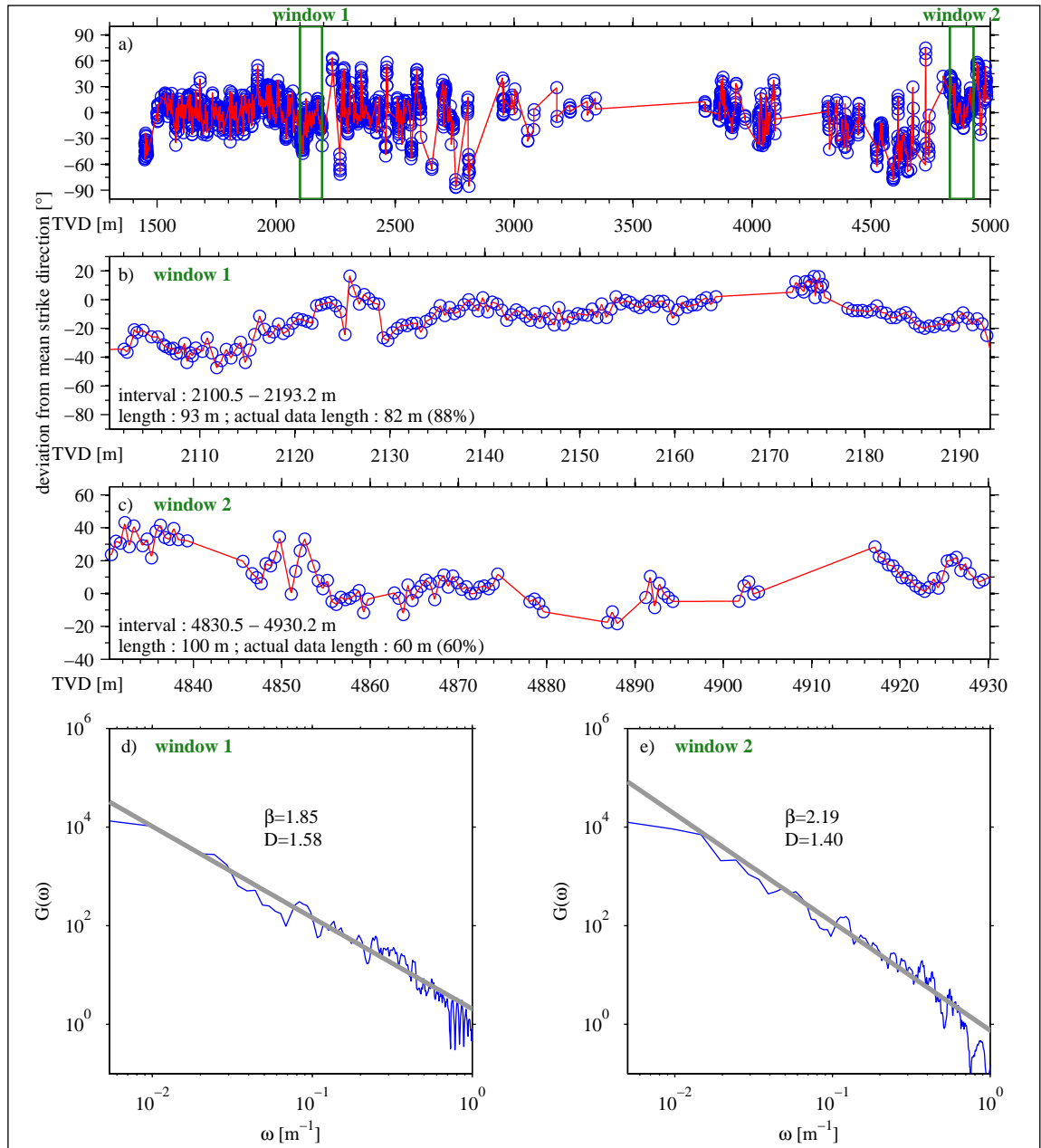


Figure 5.6: Power spectral analysis of the stress orientation variations in GPK3. a) Variation about the mean for the entire borehole. The blue circle are the data, and the red line is the linear interpolation of the data. The data sections used in the analysis are indicated b) expanded view of the data window near the upper part of the borehole where DITFs occur. c) expanded view of the data window near the lower part of the borehole where breakouts occur. d) power spectrum of the data shown in b). The slope, β of the high-frequency roll-off and the fractal dimension, D , are indicated. e) power spectrum of the data shown in c).

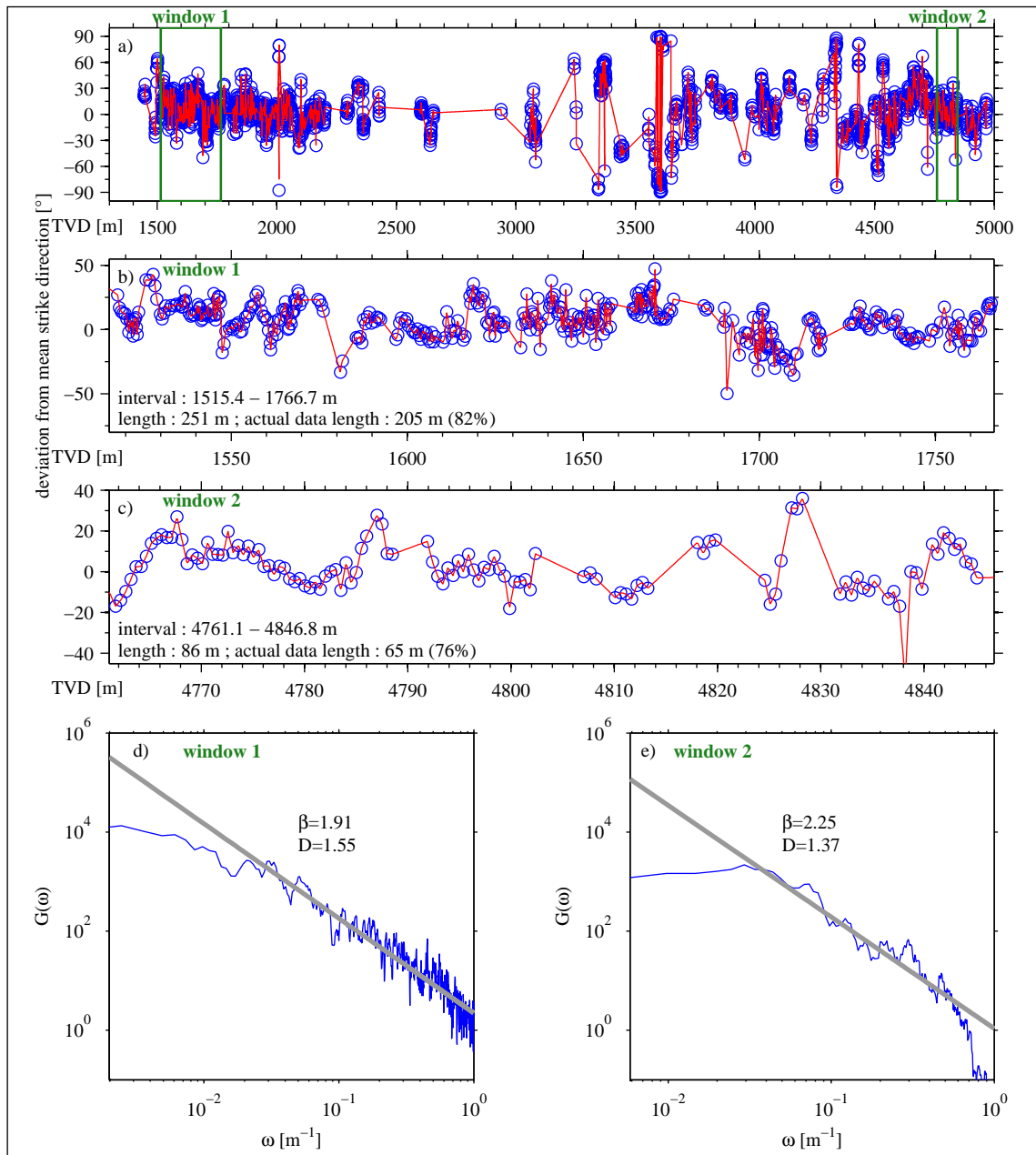


Figure 5.7: As in Figure 5.6 but for GPK4.

Table 5.1: Summary of the power spectral density analysis (see Figures 5.6 and 5.7)

borehole	interval depth [m]	interval length	actual data length	% with data	power law index β	fractal dim. D
GPK3	2100.5–2193.2	93 m	82 m	88%	1.85	1.58
	4830.5–4930.2	100 m	60 m	60%	2.19	1.40
GPK4	1515.4–1766.7	251 m	205 m	82%	1.91	1.55
	4761.7–4846.8	86 m	65 m	76%	2.25	1.37

The variations occur at all scales. This is demonstrated in Figure 5.6d/e and 5.7d/e where the power spectral density, $G(\omega)$, of the variations in breakout- or DITF-orientation over the depth windows are shown. The windows were chosen to correspond to depth sections with relatively continuous data so as to reduce the bias introduced by gap-filling. The inevitable gaps were filled with linear interpolations and the series resampled with constant spacing. The spectra were computed using the periodogram method (e.g. *Stoica and Moses, 1997*) and the resulting spectra smoothed with a 5 point moving-average filter. Results are shown on log-log plots for the full range of spatial frequencies obtained from the analysis (i.e. from the highest, the Nyquist, down to the lowest, the reciprocal of the total window length).

It is evident that at high spatial frequencies, the spectral decay conforms relatively closely with a linear trend of slope, β , indicating that the orientation variations follow a power law of the type $G(\omega) \sim \omega^{-\beta}$. The slopes, β , of the linear ‘roll-offs’ were determined by least-square fitting over the appropriate frequency band, ignoring deviations from linearity in the spectra extremities, and found to be close to 2.0 (Table 5.1). Power laws with slopes greater than -3.0 (e.g. -2.0) indicate a fractal process, the fractal dimension, D , being given by $D = \frac{5-\beta}{2}$ (*Power and Tullis, 1991; Turcotte, 1989*). A slope of -3.0 indicates self-similarity (i.e. scale invariance). Orientation variations that follow a power law with a slope of -3.0 would thus look identical at all scales (*Power and Tullis, 1991*). Slopes greater than -3.0 indicate self-affine behaviour, where variations look progressively rougher at smaller scales. The proportionate reduction with increasing wavelength of the magnitude of the variations relative to wavelength as expressed by the self-affine scaling laws is expected for directional data where the maximum deviation is ceiled at 90° . These power laws hold for wavelengths from 4 m up to 80 m, the longest wavelength that could be resolved from the short data spans. So it is clear that variations in horizontal principal stress orientation occur at various scales.

In the following, the variations that occur at long and short wavelengths will be examined in more detail. Long wavelength variations are taken to be those that are coherent at scales larger than 50 m. Since this is larger than the spacing between the wells between 1.5 and 2.5 km, where DITFs dominate, such variations seen in the vertical profiles of stress orientation should be relatively coherent between wells,

assuming that their lateral extent is similar to their vertical.

5.5.4 Large scale stress variations

Long-wavelength variations in horizontal principal stress orientation can only be detected where wellbore failure occurs more or less continuously over large sections of hole. This essentially restricts the study to the uppermost 1000 m of the granite where DITF failure occurs, and the lowermost 1.2 km where compressional failure is frequent. Long-wavelength variations in SHmax orientation can be seen in both sections in the plots of breakouts and DITFs azimuths in Figures 5.1c and 5.2c.

5.5.4.1 Large scale stress variations in the lower wells sections

Considering the lower sections first, significant variations in breakout orientation with wavelengths of several hundred metres and deviations from the mean of several tens of degrees can be seen near the bottom of both wells. In GPK3, a large excursion with a wavelength of about 400 m is centred at about 4650 m and has a maximum deviation from the mean of 50° to the west. Another deviation to the west with an amplitude of 30° occurs at 4050 m, whilst at hole bottom, the deviation is 20° to the east, both having wavelengths of ~200 m. In GPK4, the only large scale excursion is centred at 4690 m. This has a deviation of about 50° to the east, and a wavelength of about 250 m.

The probable explanation for the 400 m wavelength deviation in GPK3 is that it reflects the stress perturbation associated with a major fault that is penetrated at 4697 m TVD. This fault strikes approximately N160°E and dips at 50–60° to the west (*Dezayes et al.*, 2004; *Sausse et al.*, 2007), and is almost certainly a structure that extends many hundreds of metres. If the structure dips at 60°, then it would lie within 100 m of the borehole over the ±200 m length of the stress orientation perturbation. A transition from breakouts to DITFs is seen to occur near the intersection of this structure with the well, indicating that stress magnitudes are also perturbed. A major deviation in breakout orientation is also seen in GPK4 at a similar depth, but it occurs in the opposite direction. Since the well bottoms are separated by ~650 m, there is no compelling reason to expect that the two perturbations should be associated with the same fault, although that is possible. It is noteworthy that the difference in the orientations of the breakouts in GPK3 and 4 at 4650 m TVD, two points within the reservoir 650 m apart, amounts to 80°.

Another potential contribution to the stress heterogeneity near the bottoms of the holes might arise from a lithological change from standard ‘Saultz’ porphyritic granite to a ‘two-mica’ granite that occurs near 4720 m TVD. The change is believed to reflect the interface between two separate intrusions. Stress perturbations might result from contrasts in elastic moduli. Since the elastic moduli of the two mica

granite has currently not been measured, this possibility remains uncertain. In any case, the dominant factor is almost certainly the fault at 4697 m TVD in GPK3.

The preferred explanation of the large-wavelength variations is that they reflect the stress generated by slip on faults. Based on the modelling results of *Shamir* (1990), perturbations with long wavelengths require slip on surfaces at least as large as the variations' wavelength, which, for the present data, implies structures that are at least 200 to 450 m in length. Such sizes correspond well with the expected lengths of fracture zones within the Soultz granite as describes in Chapter 3. There are many fracture zones intersected by the wells, although none produce a long-wavelength perturbation as large as that associated with the fault in GPK3 at 4697 m TVD. In part, this may reflect the gaps in the definition of the stress field orientation in wellbore sections where there are neither breakouts nor DITFs. However, it is also probably an indication of the uncommonly large size of the 4697 m structure, which is manifest by its hydraulic (*Tischner et al.*, 2007) and seismic (*Dorbath and Charléty*, 2007) properties, and its impact on drilling operations (*Hettkamp et al.*, 2004).

Finally, it should also be noted that it is not strictly necessary that a fracture zone which produces a stress perturbation at a well actually intersect that well. Indeed, given than the fracture zones in the rock mass are high-angled, and separated by ~ 40 m on average (see Section 3.6), it is quite probable that significant structures lie within several tens of metres of almost any point of the boreholes, although perhaps not structures of the scale of the zone in GPK3 at 4697 m TVD.

5.5.4.2 Large scale stress variations in the upper wells sections

The long-wavelength perturbations in the upper section are particularly interesting because the two wells are less than 20 m apart and thus significant coherence between the variations in the wells might be expected. Figure 5.8 shows the DITF strike determinations for the upper section of both wells. These raw data series were resampled at the same constant depth interval in order to permit comparison between the wells. For depths where data are present in both wells, a cross-plot was made (Figure 5.8b) and the correlation coefficient (e.g. *Davis*, 2002, p. 43) between the data-pairs computed. The procedure was repeated after applying moving window (boxcar) filters of lengths 20 m, 50 m and 100 m, to smooth the data and better reveal the long-wavelength variations. Interpolation points filling the data gaps were given zero weighting in the averaging, and so the effective filter length is shorter near gaps.

When no smoothing is applied (Figure 5.8a/b), the coefficient of correlation is very low as variations at short wavelength are not coherent between the boreholes. When progressively stronger smoothing is applied to reduce the high frequency content (Figure 5.8c to h), the coefficient of correlation increases, indicating that long wavelength variations are better correlated between the wells.

The long wavelength components of the variations are most clearly seen after

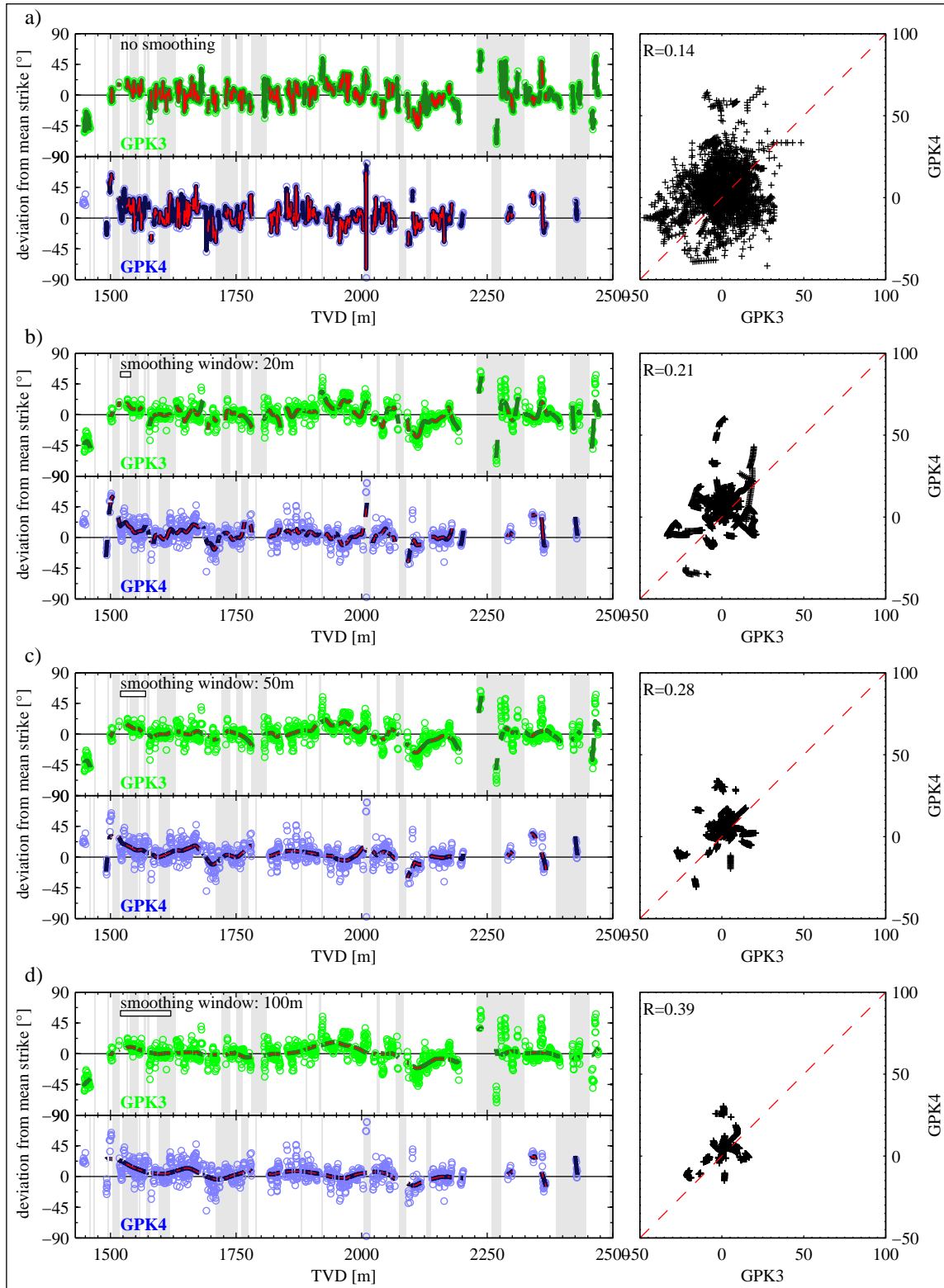
smoothing with a window length of 100 m (Figure 5.8g). Since the horizontal distance between the holes is only about 20 m in this depth range, it might reasonably be expected that the long wavelength variations would be coherent. However, they are evidently only partly correlated.

Figure 5.9 shows a superposition of the two filtered series to assist comparison. For the depth range between 1535 m and 2200 m, which is relatively well sampled, three sections where the two series are reasonably correlated are found. These are denoted A (1535–1621 m), C (1783–1876 m), and E (2006–2200 m). However, between these lie to sections where the orientation variations in the holes are decidedly different. These are denoted as B (1621–1783 m) and D (1876–2006 m), and are marked by the light red bands in Figure 5.9. In section B, the two curves deviate from each other by only 9° over 60 m length scales, which is not a major inconsistency. However, the discrepancy for section D is much larger, amounting to 23° over a 130 m length scale. This is a surprising result, and it poses the question of how such a large change in stress orientation can occur vertically over a scale of 130 m yet not extend laterally only 20 m.

The origin of this discrepancy is uncertain, although a reasonable working hypothesis is that it is related to a major fracture zone that intersects the wells near this depth (indicated by the black arrows in Figure 5.9). This fracture zone is most certainly a major structure, perhaps of the same scale as the fault intersected at 4697 m TVD in GPK3 that was associated with the primary large-scale perturbation in the lower section of the reservoir. The zone was first intersected in GPK2 at 2110 m during the initial drilling of the well in 1995, and resulted in total loss of circulation fluid. No cuttings were obtained from the well during the subsequent drilling to 3876 m because they were swept into the fracture zone along with the drilling fluid. The zone was eventually plugged with 23 m³ of cement during the extension of GPK2 to 5000 m in 1999. It is thus a zone of enormous capacity that has had a great deal of

Figure 5.8: (on page 141) Correlation of the DITF strike variations between GPK3 (green circles) and GPK4 (blue circles) over the depth range 1450 and 2500 m where the wells are vertical and only 20 m apart. a) The leftmost frame shows raw data with points present in both wells marked with a red overprint. The grey vertical bars in the background denote the location and width of fracture zones intersected in the wells. The frame at right is a cross-plot of the data points present in both wells. The correlation coefficient measures the degree to which the data points fall on the dotted line b) Same as ‘a’ but with the series smoothed with a 20 m moving average boxcar filter with points filling gaps assigned zero weighting. c) Same as b) but for a 50 m moving window. d) Same as b) but for a 100 m moving window.

5.5 Analysis of variability of stress induced failure orientation



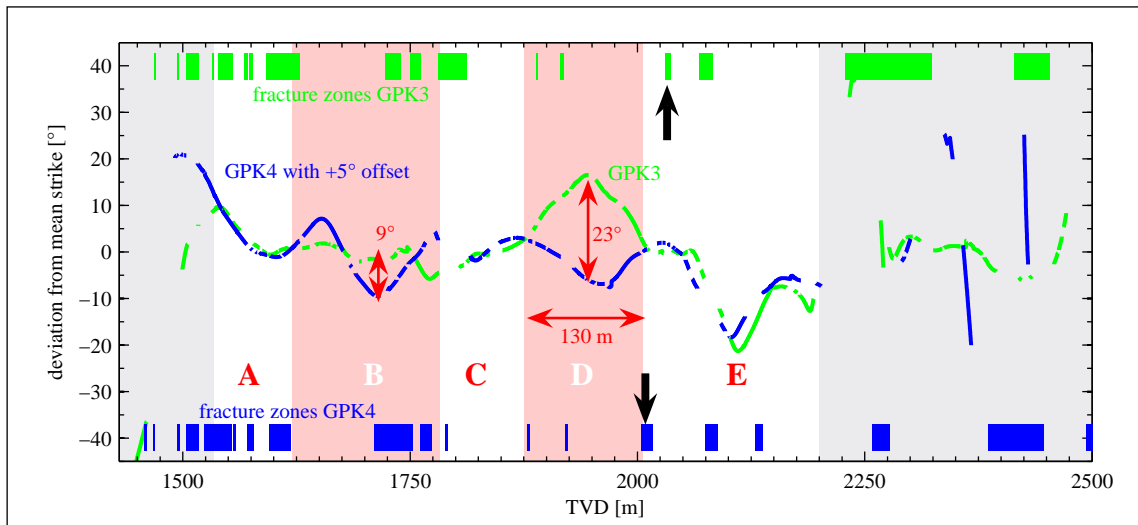


Figure 5.9: Superposition of the long wavelength components of the strike variations from GPK3 (green) and GPK4 (blue) as shown in Figure 5.8d. Note that the curve for GPK4 has been shifted by 5° to compensate for the apparent discrepancy in orientation measurement between the two holes. The two curves are essentially identical in zones A, C and E denoted by the white bands, but deviate significantly from each other in Zones B and D (light red bands). The distribution and width of fracture zones intersected in the two wells are shown at the top (GPK3) and bottom (GPK4) of the figure. Black arrows point to the major fracture zone crossed by the boreholes at about 2100 m.

solid material injected into it. The structure dips at 74° to N95°E and crosses both wells at the bottom of the orientation discrepancy (section D in Figure 5.9). It is thus very close (<40 m) to the wells over the 130 m section of zone D. The discrepancy might thus reflect a particularly strong lateral gradient in stress arising from the perturbation associated with this fracture zone.

Another manifestation of stress heterogeneity is given by gaps in wellbore failure in sections where it is more or less ubiquitous. As noted earlier, this can arise from perturbation of either stress magnitudes or orientation. Gaps in DITF formation of at least 16 m (i.e. the well separation) that occur in each well between 1425 m and 2500 m TVD are marked in Figure 5.10. Both wells have gaps of up to 55 m immediately below the 13 3/8" casing shoe. These may relate more to the thermal history of the holes than natural stress heterogeneity. The installation of the 13 3/8" casing in each well took about 6 days, which is sufficient time for the borehole to heat up. When drilling commenced with the 12 1/4" bit, the first 55 m were achieved within about five hours, and it is likely that the borehole wall of this section remained hotter than would have been the case had circulation not been interrupted. The resulting thermal

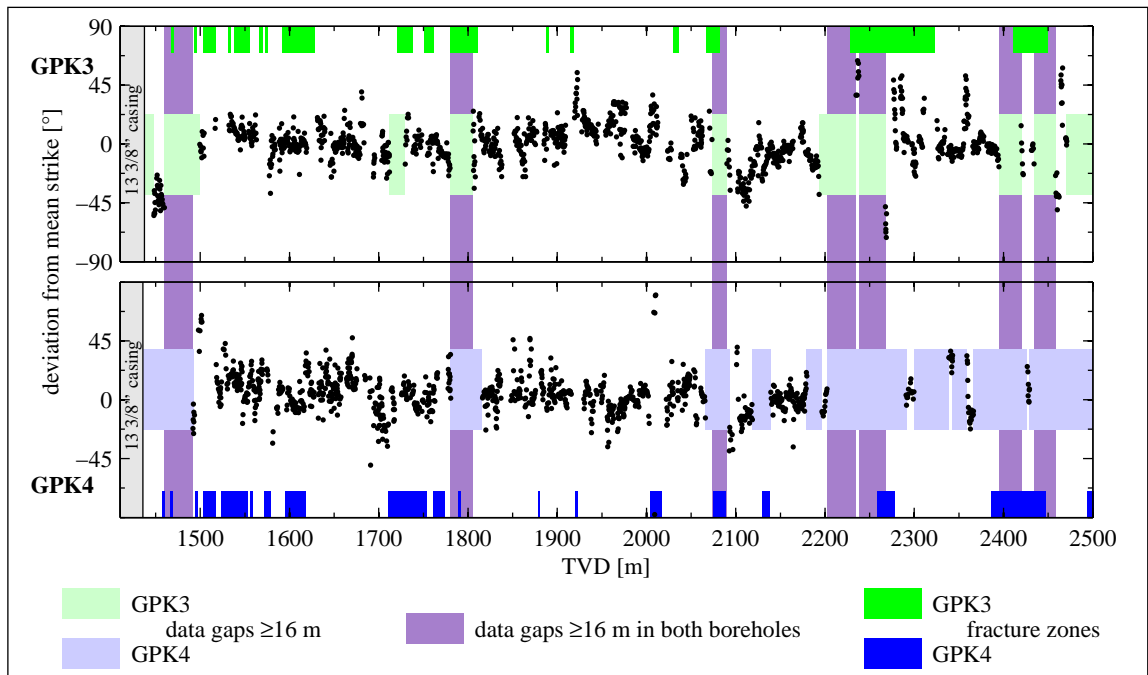


Figure 5.10: Comparison of gaps in wellbore failure that exceed 16 m seen in GPK3 and GPK4. In most of the cases, the gaps occur at the same depth and have similar width in each well. Most gaps can be associated with a mapped fracture zone in the well.

cooling stress would have been reduced. In any case, below this depth it is evident that gaps in wellbore failure longer than 16 m consistently occur in both wells at more-or-less the same depth (marked in Figure 5.10). Numerous gaps shorter than 16 m that appear to correlate, albeit with slight offsets, can also be seen. These gaps are clearly related to natural fracture zones intersected by the wells, which are marked on the Figure. Below 2200 m depth, the size of the gaps in GPK4 become much larger than those in GPK3. This contrast reflects the approach of limit of DITF formation in the wells, which occurs higher in GPK4 than in GPK3 (Figures 5.1 and 5.2). This is more likely to be due to greater cooling of GPK4 during drilling, than lateral stress heterogeneity.

In summary, interruptions of stress induced wellbore failure which occur over lengths equal or larger than the horizontal borehole distance are coherent between the wells. Such interruptions are probably related to the stress heterogeneities induced by natural fractured zones, with the probable exception of the 55 m sections directly below the casing shoe and the section of GPK4 below 2200 m where thermal history of the well may have played the dominant role.

5.5.5 Small scale stress variations

Small-scale variations are considered to have wavelengths less than 50 m. As noted earlier, it is rare for the strike of breakouts or DITFs to remain stable over tens of metres of borehole. More commonly, they rotate systematically in one direction or another for a short distance, giving rise to the seemingly horizontal streaks in Figures 5.1c and 5.2c. Deviations from the mean orientation of more than 45° occasionally occur (Figure 5.3).

This behaviour is made clear in Figure 5.11 which shows vertically-expanded plots of DITFs from GPK3 and 4 between 1520–1595 m TVD. Again, the wells are vertical and separated by only 20 m in this depth range. The variations in strike indicate that, more often than not, the azimuths of the principal horizontal stress axes are rotating as one moves along the borehole. The trends are maintained for only a short distance before they reverse. The reversal points are almost always associated with the intersection of fractures and fracture zones with the boreholes, indicating that the rotations are related to stress perturbations localised at the fractures (Figure 5.11). As noted in the next section, many DITFs either terminate or change their form (e.g. A-DITF becomes E-DITF) at natural fractures. So definitively, natural fractures have a large influence on the variability of stress induced failure.

5.5.5.1 Characteristics of DITF changes at natural fractures

At most intersections of DITFs with natural fractures, the DITF is unaffected and cuts through. However, in many cases, some change is seen. The types of terminations and transformations that DITFs generally undergo and their relative frequency of occurrence are shown in Figure 5.12a. About 70% of all observed DITFs either terminate or change from one form to the other (i.e. A-DITF to E-DITF) at natural fractures. Only 12–23% change from one form to the other remote from natural fractures (these are the type described in Figure 5.4). Of the remainder, 5–11% terminate remote from natural fractures, and a few stop near but not precisely at a natural fracture. In what follows we focus on the 70% that terminate or transform precisely at natural fractures since these suggest that the fractures are the source of the discontinuities in stress conditions at the borehole wall.

The types of change in DITFs that can occur at natural fractures are illustrated in Figure 5.13. Two types of E-DITFs are recognised according to whether they form in planes that are sub-parallel or oblique to the natural fracture. The relative frequency of occurrence of the various possible changes is shown in Figure 5.12b. Terminations of E-DITFs that are sub-parallel to the natural fractures are the most frequent in both wells, accounting for 41%, followed by termination of A-DITFs with 34–37%. Terminations of E-DITFs oblique to the natural fractures are rare. Of the transformations, only A-DITFs to E-DITFs that are sub-parallel to the fracture occur relatively frequently, the other two types being rare or non-existent. These changes

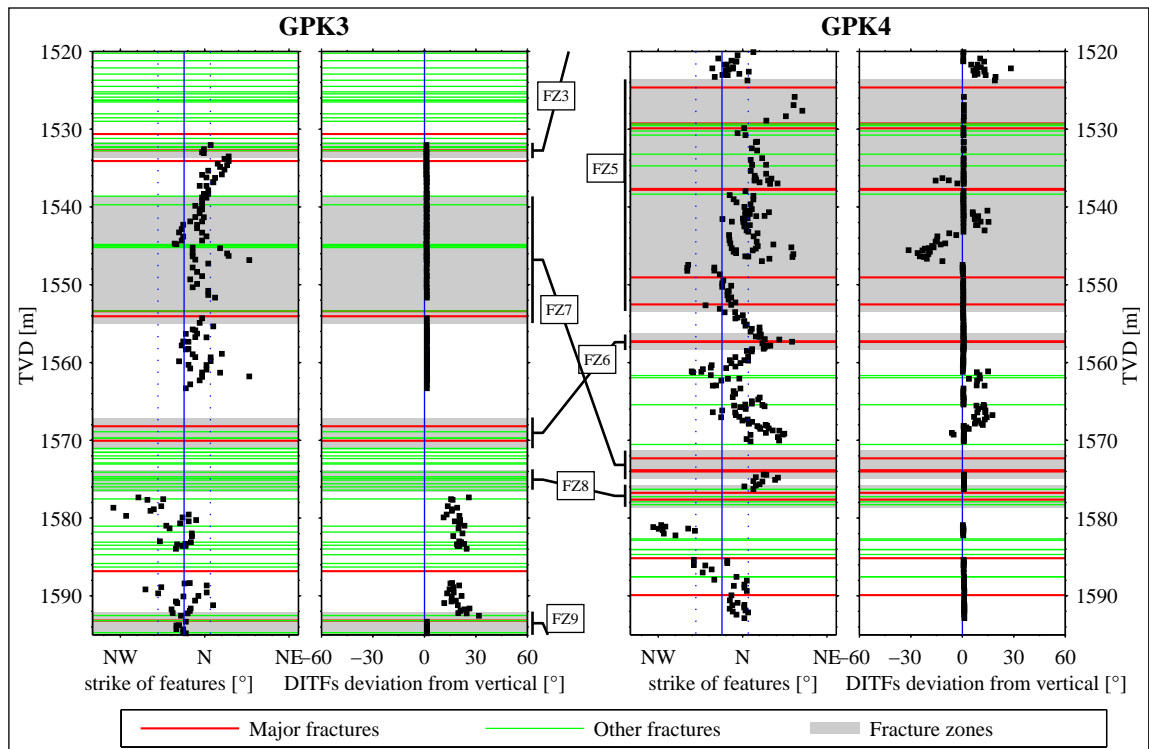


Figure 5.11: Expanded view (1520–1595 m TVD) of the variation of DITF strike and inclination from vertical in the upper granite sections of GPK3 (left) and GPK4 (right) illustrating the character of short wavelength (<50 m) variations. These are essentially uncorrelated between the wells, which are only 20 m apart. Reversals in trend are abrupt and tend to occur at fracture zones, which are indicated.

for the most part indicate discontinuities in stress along the borehole wall that occur at natural fractures. Whilst the well-known tendency for natural fractures to arrest the propagation of tensile fractures might be a factor for some cases of termination, a change in either stress conditions or rock tensile strength on either side of the natural fracture must be present since otherwise DITFs would form on each side because of identical conditions.

5.5.5.2 E-DITFs parallel to natural fractures

A relatively large number of terminations or transformations at natural fractures involve E-DITFs which form in a plane that is sub-parallel to that of a natural fracture. There are also many other instances where E-DITFs form sub-parallel to natural fractures on both sides (these are not counted in the previous section because they do not transform or terminate at the natural fracture). Indeed, natural fractures with

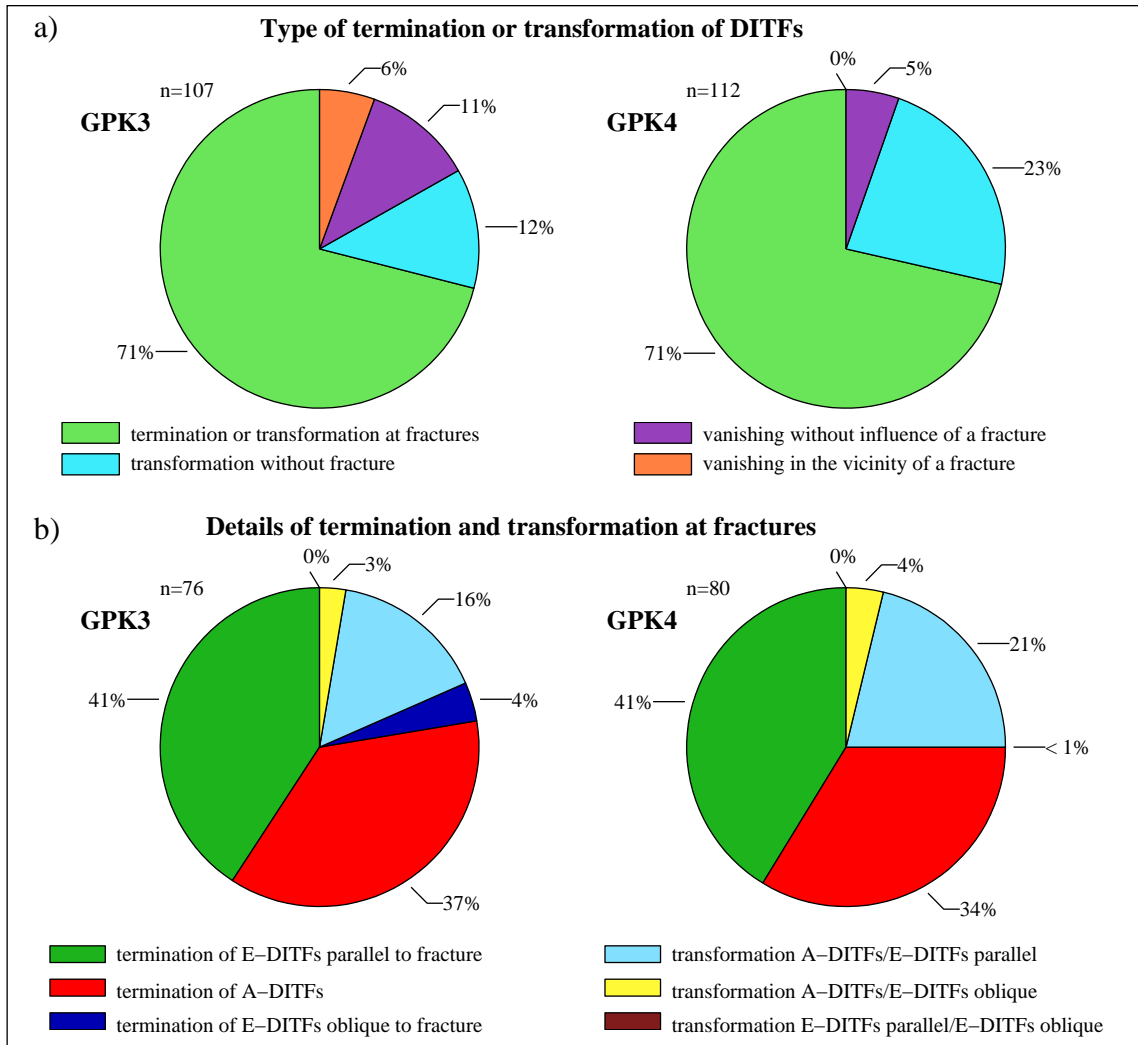


Figure 5.12: Terminations and transformations of DITFs. a) Relative frequency of types of termination or transformation of DITFs with regard to the proximity of natural fractures. b) Detail of the relative frequency of the types of terminations or transformation that occur at natural fractures (see Figure 5.13 for illustrations of the possible types).

sub-parallel E-DITFs on one or both side represent 3.6% (GPK4) to 4.8% (GPK3) of the entire fracture population. The high frequency of occurrence of this special geometry suggests that either a tensile strength anisotropy is present around the natural fractures that favours fracture formation parallel to the natural fracture, or some very specific state of stress exists around the natural fractures.

Considering the tensile strength anisotropy explanation first, it is probable that a microcrack fabric extends some distance away from the fracture damage zone visible

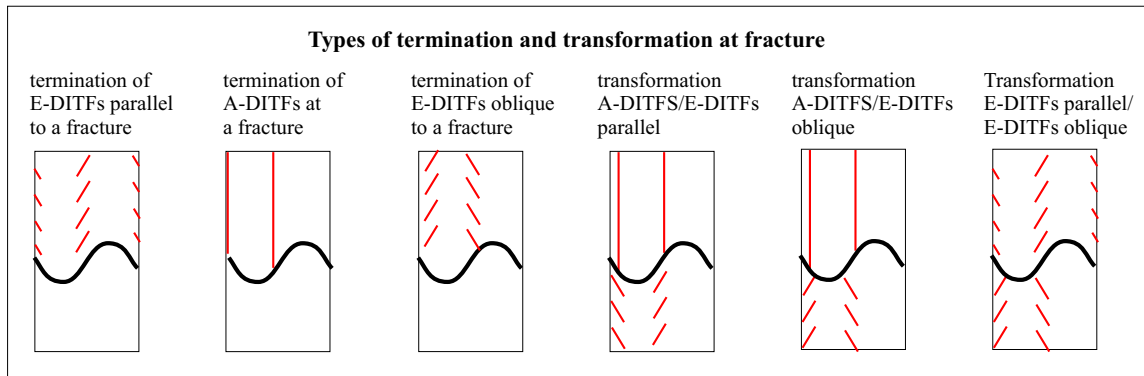


Figure 5.13: Types of terminations or transformation that occur at natural fractures (see Figure 5.12b for relative frequency of occurrence).

on the imaging logs. Such fabrics have been inferred to be present around large-scale *in-situ* faults (Anders and Wiltschko, 1994; Cowie and Scholz, 1992; Vermilye and Scholz, 1998; Wilson *et al.*, 2003) and small scale simulated faults in laboratory experiments on core samples (Stanchits *et al.*, 2006; Thompson *et al.*, 2006). A microcrack population associated with the development in shear of a fracture structure would be expected to form such that the planes of the microcracks lie normal to the local minimal principal stress. As such, the planes of the microcracks would not be aligned with the macroscopic fracture, but would subtend an angle of 20–30° to it. The microcracks would be expected impart a tensile strength anisotropy to some degree. However, it would not favour tensile failure in a plane parallel to the parent structure. Thus, we discount this explanation.

The explanation that the DITFs form sub-parallel to natural fractures because of stress control is examined in Figure 5.14. The natural fracture is assumed to dip at 60° to N90°E, which is typical for fractures that show sub-parallel DITFs at Soultz (Figure 5.16a). The state of stress was taken as given by the linear characterisation for Soultz at a depth of 1900 m, which is within the depth range where DITFs form (see Chapter 4). For convenience, SH_{max} was assumed to be oriented N–S, and thus aligned with the strike of the fracture. Figure 5.14a shows the amount by which the stress tensor must be rotated about the SH_{max} axis to generate a minimum tangent stress at the borehole wall in a direction that lies normal to the plane of the natural fracture. At the depth considered, the minimum tangent stress computed from the equations of Peška and Zoback (1995) is less than -5 MPa, and thus E-DITFs parallel to the fracture would form. The required rotation is 21.9°, implying that the Sh_{min} principal stress axis lies 8.1° from the normal to the natural fracture. The component of shear stress resolved on the natural fracture is $0.07Sv$, significantly less than the value $0.20Sv$ predicted to prevail for the ambient (i.e. linear characterisation) stress state. To completely eliminate the shear stress (i.e. to produce an Sh_{min} orientation

Table 5.2: Relation of the angle between natural fracture and E-DITFs, ϕ , the stress deviation from verticality θ and the shear stress on the fracture, τ for the case presented on Figure 5.14

Sv deviation from vertical θ		0°	2°	4°	6°	8°					
angle natural fracture/E-DITFs ϕ		30°	26.9°	23.9°	20.8°	17.9°					
shear stress on the natural fracture τ [$\cdot Sv$]		0.2	0.19	0.19	0.17	0.16					
θ	10°	12°	14°	16°	18°	20°	22°	24°	26°	28°	30°
ϕ	15°	12.3°	9.6°	7°	4.6°	2.2°	-0.1°	-2.3°	-4.4°	-6.4°	-8.4°
τ	0.15	0.14	0.12	0.11	0.10	0.08	0.06	0.05	0.03	0.02	0.0

normal to the fracture plane) requires an $Shmin$ -axis rotation of 30°, as illustrated in Figure 5.14b. The predicted plane of DITF formation is now no longer precisely parallel to that of the natural fracture but deviates by -8.4° (the negative value indicates the dip of the E-DITF is less than the natural fracture). Thus, sub-parallel E-DITFs indicate low shear stress on the planes of the associated natural fractures, the implied magnitude depending upon their relative dip.

The observed relative dip of the E-DITFs with respect to the natural fractures is shown in Figure 5.15a. The mean relative dip is 0.0° for both GPK3 and 4 with maxima and minima of -8.0° to 9° . The uncertainty of the individual relative dip estimates is $\pm 3.0^\circ$ being composed of the uncertainty in the estimated dips of the natural fractures and E-DITFs of $\pm 0.75^\circ$ and $\pm 2.5^\circ$ respectively. The level of shear stress implied by the observed relative dips is given in Table 5.2. The mean value is $0.07Sv$, corresponding to the case of perfect parallelism, and the extrema are $0.0Sv$ and $0.12Sv$. When the relative uncertainty of the estimates is considered, it is concluded that the shear stress prevailing on natural fractures associated with sub-parallel E-DITFs is low but not zero. The same conclusion holds when relative strike variations are considered. The strikes of natural fracture associated with sub-parallel E-DITFs do not differ greatly from the example considered in Figure 5.14 where the orientation of $SHmax$ was taken parallel to the strike of natural fractures, resulting in zero horizontal shear stress. In general, some horizontal component is expected under the linear characterisation. However, the strike of the E-DITFs are closely parallel to the natural fractures (Figure 5.15b), the mean relative strike being 0.0° and the extremes only -10° and 10° . The uncertainty of the relative strike estimates is $\pm 6^\circ$, being derived from the natural fracture and E-DITF strike estimation uncertainties of $\pm 2.5^\circ$ and $\pm 4.0^\circ$. For convenience of exposition, we will ignore the horizontal component of the shear stress and assume the net in-plane shear stress is dominated by the down-dip component, and hence is governed by the relative dips of the E-DITFs with their natural fractures.

Barton and Zoback (1994) report several examples of faults or fracture zones which show patterns of variation in breakout orientation that are consistent with the

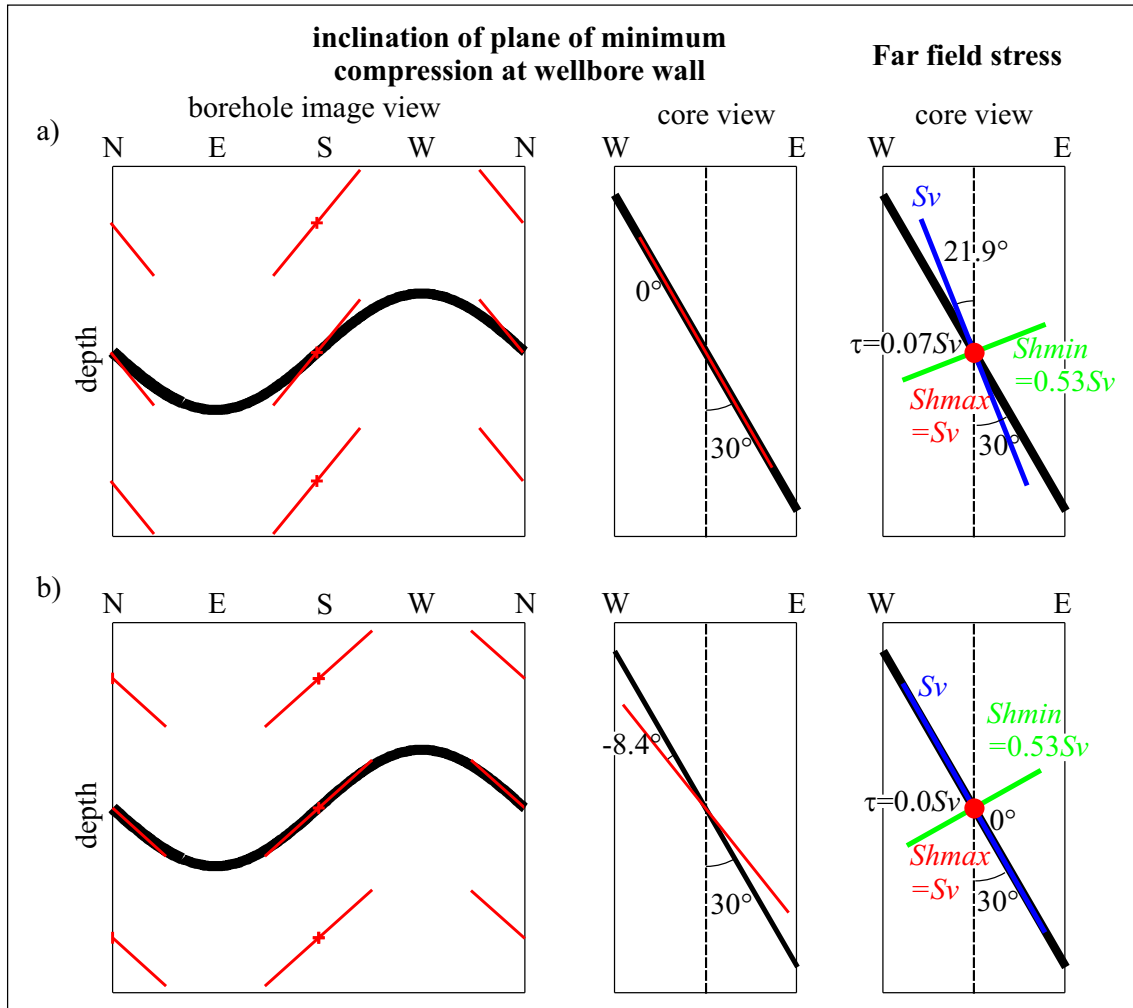


Figure 5.14: Illustration of the perturbation of the local ‘far-field’ stress required to produce E-DITFs that are sub-parallel to a natural fracture that dips at 60° to $N90^\circ E$. For simplicity it is assumed that SH_{max} is N-S and thus parallel to the strike of the natural fracture. The stress state is taken as given by the linear characterisation at a depth of 1900 m TVD. a) Pattern of E-DITFs generated by locally rotating the stress tensor around the SH_{max} axis by 21.9° so that Sv is inclined by this amount. The E-DITFs form precisely parallel to the natural fracture, and the Sh_{min} axis is 8.1° from normal to it, resulting in a resolved shear stress of $0.07Sv$. b) Pattern generated by rotating by 30° so that Sh_{min} is precisely normal to the natural fracture. Thus, the natural fracture supports no shear stress. The E-DITFs now form at a dip that is -8.4° from parallel to the natural fracture (the negative value indicates the dip angle is less than that of the natural fracture).

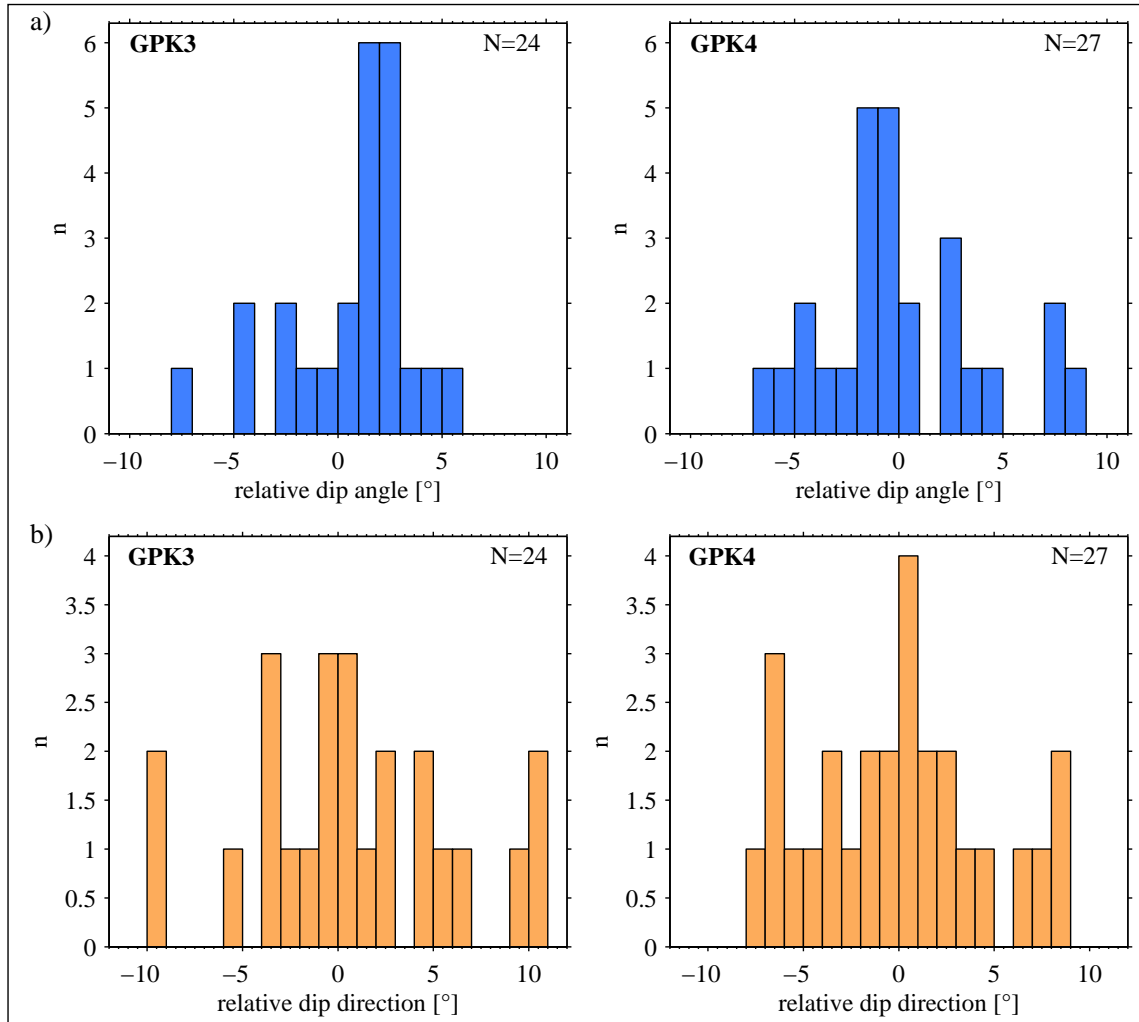


Figure 5.15: a) Histograms of relative dip angles measured between natural fractures and their associated sub-parallel E-DITFs in GPK3 and GPK4. Negative values indicate that the dip of an E-DITF is less than that of the associated natural fracture. b) Same as a) but for dip direction. A positive value indicates the dip direction of the E-DITF is less than that of the natural fracture.

stress perturbations expected from the complete relaxation of the ambient shear stress (i.e. the shear stress resolved on the fault plane under the linear stress characterisation for the site). The examples stem from diverse localities, and were interpreted as indicating near complete stress drop during earthquake faulting. The modelling followed the approach of *Shamir* (1990) which involved many simplifying assumptions, particularly with regard to the problem geometry. It is difficult to place constraints on the conclusion that the shear stress on these faults was strictly zero.

The inferences on shear stress magnitude presented here are relatively direct in comparison to those of *Barton and Zoback* (1994), and indicate low but non-zero shear stress on the fracture zones in GPK3 and 4 which have sub-parallel E-DITFs. For the Soultz wells, such fractures constitute 3.5–5% of all fractures perforated by the wells between approximately 1450 m and 2340 m, the depth range where DITFs form. The orientations of these fractures are shown in Figure 5.16a. All are high-angle, and the vast majority strike within 15° of parallel to the mean SH_{max} direction and dip to the east. They are preferentially type ‘11’, ‘21’, ‘13’ or ‘23’ fractures (see fracture typology of Annex A), indicating their traces were near complete on the UBI reflectivity log. The shear stress resolved on natural fractures with sub-parallel E-DITFs under the linear stress characterisation for the site is shown in the Mohr circle plots in Figure 5.16c. Of these, 83% in GPK3 and 96% in GPK4 are critically-stressed inasmuch as they would fail if their strength was governed by a Coulomb friction law with a coefficient of 0.6. This compares with ~77% for the entire fracture population (Figure 5.16b). The fractures with sub-parallel E-DITFs support shear stress levels ranging from $0.11S_v$ to $0.23S_v$ under the linear characterisation. As noted earlier, this is significantly higher than the mean shear stress of $0.07S_v$ prevailing on the fractures at the time the E-DITFs formed during drilling. Thus, the shear stress levels on these fractures appear to be anomalously low, assuming the dip of the associated sub-parallel E-DITFs is stress-controlled.

In seeking an explanation for the inferred low stress levels on the natural fractures with parallel E-DITFs, it is important to note that there is a large difference between zero shear stress and low shear stress. The complete relaxation of shear stress on a fracture that is initially critically-stressed would seem to implicate either dynamic earthquake faulting with total stress drop (*Barton and Zoback*, 1994) or internal pore pressures that approach the normal total stress acting on the fracture. The mechanics of the latter case has been well-studied in the attempt to explain the apparent low strength of the San Andreas fault (*Zoback et al.*, 1987). To prevent hydrofracture of the external (country) rock around the fault occurring as the internal pore pressure approaches the normal total stress requires very special hydraulic properties for the fault that prohibit the internal fluid pressure leaking into the surrounding medium (*Rice*, 1992). It is doubtful that the inferred, low-shear stress faults at Soultz have such hydraulic properties. Moreover, even if zero shear stress develops on a fracture due to dynamic earthquake faulting or high pore pressures, the events must have occurred sufficiently recently in geological terms so that no subsequent change in

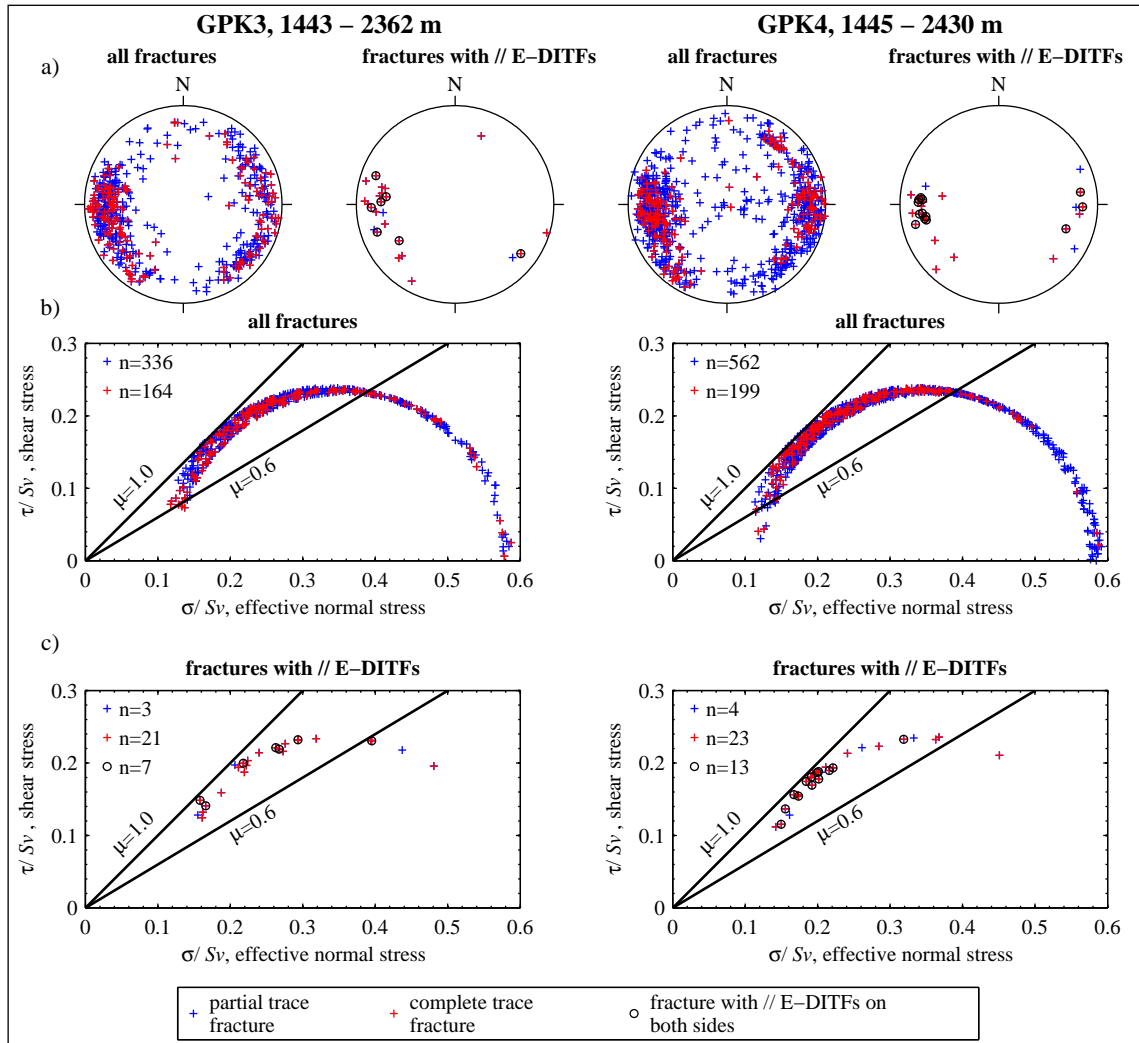


Figure 5.16: a) Comparison of the orientation distribution of all natural fracture in GPK3 and 4 in the depth ranges where DITFs form with the orientation distribution of fractures that are associated with sub-parallel E-DITFs. Fractures that have complete trace on the UBI- reflectivity images are distinguished from those with partial traces. The circles denote natural fractures with parallel E-DITFs on both sides. b) Mohr circle plots for the shear and effective normal stress resolved on all fractures shown in a) assuming the linear stress characterisation given in Chapter 4. c) As b) but for the subset of the fracture population that is associated with sub-parallel E-DITFs.

rock mass stress state occurred that produced a component of shear stress across the fracture in question. The results of this study do not demand consideration of total stress drop fractures. In only two cases were relative dips between E-DITFs and their associated natural fractures found to be -8.0° , the value that implies zero shear stress, and these were extreme values of a distribution, where the uncertainty on the individual estimates of relative dip was $\pm 3^\circ$.

A key question is whether the apparent shear stress reduction was pre-existing, associated with the raising of pore-pressure in the rock mass during stimulation injections, or a consequence of drilling. The observation of E-DITFs sub-parallel to natural fractures on logs run in well GPK1 before any injections had taken place into the rock mass rules out the second hypothesis. That the low shear stress is pre-existing is possible. Consider a rock mass that has passed through several different epochs where the stress state was different (including episodes of burial and erosion). In general, each epoch will host the creation or activation of non-identical fault sets. This evolution will leave the rock mass in a heterogeneous stress state with fractures supporting a wide range of shear stress levels, from 'critical' to zero. The latter case might come about because the shear stress prevailing on the fracture after failure in an earlier epoch becomes superposed during a later epoch with a further shear stress component (perhaps reflecting uniform straining of the rock mass) that is equal and opposite. In other words, the shear-stress path of the fracture through time sums to zero. However, this general scenario cannot explain the clear preference for the E-DITFs to form precisely parallel to the natural fractures they are associated with.

The final possibility we examine is that the shear stress is partly relaxed during drilling. Since DITFs are believed to form shortly after drilling, when the cooling stress is greatest, this hypothesis implies that the partial stress drop occurs on the natural fractures at the moment of drilling. The stress conditions prevailing at the interface between the drill bit and the borehole 'face' are difficult to constrain, although it is possible that the fluid pressure is relatively high at the interface. Above the bit, say one wellbore diameter from the bit, it is likely that wellbore pressure is essentially hydrostatic, as the annulus is large and would not give rise to a significant pressure gradient due to the flow of mud, which was brine. However, at the interface itself it is possible that pressures exceeded hydrostatic, perhaps significantly so since surface pump pressures were typically 20 MPa, although most of this pressure might have been dropped in the drill tubing and the nozzle, as it is commonly assumed (*Mastin*, 1988). If significant overpressures existed at the interface, then these would have pressurised fracture zones when they were penetrated. Critically-stressed fracture zones that are permeable would thus be expected to fail, thereby reducing their shear stress level to equilibrium under the prevailing overpressured conditions. This would lead to the reduction of the shear stress supported by the fracture by an amount set by the overpressure. Given penetration rates of typically 5 m/hour, a thin fracture zone dipping at 65° would remain in contact with the drill bit for some 8 minutes, although whether this has any effect on the stability of a critically-stressed fracture depends

upon the permeability structure of the fracture at the point it is penetrated. A slip zone that is approximately centred on the borehole is expected. This is consistent with the modelling results in Section 5.5.5.3 which indicate that E-DITFs paralleling fractures both above and below imply that the borehole penetrates the fracture near the centre of the slip zone. A corollary of this scenario is that DITFs cannot form within a metre of the drill bit, for otherwise non-parallel DITFs (not necessarily E-DITFs) would form above the fracture before it had been penetrated by the bit and hence before it had slipped and generated the stress perturbation that produces the parallel E-DITFs.

In summary, the dip of the E-DITFs seen to form sub-parallel to many natural fractures is most likely governed by the local inclination of the stress tensor than a rock fabric that favours tensile failure parallel to the fractures. The inferred inclination of the stress tensor suggests that shear stress on the natural fractures is significantly lower than expected under the linear stress characterisation where they would constitute critically-stressed fractures. The origin of the low shear stress may reflect pre-existing stress heterogeneity of the rock mass developed over several stress epochs, or induced failure during the drilling process produced by high wellbore pressure at the drill bit. The former explanation cannot explain the preference for the E-DITFs to form precisely parallel to natural fractures.

5.5.5.3 Stress perturbation around fractures correlated between the wells

The analysis of the natural fractures in the upper part of GPK3 and 4 where borehole separation is less than 20 m led to the identification of 101 fractures that cut both wells (see Chapter 3). Since DITFs occur over this section, it is of interest to examine the types of perturbation these fractures induce in each well to see whether they are consistent or not. The comparison is carried out according to the scheme illustrated in Figure 5.17. Four types of failure state were recognised: parallel E-DITFs, oblique E-DITFs, A-DITFs and no failure. Each type was represented by a number, as shown in Figure 5.17. These numbers provided a convenient way of describing the type of failure seen immediately above and below the fractures, and are denoted by the symbols X and Y respectively in Figure 5.17b. The subscript 1 and 2 denotes the fracture intersections with boreholes GPK3 and GPK4 respectively. It should be noted that ‘no failure’ was included as a failure state because DITFs extend over 56% of the length of GPK3 and 51% of GPK4 for the section in question, and so the presence of a DITF in one of the three forms is more probable than not.

The relative frequency of the four types of failure for the 404 determinations is shown in Figure 5.17c. No failure is seen in 70% of cases, which is higher than expected for the section. E-DITFs that parallel the fractures occur in 16% of cases and A-DITFs account for the remaining 13%. Oblique E-DITFs are not seen, consistent with the general rarity of this type of failure (Figure 5.12b).

The result of simultaneously comparing both upper and lower failure styles in

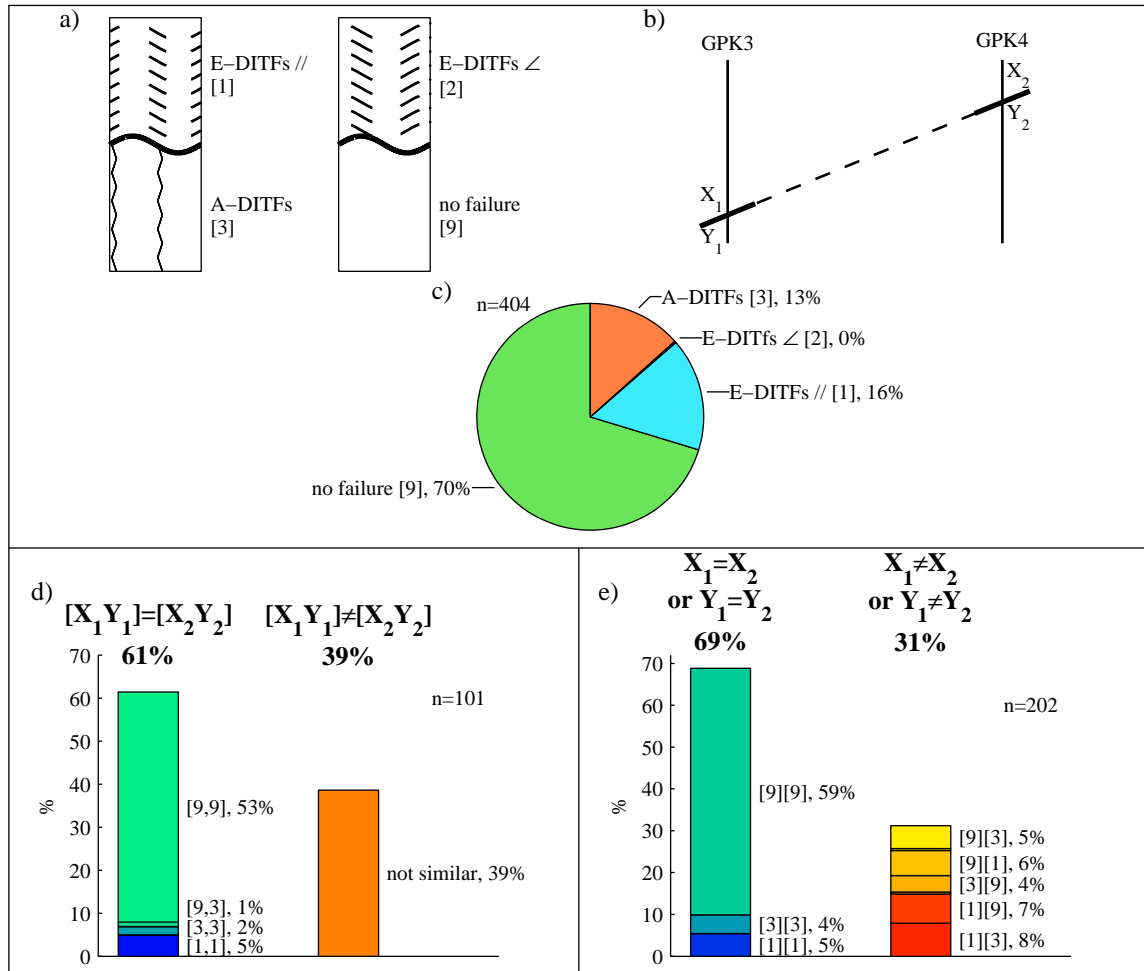


Figure 5.17: Comparison of failure styles about the 101 natural fractures that can be correlated between GPK3 and GPK4. These fractures lie in the borehole sections above 2400 m where the wells are separated by 20 m and tensile failure occurs more often than not. a) Types of failure state and the code number assigned to represent them b) Designation of failure state above (X) and below (Y) each intersecting fracture. The wells GPK3 and 4 are designated by the subscripts '1' and '2'. Thus 'Y₂' denotes the type of failure below the fracture in question in GPK4. c) Relative frequency of the four failure states (there are 101 fractures and thus 404 observations). d) Assessment of whether the fractures have an identical pattern of failure between wells. The combination of failure types above and below the fracture intersections is denoted by the code [X,Y], where X and Y are the code numbers given in a). e) Comparison of the types of failure above and below the intersections considered independently. The observed combinations are denoted by [X₁][X₂] and [Y₁][Y₂] for the upper and lower pairs respectively.

the two wells is shown in Figure 5.17d. Some 61% of the 101 fracture intersections have identical failure patterns in each well, with 'no failure' both above and below accounting for 53%. E-DITFs parallel to the fracture and A-DITFs both above and below add a further 5% and 2% respectively, whilst only one change in style, the termination of an axial fracture, is seen in both wells.

The result of considering the match between the upper and lower failure styles independent of each other is shown in Figure 5.17e. Some 69% of the 202 pairs are seen to have the same failure style, with 'no failure' accounting for 60%, and A-DITFs and E-DITFs parallel to the fracture a further 4–5% each. 31% were mismatches.

The results indicate that the failure style at the wellbore intersections of the fractures that can be correlated between wells has a higher fraction of 'no failure' than might be expected from the relative frequency of DITFs over the ~ 1900 m borehole section analysed. This suggests that at least some of these matches reflect similar stress perturbations around the fractures in both wells, perturbations that suppress DITF formation. What can be concluded is that, apart from intersections that show no failure, the match in the pattern of failure between the wells is rather poor.

To evaluate why the correlation was not better than observed, the stress field generated by slip on a 2-D fracture was examined using a 2D FEM code 'phase2' (*Rocsience Inc.*, 2005). The model is shown in Figure 5.18, and features a 20 m long fracture dipping at 60° to $N85^\circ E$, characteristic of many of those found above 2500 m at Soultz. The initial stress conditions were taken as those predicted at 2000 m at Soultz from the linear characterisation (i.e. $S_v = SH_{max} = 49.7$ MPa, $Sh_{min} = 26.4$ MPa, $P_p = 20.5$ MPa). Thus, the model lies in the S_v – Sh_{min} plane. Zero-displacement model boundaries were taken at ± 50 m, and the Young's modulus and Poisson's ratio taken as 54 GPa and 0.225 respectively. The stress perturbation on the fracture was generated by reducing its shear strength to that given by a Coulomb friction criterion with a coefficient of 0.31. This led to a uniform reduction in shear stress on the fracture from 11.5 MPa to 3.5 MPa. The perturbation is thus appropriate for a uniform stress drop on the fracture of 8.0 MPa, the maximum slip being 4.1 mm. The variations of the orientation and magnitude of the total principal stresses are shown by the crosses in Figure 5.18. It is evident that significant changes in the stress state occur both down-dip and across the fracture. The stress perturbation is anti-symmetric about the vertical line passing through the centre point of the fracture.

To evaluate the effect these changes would have on wellbore failure, vertical profiles of stress were taken along the four lines indicated in Figure 5.18, and the pattern of wellbore failure expected in boreholes drilled along those lines computed. The low shear strength of the fault of $\mu = 0.31$ was chosen so that the shear stress on the fracture after failure would be 3.5 MPa (or $0.07S_v$), the value needed to generate E-DITFs that are sub-parallel to the fracture. The resulting profiles are shown in Figures 5.19 and 5.20. Profile (a) intersects the fracture at its centre. E-DITFs that are sub-parallel to the fracture occur both above and below. Profile (b)

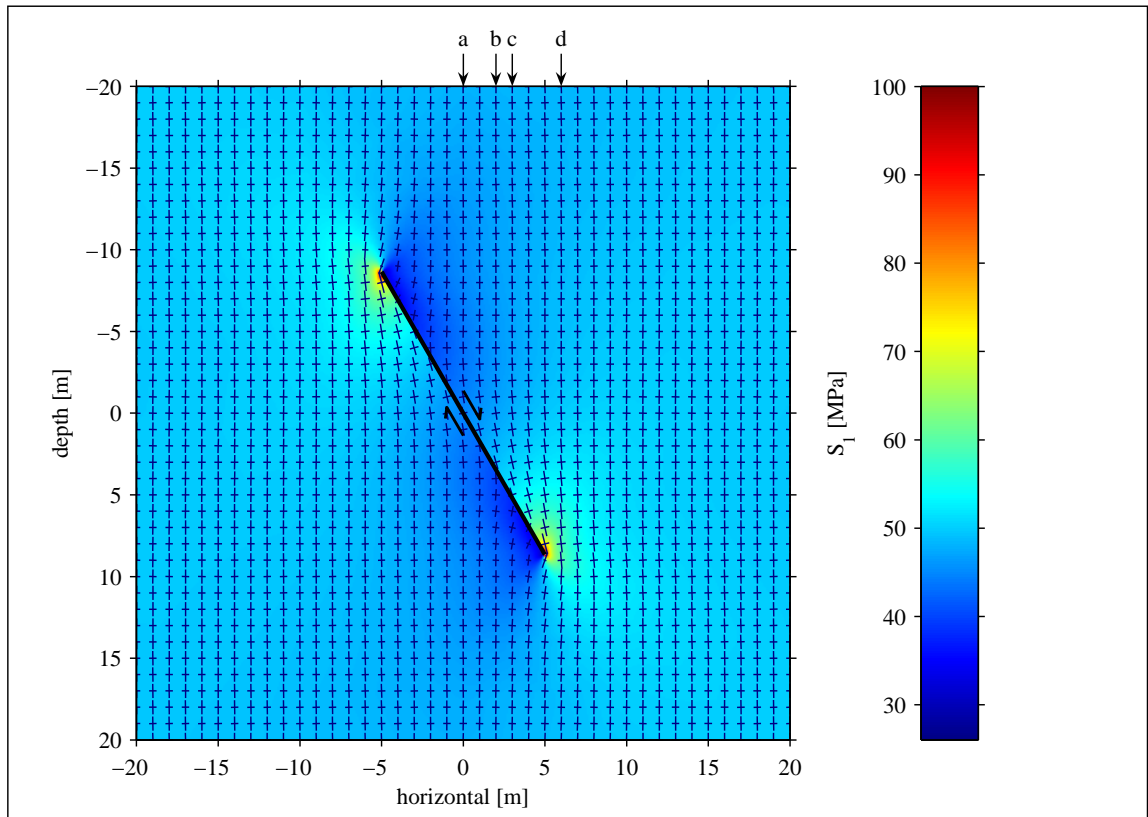


Figure 5.18: Stress perturbation around a fault that has slipped with uniform shear stress drop computed using the 2D FEM code ‘phase2’ (*Rocscience Inc.*, 2005). The fracture is 20 m long and dips at 60° in the Sh_{min} direction. The initial conditions are the stress level which prevail at 2 km at Soultz-sous-Forêts. The magnitude and direction of the perturbed principal stresses are shown by the crosses, and the colour scale denotes the magnitude of the maximum principal stress. The label a to d indicate the location of the vertical profiles of borehole failure shown in Figure 5.19 and 5.20.

intersects the fracture 4 m down-dip from the centre, corresponding to 20% of the fracture length. A significantly different pattern of failure is seen below the fracture, the E-DITFs being initially sub-parallel to the fracture but rotating anti-clockwise rapidly as one moves downhole. At profile (c), which intersects the fracture 6 m from the centre, the E-DITFs below the intersection are no longer parallel. Profile (d) does not intersect the fracture at all but passes close to the tip. It is evident from profiles (a)–(c) that radically different failure patterns are seen, depending upon the distance of the intersection point from the fracture centre. This suggests that similar patterns of failure would be seen in two boreholes only if they penetrate the fracture

at points that are close in comparison to the fracture length. For fractures dipping at 60° , and borehole separations of 20 m, significant variation in the patterns of failure can be expected for fractures whose down-dip extent is less than several hundred metres. Another result of note is that fracture-parallel E-DITFs occur on both sides of the fracture only if the borehole penetrates near the centre of the fracture. There are many observations in the wells of patterns similar to profile (a). Thus, if the modelling results are accepted, the borehole would intersect the fractures near the centre of the slip zone that generates the stress perturbation. This would favour the hypothesis that the slip took place as a result of pore-pressure elevation as the drill bit penetrates the fracture.

5.6 Stress-perturbing fractures

The preceding sections have served to establish the association of stress perturbations with natural fractures. In all, 144 fractures natural fractures in GPK4 could be identified as being associated with a stress perturbation through one of the following ways:

1. Orientation of induced failure (breakouts or DITFs) is modified in the vicinity of such fractures.
2. Induced failure stops on one side or the other of such fractures.
3. Induced failure changes form (i.e. A-DITFs to E-DITFs) in the vicinity of such fractures.
4. Induced failure is interrupted (i.e. no failure) in the vicinity of such fractures.

The 144 stress-perturbing fractures most surely underestimate the total number of stress-perturbing fractures since there are possibly many others that occur in regions of the borehole where conditions of wellbore failure were not met and thus there is no stress indicator generated in their vicinity. The distribution of the orientations of these fractures is shown in Figure 5.21a, together with the orientation distribution of all 2215 fractures identified in GPK4. The orientations of stress-perturbing fractures are more closely distributed than the latter, and fall into two major families (272/78 and 080/66), which are also the dominant orientations for the complete dataset.

The effective normal and shear stress resolved on the stress-perturbing and complete fracture datasets under the linear stress characterisation with ambient pore pressure are shown in the Mohr circle plots of Figure 5.21. All stresses have been normalised by the vertical stress, S_v . Evidently, almost all of the stress-perturbing fractures are critically-stressed in the sense that failure would occur of their strength were described by a Coulomb friction criterion with the coefficient of 0.6 (e.g. *Barton et al.*, 1995; *Evans*, 2005; *Ito and Zoback Mark*, 2000; *Zhang et al.*, 2002). As such,

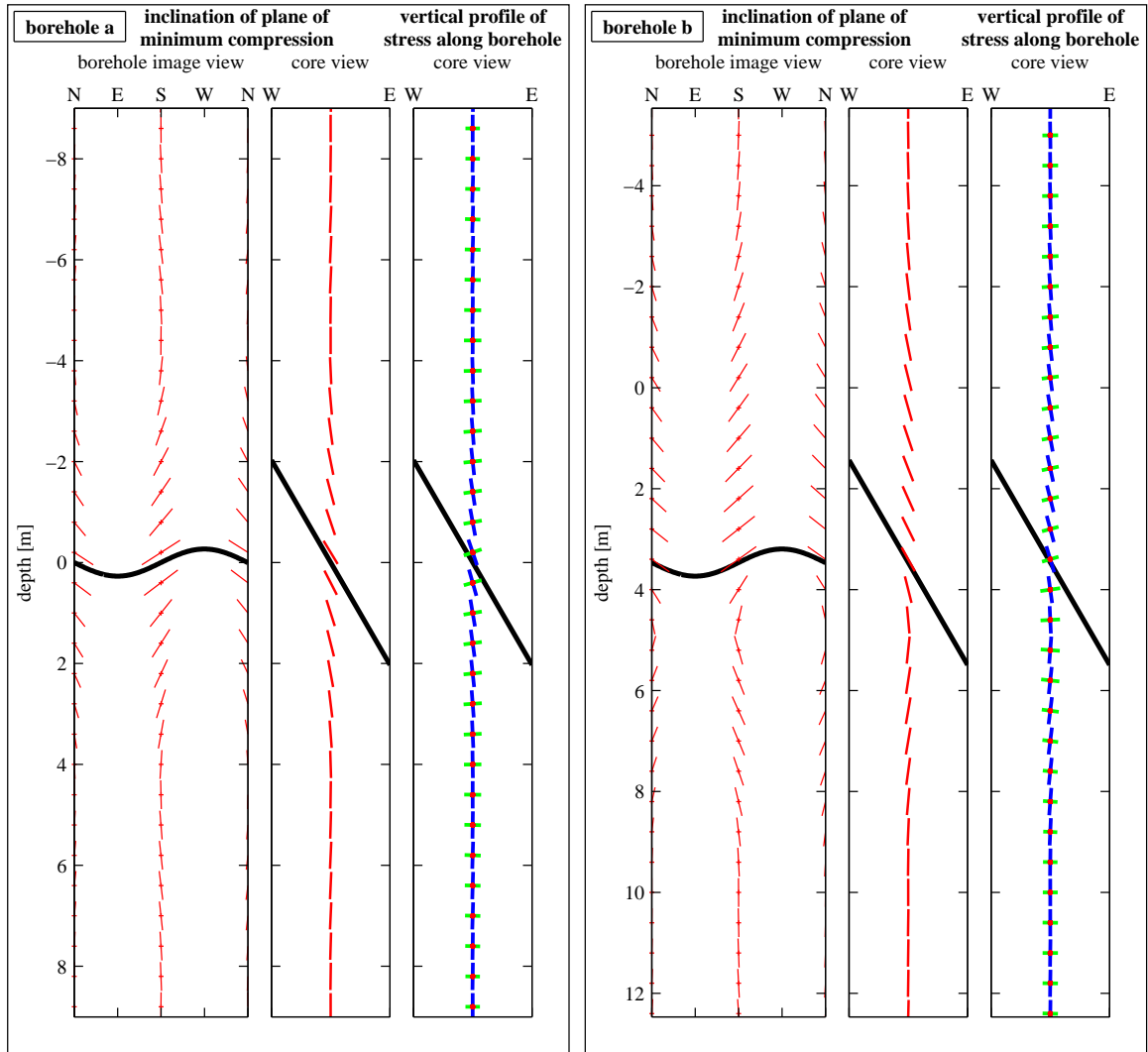


Figure 5.19: Two vertical profiles of borehole failure that intersect the fracture at the points shown in Figure 5.18. The unwrapped view of failure as seen in fracture imaging logs is shown at left in each frame. It is evident that the pattern of failure at the fracture intersection changes strongly along the fracture. (a) Profile intersects the fracture at its centre. b) Intersection 4 m from fracture centre (i.e. 20% of fracture length). c) Intersection 6 m from fracture centre. d) Profile passes 2 m beyond fracture tip measured along dip. See Figure 5.18 for profile locations.

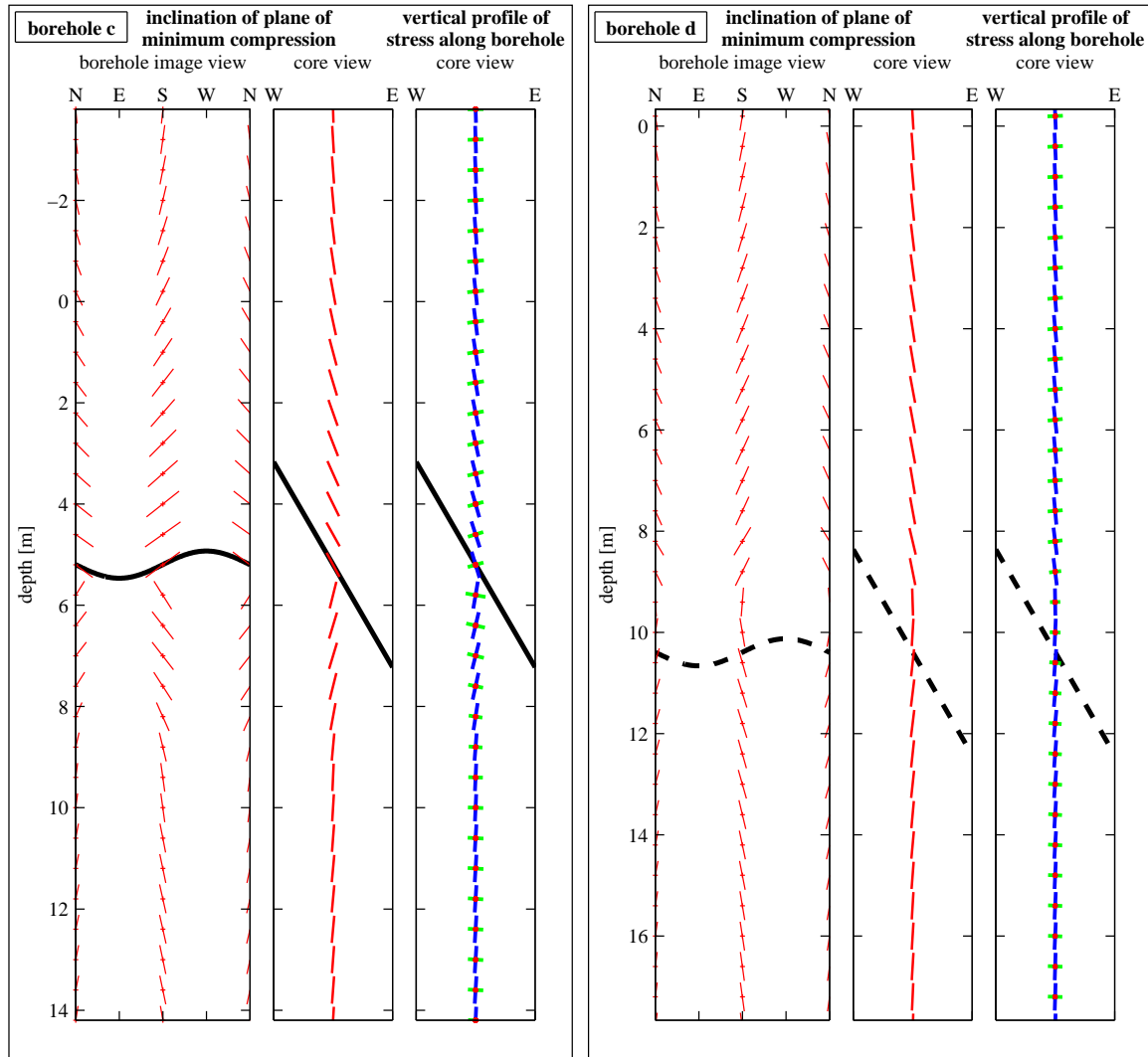


Figure 5.20: Idem than Figure 5.19 but for profile (c) intersecting 6 m from fracture centre and profile (d) passing 2 m beyond fracture tip measured along dip.

these fractures would be verging on failure under the simplified, linear representation of the prevailing stress field. The failure of these fractures will induce a stress perturbation, and thus the stress supported by these fractures will be modified from the values shown in Figure 5.21. The shear stress level supported by the fracture will be reduced, and this is particularly significant for fractures associated with sub-parallel E-DITFs. So it is possible that the perturbations in part reflect relatively recent failure associated with the on-going accommodation of crustal deformation (*Zoback and Townend, 2001*). However, it is also possible that they reflect failure that predates

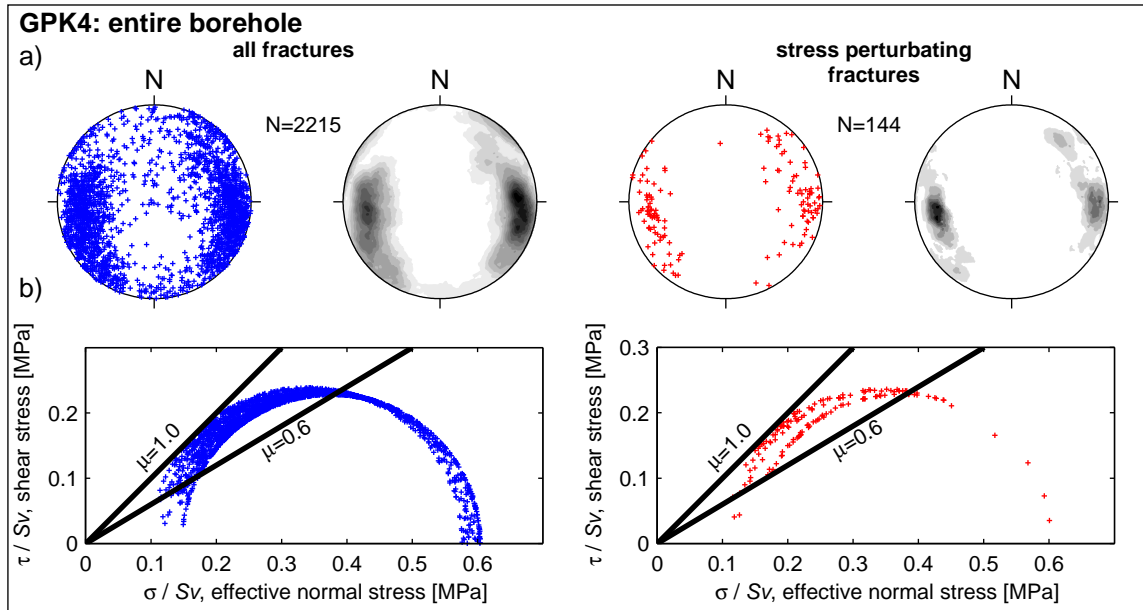


Figure 5.21: a) Stereographic plot of poles to all natural fractures identified in GPK4 (left) and the subset that were associated with stress perturbations (right). b) Mohr circle plots of the shear and effective normal stresses resolved on fracture sets in a). The stress was taken as given by the linear characterization for Soultz and the pore pressure as ambient.

the contemporary stress situation.

5.7 Conclusions

Variations in the orientation of breakouts and DITFs about the mean orientations have been analyzed to investigate stress heterogeneity along the trajectory of the 5 km deep boreholes GPK3 and GPK4 at the Soultz site. The results suggest:

1. Variations in the stress orientation indicators occur at all scales amenable to analysis. Power spectra of the variations indicate power law behaviour between wavelengths 4 and 80 m, with slopes close to -2 , indicative of self-affine behaviour. This indicates the relative amplitude of the variations with respect to wavelength decreases with larger scale.
2. The two most prominent large scale variations in horizontal principal stress orientation with wavelengths in excess of 100 m coincide with the two most significant fracture zones intersected by the wells. One of these occurs near 2000 m where the wells are only 20 m apart. Despite this lateral proximity, the large-scale variation is only partly correlated between wells, suggesting the

presence of high lateral gradients in stress associated with the causal fracture zone.

3. Short-wavelength (<50m) variations in stress orientation with deviations from the mean of up to 90° occur frequently and are generally associated with natural fractures. Changes in stress across natural fractures are also indicated by coincident termination and transformation of DITFs from one form to another. Such variations are not usually correlated between wells in the section above 2000 m where the holes are 20 m apart. This suggests that fractures are for the most part not much larger than 40 m. This is in agreement with the study of fracture size at Soultz presented in Chapter 3.
4. Many E-DITFs are seen to be sub-parallel to natural fractures. This geometry is most likely governed by the local inclination of the stress tensor than a rock fabric that favours tensile failure parallel to the fractures. The inferred inclination of the stress tensor suggests that shear stress on the natural fractures is significantly lower than expected under the linear stress characterisation where they would constitute critically-stressed fractures. The origin of the low shear stress may reflect pre-existing stress heterogeneity of the rock mass developed over several stress epochs, or induced failure during the drilling process produced by high wellbore pressure at the drill bit. The former explanation cannot explain the preference for the E-DITFs to form precisely parallel to natural fractures.
5. Almost all of the fractures which are associated with stress perturbations are critically stressed under the large-scale linear stress characterisation of the site. Thus, it is possible that they failed and generated the stress perturbations relatively recently, reflecting accommodation of on-going tectonic deformation of the crust. However, the data do not require this, and it is just as likely that the slip that generated the stress perturbations is much older.

6 Conclusions and outlook

IN order to design and proceed to the development of an engineered geothermal reservoir, knowledge about the natural structures which cross it and a characterisation of the stress state which prevails at the reservoir depth are necessary. The analysis of borehole images permits us to address these two aspects: the natural fractures can be mapped to obtain a description of the structures at the reservoir depth, and the stress induced wellbore failures can be used as indicators for the current stress state at depth.

In this study, the borehole images from the 5 km deep boreholes of the Soultz-sous-Forêts geothermal project have been analysed. The two most recent boreholes of the project, GPK3 and GPK4, have been imaged using an ultrasonic borehole televiewer from Schlumberger (UBI) for the entire granitic section, i.e. from 1.4 to 5 km depth, providing data over more than 7 km. The boreholes have been drilled from the same pad and deviated in order to build up a borehole spacing of about 700 m at 5 km depth. These particular borehole trajectories are interesting for our analysis because the boreholes are separated by only about 20 m between the basement top and to a depth of 2.5 km. Below 2.5 km, the distance increases, reaching about 700 m toward holes' bottoms. This configuration permits us to perform cross-correlation between the boreholes and to study variations of stress orientation occurring at various scales. Indeed, one challenge in reservoir characterisation from borehole data is interpreting data collected at the borehole scale, i.e. over a borehole perimeter of about 1 m, and to extract from it relevant information at the scale of the reservoir, i.e. up to approximately 2 km.

Also, in order to optimise geothermal reservoir development, one needs to acquire quantitative information on various rock mass characteristics. In this thesis, a particular effort has been made in bringing quantitative constraints on the physical quantities analysed. The favourable borehole trajectories have been used to quantify the size (length, spacing,...) of the natural structures. The repartition of the wellbore failure has been used to put bounds on the principal stress magnitudes. However, often in natural sciences, knowledge about the variability of a physical quantity is as important as knowing its mean value. Here again, we took advantage of the favourable borehole trajectories to assess the variations that take place at the scale of the reservoir.

The following section summarizes the main findings presented in Chapter 3 (natural fracturing), Chapter 4 (stress characterisation) and Chapter 5 (stress heterogeneities).

6.1 Multi-scale fracturing from borehole images analyses

Natural fracturing occurs at all scales. Our investigation methods are well adapted for characterising fracturing occurring at metre scale (borehole imagery) and at plurikilometric to tens of kilometer scale (geological mapping, tectonic analysis, surface seismic). However our ability to recognise structures at the reservoir scale is limited. We used the favourable borehole trajectories and developed innovative methodology based on cross hole correlations in order to quantify the fracture size and to characterise structures at the reservoir scale.

We first performed a detailed analysis of fracturing at the borehole scale. Four major sets of fractures were present with the following mean orientations: Set 1: 272/68; Set 2: 084/63; Set 3: 219/88; and Set 4: 320/82. The same dominant orientations were also found at the graben scale. 60% of the fractures are in Set 1 and 2; these sets have the typical N–S orientation described as Rhenish orientation. Set 3 and 4 contain 30% of the fractures. East dipping fractures are more present in the upper part of the basement and West dipping fractures dominate at 5 km depth. Mean fracture length and spacing have been quantified to take the following value: 15 to 40 m for mean fracture length and 1 to 6 m for fracture mean spacing. Spacing distributions follow a log normal law but this probably reflects a sampling bias on an original power law distribution.

Natural fractures form clusters that we call fracture zones. Borehole cross correlations were used to describe their internal architecture: they are built by an anastomosed network of fractures delimiting shear lenses. Major variations in thickness and architecture have been observed over distances of 10 to 20 m. The spacing of these fracture zones is evaluated to be in the range of 40 to 400 m. Their mean size cannot be determined with our data. We estimate it to be about 50 to 500 m long, but this should be quantified using other methods, for example microseismic monitoring or vertical seismic profiling. Their orientations include the four major directions seen at borehole scale as well as at graben scale.

East dipping fracture zones dominate in the upper part of the granite while west dipping fractures zones are predominant at 5 km depth. A possible explanation for this change of dominant orientation with depth is presented on the conceptual cross section of Figure 6.1. In the Soultz area, major faults have antithetic orientations relative to the western border fault, i.e. they dip to the west. The Soultz boreholes cut one of these major faults, called the Hermerswiller-Soultz fault, within the sedimentary cover. If we make the assumption that the fracture zones are themselves antithetic to the major faults, they will be east dipping and the Soultz borehole will be in their influence below the Hermerswiller-Soultz fault at basement top. However, due to the spacing of the major faults, at a 5 km depth, the Soultz borehole may be again in the influence of a west dipping major fault, which will explain the dominance of west

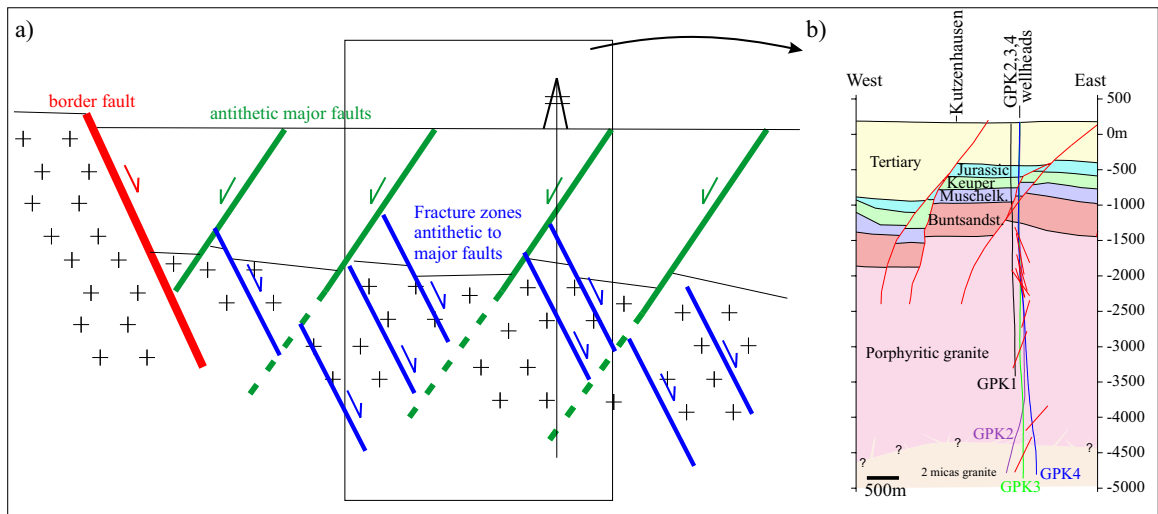


Figure 6.1: a) Conceptual general organisation of fault in the Western part of the URG close to Soultz-sous-Forêts. The frame approximately localises the cross section on b). b) W–E geological cross section going through GPK2-3-4 wellhead including the major faults mapped in the sedimentary section as well as the flowing fracture zones (see also Figure 3.15)

dipping structures at that depth.

In the development of the geothermal reservoir, the fracture zones are believed to be the most relevant structures. Indeed, their size and spacing are such that these zones could form the flow path within the heat exchanger that we try to build. Also, petrological studies of these zones have shown that these zones were or are still the natural path where hydrothermal fluids circulate (e.g. *Genter et al.*, 2000). Permeability creation and enhancement during massive injection of water was also found to be limited to these hydrothermally altered fractures zones (*Evans et al.*, 2005a).

6.2 Stress characterisation

The main result of this work for the Soultz project is the derivation of a complete and robust stress characterisation for the reservoir down to 5 km depth. The obtained stress characterisation is presented in Figure 6.2.

Analysis of wellbore failure observations allows the principal stress orientations to be determined. Axial and en echelon drilling induced tension fractures (DITFs) were the most valuable indicators because they permit the assessment of deviations from verticality of one principal stress, and they give a more precise indication of the local orientation of the maximum principal horizontal stress than do breakouts.

At Soultz, the presence of an echelon drilling induced tension fractures along vertical borehole section indicates local deviation of one principal stress from verticality. However, on average, the DITFs are vertical, suggesting that one principal stress can be considered to be vertical. The orientation of the maximal horizontal stress direction was estimated from the azimuthal distributions of breakouts and axial drilling induced tension fractures to be $N169^\circ \pm 14^\circ$.

As one principal stress is generally vertical, its magnitude can be computed by compiling rock density profile and integrating it. A careful analysis of the uncertainty of the density of the sedimentary units was conducted to derive realistic error bars on the vertical stress profile (see Equation 4.2).

The profile of minimum horizontal principal stress magnitude is obtained by combining existing point determinations above 3.5 km (*Bérard and Cornet, 2003*) with estimates obtained at the depth of the casing shoes of the three wells from the maximum pressures attained during massive fluid injections. This approach assumes that the jacking pressure is reached during the injections, for which we present evidence, and has advantage over small-volume injections in that the rock volume involved is large and the resulting estimate of Sh_{min} is less subjected to local heterogeneities. The resulting minimal horizontal stress magnitude profile is given in Equation 4.3

The most difficult parameter to constrain is the magnitude of the maximum horizontal stress. Our approach is to derive constraints on the value SH_{max} at each depth by considering whether tensile (i.e. DITF) or compressive (i.e. breakouts) failure occurs. While the estimates obtained are not precise, being upper and lower bounds, they are in our opinion more robust than other methods based on the analysis of breakout width (*Barton and Zoback, 1988*). Our analysis includes thermal stresses induced by the cooling of the wellbore walls during drilling. For the DITFs, this calls for the estimation of the coolest temperature the rock has seen during drilling, which we take to be the temperature at the drill bit. This profile is estimated from measurement while drilling or MWD data (i.e. temperature recorded at drill bit during drilling). For the breakouts, the relevant temperature profile is that which exists at the time the breakouts were imaged. This was obtained from temperature sensors on board the imaging sonde. The constraints imposed on the profile of SH_{max} are shown in Figure 6.2 and are not very tight. They are consistent with what remains the best working hypothesis for SH_{max} : that its magnitude is nearly equal to the magnitude of the vertical stress, as suggested by the observation that both strike-slip and normal faulting earthquake occurs within the rock mass during stimulation. The utility of the present study is to quantify the allowable deviations from that equality. The bounds imposed on the magnitude of the maximal horizontal stress are given in Equation 4.9.

A corollary of the analysis of DITF formation concerns the effective stress law for the formation of tensile fractures at the wellbore wall. Our analyses show that the coefficient in the effective stress law for tensile failure cannot be equal to 1, but has to be equal or less than 0.8.

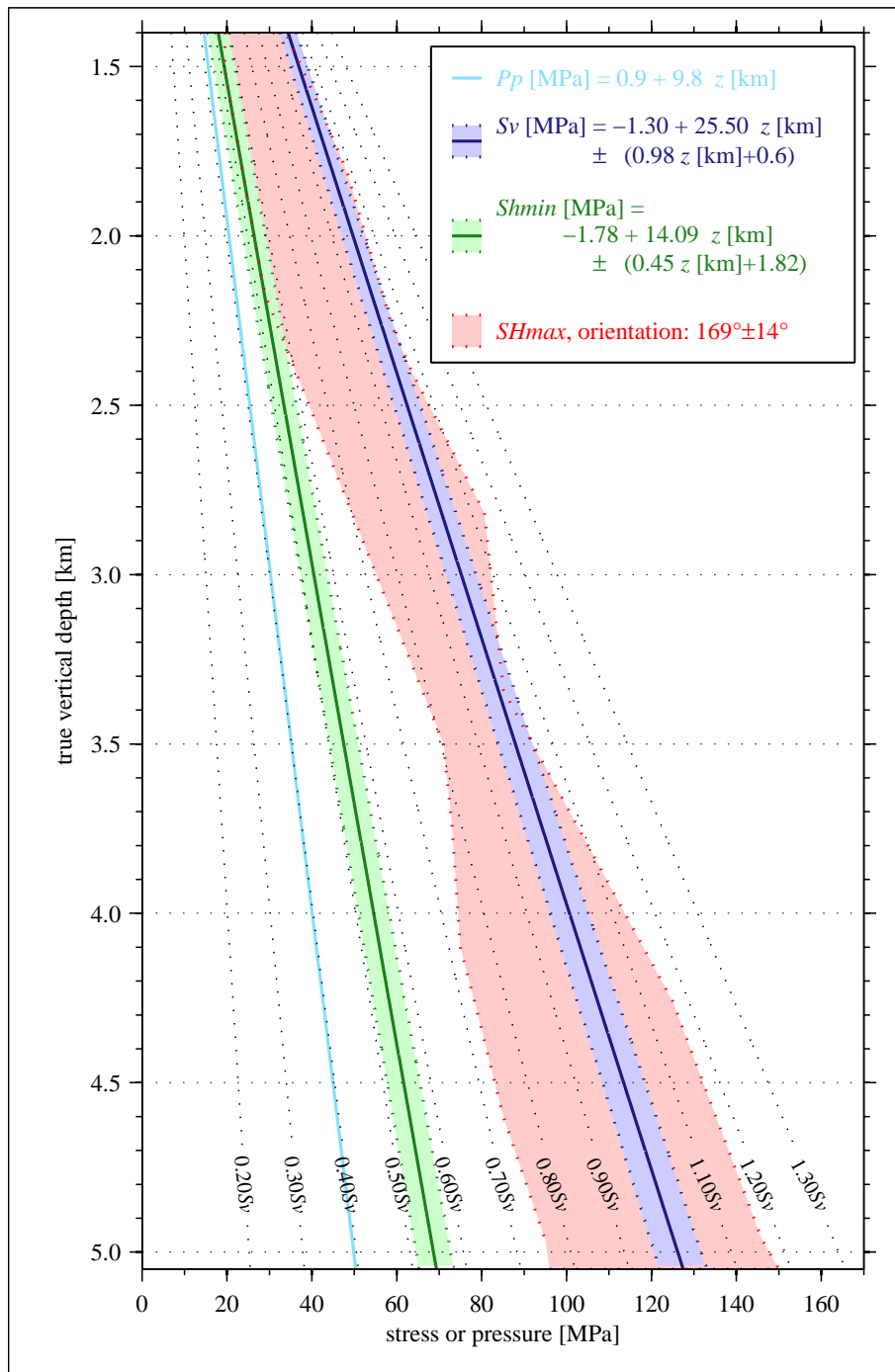


Figure 6.2: Stress characterisation at Soultz-sous-Forêts. The natural formation pressure P_p is from *Evans et al.* (1992). The vertical stress profile S_v is computed by integrating the overburden (see Figure 4.6). The minimum horizontal stress magnitude Sh_{min} is evaluated by analysing pressure at casing shoe during massive fluid injections (see Figure 4.7). The maximum horizontal stress magnitude SH_{max} is constrained by the analysis of the presence or absence of compressive and tensile failure of the wellbore (see Figure 4.9).

The map of Figure 6.3 compares the SH_{max} orientation at Soultz with that obtained from the wellbore failure analysis of other deep wells in (mostly) crystalline rock in Western Europe. At all locations, the azimuth of SH_{max} falls in the NW quadrant. *Cornet et al.* (2007) note that the three data points at Soultz, Urach and KTB, which are all located significantly north the Alpine front, present a NNW–SSE orientation, and they propose that this orientation characterises the stress orientation at depth in Central Europe. However, an equally reasonable interpretation of the collective data is that the orientation of SH_{max} for Western Europe is in general NW–SE to NNW–SSE, with local variations reflecting stress heterogeneity (see Chapter 5) due to local structures (faults).

6.3 Stress heterogeneities

The detailed analysis of wellbore failure reveals significant local deviations from the depth-averaged constant SH_{max} orientation found to apply to the wellbore failure observations in the Soultz wells (Chapter 4). These deviations reflect stress heterogeneity, which is believed to play an important role in earthquake complexity, discrepancies in stress estimates obtained from inversion of earthquake focal mechanism solutions, and reservoir stimulation processes. However, there is few opportunities to identify or quantify such stress heterogeneities in situ. The borehole image data set of Soultz provides an excellent opportunity to examine this heterogeneity through its expression in the variation of SH_{max} orientation, both vertically along the wells, but also laterally between the wells where that are only several tens of metres apart.

Spectral analyses of the SH_{max} orientation variations along the wells show that they follow a power law with a slope close to -2 between wavelengths of 4 to 80 m. This self-affine behaviour indicates that the relative amplitude of the variations with respect to wavelength decreases with larger scale, as must be the case with circular data to avoid cork screw variations.

The large scale variations (i.e. >50 m) are generally associated with fracture zones. The two most prominent large scale variations in horizontal principal stress orientations with wavelengths in excess of 100 m coincide with the two most significant fracture zones intersected by the wells. One of these occurs near 2000 m, where the wells are only 20 m apart. Despite this lateral proximity, the large-scale variation is only partly correlated between wells, indicating the presence of high lateral gradients in stress, associated with the causal fracture zone.

The shortwave length variations (<50 m) are generally not well correlated between the wells but are clearly systematically related with natural fractures. The match in the pattern of failure around fractures that are correlated between the well is rather poor. This suggests that fractures are for the most part not much larger than 40 m, a result in agreement with the conclusions of the study of fracture size at Soultz presented in Chapter 3.

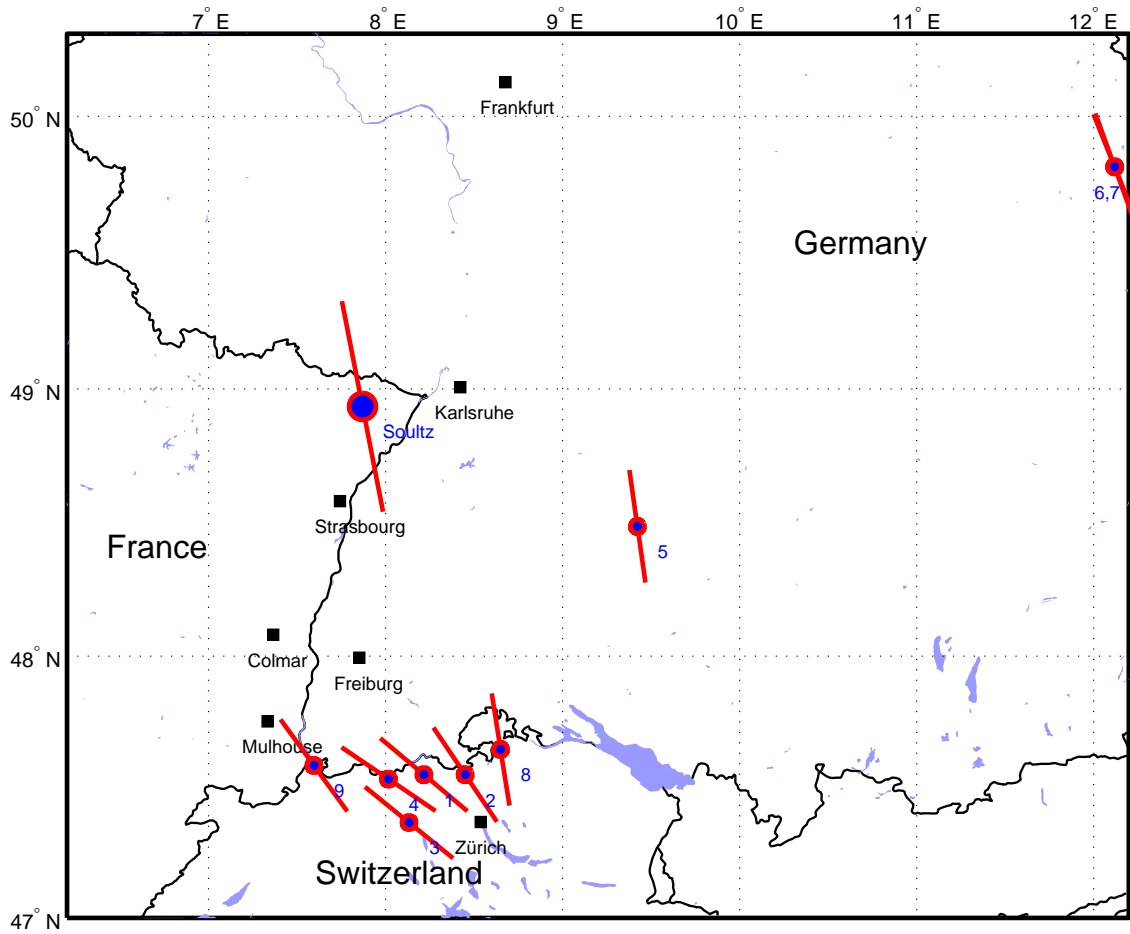


Figure 6.3: Maximum horizontal stress orientations obtained from wellbore failure analysis of deep boreholes in central Europe. 1. Boettstein; 2. Weiach; 3. Schafisheim; 4. Kaisten; 5. Urach (*Blüming, 1986*); 6,7. KTB pilot and main hole (*Brudy and Zoback, 1999*); 8. Benken (*Deichmann et al., 2000*); 9. Basel (*Valley and Evans, 2006c*).

Many en-echelon DITFs are seen to be sub-parallel to natural fractures, an observation that is not unique to Soultz. Since E-DITFs form during drilling, most likely near the drill bit where cooling is greatest, the parallelism suggests that the shear stress on the natural fractures is significantly lower than expected under the linear stress characterisation, which is near critical stress levels for most fractures. In all, 3.6% to 4.8% of the natural fractures are surrounded by parallel en echelon drilling induced tension fractures (E-DITFs). The origin of the low shear stress may reflect pre-existing stress heterogeneity of the rock mass developed over several stress epochs, or failure induced during the drilling process, produced by high wellbore pressures at the drill bit. The former explanation would more likely give rise to a

range of prevailing shear stress levels on the natural fracture population, rather than the strong preponderance of low shear stress levels suggested by the sub-parallelism. Thus, the best explanation is that the natural fractures fail during drilling, but before the E-DITFs form. Since the latter probably develop near the bit where cooling is strongest, this suggests the natural fractures with sub-parallel E-DITFs failed during drilling itself, perhaps in response to elevated wellbore pressure at the nozzle of the drill bit.

Almost all of the fractures associated with stress perturbations are critically stressed under the large-scale linear stress characterisation of the site. Thus, it is possible that they failed and generated the stress perturbations relatively recently, reflecting accommodation of on-going tectonic deformation of the crust. However, the data do not require this, and it is just as likely that the slip that generated the stress perturbations is much older.

6.4 Suggestions for improvements and further investigations

Natural fracturing

Concerning the natural fracturing, the most important missing information concerns the extent of the fracture zones within the reservoir volume. Indeed, if the work presented here permits us to increase our understanding concerning the spacing and architecture of the fracture zones, our knowledge is limited to the borehole vicinity. If we know where the main fracture zones cut the boreholes, their extension within the reservoir remains uncertain. This limitation will hopefully be addressed by the VSP (vertical seismic profiling) surveys that have recently been conducted at Soultz. Such methods may be able to illuminate the major structures within the reservoir, which is currently only possible with microseismic imaging.

Analysis of wellbore failure

The analysis of wellbore failure requires the estimation of the thermal stress. This is of crucial importance for the analysis of the conditions of formation of drilling induced tension fractures. In geothermal wells, where the rock mass temperature is believed to be significantly higher than the drilling fluid, this thermal effect is certainly non-negligible.

Attempts to numerically model the temperature history of a well are difficult, because the flow of heat within the rock/hole/drill-pipe system is very complicated, and is compounded by the discontinuous nature of drilling operations. Thus, downhole temperature measurements from measurement-while-drilling systems (MWD) are essential if the temperature at the drill bit is to be estimated. In contrast to other

authors (e.g. *Bérard and Cornet, 2003*) we regard this as the coolest temperature that the rock will see during the drilling operation. Unfortunately, MWD data are usually sparse or absent. For deviated holes, MWD data are required to monitor the well trajectory. Such equipment usually has an on-board temperature sensor, but the drilling engineers are not necessarily aware of the importance of archiving systematically this information. In Soultz, partial, but nevertheless worthwhile data was recorded for the well GPK4 only.

Information on the well temperatures at any time during drilling is essential not only for wellbore failure considerations but also for key drilling-related operations, such as cementing, and for the estimation of the natural formation temperature at total depth. For these reasons, it is recommended that temperature monitoring equipment is developed and deployed during the drilling of geothermal wells.

Another aspect which should be better studied is the complex situation that occurs at the drill bit and its influence on natural and induced fractures and breakouts. Here again, we think that the collection of MWD data, particularly fluid pressure and the temperature, would help address this problem.

Details on the sources of stress heterogeneities

One question, which remains partially open, is the source of the short wavelength variations. Are they due to slip on fractures that occurs during the geological history or do they reflect slip during drilling, promoted perhaps by high pressures at the drill bit ? The preference for the E-DITFs to form sub-parallel to natural fractures favours second explanation, at least for those fractures that have a ‘halo’ of sub-parallel E-DITFs. However, here again it would be necessary to better understand the conditions prevailing at the drill bit.

We have seen that long wave length variations are related to fracture zones, but they are not always well correlated between the wells. We were limited in the interpretation of the long wavelength variations as the geometry of large structures in the Soultz reservoir is unknown. The VSP survey that is currently underway at Soultz may improve our knowledge on the geometry of these structures. It will be then interesting to incorporate these results with our description of long wavelength stress heterogeneities to see if we can better explain the observed variations. It will be also necessary to use more complex modelling scheme of the stress perturbation around a fault, in order to be able to consider the 3D effects.

Bibliography

- Achauer, U., and F. Masson (2002), Seismic tomography of continental rifts revisited: from relative to absolute heterogeneities, *Tectonophysics*, 358(1-4), p. 17–37.
- Ahorner, L. (1975), Present-day stress field and seismotectonic block movements along major fault zones in Central Europe, *Tectonophysics*, 29(1-4), p. 233–249.
- Al-Ajmi, A. M., and R. W. Zimmermann (2006), Stability of vertical boreholes using the Mogi-Coulomb failure criterion, *International Journal of Rock Mechanics and Mining Science*, 43, p. 1200–1211.
- Anders, M. H., and D. V. Wiltschko (1994), Microfracturing, paleostress and the growth of faults, *Journal of Structural Geology*, 16(6), p. 795–815, doi:10.1016/0191-8141(94)90146-5.
- Angelier, J., and F. Bergerat (1983), Systèmes de contrainte en extension intracontinentale, *Bulletin du centre de recherche Exploration-Production. Elf Aquitaine*, 7(1), p. 137–147.
- Arthaud, F., and P. Matte (1977), Late Paleozoic strike-slip faulting in southern Europe and northern Africa: Result of a right-lateral shear zone between the Appalachians and the Urals, *Geological Society of America Bulletin*, 88(9), p. 1305–1320.
- Bankwitz, P. (1965), Über Klüfte I. Beobachtung im Thüringischen Schiefergebirge, *Geologie*, 14(3), p. 241–253.
- Bankwitz, P. (1966), Über Klüfte II. Die Bildung der Kluftfläche und eine Systematik ihrer Strukturen, *Geologie*, 15(8), p. 896–941.
- Baria, R., J. Garnish, J. Baumgärtner, A. Gérard, and R. Jung (1995), Recent developments in the European HDR Research programme at Soultz-sous-Forêts (France), in *World Geothermal Congress*, edited by E. Barbier, pp. 2631–2637, Reykjavik, Iceland.
- Barton, C. A., and M. D. Zoback (1988), In-situ stress orientation and magnitude at the Fenton geothermal site, New Mexico, determined from wellbore breakouts, *Geophysical Research Letters*, 15(5), p. 467–470.

- Barton, C. A., and M. D. Zoback (1994), Stress perturbations associated with active faults penetrated by boreholes: Possible evidence for near-complete stress drop and a new technique for stress magnitude measurements, *Journal of Geophysical Research*, 99(B5), p. 9373–9390.
- Barton, C. A., M. D. Zoback, and D. Moos (1995), Fluid flow along potentially active faults in crystalline rock, *Geology*, 23(8), p. 683–686.
- Behrmann, J. H., O. Hermann, M. Horstmann, D. C. Tanner, and G. Bertrand (2003), Anatomy and kinematics of oblique continental rifting revealed: A three-dimensional case study of the southeast Upper Rhine graben (Germany), *AAPG Bulletin*, 87(7), p. 1105–1121.
- Bell, J. S., and D. I. Gough (1979), Northeast-southwest compressive stress in Alberta: Evidence from oil wells, *Earth and Planetary Science Letters*, 45, p. 475–482.
- Bérard, T. (2003), Estimation du champ de contrainte dans le massif granitique de Soultz-sous-Forêts, implication sur la rhéologie de la croûte fragile, Ph.D. thesis, Institut de Physique du Globe de Paris, 264 pp.
- Bérard, T., and F. Cornet (2003), Evidence of thermally induced borehole elongation: A case study at Soultz, France, *International Journal of Rock Mechanics and Mining Science*, 40, p. 1121–1140.
- Berger, J.-P., D. Becker, and L. Picot (2000), Chronostratigraphic chart for the South and North Jura Molasse, the South Rhine Graben, the North Rhine Graben and the Mainzer Becken, web page, access date: 20/10/2006, http://comp1.geol.unibas.ch/groups/3_3/berger/berger.htm.
- Bergerat, F. (1985), Déformations cassantes et champs de contraintes tertiaires dans la plateforme européenne., Ph.D. thesis, Université Pierre & Marie Curie, Paris VI.
- Bergerat, F. (1987), Stress field in the european platform at the time of Africa-Eurasia collision, *Tectonics*, 6(2), p. 99–132.
- Bieniawski, Z. T., and M. J. Bernede (1979), Suggested methods for determining the uniaxial compressive strength and deformability of rock materials, *International Journal of Rock Mechanics and Mining Science & Geomechanics Abstracts*, 16(2), p. 137–140.
- Blüming, P. (1986), In-situ Spannungsmessungen mit Hilfe von Bohrlochrandausbrüchen und die Spannungsverteilung in der Kruste Mitteleuropas und Australiens, Ph.D. thesis, Karlsruhe University – Germany.

- Bois, C. (1993), Initiation and evolution of the Oligo-Miocene rift basins of southwestern Europe: Contribution of deep seismic reflection profiling, *Tectonophysics*, 226(1-4), p. 227–252.
- Bonjer, K. P. (1997), Seismicity pattern and style of seismic faulting at the eastern borderfault of the southern Rhine Graben, *Tectonophysics*, 275(1-3), p. 41–69.
- Bonnet, E., O. Bour, N. E. Odling, P. Davy, I. Main, P. A. Cowie, and B. Berkowitz (2001), Scaling of fracture systems in geological media, *Reviews of Geophysics*, 39(3), p. 347–383.
- Brace, W. F., and D. L. Kohlstedt (1980), Limits on lithospheric stress imposed by laboratory experiments, *Journal of Geophysical Research*, 85(B11), p. 6248–6252.
- Brace, W. F., and R. J. Martin (1968), A test of the law of effective stress for crystalline rock of low porosity, *International Journal of Rock Mechanics and Mining Science*, 5(5), p. 415–426.
- Brereton, R., B. Muller, P. Hancock, T. Harper, M. H. P. Bott, D. Sanderson, and N. Kuszniir (1991), European Stress: Contributions from Borehole Breakouts [and Discussion], *Philosophical Transactions: Physical Sciences and Engineering*, 337(1645), p. 165–179.
- Brudy, M., and M. D. Zoback (1993), Compressive and Tensile failure of boreholes arbitrarily-inclined to principal stress axes: application to the KTB boreholes, Germany, *International Journal of Rock Mechanics, Mining Science and Geomechanics Abstracts*, 30(7), p. 1035–1038.
- Brudy, M., and M. D. Zoback (1999), Drilling -induced tensile wall-fractures: Implications for determination of in-situ stress orientation and magnitude, *International Journal of Rock Mechanics and Mining Science*, 36, p. 191–215.
- Brun, J. P., F. Wenzel, and ECORS-DEKORP team (1991), Crustal-scale structure of the southern Rhinegraben from ECORS-DEKORP seismic reflection data, *Geology*, 19, p. 758–762.
- Brun, J. P., M. A. Gutscher, and DEKORP-ECORS teams (1992), Deep crustal structure of the Rhine Graben from seismic reflection data: A summary, *Tectonophysics*, 208(1-3), p. 139–147.
- Cataldi, R., S. F. Hodgson, and J. W. Lund (1999), *Stories from a Heated Earth, Our Geothermal Heritage*, 588 pp., Geothermal Resources Council, ISBN: 978-0934412193.
- Charlez, P. A. (1997), *Rock mechanics, 2. Petroleum applications*, vol. 2, 661 pp., Editions Technip, ISBN: 2-7108-0586-3.

- Chilès, J. P. (1988), Fractal and geostatistical methods for modeling of a fracture network, *Mathematical Geology*, 20(6), p. 631–654.
- Clarke, D. (2007), *The Battle for Barrels: Peak Oil Myths and World Oil Futures*, 224 pp., Profile Books, ISBN: 978-1846680120.
- Cloetingh, S., P. A. Ziegler, F. Beekman, P. A. M. Andriessen, L. Matenco, G. Bada, D. Garcia-Castellanos, N. Hardebol, P. Dezes, and D. Sokoutis (2005), Lithospheric memory, state of stress and rheology: neotectonic controls on Europe's intraplate continental topography, *Quaternary Science Reviews*, 24(3-4), p. 241–304.
- Cloetingh, S., T. Cornu, P. A. Ziegler, and F. Beekman (2006), Neotectonics and intraplate continental topography of the northern Alpine Foreland, *Earth-Science Reviews*, 74(3-4), p. 127–196.
- Cloos, H. (1922), Über Ausbau und Anwendung der Granit-tektonischen Methode, *Abh. Preuss. Geol. Landesans.*, 89, p. 1–18.
- Cocherie, A., C. Guerrot, C. M. Fanning, and A. Genter (2004), Datation U-Pb des deux faciès du granite de Soultz (Fossé rhéna, France), *C. R. Géosciences, Géochimie (Géochronologie)*, 336(9), p. 775–787, doi:10.1016/j.crte.2004.01.009.
- Cochet, Y. (2005), *Pétrole apocalypse*, 274 pp., Fayard, France, ISBN: 978-2213622040.
- Cornet, F. H., and T. Bérard (2003), A case example of integrated stress profile evaluation, in *3rd International Symposium on Rock stress, Kumamoto, Japan*, edited by U. Sujawara, Y. Obara, and A. Sato, Balkema.
- Cornet, F. H., and Y. Jianmin (1995), Analysis of induced seismicity for stress field determination and pore pressure mapping, *Pure and Applied Geophysics*, 145(3), p. 677–700.
- Cornet, F. H., Y. Jianmin, and L. Martel (1992), Stress Heterogeneities and Flow Paths in a granite Rock Mass, Pre-Workshop Volume for the Workshop on Induced Seismicity, in *33rd U.S. Symposium on Rock Mechanics 184*.
- Cornet, F. H., T. Bérard, and S. Bourouis (2007), How close to failure is natural granite rock mass at 5 km depth ?, *International Journal of Rock Mechanics and Mining Sciences*, 44, p. 47–66.
- Corpel, J., and N. Debeglia (1994), Synthèse région de Soultz: interprétation gravimétrique, *Tech. Rep. R-38027*, BRGM.

- Cowie, P. A., and C. H. Scholz (1992), Physical explanation for the displacement-length relationship of faults using a post-yield fracture mechanics model, *Journal of Structural Geology*, 14(10), p. 1133–1148.
- Cuenot, N., J. Charléty, L. Dorbath, and H. Haessler (2005), Faulting mechanisms and stress tensor at the european HDR site of Soultz-sous-Forêts, in *EHDRA scientific conference, 17 - 18 March 2005*, Soultz-sous-Forêts, France.
- Cuenot, N., J. Charlety, L. Dorbath, and H. Haessler (2006), Faulting mechanisms and stress regime at the European HDR site of Soultz-sous-Forets, France, *Geothermics*, 35(5-6), p. 561–575.
- Cuss, R. J., E. H. Rutter, and R. F. Holloway (2003), Experimental observations of the mechanics of borehole failure in porous sandstone, *International Journal of Rock Mechanics and Mining Sciences*, 40(5), p. 747–761, doi:10.1016/S1365-1609(03)00068-6.
- Davis, J. C. (2002), *Statistics and data analysis in geology*, 638 pp., John Wiley and Sons, Inc., ISBN: 0-471-17275-8.
- Debrand-Passard, S., and S. Courbouleix (1984), Synthèse géologique du sud-est de la France, *Tech. rep.*, BRGM.
- Deichmann, N., D. Ballarin Dolfin, and U. Kastrup (2000), Seismizität der Nord- und Zentralschweiz, *Tech. Rep. NTB 00-05*, NAGRA.
- Dezayes, C. (1996), Caractérisation et interprétation d'un volume rocheux fracturé à partir de données de forages, les forages géothermiques de Soultz-sous-Forêts, Ph.D. thesis, Université de Savoie, Chambéry France, 200 pp.
- Dezayes, C., A. Genter, G. Homeier, M. Degouy, and G. Stein (2003), Geological Study of GPK3 HFR borehole (Soultz-sous-Forêts, France), *Tech. Rep. RP-52311-FR*, BRGM.
- Dezayes, C., A. Genter, and S. Gentier (2004), Fracture network of the EGS geothermal reservoir at Soultz-sous-Forêts (Rhine graben, France), in *Geothermal Research Council 2004*.
- Dezayes, C., P. Chevremont, B. Tourlière, G. Homeier, and A. Genter (2005a), Geological study of the GPK4 HFR borehole and correlation with the GPK3 borehole (Soultz-sous-Forêts, France), *Tech. Rep. RP-53697-FR*, BRGM.
- Dezayes, C., S. Gentier, and A. Genter (2005b), Deep Geothermal Energy in Western Europe: The Soultz Project, *Tech. Rep. RP-54227-FR*, BRGM.

- Dèzes, P., S. M. Schmid, and P. A. Ziegler (2004), Evolution of the European Cenozoic Rift System: interaction of the Alpine and Pyrenean orogens with their foreland lithosphere, *Tectonophysics*, 389, p. 1–33, doi:10.1016/j.tecto.2004.06.011.
- Dèzes, P., S. M. Schmid, and P. A. Ziegler (2005), Reply to comments by L. Michon and O. Merle on "Evolution of the European Cenozoic Rift System: interaction of the Alpine and Pyrenean orogens with their foreland lithosphere" by P. Dezes, S.M. Schmid and P.A. Ziegler, *Tectonophysics* 389 (2004) 1-33, *Tectonophysics*, 401(3-4), p. 257–262.
- Diebold, P., H. Naef, and M. Ammann (1991), Zur tektonik der zentralen Nord-schweiz: interpretation aufgrund regionaler Seismik, Oberflächengeologie und Tiefbohrungen, *Tech. Rep. NTB 90-04*, NAGRA.
- Diederichs, M. S., P. K. Kaiser, and E. Eberhardt (2004), Damage initiation and propagation in hard rock during tunnelling and the influence of near-face stress rotation, *International Journal of Rock Mechanics and Mining Sciences*, 41(5), p. 785–812.
- Donsimoni (1981), Le bassin houiller lorrain: synthèse géologique, *Tech. rep.*
- Dorbath, L., and J. Charléty (2007), What can we learn from large induced earthquakes at Soultz-sous-Forêts, in *EHDRA scientific conference, 28 - 29 June 2007*, Soultz-sous-Forêts, France.
- Duchane, D. (1998), The history of HDR research and development, in *International conference 4th HDR forum*, vol. E1, edited by R. Baria, J. Baumgärtner, A. Gérard, and R. Jung, pp. 7–17, Geologisches Jahrbuch Sonderheft.
- Dunbar, S. (1984), DIS3D a three dimensional fault modelling program, Computer Program, Stanford University.
- Edel, J. B., and K. Weber (1995), Cadomian terranes, wrench faulting and thrusting in central Europe Variscides : Geophysical and geological evidences, *Geologische Rundschau*, 84, p. 412–432.
- Edel, J. B., K. Schulmann, and Y. Rotstein (2004), The Variscan tectonic inheritance of the Upper Rhine Graben: evidence of reactivations in the Lias, Late Eocene-Oligocene up to the recent, *International Journal of Earth Sciences*, doi:10.1007/s00531-006-0092-8.
- Einstein, H. H., and G. B. Baecher (1983), Probabilistic and statistical methods in engineering geology, *Rock Mechanics and Rock Engineering*, 16(1), p. 39–72.

- Eissa, E. A., and A. Kazi (1988), Relation between Static and dynamic Young's moduli of rocks, *International Journal of Rock Mechanics, Mining Science and Geomechanics Abstracts*, 25(6), p. 479–482.
- Erickson, L. (1987), User's manual for DIS3D: A three dimensional dislocation program with applications to faulting in the earth, Computer Program, Stanford University.
- Evans, K. F. (2005), Permeability creation and damage due to massive fluid injections into granite at 3.5 km at Soultz: 2. Critical stress and fracture strength, *Journal of Geophysical Research*, 110(B4).
- Evans, K. F., T. Kohl, R. J. Hopkirk, and L. Rybach (1992), Modelling of energy production from Hot Dry Rock systems, *Tech. rep.*, Bundesamt für Bildung und Wissenschaft.
- Evans, K. F., F. H. Cornet, T. Hashida, H. Kazuo, T. Ito, K. Matsuki, and T. Wallroth (1999), Stress and rock mechanics issues of relevance to HDR/HWR engineered geothermal systems: review of developments during the past 15 years, *Geothermics*, 28, p. 455–474.
- Evans, K. F., A. Genter, and J. Sausse (2005a), Permeability creation and damage due to massive fluid injections into granite at 3.5 km at Soultz: 1. Borehole observation, *Journal of Geophysical Research*, 110(B4).
- Evans, K. F., H. Moriya, H. Niitsuma, R. H. Jones, W. S. Phillips, A. Genter, J. Sausse, R. Jung, and R. Baria (2005b), Microseismicity and permeability enhancement of hydrogeologic structures during massive fluid injections into granite at 3km depth at the Soultz HDR site, *Geophysical Journal International*, 160, p. 388–412.
- Faulkner, D. R., T. M. Mitchell, D. Healy, and M. J. Heap (2006), Slip on 'weak' faults by the rotation of regional stress in the fracture damage zone, *Nature*, 444(7121), p. 922–925.
- Franke, W. (1989), Variscan plate tectonics in Central Europe—current ideas and open questions, *Tectonophysics*, 169(4), p. 221–228.
- Genter, A. (1989), Géothermie roches chaudes sèches: le granite de Soultz-sous-Forêts. (Bas-Rhin, France), Fracturation naturelle, altérations hydrothermales et interaction eau-roche, Ph.D. thesis, Université d'Orléans, 201 pp.
- Genter, A., and H. Tenzer (1995), Geological monitoring of GPK2-HDR borehole, 1420-3880m (Soultz-sous-Forêts, France), *Tech. Rep. R-38629*, BRGM.

- Genter, A., and H. Traineau (1992), Borehole EPS-1, Alsace, France: preliminary geological results from granite core analyses for Hot Dry Rock research, *Scientific Drilling*, 3, p. 205–214.
- Genter, A., and H. Traineau (1996), Analysis of macroscopic fractures in granite in the HDR geothermal well EPS-1, Soultz-sous-Forêts, France, *Journal of Volcanology and Geothermal Research*, 72(1-2), p. 121–141.
- Genter, A., P. Martin, and P. Montaggioni (1991), Application of FMS and BHTV tools for evaluation of natural fractures in the Soultz geothermal borehole GPK1, *Geothermal Science and Technology*, 3(1-4), p. 69–82.
- Genter, A., C. Castaing, C. Dezayes, H. Tenzer, H. Traineau, and T. Villemin (1997), Comparative analysis of direct (core) and indirect (borehole imaging tools) collection of fracture data in the Hot Dry Rock Soultz reservoir (France)., *Journal of Geophysical Research*, 102(B7), p. 15,419–15,431.
- Genter, A., C. Dezayes, S. Gentier, B. Ledesert, and J. Sausse (1998), Conceptual fracture model at Soultz based on geological data, in *4th international HDR forum*, vol. E1, edited by R. Baria, J. Baumgärtner, A. Gérard, and R. Jung, Geologisches Jahrbuch Sonderheft.
- Genter, A., H. Traineau, B. Ledesert, B. Bourguine, and S. Gentier (2000), Over 19 years of geological investigation within the HDR Soultz project, France, in *World Geothermal Congress 2000, Beppu and Morioka, Japan from May 28 to June 10, 2000*.
- Gérard, A., J. Baumgärtner, R. Baria, R. Jung, S. Gentier, and A. Genter (1998), Elements for a conceptual model of the underground heat exchanger at Soultz-sous-Forêts, in *International conference 4th HDR forum*, vol. E1, edited by R. Baria, J. Baumgärtner, A. Gérard, and R. Jung, pp. 281–290, Geologisches Jahrbuch Sonderheft.
- Geraud, Y., F. Surma, and M. Rosener (2005), Porosity network of Soultz-sous-Forêts granite: the importance of the damaged zone around faults and fractures, in *EHDRA scientific conference, 17 - 18 March 2005*, Soultz-sous-Forêts, France.
- Gillespie, P. A., J. Walsh, J. Watterson, C. G. Bonson, and T. Manzocchi (2001), Scaling relationships of joint and vein arrays from the Burren, Co. Clare, Ireland, *Journal of Structural Geology*, 23, p. 183–201.
- Groschong, R. H. J. (1996), *Construction and validation of extensional cross section using lost area and strain, with application to the Rhine graben*, in *Modern developments in structural interpretation, validation and Modelling*, vol. 99, edited by

- P. Buchanan and D. A. Nieuwland, vol. 99, Geological Society Special Publication, ISBN: 1897799438.
- Haimson, B. C. (2007), Micromechanisms of borehole instability leading to breakouts in rocks, *International Journal of Rock Mechanics and Mining Sciences*, 44(2), p. 157–173.
- Haimson, B. C., and C. Chang (2005), *Brittle fracture in two crystalline rocks under true triaxial compressive stresses.*, in *Petrophysical properties of crystalline rocks.*, vol. 240, edited by P. K. Harvey, T. S. Brewer, P. P. A., and P. V. A., vol. 240, Geological Society Special Publications, ISBN: 1-86239-173-4.
- Haimson, B. C., and C. G. Herrick (1986), *Borehole breakouts-a new tool for estimating in situ stress?*, in *Rock Stress*, edited by O. Stephansson, CENTEK Publisher, Lulea, Sweden.
- Haimson, B. C., and C. G. Herrick (1989), Borehole breakouts and in situ stress, in *Drilling Symposium*, The American Society of Mechanical Engineers, New York.
- Haimson, B. C., and J. Kovacich (2003), Borehole instability in high-porosity Berea sandstone and factors affecting dimensions and shape of fracture-like breakouts, *Engineering Geology*, 69(3-4), p. 219–231.
- Haimson, B. C., and H. Lee (2004), Borehole breakouts and compaction bands in two high-porosity sandstones, *International Journal of Rock Mechanics and Mining Sciences*, 41(2), p. 287–301.
- Haimson, B. C., and I. Song (1993), Laboratory study of borehole breakouts in Cordova Cream: a case of shear failure mechanism, *International Journal of Rock Mechanics and Mining Science & Geomechanics Abstracts*, 30(7), p. 1047–1056.
- Harris, R. A. (1998), Introduction to special section: Stress triggers, stress shadows, and implications for seismic hazard, *Journal of Geophysical Research*, 103(B10), p. 24,347–24,358, doi:10.1029/98JB01576.
- Heinemann-Glutsch, B. (1994), Results of scientific investigations at the HDR test site, Soultz-sous-Forêts, *Tech. rep.*, Socomine, BP 39, Route de Kutzenhausen, F-67250 Soultz sous Forets., France.
- Helm, J. A. (1996), The natural seismic hazard and induced seismicity of the European HDR (Hot Dry Rock) geothermal energy project at Soultz-sous-Forêts, France, Ph.D. thesis, Univ. Louis-Pasteur, Strasbourg, France.
- Hettkamp, T., J. Baumgärtner, R. Baria, A. Gérard, T. Gandy, S. Michelet, and D. Teza (2004), Electricity production from hot rocks, in *29th workshop on geothermal reservoir engineering*, Stanford.

- Hickman, S., M. D. Zoback, C. A. Barton, R. Benoit, J. Svitek, and R. Summers (2000), Stress and permeability heterogeneity within the Dixie valley geothermal reservoir: recent results from well 82-5, in *25th Workshop on Geothermal Reservoir Engineering, Stanford*, pp. 256–264, Stanford.
- Hiramatsu, Y., and Y. Oka (1968), Determination of the stress in rock unaffected by boreholes or drifts, from measured strains or deformations, *International Journal of Rock Mechanics and Mining Science*, 5, p. 337–353.
- Hoek, E., and E. T. Brown (1997), Practical estimates of rock mass strength, *International Journal of Rock Mechanics and Mining Sciences*, 34(8), p. 1165–1186.
- Hosni, A. (1997), Modélisation par la méthode des éléments distincts du champ de contraintes à l'échelle du Fossé rhénan et de Soultz-sous-Forêts, Ph.D. thesis, Ecole Nationale Supérieure des Mines de Nancy.
- Illies, H. (1962), Oberrheinisches Grundgebirge und Rheingraben, *Geologische Rundschau*, 52, p. 317–332.
- Illies, H. (1965), Bauplan und Baugeschichte des Oberrheingrabens, *Oberrheinische Geologische Abhandlungen*, 14, p. 1–54.
- Illies, H. (1972), The Rhine graben rift system - plate tectonic and transform faulting, *Geophysical Survey*, 1, p. 27–60.
- Illies, H. J., and G. Greiner (1979), Holocene movements and state of stress in the rhinegraben rift system, *Tectonophysics*, 52(1-4), p. 349–359.
- Illies, J. H. (1975), Recent and paleo-intraplate tectonics in stable Europe and the Rhinegraben rift system, *Tectonophysics*, 29(1-4), p. 251–264.
- Ito, T., and D. Zoback Mark (2000), Fracture permeability and in situ stress to 7 km depth in the KTB Scientific Drillhole, *Geophysical Research Letters*, 27(7), p. 1045–1048.
- Ito, T., K. Kurosawa, and K. Hayashi (1998), Stress concentration at the bottom of a borehole and its effect on borehole breakout formation, *Rock Mechanics and Rock Engineering*, 31(3), p. 153–168.
- Ito, T., K. F. Evans, K. Kawai, and K. Hayashi (1999), Hydraulic fracture reopening pressure and the estimation of maximum horizontal stress, *International Journal of Rock Mechanics and Mining Science*, 36, p. 811–826.
- Ito, T., D. Zoback Mark, and P. Peska (2001), Utilization of Mud Weights in Excess of the Least Principal Stress to Stabilize Wellbores: Theory and Practical Examples, *SPE Drilling and Completion*, 16(4), p. 221–229.

- Jaeger, J. C. (1963), Extension Failures in Rocks subject to fluid Pressure, *Journal of Geophysical Research*, 68(21), p. 6066–6067.
- Jaeger, J. C., and N. G. W. Cooke (1963), Pinching-off and diskings in rocks, *Journal of Geophysical Research*, 68(6), p. 1759–1765.
- Jaeger, J. C., N. G. W. Cook, and R. W. Zimmerman (2007), *Fundamentals of rock mechanics*, Blackwell, ISBN: 978-0-632-05759-7.
- Jones, R. H., and R. C. Steward (1997), A method for determining significant structures in a cloud of earthquakes, *Journal of Geophysical Research*, 102(B4), p. 8245–8254.
- Kabir, C. S., A. R. Hassan, G. E. Kouba, and M. Ameen (1996), Determining circulating fluid temperature in drilling, workover, and well control operations, *SPE Drilling & Completion*, 11(2), p. 74–79.
- Kaiser, P. K., D. McCreath, and D. Tannant (1995), Canadian rockburst support handbook, *Tech. rep.*, Geomechanics Research Center, Laurentian University, Sudbury.
- Kappelmeyer, O., A. Gérard, W. Schloemer, R. Ferrandes, F. Rummel, and Y. Benderitter (1991), European HDR project at Soultz-sous-Forêts general presentation, *Geothermal Science and Technology*, 2(4), p. 263–289.
- Kastrup, U., M. L. Zoback, N. Deichmann, D. Giardini, K. F. Evans, and A. J. Michael (2004), Stress field variations in the Swiss Alps and the northern Alpine foreland derived from inversion of fault plane solutions, *Journal of Geophysical Research*, 109(B01402), doi:10.1029/2003JB002550.
- Kim, Y.-S., and D. J. Sanderson (2005), The relationship between displacement and length of faults: a review, *Earth-Science Reviews*, 68(3-4), p. 317–334.
- Kim, Y.-S., D. C. P. Peacock, and D. J. Sanderson (2003), Mesoscale strike-slip faults and damage zones at Marsalforn, Gozo Island, Malta, *Journal of Structural Geology*, 25(5), p. 793–812.
- Klee, G., and F. Rummel (1993), Hydrofrac stress data for the European HDR research project test site Soultz-sous-Forêts, *International Journal of Rock Mechanics, Mining Science and Geomechanics Abstracts*, 30, p. 973–976.
- Klerk, P. A. (2000), The finite element modelling of discrete fracture of brittle materials., Ph.D. thesis, University of Wales, Swansea.
- Kneuper, G. (1976), Regional-geologische Folgerungen aus der Bohrung Saar, 1, *Geol. Jahrb.*, 27(499-510).

- Krohe, A., and A. P. Willner (1995), *The Odenwald Crystalline Complex*, in *Pre-Permian Geology of Central and Eastern Europe*, edited by R. D. Dallmeyer, W. Franke, and K. Weber, Springer, ISBN: 3-540-55472-6.
- Larroque, J. M., and P. Laurent (1988), Evolution of the stress field pattern in the south of the Rhine Graben from the Eocene to the present, *Tectonophysics*, 148(1-2), p. 41–58.
- Larroque, J. M., A. Etchecopar, and H. Philip (1987), Evidence for the permutation of stresses σ_1 and σ_2 in the Alpine foreland: the example of the Rhine graben, *Tectonophysics*, 144(4), p. 315–322.
- Laubscher, H. (2001), Plate interactions at the southern end of the Rhine graben, *Tectonophysics*, 343(1-2), p. 1–19.
- Lofts, J. C., and L. T. Bourke (1999), *The recognition of artefacts from acoustic and resistivity borehole image devices*, in *Borehole Imaging: applications and case histories*, vol. 159, edited by M. A. Lovell, G. Williamson, and P. K. Harvey, vol. 159, Geological Society special publications.
- Lopes Cardozo, G. G. O., and J. H. Behrmann (2006), Kinematic analysis of the Upper Rhine Graben boundary fault system, *Journal of Structural Geology*, 28(6), p. 1028–1039.
- Lopes Cardozo, G. G. O., J. B. Edel, and M. Granet (2005), Detection of active crustal structures in the Upper Rhine Graben using local earthquake tomography, gravimetry and reflection seismics, *Quaternary Science Reviews*, 24(3-4), p. 337–344.
- Luthi, S. M. (2001), *Geological well logs : their use in reservoir modeling*, 373 pp., Springer, ISBN: 3-540-67840-9.
- Mandelbrot, B. (1975), *Les objets fractals, forme, hasard et dimension*, 212 pp., Flammarion, ISBN: 2-08-081301-3.
- Maqua, E. (2003), Fracturation dans la partie supérieure du forage GPK3 et corrélation avec les autres puits du site de Soultz-sous-Forêts (Alsace, France), *Tech. rep.*, BRGM.
- Martel, S. J. (1990), Formation of compound strike-slip fault zones, Mount Abbot quadrangle, California, *Journal of Structural Geology*, 12(7), p. 869–877.
- Martel, S. J. (2006), Effect of topographic curvature on near-surface stresses and application to sheeting joints, *Geophysical Research Letters*, 33(L01308).

- Martin, C. D., and B. Stimpson (1994), The effect of sample disturbance on laboratory properties of Lac du Bonnet granite, *Canadian Geotechnical Journal*, 31(5), p. 692–702.
- Mastin, L. (1988), Effect of borehole deviation on breakout orientations, *Journal of Geophysical Research*, 93(B8), p. 9187–9195.
- Mayer, G., P. Mai, T. Plenefisch, H. Echtler, E. Lüschen, V. Wehrle, B. Müller, K.-P. Bonjer, C. Prodehl, and K. Fuchs (1997), The deep crust of the Southern Rhine Graben: reflectivity and seismicity as images of dynamic processes, *Tectonophysics*, 275, p. 15–40.
- Menjot, A., J. P. Cautru, A. Criaud, and A. Genter (1989), Roches sèches chaudes. Caractérisation des réservoirs fracturées: Rapport annuel d’activités, *Tech. rep.*, BRGM.
- Michelet, S., and M. N. Toksöz (2007), Fracture mapping in the Soultz-sous-Forêts geothermal field using microearthquake locations, *Journal of Geophysical Research*, 112(B07315), doi:10.1029/2006JB004442.
- Michon, L., and O. Merle (2005), Discussion on ”Evolution of the European Cenozoic Rift System: interaction of the Alpine and Pyrenean orogens with their foreland lithosphere” by P. Dezes, S.M. Schmid and P.A. Ziegler, *Tectonophysics* 389 (2004) 1-33, *Tectonophysics*, 401(3-4), p. 251–256.
- Michon, L., R. T. Van Balen, O. Merle, and H. Pagnier (2003), The Cenozoic evolution of the Roer Valley Rift System integrated at a European scale, *Tectonophysics*, 367(1-2), p. 101–126.
- Miller, S. M. (1979), Geostatistical analysis for evaluating spatial dependence in fracture set characteristics, in *16th APCOM Symposium, Tucson*, pp. 537–545, Tucson.
- Moriya, H., H. Niitsuma, and R. Baria (2003), Multiplet-Clustering Analysis Reveals Structural Details within the Seismic Cloud at the Soultz Geothermal Field, France, *Bulletin of the Seismological Society of America*, 93(4), p. 1606–1620.
- Müller, B., M. L. Zoback, K. Fuchs, L. Mastin, S. Gregersen, N. Pavoni, O. Stephansson, and C. Ljunggren (1992), Regional Patterns of Tectonic Stress in Europe, *Journal of Geophysical Research*, 97(B8), p. 11,783–11,803.
- Muller, B., V. Wehrle, H. Zeyen, and K. Fuchs (1997), Short-scale variations of tectonic regimes in the western European stress province north of the Alps and Pyrenees, *Tectonophysics*, 275(1-3), p. 199–219.

- Nagel, R. (1994), Das Spannungsfeld in der Geothermiebohrung Soultz-sous-Forêts abgeleitet aus vertikalen Strukturen in eine Tiefe von 1.9 bis 3.6 km, Master's thesis, Universität Karlsruhe.
- Naylor, M. A., G. Mandl, and C. H. K. Supesteijn (1986), Fault geometries in basement-induced wrench faulting under different initial stress states, *Journal of Structural Geology*, 8(7), p. 737–752.
- Peacock, D. C. P., R. J. Knipe, and D. J. Sanderson (2000), Glossary of normal faults, *Journal of Structural Geology*, 22(3), p. 291–305.
- Peška, P., and M. D. Zoback (1995), Compressive and tensile failure of inclined well bores and determination of in situ stress and rock strength, *Journal of Geophysical Research*, 100(B7), p. 12,791–12,811.
- Plenefisch, T., and K. P. Bonjer (1997), The stress field in the Rhine Graben area inferred from earthquake focal mechanisms and estimation of frictional parameters, *Tectonophysics*, 275(1-3), p. 71–97.
- Potter, R. M., E. S. Robinson, and M. C. Smith (1974), Method of extracting heat from dry geothermal reservoirs, patent, Patent, United States, 3786858.
- Power, W. L., and T. E. Tullis (1991), Euclidian and Fractal Models for the Description of Rock Surface Roughness, *Journal of Geophysical Research*, 61(B1), p. 415–424, doi:10.1029/90JB02107.
- Priest, S. D. (1993), *Discontinuity analyses for rock engineering*, 473 pp., Chapman and Hall, ISBN: 0-412-47600-2.
- Rajmeny, P. K., U. K. Singh, and S. S. Rathore (2004), A new model to estimate rock mass strength accounting for the scale effect, *International Journal of Rock Mechanics and Mining Sciences*, 41(6), p. 1013–1021, doi:10.1016/j.ijrmms.2004.03.008.
- Read, R. S., C. Derek Martin, and E. J. Dzik (1995), Assymmetric borehole breakouts at URL, in *35th U.S. Symposium on Rock Mechanics*, edited by J. K. Daemen and R. A. Schulz, Reno, Nevada.
- Renard, P., and G. Courrioux (1994), Three-dimensional geometric modeling of a faulted domain: The Soultz Horst example (Alsace, France), *Computers & Geosciences*, 20(9), p. 1379–1390.
- Rice, J. R. (1992), *Fault stress states, pore pressure distributions, and the weakness of the San Andreas Fault.*, in *Fault mechanics and transport properties of rocks*, edited by B. Evans and T.-F. Wong, Academic Press, ISBN: 0-12-243780-2.

- Rocsience Inc. (2005), Phase² version 6.0 - Finite element analysis for excavations and slopes. www.rockscience.com, Toronto, Ontario, Canada, Computer Program.
- Rotstein, Y., J. B. Edel, G. Gabriel, D. Boulanger, M. Schaming, and M. Munsch (2006), Insight into the structure of the Upper Rhine Graben and its basement from a new compilation of Bouguer Gravity, *Tectonophysics*, 425(1-4), p. 55–70.
- Rummel, F. (1987), *Fracture mechanics approach to hydraulic fracturing stress measurements*, in *Fracture mechanics of Rock*, edited by B. Atkinson, pp. p. 217–219, Academic Press.
- Rummel, F. (1991), Physical properties of the rock in the granitic section of borehole GPK1, Soultz-sous-Forêts, *Geothermal Science and Technology*, 3, p. 199–216.
- Rummel, F., and J. Baumgärtner (1991), Hydraulic fracturing stress measurements in the GPK1 borehole, Soultz-sous-Forêts, *Geothermal Science and Technology*, 3(1-4), p. 119–148.
- Rummel, F., and E. König (1991), Physical properties of Core samples, borehole EPS1, Soultz-sous-Forêts: Velocity-, Density- and magnetic susceptibility- logs, depth interval 933-2227 m., *Tech. Rep. Yellow Report 6*, Ruhr - Universität.
- Rummel, F., and D. Schreiber (1993), Physical properties of the core K21, borehole GPK1, Soultz-sous-Forêts, depth interval 3522.58-3525.88 m., *Tech. Rep. Yellow Report 12*, Ruhr - Universität.
- Rummel, F., L. te Kamp, and T. Schäfer (1989), Fracture mechanic properties of granite cores from GPK1., *Tech. Rep. Yellow Report 7*, Ruhr - Universität.
- Rummel, F., E. König, and B. Thieme (1992), Fracture mechanics parameters of EPS1 Soultz granite cores., *Tech. Rep. Yellow Report 10*, Ruhr - Universität.
- Rutqvist, J., C. F. Tsang, and O. Stephansson (2000), Uncertainty in the maximum principal stress estimated from hydraulic fracturing measurements due to the presence of the induced fracture, *International Journal of Rock Mechanics and Mining Science*, 37, p. 107–120.
- Sausse, J., C. Dezayes, and A. Genter (2007), From geological interpretation and 3D modelling of the characterization of the deep seated EGS reservoir of Soultz (France), in *EHDRA scientific conference, 28 - 29 June 2007*, Soultz-sous-Forêts, France.
- Schäfer, T. (1990), Ultraschalluntersuchungen an Granitbohrkerne der Bohrung Soultz-sous-Forêts bezüglich einer Abschätzung von in-situ Spannungen anhand von Riessschliessungdrücken., Master's thesis, Ruhr - Universität, p. 119.

- Schlumberger (2002), UBI, advanced borehole imaging independent of mud type., *Schlumberger brochure*, www.slb.com.
- Schmitt, D. R., and M. D. Zoback (1992), Diminished pore pressure in low-porosity crystalline rock under tensional failure; apparent strengthening by dilatancy., *Journal of Geophysical Research*, *97*(1), p. 273–288.
- Schneider, C. (1984), Les granitoïdes de la partie Nord-Est des Vosges moldanubiennes : évolution magmatique et structural, Master's thesis, Université Louis Pasteur, Strasbourg, France, p. 202.
- Schulmann, K., J. Jezek, and Z. Verena (1997), *Perpendicular linear fabrics in granite: markers of combined simple shear and pure shear flows*, in *Granite : from segregation of melt to emplacement fabrics*, edited by J. L. Bouchez, D. H. W. Hutton, and W. E. Stephens, Kluwer Academic Publishers, ISBN: 0-7923-4460-X.
- Schumacher, E., Markus (2002), Upper Rhine Graben: Role of preexisting structures during rift evolution, *Tectonics*, *21*(1), p. 1006, doi:10.1029/2001TC900022.
- Scotti, O., and F. H. Cornet (1994), In Situ Evidence for fluid-induced aseismic slip events along fault zones, *International Journal of Rock Mechanics and Mining Science & Geomechanics Abstracts*, *31*(4), p. 347–358.
- Seber, G. A. F. (2004), *Multivariate observations*, 686 pp., Wiley, ISBN: 0-471-69121-6.
- Segall, P., and D. D. Pollard (1983), Joint formation in granitic rock of the Sierra Nevada, *Geological Society of America Bulletin*, *94*(5), p. 563–575.
- Shamir, G. (1990), Crustal stress orientation profile to a depth of 3.5 km near the San Andreas Fault at Cajon Pass, California, Ph.D. thesis, Stanford University.—Dept. of Applied Earth, Sciences.
- Shamir, G., and M. D. Zoback (1992), Stress orientation profile to 3.5 km depth near the San Andreas Fault at Cajon Pass, California., *Journal of Geophysical Research*, *97*(B4), p. 5059–5080.
- Shaw, B. E. (2004), Dynamic heterogeneities versus fixed heterogeneities in earthquake models, *Geophysical Journal International*, *156*(2), p. 275–286.
- Shen, B., O. Stephansson, and M. Rinne (2002), Simulation of borehole breakouts using FRACOD2D, *Oil & Gas Science and Technology - Rev. IFP*, *57*(5), p. 415–422.

- Sissingh, W. (1998), Comparative Tertiary stratigraphy of the Rhine Graben, Bresse Graben and Molasse Basin: correlation of Alpine foreland events, *Tectonophysics*, 300(1-4), p. 249–284.
- Sissingh, W. (2003), Tertiary paleogeographic and tectonostratigraphic evolution of the Rhenish Triple Junction, *Palaeogeography, Palaeoclimatology, Palaeoecology*, 196(1-2), p. 229–263.
- Song, I., and B. C. Haimson (1997), Polyaxial strength criteria and their use in estimating in situ stress magnitudes from borehole breakout dimensions, *International Journal of Rock Mechanics and Mining Sciences*, 34(3-4), p. 116.e1–116.e16.
- Stanchits, S., S. Vinciguerra, and G. Dresen (2006), Ultrasonic Velocities, Acoustic Emission Characteristics and Crack Damage of Basalt and Granite, *Pure and Applied Geophysics*, 163(5), p. 975–994, doi:10.1007/s00024-006-0059-5.
- Stephens, G., and B. Voight (1982), Hydraulic fracturing theory for conditions of thermal stress, *International Journal of Rock Mechanics, Mining Science and Geomechanics Abstracts*, 19, p. 279–284.
- Stoica, P., and R. Moses (1997), *Introduction to Spectral Analysis*, 319 pp., Prentice-Hall, ISBN: 0132584190.
- Stussi, J.-M., A. Cheilletz, J.-J. Royer, P. Chèvremont, and G. Féraud (2002), The hidden monzogranite of Soultz-sous-Forêts (Rhine Graben, France), Mineralogy, petrology and genesis, *Géologie de la France*, 1, p. 45–64.
- Surma, F., and Y. Geraud (2003), Porosity and Thermal Conductivity of the Soultz-sous-Forêts Granite, *Pure and Applied Geophysics*, 160(5), p. 1125–1136.
- Tait, J. A., V. Bachtadse, W. Franke, and H. C. Soffel (1997), Geodynamic evolution of the European Variscan fold belt: palaeomagnetic and geological constraints, *Geologische Rundschau*, 86(3), p. 585–598.
- Tenzer, H., L. Mastin, and B. Heinemann (1991), Determination of planar discontinuities and borehole geometry in crystalline rock of borehole GPK-1 at Soultz sous forets, *Geothermal Science and Technology*, 3(1-4), p. 31–67.
- Tenzer, H., P. Budeus, and R. Schellschmidt (1992), Fracture analyses in Hot Dry Rock drillholes at Soultz and Urach by Borehole Televiewer measurements, *Geothermal Resource Council Transactions*, 16, p. 317–321.
- Tesauro, M., C. Hollenstein, R. Egli, A. Geiger, and H.-G. Kahle (2006), Analysis of central western Europe deformation using GPS and seismic data, *Journal of Geodynamics*, 42(4-5), p. 194–209.

- Thompson, B., R. Young, and D. Lockner (2006), Fracture in Westerly Granite under AE Feedback and Constant Strain Rate Loading: Nucleation, Quasi-static Propagation, and the Transition to Unstable Fracture Propagation, *Pure and Applied Geophysics*, doi:10.1007/s00024-006-0054.
- Tischner, T., M. Schindler, R. Jung, and P. Nami (2007), HDR project Soultz: hydraulic and seismic observations during stimulation of the 3 deep wells by massive water injections, in *32nd Workshop on Geothermal Reservoir Engineering*.
- Traineau, H., A. Genter, J. P. Cautru, H. Fabriol, and P. Chevremont (1991), Petrography of the granite massif from drill cutting analysis and well log interpretation in the geothermal HDR borehole GPK1 (Soultz, Alsace, France), *Geothermal Science and Technology*, 3(1-4), p. 1–29.
- Turcotte, D. L. (1989), Fractals in geology and geophysics, *Pure and Applied Geophysics*, 131(1), p. 171–196.
- Twidale, C. R. (1973), On the origin of sheet jointing, *Rock Mechanics and Rock Engineering*, 5(3), p. 163–187.
- Valley, B., and K. F. Evans (2005), Stress estimates from analysis of breakouts and drilling-induced tension fractures in GPK1 and GPK4, in *EHDRA scientific conference, 17 - 18 March 2005*, vol. 1, Soultz-sous-Forêts, France.
- Valley, B., and K. F. Evans (2006a), Stress state at Soultz to 5km depth from wellbore failure and hydraulic observations, in *EHDRA scientific conference, 15 - 16 June 2006*, Soultz-sous-Forêts, France.
- Valley, B., and K. F. Evans (2006b), Strength and elastic properties of the Soultz granite, in *EHDRA scientific conference, 15 - 16 June 2006*, Soultz-sous-Forêts, France.
- Valley, B., and K. F. Evans (2006c), Stress orientation at the Basel geothermal site from wellbore failure analysis in BS1, *Tech. Rep. ETH 3465/56*, ETH Zürich.
- Valley, B., and K. F. Evans (2007), Stress state at Soultz-sous-Forêts to 5 km depth from wellbore failure and hydraulic observations, in *32nd workshop on geothermal reservoir engineering*, Stanford.
- Valley, B., C. Dezayes, and A. Genter (2007), Multi-scale fracturing in the Soultz-sous-Forêts basement from borehole images analyses, in *EHDRA scientific conference, 28 - 29 June 2007*, Soultz-sous-Forêts, France.
- Vermilye, J. M., and C. H. Scholz (1998), The process zone: A microstructural view of fault growth, *Journal of Geophysical Research*, 103(B6), p. 12,223–12,238.

- Villaescusa, E., and E. T. Brown (1990), *Characterizing joint spatial correlation using geostatistical methods*, in *Rock Joints*, edited by C. A. Barton and O. Stephansson, Balkema, ISBN: 90-6191-109-5.
- Villemin, T. (1986), *Tectonique en extension, fracturation et subsidence : Le Fossé Rhénan et le bassin de Sarre-Nahe.*, Ph.D. thesis, Paris VI, 270 pp.
- Villemin, T., and F. Bergerat (1985), *Tectonique cassante et paléocontrainte tertiaires de la bordure NE du Fossé Rhénan (R.F.A.)*, *Oberrheinische Geologische Abhandlungen*, 34, p. 63–87.
- Villemin, T., and F. Bergerat (1987), *L'évolution structurale du fossé rhénan au cours du Cénozoïque : un bilan de la déformation et des effets thermiques de l'extension.*, *Bulletin de la Société Géologique de France*, 3(2), p. 245–255.
- Villemin, T., F. Alvarez, and J. Angelier (1986), *The Rhinegraben: Extension, subsidence and shoulder uplift*, *Tectonophysics*, 128(1-2), p. 47–59.
- Walsh, J. J., and J. Watterson (1988), *Analysis of the relationship between displacements and dimensions of faults*, *Journal of Structural Geology*, 10(3), p. 239–247.
- Weidler, R., A. Gérard, R. Baria, J. Baumgärtner, and R. Jung (2002), *Hydraulic and micro-seismic results of a massive stimulation test at 5 km depth at the european hot-dry-rock test site Soultz, France*, in *27th workshop on geothermal reservoir engineering*, Stanford.
- Wiebols, G. A., and N. G. W. Cook (1968), *An energy criterion for the strength of rock in polyaxial compression*, *International Journal of Rock Mechanics and Mining Science*, 5(6), p. 529–549.
- Wilson, J. E., J. S. Chester, and F. M. Chester (2003), *Microfracture analysis of fault growth and wear processes, Punchbowl Fault, San Andreas system, California*, *Journal of Structural Geology*, 25(11), p. 1855–1873.
- Wingert, J.-L., and J. Laherrère (2005), *La vie après le pétrole : De la pénurie aux énergies nouvelles*, Autrement, France, ISBN: 978-2746706057.
- Zemanek, J., E. E. Glenn, L. J. Norton, and R. L. Caldwell (1970), *Formation evaluation by inspection with the borehole televiewer*, *Geophysics*, 35, p. 254–269, doi:10.1190/1.1440089.
- Zhang, X., D. J. Sanderson, and A. J. Barker (2002), *Stress control of hydraulic conductivity in fracture-saturated Swedish bedrock*, *Geophysical Journal International*, 151(2), p. 452–468.

- Ziegler, P. A. (1986), Geodynamic model for the Palaeozoic crustal consolidation of Western and Central Europe, *Tectonophysics*, 126(2-4), p. 303–328.
- Ziegler, P. A. (1992), European Cenozoic rift system, *Tectonophysics*, 208(1-3), p. 91–111.
- Ziegler, P. A., and P. Dèzes (2005), Evolution of the lithosphere in the area of the Rhine Rift System, *International Journal of Earth Sciences*, V94(4), p. 594–614.
- Zoback, M. D., and J. H. Healy (1984), Friction, faulting and "in situ" stress, *Annales geophysicae*, 2(6), p. 689–698.
- Zoback, M. D., and J. Townend (2001), Implications of hydrostatic pore pressures and high crustal strength for the deformation of intraplate lithosphere, *Tectonophysics*, 336(1-4), p. 19–30.
- Zoback, M. D., and M. L. Zoback (2001), *Stress in the Earth's Lithosphere*, in *Encyclopedia of Physical Science and Technology*, edited by R. A. Meyers, Academic Press, ISBN: 78-0-12-227410-7.
- Zoback, M. D., D. Moos, L. Mastin, and R. N. Anderson (1985), Well bore breakouts and in situ stress, *Journal of Geophysical Research*, 90(B7), p. 5523–5530.
- Zoback, M. D., M. L. Zoback, S. Van Mount, J. Suppe, J. P. Eaton, J. H. Healy, D. Oppenheimer, P. Reasenberg, L. Jones, C. B. Raleigh, I. G. Wong, O. Scotti, and C. Wentworth (1987), New Evidence on the State of Stress of the San Andreas Fault System, *Science*, 238(4830), p. 1105–1111.
- Zoback, M. D., C. A. Barton, M. Brudy, D. A. Castillo, T. Finkbeiner, B. R. Grolimund, D. B. Moos, P. Peska, C. D. Ward, and D. J. Wiprut (2003), Determination of stress orientation and magnitude in deep wells, *International Journal of Rock Mechanics and Mining Sciences*, 40(7-8), p. 1049–1076.
- Zoback, M. L. (1992), First- and second-order patterns of stress in the lithosphere: The World Stress Map project, *Journal of Geophysical Research*, 97(B8), p. 11,703–11,728.
- Zoback, M. L., M. D. Zoback, J. Adams, M. Assumpcao, S. Bell, E. A. Bergman, P. Blumling, N. R. Brereton, D. Denham, J. Ding, K. Fuchs, N. Gay, S. Gregersen, H. K. Gupta, A. Gvishiani, K. Jacob, R. Klein, P. Knoll, M. Magee, J. L. Mercier, B. C. Muller, C. Paquin, K. Rajendran, O. Stephansson, G. Suarez, M. Suter, A. Udias, Z. H. Xu, and M. Zhizhin (1989), Global patterns of tectonic stress, *Nature*, 341(6240), p. 291–298.

Zöller, G., M. Holschneider, and Y. Ben-Zion (2005), The Role of Heterogeneities as a Tuning Parameter of Earthquake Dynamics, *Pure and Applied Geophysics*, 162(6), p. 1027–1049.

Appendix

A First appendix - Typology of natural fractures characterised on UBI images

THE characterisation of natural fracture on acoustic borehole image has been done using a modified typology initially developed in BRGM (*Maqua*, 2003). The fracture types are coded on two digits. The first digit permits to distinguish between ‘open’ (1) and ‘closed’ (2) fractures. The second digit estimates the ‘physical importance’ (persistence, thickness, alteration,...) of the fracture (1-4) or the reliability of the sinusoidal fitting (5). In order to give an objective tool to estimate the ‘physical importance’ of the fracture, its visible length in comparison with the full length of the fitted sinusoid is used (1 = 100-80%; 3 = 80-50%; 4 = 50-0%; ‘2’ is reserved for alteration zone). Alteration is understood as a change of the image texture or color. Such thing occurs usually around well defined fractures, but not always. It may make a sinusoidal trace, indication of a planar structures cutting the borehole, but sometimes also the borders of such a zone are diffuse and unstructured. As usually such zones occur in halo around natural fracture traces, measuring them as independent fractures will induced that the same structure is measured twice. So I decided to exclude this class in my topology (this is the main difference with the original typology presented in *Maqua* (2003)), but in order to keeping the coding of fractures consistent with *Maqua* (2003), I didn’t change the numbering and so ‘2’ as a second digit never occurs. A summary of this topology is presented in the table A.1.

Table A.1: Fracture typology developed by BRGM. Modified version after *Maqua* (2003).

		1st digit	
		open 1	close 2
2nd digit	fully visible (>80%) 1	11	21
	good visible (50-80%) 3	13	23
	poor visible (0-50%) 4	14	24
	uncertain sinusoidal fitting 5	15	25

In spite of a clear typology, as objective as possible, the inherent subjectivity of any analyst influence the obtained results. The wells GPK 2, 3 and 4 being analyzed by different peoples, a direct quantitative comparison between the wells has to be taken with some circumspection. In order to get an impression of this analysts dependency I look at a section of GPK3 between 2000 and 2200 mBD using the same facilities described here over than I have for GPK4, i.e. 3 media simultaneously with WellCad as main tool. I compare then my results with the ones obtain by *Maqua* (2003). The two analyze show reasonably similar results. Looking closer to the two data sets, some discrepancies are noticeable. The main source of these discrepancies is the interpretative process which consists in differentiating between natural and induced fracture. Indeed 'en echelon' type of induced fractures is sometime hard to objectively differentiate with the poor visible fractures. To avoid confusion, it is recommended to pick induced and natural fracture simultaneously. This permits to add a conscious active process managing this difficulty in the analysis procedure. Another source of discrepancy is due to the subjective fixing of the uncertainty level potentially varying with each analyst.

A.1 Some other reflection on significance of UBI-images

In order to do sensible interpretation of UBI image in terms of geology, hydraulic or stress determination some important things to know are listed and commented in this section. The main message to be understood is while reading the results of fracture determination, it is necessary to keep in mind a distinction between the picking criteria and the physical (geological) significance of the picked structure. Moreover some terminology used in the typology has the default to mix somehow these two points.

Open–close

By ‘open’ or ‘close’ determination, the underpinning picking criteria is ‘visible on the transit time log’, respectively ‘not visible on the transit time log’. An interpretation of this in term of open or close fracture is sensible but should not be understood with too much confidence in its hydraulic sense. Example of the possible interpreting of an ‘open’ fracture are shown on figure A.1. First the presence of a trace on the transit time could be due to an artefact on first arrival picking (cycle skipping). Second opening of the fracture at the borehole wall do not imply that this opening as a significant persistence. Same UBI signature of the same fracture could have very distinct hydraulic sense depending on the interpretation made (totally or partially fracture filled with attenuating material).

Alteration

To discuss geological alteration on UBI image is somehow difficult while geologic and non-geologic features may produce ‘alteration’ of the UBI image. It is then recommended to compare with other logs (e.g. gamma ray log, cuttings) before definitively interpreting alteration seen on UBI images to be rock alteration in its geological sense. The alteration zone orientations are although sometimes difficult to estimate. If some alteration zones have clear border permitting sensible sinusoid fitting, other are more diffuse and then determining their orientation become very hazardous.

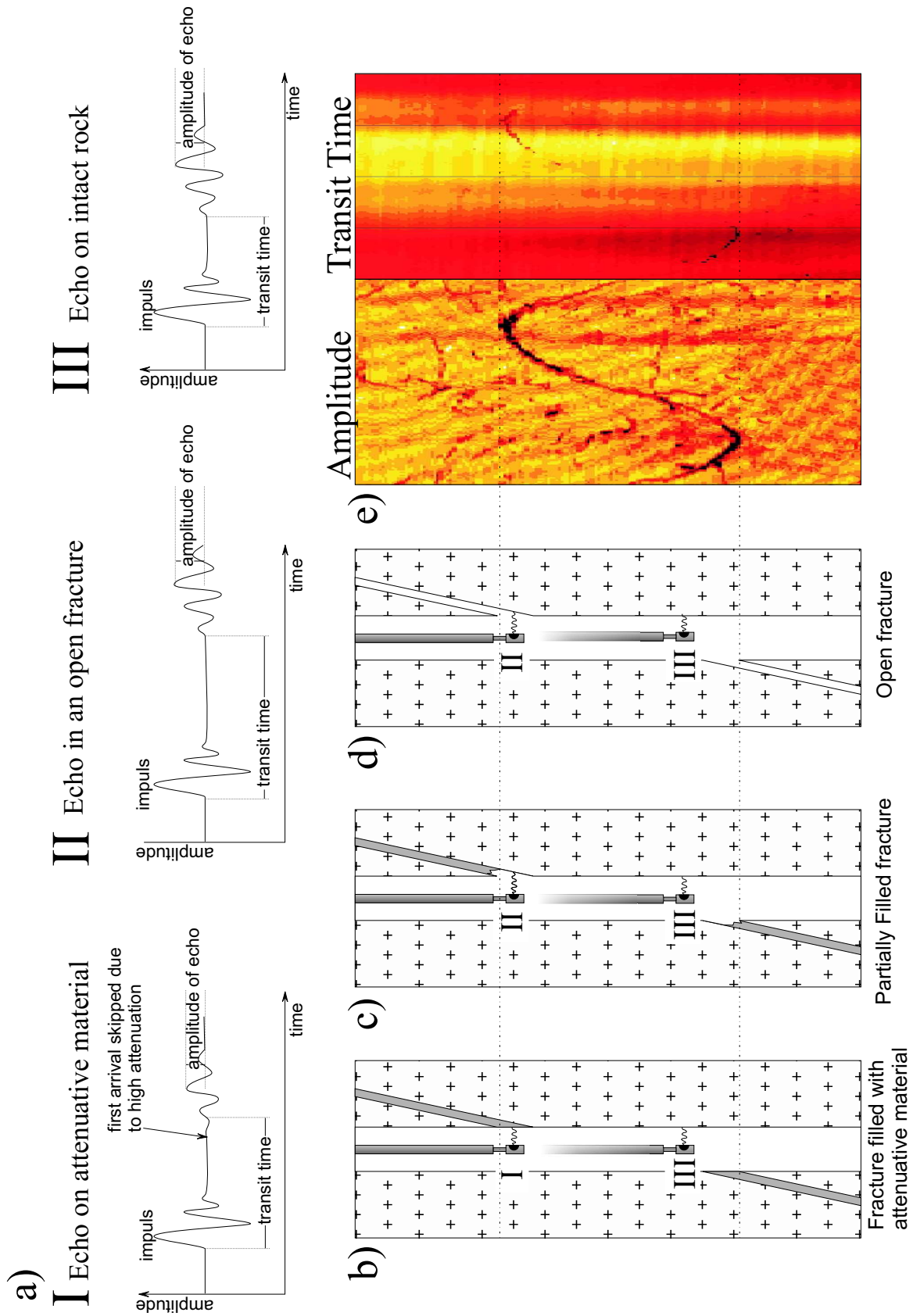


Figure A.1: (on page 200 Explanation of the Open-Close concept for BHTV images. a) Determination of the transit time. I) if there is strong attenuations the first arrival may be skipped. This will produce a trace on the Transit Time image which do not reflect a true open fracture. II) In an open fracture, the borehole cross-section is truly enlarged which will be seen as higher Transit Time. III) Again intact borehole wall, the echo will reflect directly and the Transit Time will be shorter than in the case of open fracture. a) b) and c) are three possible interpretations of the borehole images displayed in e).

B Second appendix - Variogram analysis of synthetic data

THE analysis of variogram in term of their geological meaning is not trivial. That appendix presents variogram analysis of simple synthetic data which help to understand the impact of fracture organisation changes on variograms.

The variogram permits to examine the spatial relation within a data set. The general principle is to compare the variance of the entire sample to the variance with subset of the sample. Subsets are built after their spatial relation, i.e. after their distance to each other. If the fractures are clustered, groups of fractures with small spacing will be seen, separated by fractures with relatively large spacings. So a subset of spacing close to each other will have a smaller variance that the entire sample whereas spacing at larger distance may have variance similar that the variance of the entire sample. The variogram values γ are computed with the equation 3.1.

Figure B.1 shows this procedure as well as it introduce some terminology associated with variogram. As it has been initially in geology used two assess ore concentrations, terminology is derived from ore exploitation word pool. The nugget value is the difference of variance with directly neighboring measurements. It quantifies how strong the value at a given place influences the value at the next place. The range of influence or simply range is the distance from which variance of sub sample is not substantially different from the variance of the complete sample. The sill value is the value toward γ strives. It is usually equal to the variance of the entire sample.

On the first Figure (Figure B.2), you will see a random sample of spacing following a exponential law. As spacing organization is purely random, the variance of any subset will be not much different that the spacing of the entire sample. Indeed, you can assess on the variogram that the nugget value is about equal to the variance and that the range is about equal to zero. An other end extreme case to this is presented on figure B.3. Exactly the same spacing sample than in Figure B.2 is used, but spacings have been sorted in ascending order. So concerning the statistical descriptor used until here (mean, standard deviation, CV , ...) , no differences are noticeable, however the variogram is sensitive to this major change. As in that case small spacing as well as big spacing will be close together, for small value of distance h , variance of sub samples will be significantly lower than the variance of the entire sample whereas for high h values, variance of sub sample will be much higher than for the entire sample. Figures B.4 and B.5 show how behave the variogram if cyclicity is introduced. The samples are always exactly the same, but spacings are sorted in a way that makes

cyclicality. Variograms will catch the cyclicality in the sample and γ values will oscillate around the variance of the entire sample. In the last figure of this suite (figure B.6) some noise has been added to the spacing in order to simulate natural process. In that case, you get a non-nul nugget values, a small range and a clear cyclicality of the data.

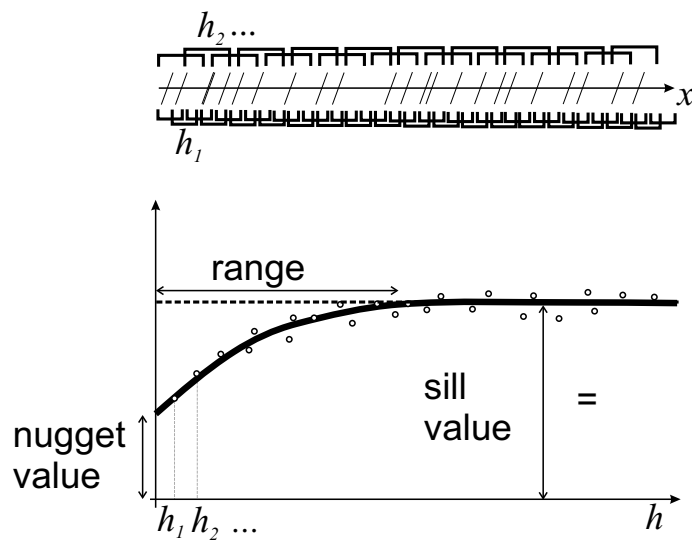


Figure B.1: Schematic display of a variogram and associated terminology. See text for details

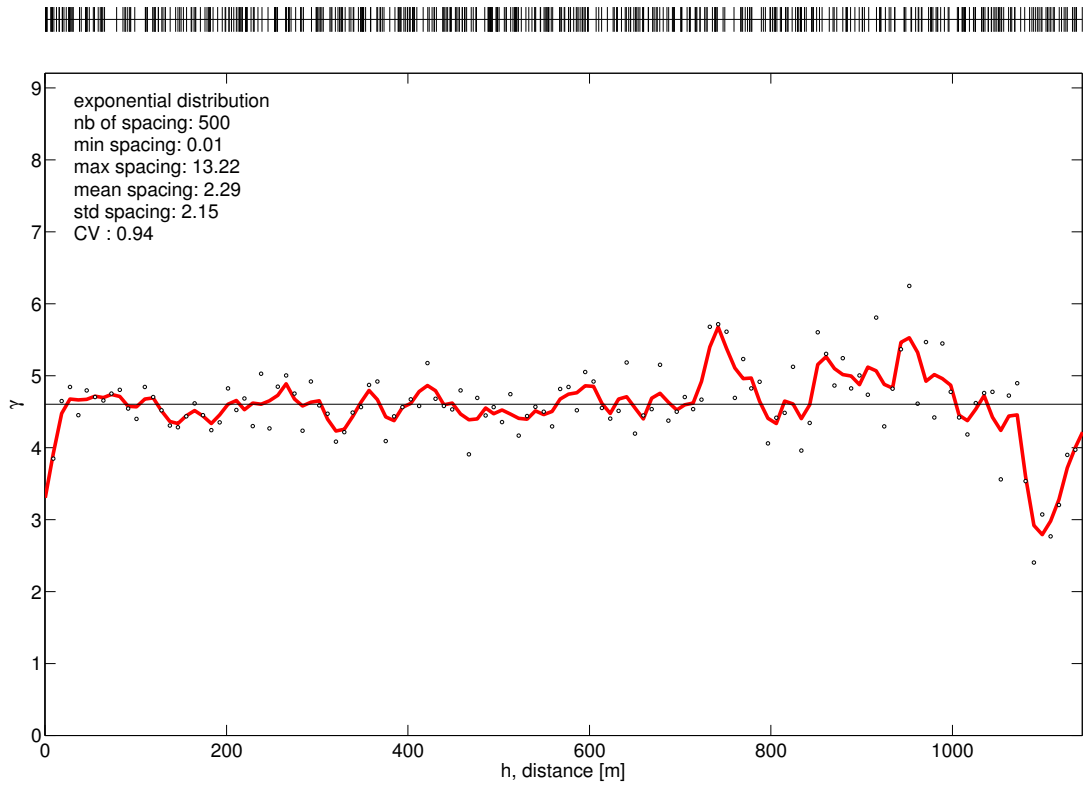


Figure B.2: Variogram for synthetic data. The dots are the computed variogram values. The red line is smoothed fit to the data using a locally weighted scatter plot smooth using least squares linear polynomial fitting. Horizontal black line is the variance of the complete sample. See text for details.

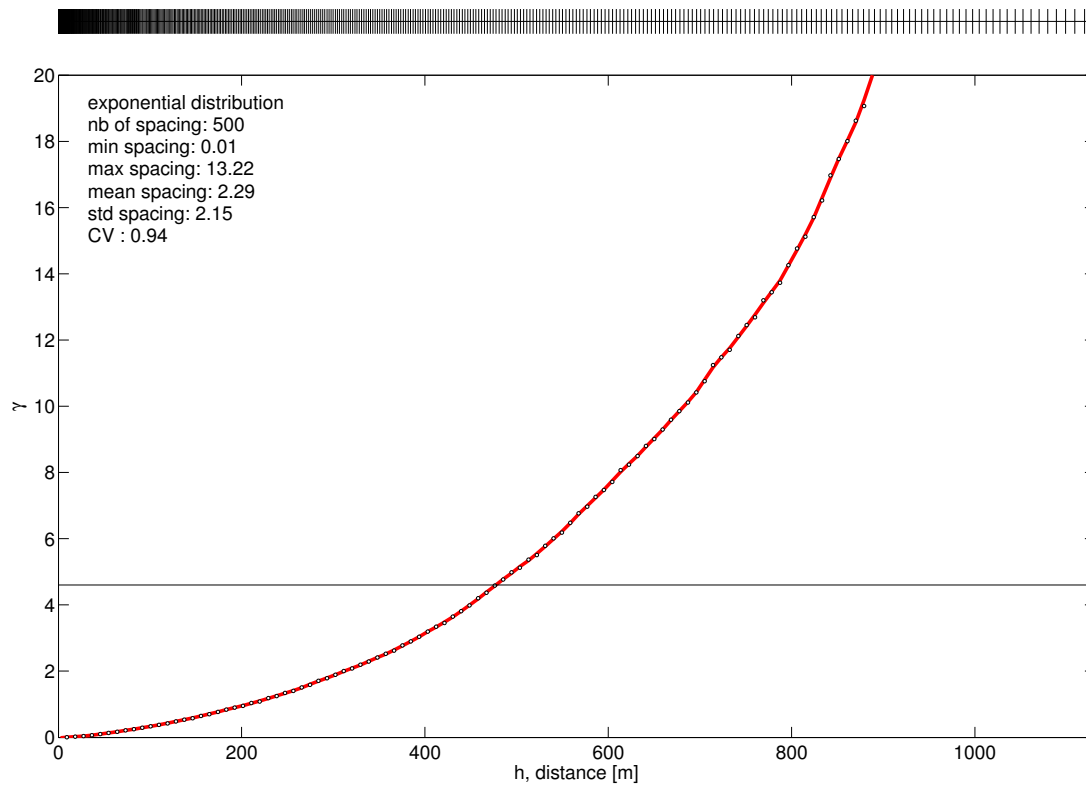


Figure B.3: Variogram for sorted synthetic data. The dots are the computed variogram values. The red line is smoothed fit to the data using a locally weighted scatter plot smooth using least squares linear polynomial fitting. Horizontal black line is the variance of the complete sample. See text for details.

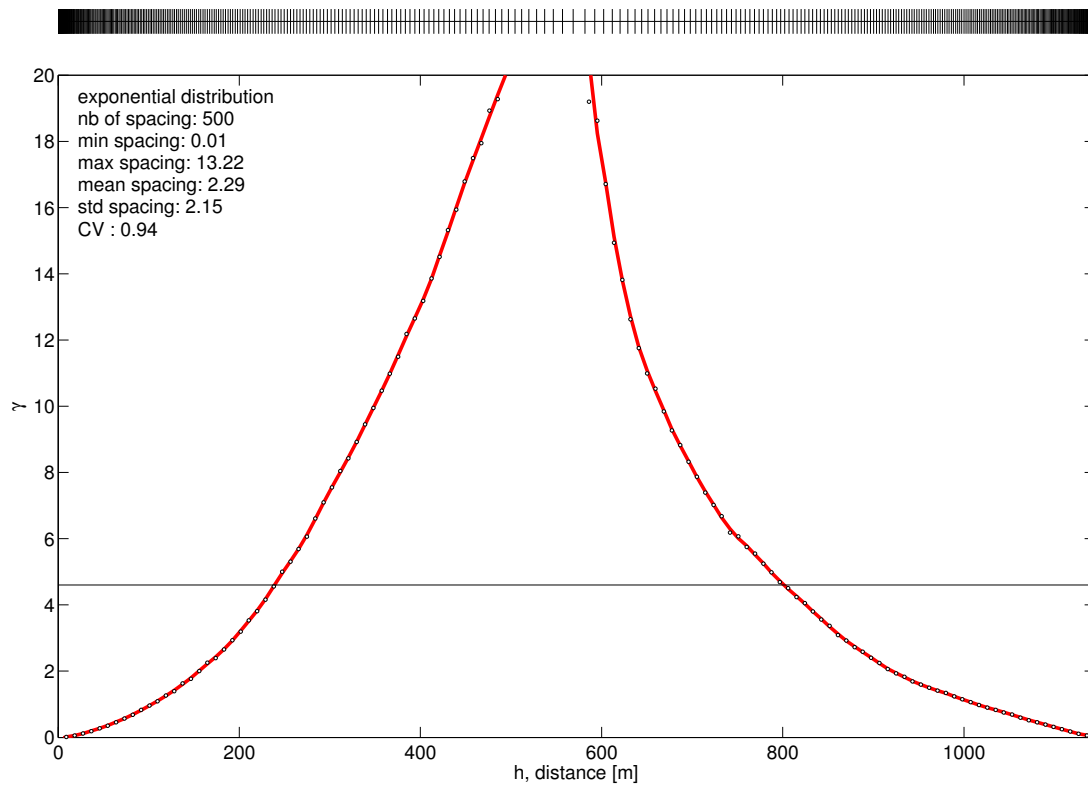


Figure B.4: Variogram for sorted synthetic one-cycled data. The dots are the computed variogram values. The red line is smoothed fit to the data using a locally weighted scatter plot smooth using least squares linear polynomial fitting. Horizontal black line is the variance of the complete sample. See text for details.

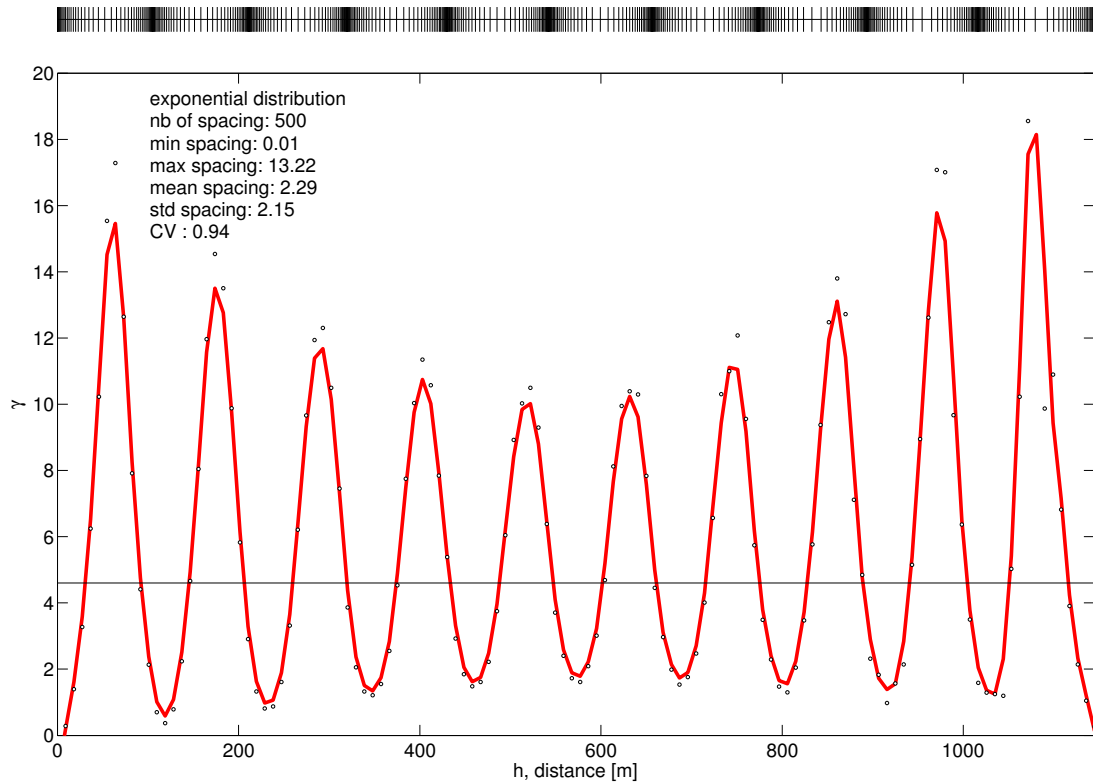


Figure B.5: Variogram for synthetic multi-cycled data. The dots are the computed variogram values. The red line is smoothed fit to the data using a locally weighted scatter plot smooth using least squares linear polynomial fitting. Horizontal black line is the variance of the complete sample. See text for details.

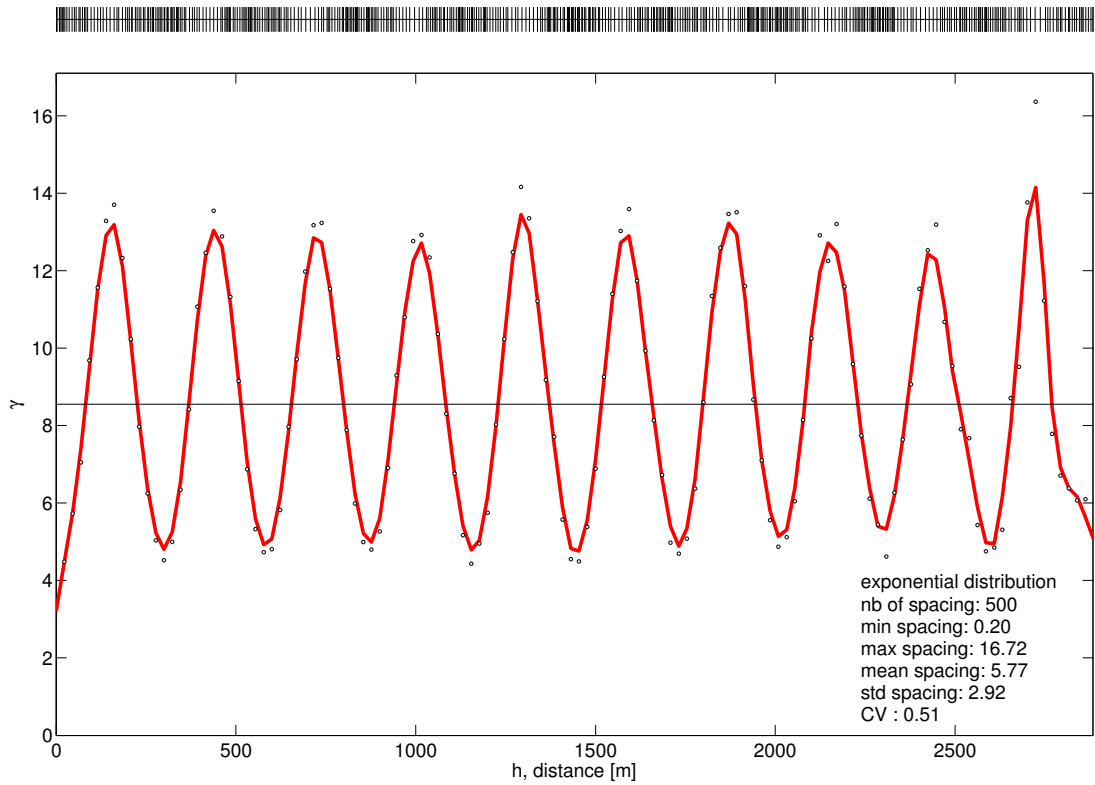


Figure B.6: Variogram for noisy synthetic multi-cycled data. The dots are the computed variogram values. The red line is smoothed fit to the data using a locally weighted scatter plot smooth using least squares linear polynomial fitting. Horizontal black line is the variance of the complete sample. See text for details.

C Third appendix - Methodology for fracture correlation

A special methodology which permits to correlate fractures between two boreholes has been developed. The present appendix gives the details of this correlation procedure.

C.1 Description of the method

Each fracture is defined by three elements, its measured depth (along borehole), its azimuth (dip direction) and its dip angle (angle with horizontal). Knowledge on the borehole trajectory and its uncertainty permit to compute a geographical position of the fracture in the easting, northing and vertical direction as well as inaccuracy related to the measurements of this position. Inaccuracies on the azimuth and dip angle are due to inaccuracies in borehole orientation survey and to inaccuracies in sinusoidal fitting. The second element has been evaluated by repeated measurements of the same features. Standard deviation on azimuth has been determined to be 2.5° and standard deviation on dip angle is 0.75° . These determinations have been made on fractures with orientation of 285/74. If the fracture is about horizontal, azimuth will be much more uncertain, but this is although not so important because angle between two about horizontal fractures do not depend much on the azimuth value. Adding to them the uncertainty on borehole trajectory leads to inaccuracies of about 4.5° on azimuth and 1° on dip angle.

So, each fracture \mathbf{F} can be describe by 5 random variable, x , y , z , α and ϕ , i.e. easting, northing, vertical depth, azimuth and dip angle. It is then assumed that each of these random variable follow a normal distribution parameterized by its mean and standard deviation. Mean for position are considered to be well approximated by deriving them from computed borehole trajectories. Mean on azimuth and dip angle are assumed to be well approximated by the measurements done on borehole images. Standard deviations for GPK3 have been determined by analysis of repeated trajectory logs to be 0.34 m in easting, 0.30 in northing, 2 m in vertical direction, 4.5° on azimuth and 1° on dip angle. For GPK4 there are in the same order, i.e. 0.40 m, 0.29 m, 2 m, 4.5° and 1° .

The distribution of these 5 variables at the location of the opposite borehole is then determined using Monte Carlo simulations: realisations for the five random

variables are drawn and for each of them, intersection with a possible trajectory of the opposite is computed. Possible trajectory for the opposite borehole are although generated through Monte Carlo process by including uncertainty on borehole azimuth and borehole deviation at each station of the borehole survey log. This process permits to compute the random variable for position at the location of the other borehole. Random variables for orientation are kept identical by changing borehole. So now for a fracture \mathbf{F} of the first borehole, an equivalent fracture $\mathbf{G}_{\mathbf{F}}$ at the level of the opposite borehole is computed. $\mathbf{G}_{\mathbf{F}}$ can be compared with all the fractures $\mathbf{G}_{i=1}^n$ of the second borehole in order to obtain their probability p to be identical. This is done by computing the area under common to both normal distributions. This complete complex process is illustrated on Figure C.1. Finally by repeating this process for all fractures, i.e for each couple of fracture on both borehole $\mathbf{F}_i\mathbf{G}_j$, the probability that both fracture are aligned can be computed.

C.2 Complete example of correlation

In order to clarify this procedure, I will show in the following step by step the process of correlation of a fracture couple. The tested fractures will be a fracture which intersects GPK3 at 1496.19 m BD, oriented 084/72 and a fracture intersecting GPK4 at 1467.64 m BD with an orientation of 083/72. Results of this analysis are presented on table C.1 and Figure C.2. The central frame of Figure C.2 (e) shows the situation. This is a projection of the boreholes and fractures in a E–W vertical plane. Because fractures are dipping to the east, they will show about their true dip in such a projection. The fracture of GPK3 is called \mathbf{F} and is presented in red in the lower right corner of the frame. GPK3 trajectory is presented in green. The fracture of GPK4 is called \mathbf{G} and is displayed in orange in the upper left corner of the frame. The dark blue line is the trajectory of GPK4. The light blue lines are 300 possible alternate trajectories for GPK4 computed using a Monte Carlo process as described above. Fracture \mathbf{F} is described by random variables following distributions presented in the four right frames (Figure C.2f – i) as derived above. For orientation, for simplification reasons both angles (azimuth and dip) have been associated and normalized to be presentable with a normal distribution. Indeed, to be perfectly rigorous, orientations data should be handled on a sphere with a Fisher distribution, but for seek of simplicity I simplify the problem and handle it with a normal distribution. Fracture \mathbf{G} is also describe by random variables. Distributions for these variables are presented in orange on the four left frames (Figure C.2a – d). Using a Monte Carlo simulation, the position of 2000 possible intersection between \mathbf{F} and GPK4 are computed. These intersections are called $\mathbf{G}_{\mathbf{F}}$. Histograms in the three geographical directions are present in light violet on Figure C.2a – d. Normal distribution are fitted to them in order to estimate the parameters of the distributions of $\mathbf{G}_{\mathbf{F}}$. It's now possible to compare the distributions for \mathbf{G} and $\mathbf{G}_{\mathbf{F}}$ in order to compute the probability that

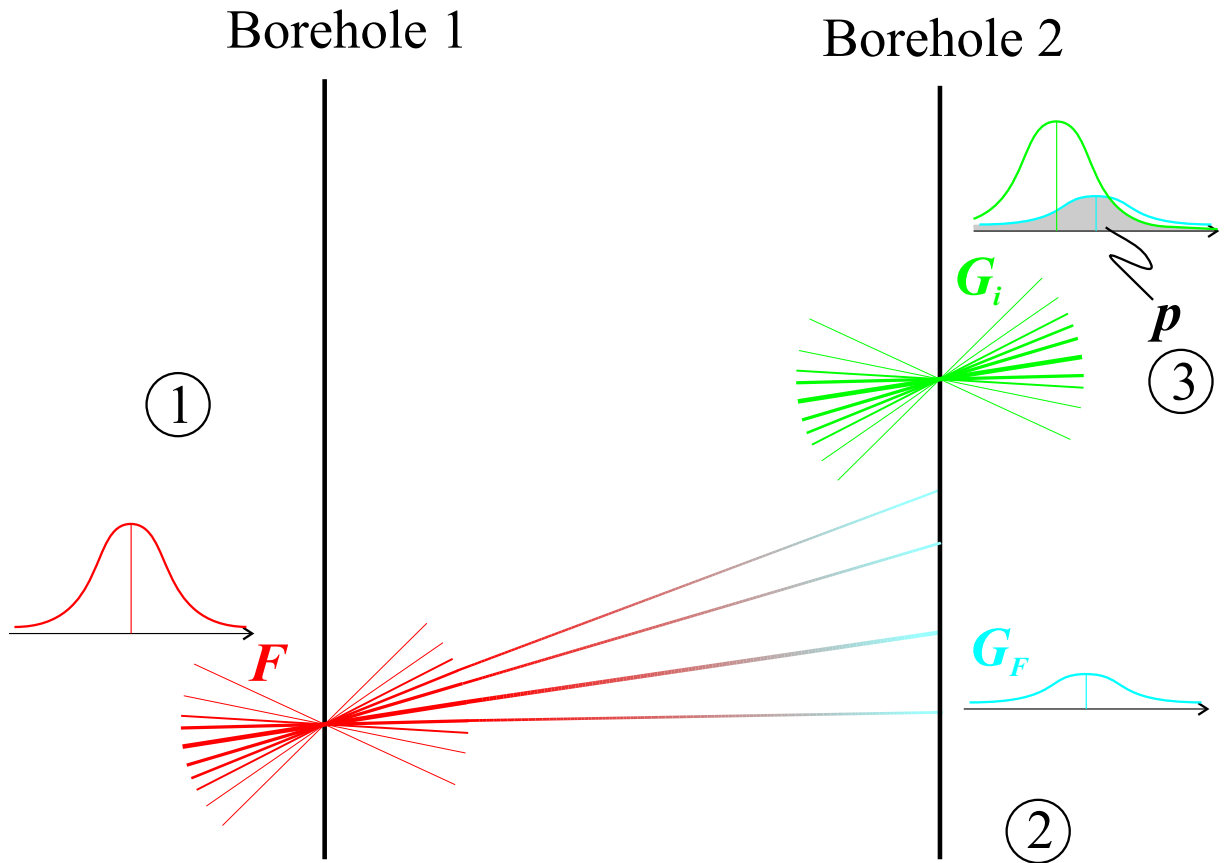


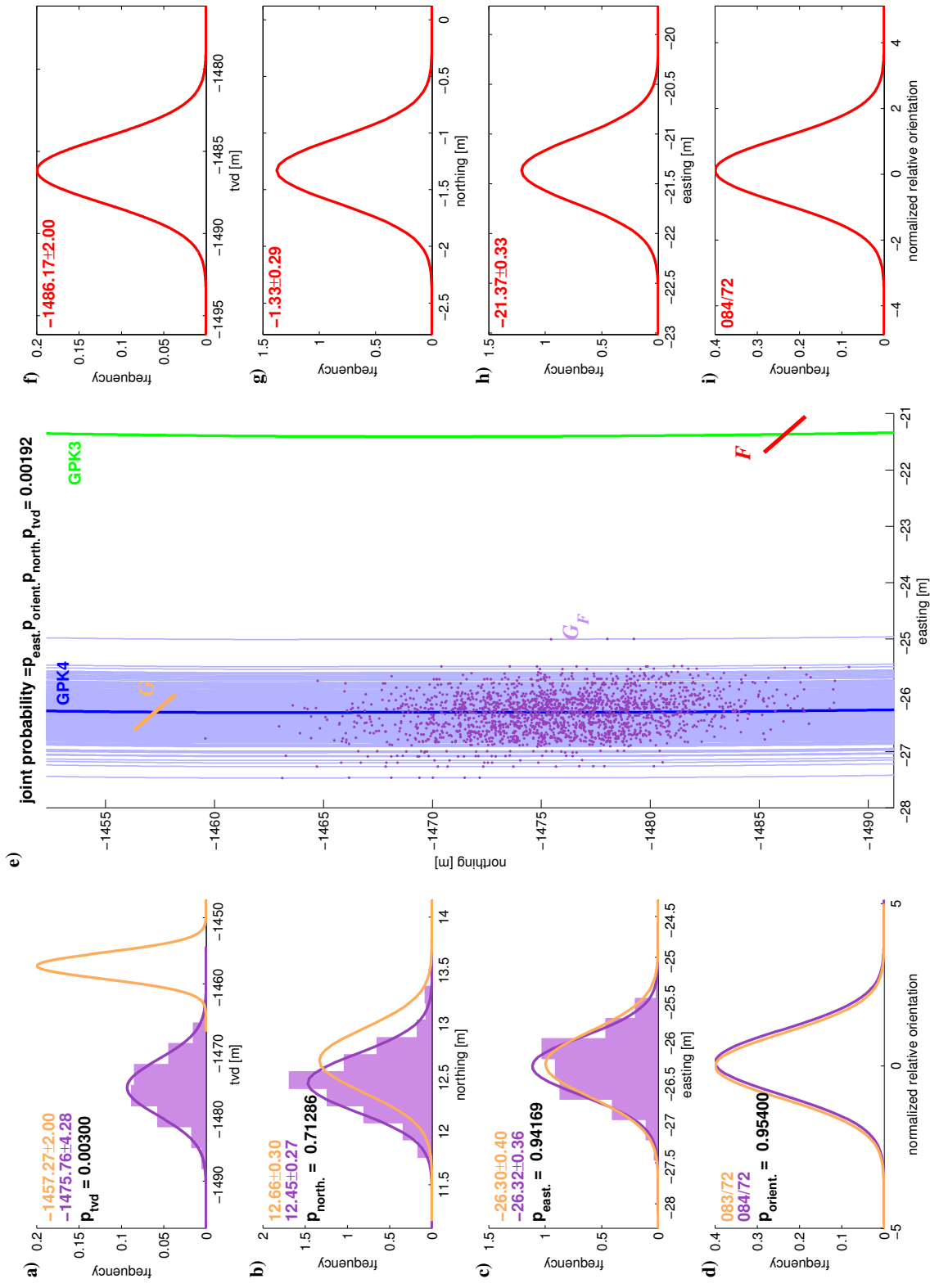
Figure C.1: The process of fracture correlation between both boreholes consists of three main steps. (1) For a given fracture F on borehole 1, the five random variables, three for position and two for orientation are parameterized. Here for schematic purpose only one gauss curve is presented, but there are five of them, one for each variable. (2) Using Monte Carlo simulations, the five random variables for the equivalent fracture G_F are parameterized at the level of the second borehole. (3) The random variables of G_F are compared with the random variables of the fractures of the second borehole $G_{i=1}^n$ in order to compute p , the probability that both fracture are identical. So finally by repeating this process for all fractures of borehole 1, for each couple $F_i G_j$, a probability can be computed.

fracture	borehole depth [m]	orient- ation [°]	easting [m]	northing [m]	tvd [m]
F in GPK3	1496.19	084/72	-21.37±0.33	-1.33±0.29	1486.17±2
G in GPK4	1467.64	083/72	-26.30±0.40	12.66±0.30	1457.27±2
F_G		084/72	-26.32±0.36	12.45±0.27	1475.76±4.28
probability of intersection		0.95	0.94	0.71	0.003
joint probability of intersection: 0.0019					

Table C.1: Results of an example of fracture correlation. See also Figure C.2

both fracture are aligned. This is done measuring the intersection area of the curves for G (orange curves) and G_F (violet curves). On vertical axis (a), intersection is very small. On easting, northing and orientations (Figure C.2b–d) probability is quite high. The joint probability is obtained by multiplying all probability together. In our case, probability is low, i.e. 0.00192. This is in agreement with what we observe in the middle frame of the Figure C.2, i.e. these fractures are poorly correlated.

Figure C.2: (on page 215) Example of fracture correlation. The situation is exposed on the central frame (e). The goal is to see if the fracture F on GPK3 is correlated with the fracture G on GPK4. In this view, boreholes and fractures are projected in e W–E vertical plane. Borehole GPK3 is the green line on the right of the frame. GPK4 is the blue line on the left. The array of light blue line represent alternative trajectory for GPK4 produced with a Monte Carlo process. Random variables determining fracture F are presented on frame (f) to (i). Using these random variables a Monte Carlo process permits to find possible intersection G_F of F with GPK4. These intersections are represented as the violet points. From this points clouds, it is possible to extract the characterization for the random variables of G_F . Obtained values are displayed on frames (a) to (d) in violet. It is then possible to compare these random variables with the ones of fracture G , presented in orange on frames (a) to (d). For each of them, the probability p of intersection can be computed by measuring the common area for both curves. By multiplying them, I obtained a joint probability of correlation of the fracture F with the fracture G .



C.3 Processing of the GPK3 and GPK4 data set

Combining the 1871 fractures of GPK3 with the 2215 fractures of GPK4 allow to test 4144265 intersections. All of them have been tested on both directions, i.e. from GPK3 to GPK4 and from GPK4 to GPK3. A scatter plot of these results is present on Figure C.3 The vast majority of these intersections are far to be confirmed as they have very little probability. Ideally, tests from GPK3 to GPK4 should produce the same results than test from GPK4 to GPK3. This is not always the case because of complex geometry of the borehole and the correlation method. An example of such a case is presented in Figure C.4. The correlation from GPK4 to GPK3 is much lower than from GPK3 to GPK4. To consider this problem I multiplied results from both directions analyzes. The final result for the example of Figure C.4 is low which is in my view in agreement with the reality. So after calculating for both correlation direction a probability of intersection and multiplying them, I obtained for each of the 4144265 potential correlation a *index for relative goodness of correlation*. Only 0.163%, i.e. 675 of them have an index higher than 0.001 . The highest index obtained is 0.46. Figure C.5 presents an histogram of the index higher than 0.001. The next step is then to choose a threshold for this index over which the correlation will be stated as accepted. This is not easy because there are a continuity between very low index to high index. There isn't in the data a clear gap between very low values which will correspond to uncorrelated fractures and high values which will correspond to correlated fractures. Nevertheless from Figure C.5 it is quite clear that index higher than 0.1 are singular and will then highly probably correspond to correlated fractures. All correlation with index higher than 0.01 are accepted and all fracture couple with index lower or equal to 0.01 are discarded. This let us with 280 possible correlation between GPK3 and GPK4 presented on Figure C.6 (a) and (c). The process do not guaranty that each correlated is linked with a unique fracture on the other borehole. The 280 fractures have then to be sorted for uniqueness giving priority to links with high index. This lead to 101 correlated fracture for which there is the guaranty that each correlated fracture of GPK3 is linked with a single fracture on GPK4 and vice versa.

As the sorting process give favor to higher index, the 101 correlated fracture couples between GPK3 and GPK4 have relatively high correlation index. This is shown on Figure C.7. About 53% of the fracture couples have correlation index higher than 0.03.

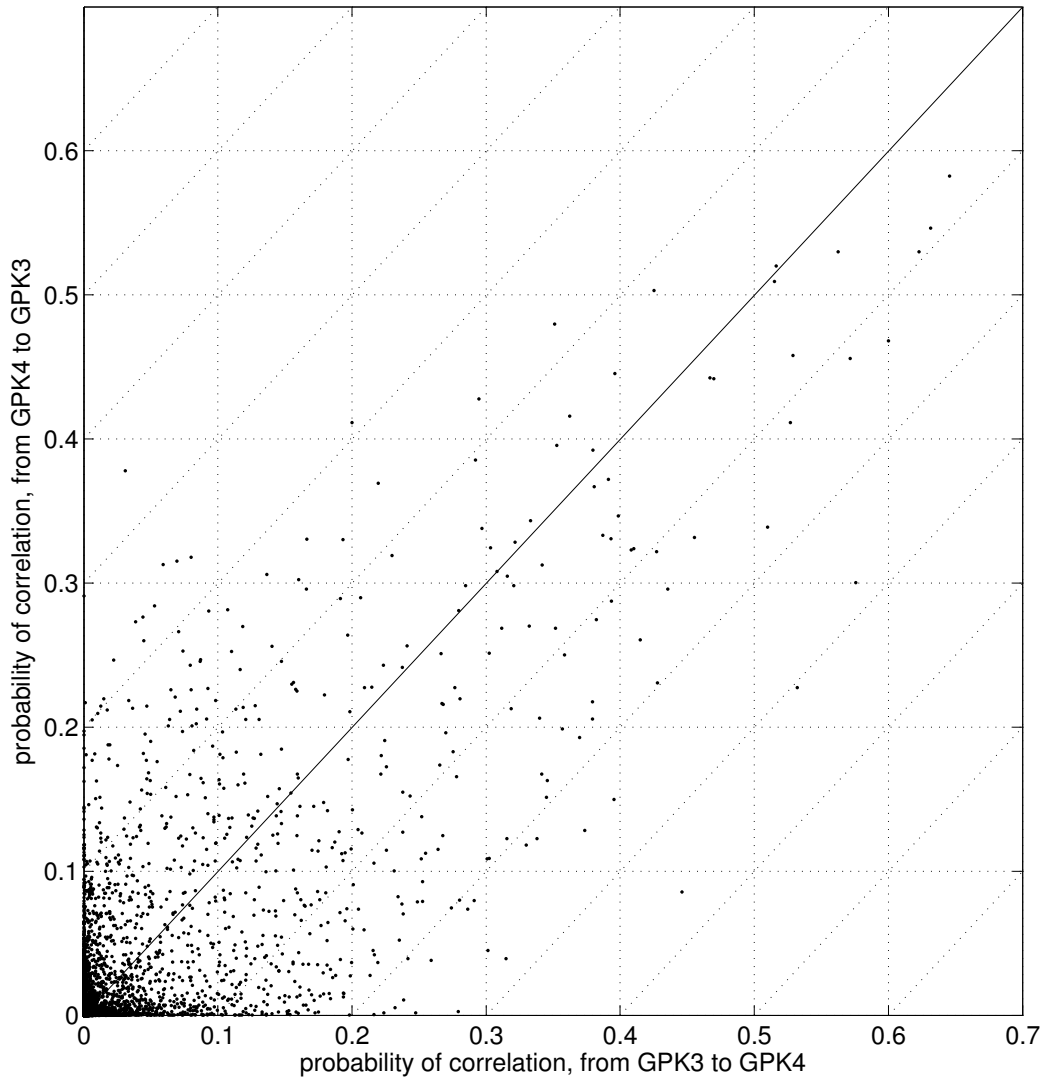


Figure C.3: Scatter plot of correlations results from GPK4 to GPK3 versus correlation results from GPK3 to GPK4 for all fracture couples.

C Third appendix - Methodology for fracture correlation

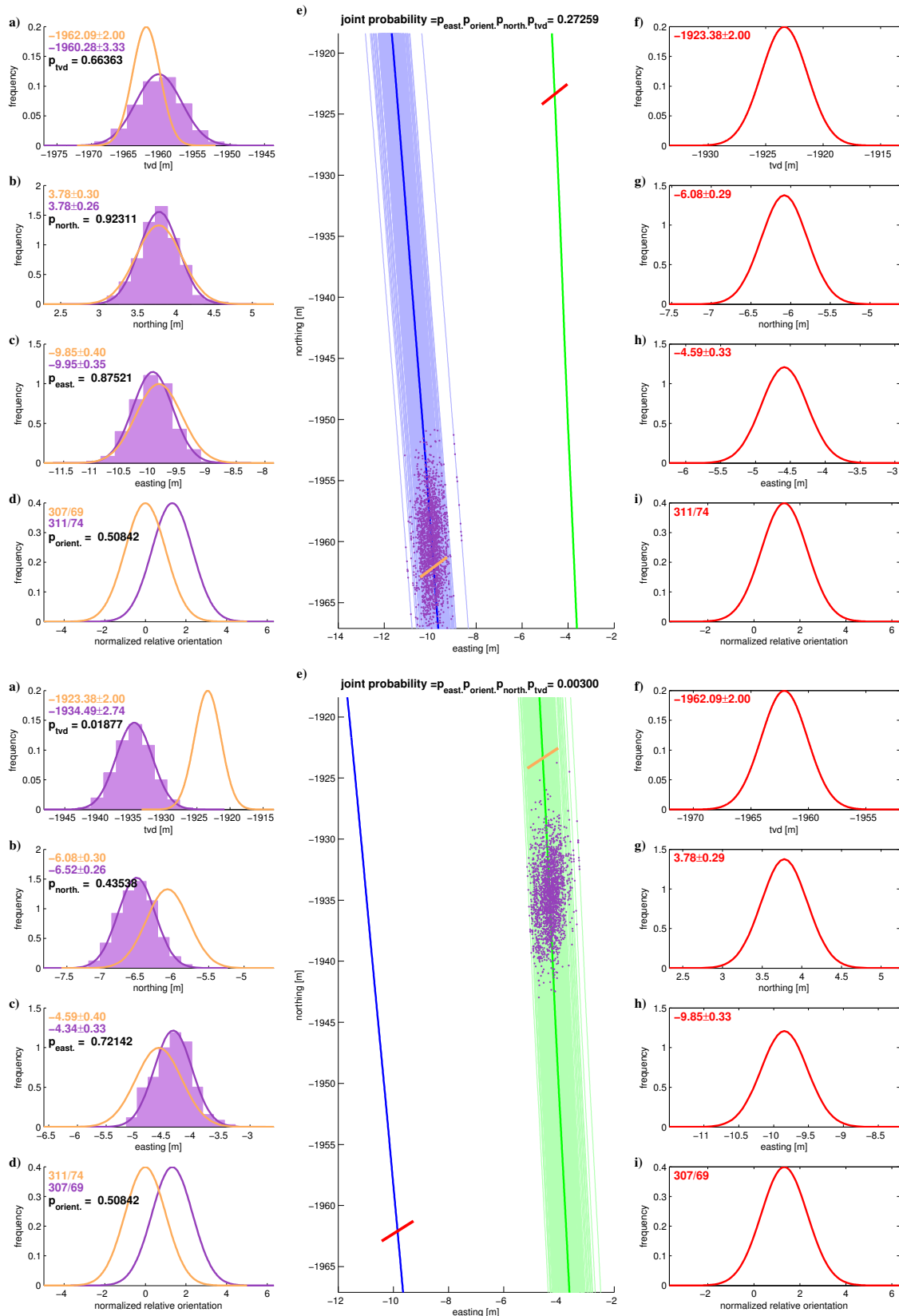


Figure C.4: (on page 218) Example of fracture correlation where the result obtained by correlating from GPK3 to GPK4 is quite high (0.27) while the result obtained by correlating from GPK4 to GPK3 is much lower (0.003). The combined result is obtained by multiplying both results and is low (0.0007) which is in my view in agreement with the situation.

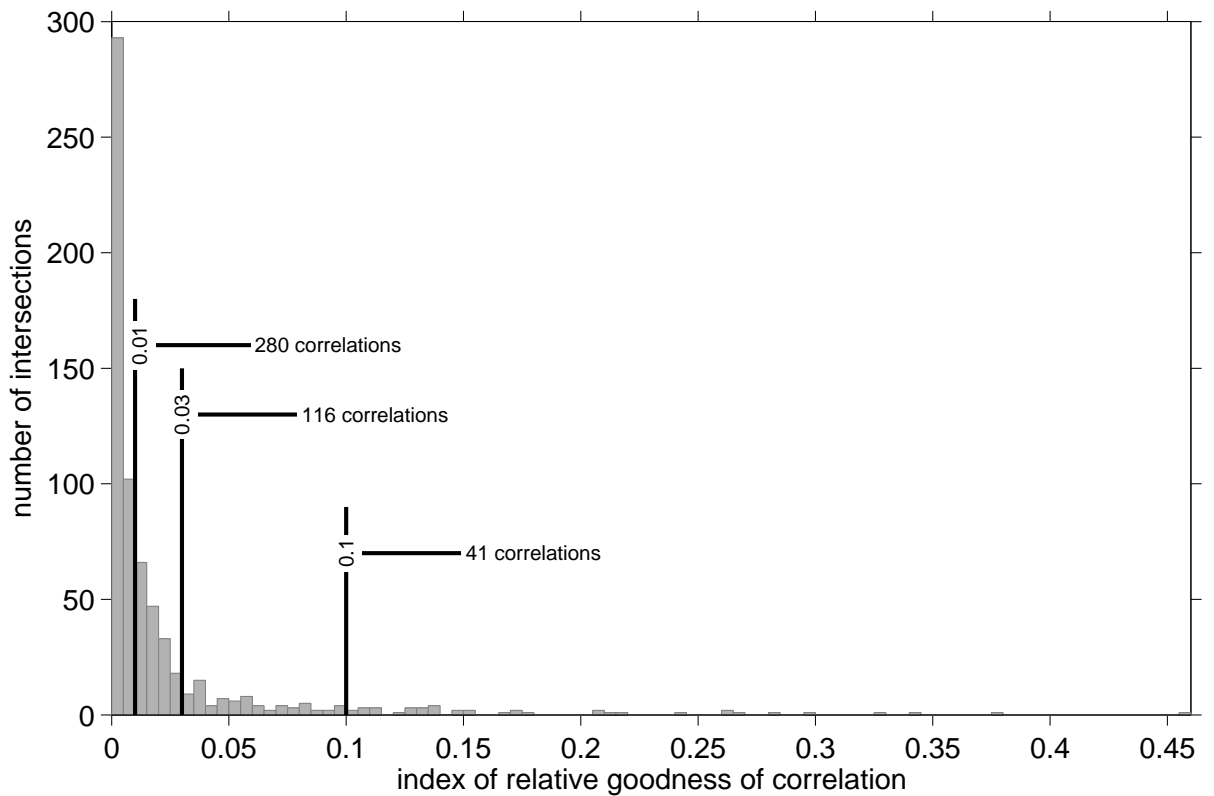


Figure C.5: Histogram of index of relative correlation.

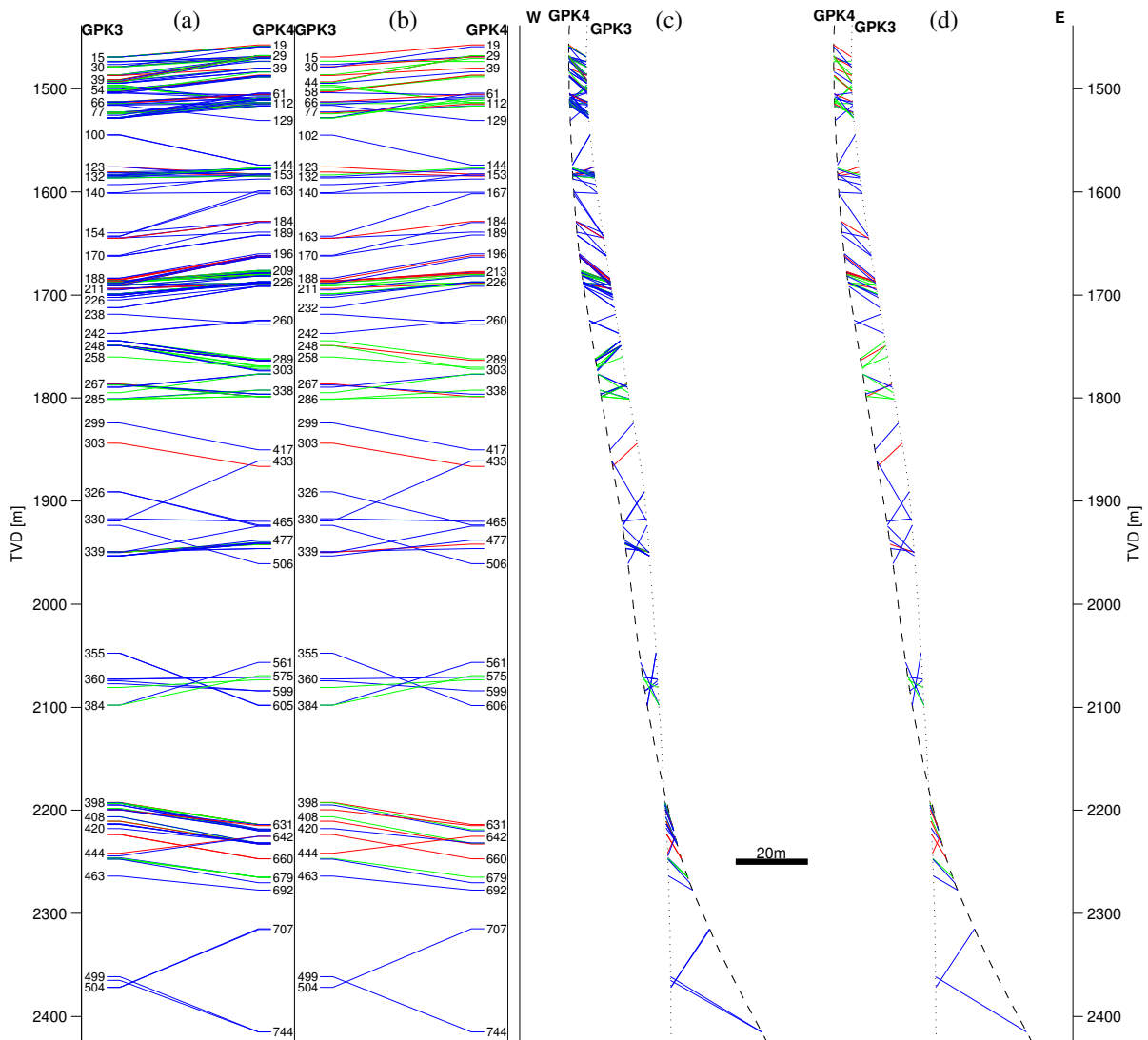


Figure C.6: This figure presents the correlated fractures between GPK3 and GPK4 using a threshold on correlation index of 0.01. (a) and (c) present the 280 possible correlations in respectively showing it as fractures numbers and in a E–W projection of the borehole trajectory. (b) and (d) present the 101 correlated fractures after sorting them for uniqueness. Blue links denote correlation index between 0.01 and 0.03. Green links between 0.03 and 0.1 and red links higher than 0.1. Notice that in frames (a) and (b) not all fracture numbers have been displayed for readability purpose.

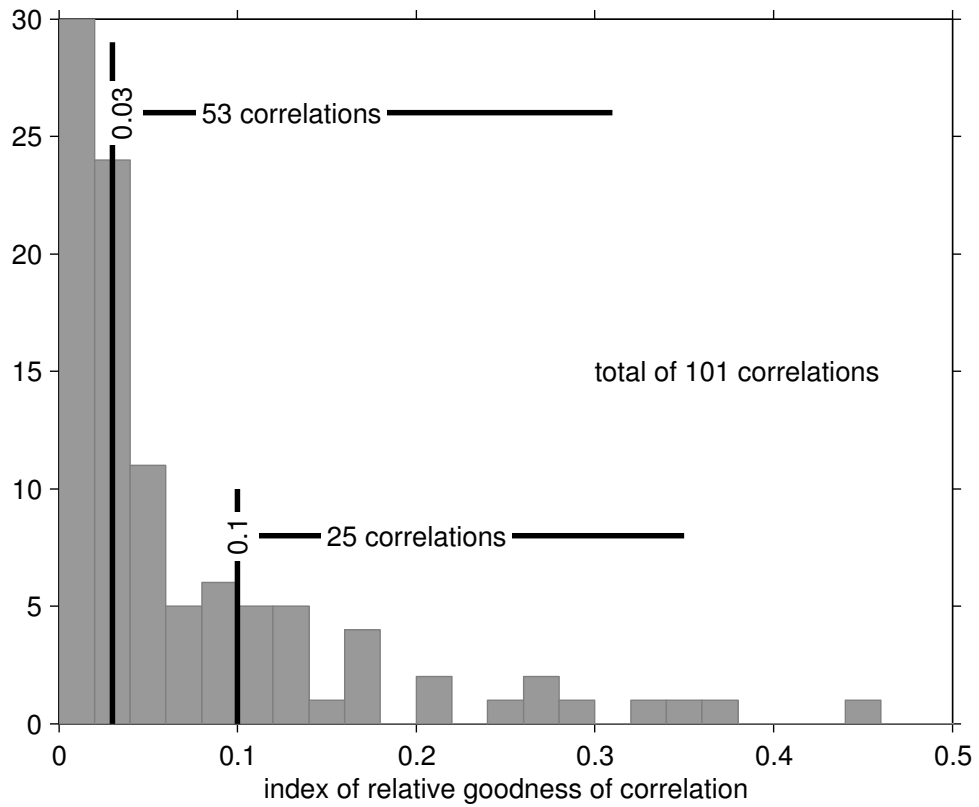


Figure C.7: Index of goodness of correlation for the 101 correlated fractures.

D Fourth appendix - Stress around a wellbore

THIS appendix contains the necessary mathematical background in order to compute the stress around a wellbore arbitrarily oriented to the principal stress directions. The general approach is the one presented in *Peška and Zoback (1995)*, Appendix A (p.12807–12808) and initially developed by *Hiramatsu and Oka (1968)*. The reason to developed that solution again here under is first that it is of key importance for most of the work done on wellbore failure analysis and second it also permits to correct a sign error occurring in the *Peška and Zoback (1995)* contribution (compare *Peška and Zoback (1995)* equation A9, with the here under equation D.11). In addition, the solutions for the thermal stress arising from the cooling of the wellbore wall are also exposed here.

D.1 Stress transformation between principal stress, geographical and borehole coordinate system

In any point in space, the stress tensor \mathbf{S}_{lmn} can be defined by six parameters, i.e. three principal stress magnitudes, S_1 , S_2 and S_3 , and three angles, α , β and γ , which define the principal stress orientations:

$$\mathbf{S}_{lmn} = \begin{bmatrix} S_1 & 0 & 0 \\ 0 & S_2 & 0 \\ 0 & 0 & S_3 \end{bmatrix} \text{ and } \alpha, \beta, \gamma \quad (\text{D.1})$$

The angles α , β and γ are called Euler angles and permit to describe the orientation or the principal stress axes $(\vec{l}, \vec{m}, \vec{n})$ (Figure D.1b) relatively to a geographical reference coordinate system $(\vec{x}, \vec{y}, \vec{z})$, with \vec{x} pointing to the North, \vec{y} pointing to the East and \vec{z} pointing downward (Figure D.1a). The relation between the geographical reference coordinate system and the principal stress coordinate system is defined by the following sequence of three rotations:

$$(\vec{x}; \vec{y}; \vec{z}) \xrightarrow{\text{rotation}(\alpha; \vec{z})} (\vec{x}'; \vec{y}'; \vec{z}') \xrightarrow{\text{rotation}(\beta; \vec{y}')} (\vec{x}''; \vec{y}''; \vec{z}'') \xrightarrow{\text{rotation}(\gamma; \vec{x}'')} (\vec{l}; \vec{m}; \vec{n}) \quad (\text{D.2})$$

So for example if S_1 is vertical, S_2 horizontal to N130° and S_3 horizontal to N40°

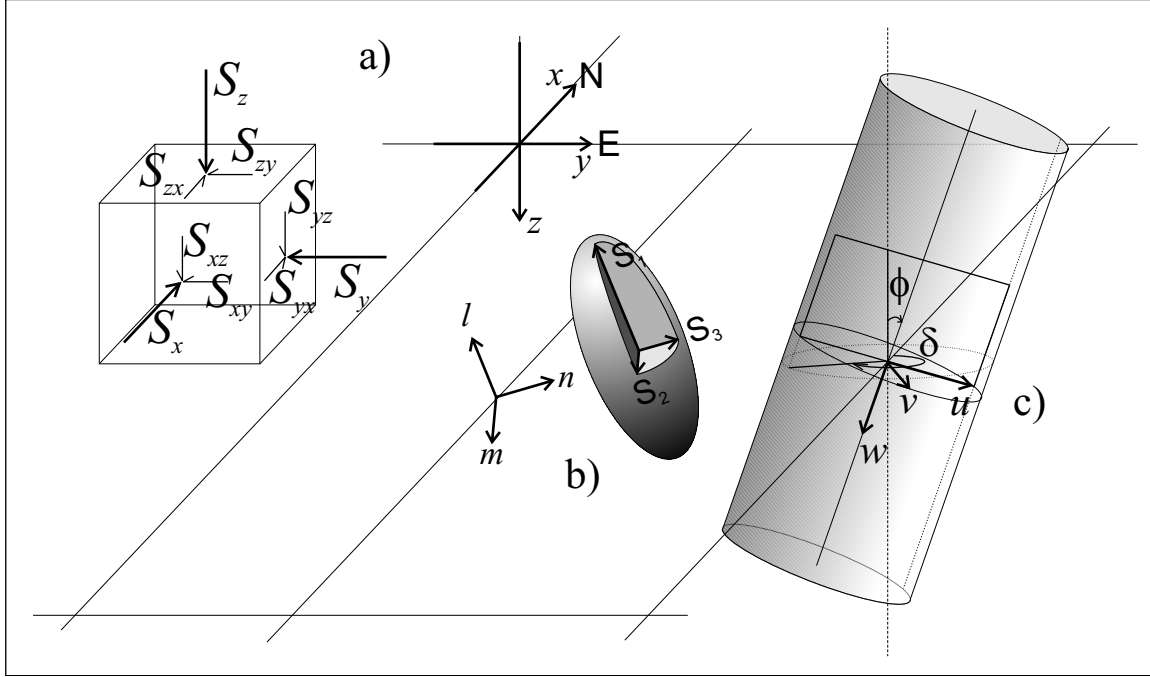


Figure D.1: coordinate systems. a) reference geographical coordinate system. b) principal stress coordinate system. c) borehole coordinate system. All systems of coordinate are positive orthonormed base.

the Euler angles will be $\alpha = 40^\circ$, $\beta = 90^\circ$ and $\gamma = 0^\circ$.

The following transformation of the principal stress matrix as to be applied in order to express the state of stress within the reference geographical coordinate system $(\vec{x}; \vec{y}; \vec{z})$:

$$\mathbf{S}_{xyz} = \mathbf{R}_{lmn}^T \mathbf{S}_{lmn} \mathbf{R}_{lmn} \quad (\text{D.3})$$

With \mathbf{R}_{lmn} being the direction cosine of $(\vec{l}, \vec{m}, \vec{n})$ relative to $(\vec{x}, \vec{y}, \vec{z})$, which can be computed using the Euler angles by the following expression:

$$\mathbf{R}_{lmn} = \begin{bmatrix} \cos \alpha \cos \beta & \sin \alpha \cos \beta & -\sin \beta \\ \cos \alpha \sin \beta \sin \gamma - \sin \alpha \cos \gamma & \sin \alpha \sin \beta \sin \gamma + \cos \alpha \cos \gamma & \cos \beta \sin \gamma \\ \cos \alpha \sin \beta \cos \gamma + \sin \alpha \sin \gamma & \sin \alpha \sin \beta \cos \gamma - \cos \alpha \sin \gamma & \cos \beta \cos \gamma \end{bmatrix} \quad (\text{D.4})$$

The stress state in the referential coordinate system will then have the following form as sketch in Figure D.1a:

$$\mathbf{S}_{xyz} = \begin{bmatrix} S_x & S_{yx} & S_{zx} \\ S_{xy} & S_y & S_{zy} \\ S_{xz} & S_{yz} & S_z \end{bmatrix} \quad (\text{D.5})$$

D.1 Stress transformation between principal stress, geographical and borehole coordinate system

In order to describe the state of stress around a borehole, the borehole coordinate system $(\vec{u}, \vec{v}, \vec{w})$ is defined with \vec{u} pointing downward perpendicular to the borehole axis and perpendicular to \vec{v} , \vec{v} horizontal and perpendicular to the borehole axis and \vec{w} aligned with the borehole axis and pointing downward (Figure D.1c). The borehole is considered as a cylinder with an orientation defined by δ , the borehole axis dip direction comprised in the interval $[0^\circ 360^\circ[$, and ϕ , the borehole axis angle with respect to verticality in the interval $[0^\circ 90^\circ]$. The natural state of stress, i.e. without the perturbation induced by the borehole, in the borehole coordinate system \mathbf{S}_{uvw} is given by the following expression:

$$\mathbf{S}_{uvw} = \mathbf{R}_{uvw} \mathbf{S}_{xyz} \mathbf{R}_{uvw}^T \quad (\text{D.6})$$

\mathbf{S}_{uvw} as the following form as shown in figure D.2:

$$\mathbf{S}_{uvw} = \begin{bmatrix} S_u & S_{vu} & S_{wu} \\ S_{uv} & S_v & S_{wv} \\ S_{uw} & S_{vw} & S_w \end{bmatrix} \quad (\text{D.7})$$

\mathbf{R}_{uvw} is the direction cosine of $(\vec{u}, \vec{v}, \vec{w})$ relative to $(\vec{x}, \vec{y}, \vec{z})$, which can be expressed in function of borehole dip direction and borehole deviation by the following expression:

$$\mathbf{R}_{lmn} = \begin{bmatrix} -\cos \delta \cos \phi & -\sin \delta \cos \phi & \sin \phi \\ \sin \delta & -\cos \delta & 0 \\ \cos \delta \sin \phi & \sin \delta \sin \phi & \cos \phi \end{bmatrix} \quad (\text{D.8})$$

Combining (D.3) and (D.6) permit to have a direct expression between the principal stresses and the stresses in the borehole coordinate system:

$$\mathbf{S}_{uvw} = \mathbf{R}_{uvw} \mathbf{R}_{lmn}^T \mathbf{S}_{lmn} \mathbf{R}_{lmn} \mathbf{R}_{uvw}^T \quad (\text{D.9})$$

D.2 Stress concentration around a wellbore

The drilling of the borehole induces a perturbation of the stresses. The total stress around an empty borehole is given by the Kirsch equations as following:

$$\begin{aligned}
 S_{rr} &= \left(1 - \frac{a^2}{r^2}\right) \left(\frac{S_u + S_v}{2}\right) + \left(1 + \frac{3a^4}{r^4} - \frac{4a^2}{r^2}\right) \left(\frac{S_u - S_v}{2}\right) \cos 2\theta \dots \\
 &\dots + \left(1 + \frac{3a^4}{r^4} - \frac{4a^2}{r^2}\right) S_{uv} \sin 2\theta \\
 S_{\theta\theta} &= \left(1 + \frac{a^2}{r^2}\right) \left(\frac{S_u + S_v}{2}\right) - \left(1 + \frac{3a^4}{r^4}\right) \left(\frac{S_u - S_v}{2}\right) \cos 2\theta \dots \\
 &\dots - \left(1 + \frac{3a^4}{r^4}\right) S_{uv} \sin 2\theta \\
 S_{ww} &= S_w - 4\nu \frac{a^2}{r^2} \left(\frac{S_u - S_v}{2}\right) \cos 2\theta - 4\nu \frac{a^2}{r^2} S_{uv} \sin 2\theta \\
 S_{r\theta} &= - \left(1 - \frac{3a^4}{r^4} + \frac{2a^2}{r^2}\right) \left(\frac{S_u - S_v}{2}\right) \sin 2\theta + \left(1 - \frac{3a^4}{r^4} + \frac{2a^2}{r^2}\right) S_{uv} \cos 2\theta \\
 S_{rw} &= \left(1 - \frac{a^2}{r^2}\right) (S_{vw} \sin \theta + S_{uw} \cos \theta) \\
 S_{\theta w} &= \left(1 + \frac{a^2}{r^2}\right) (S_{vw} \cos \theta - S_{uw} \sin \theta)
 \end{aligned} \tag{D.10}$$

with a being the borehole radius, r the distance to the borehole axis and θ the angle around the borehole from axis \vec{u} going to axis \vec{v} (Figure D.2). ν is the Poisson's ratio. The nomenclature of the perturbed stress state component is defined as in Figure D.2.

Considering the state of stress at the borehole wall, $r = a$, (D.10) can be simplified as following:

$$\begin{aligned}
 S_{rr} &= 0 \\
 S_{\theta\theta} &= S_u + S_v - 2(S_u - S_v) \cos 2\theta - 4S_{uv} \sin 2\theta \\
 S_{ww} &= S_w - 2\nu(S_u - S_v) \cos 2\theta - 4\nu S_{uv} \sin 2\theta \\
 S_{r\theta} &= 0 \\
 S_{rw} &= 0 \\
 S_{\theta w} &= 2(S_{vw} \cos \theta - S_{uw} \sin \theta)
 \end{aligned} \tag{D.11}$$

If the borehole is filled with a fluid at a pressure $P_p + \Delta P$, where P_p is the formation pressure and ΔP is the difference between the formation pressure and the borehole fluid pressure, equation D.11 is modified as following:

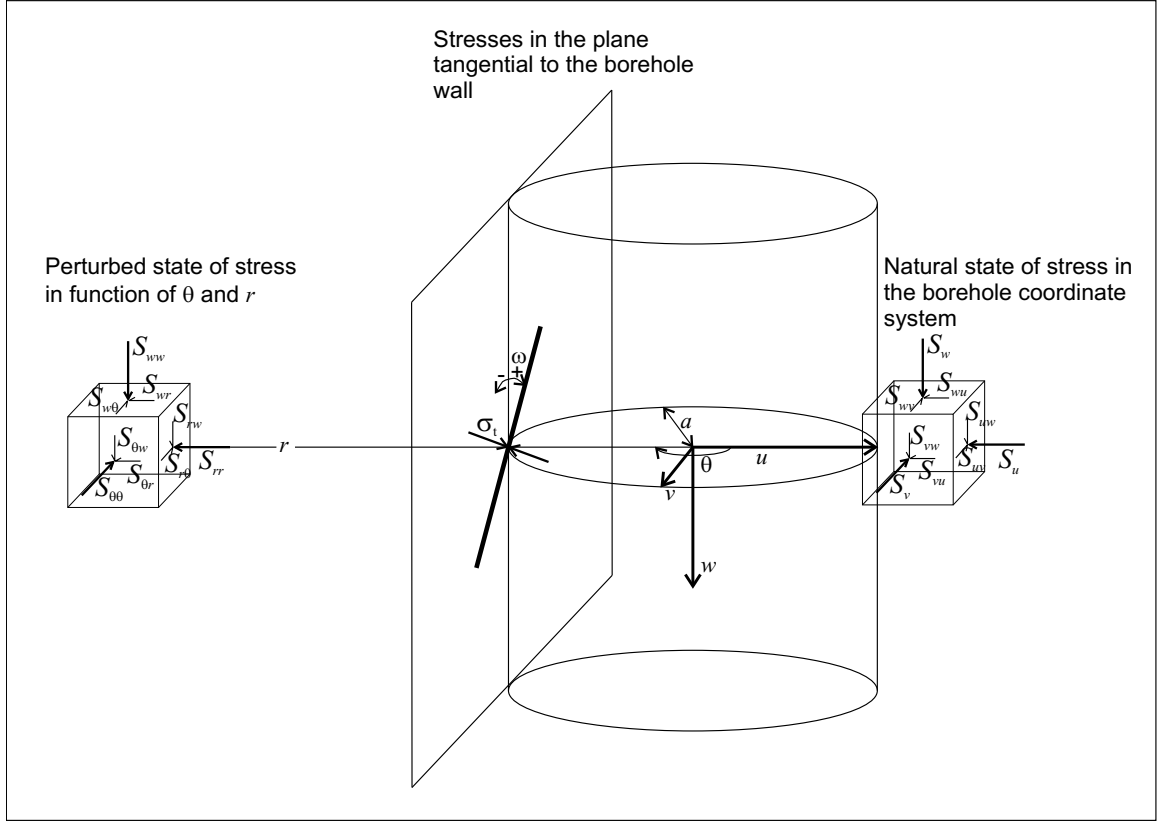


Figure D.2: state of stress around a borehole

$$\begin{aligned}
 S_{rr} &= P_p + \Delta P \\
 S_{\theta\theta} &= S_u + S_v - 2(S_u - S_v) \cos 2\theta - 4S_{uv} \sin 2\theta - P_p - \Delta P \\
 S_{ww} &= S_w - 2\nu(S_u - S_v) \cos 2\theta - 4\nu S_{uv} \sin 2\theta \\
 S_{r\theta} &= 0 \\
 S_{rw} &= 0 \\
 S_{\theta w} &= 2(S_{vw} \cos \theta - S_{uw} \sin \theta)
 \end{aligned} \tag{D.12}$$

The stresses given in equation D.12 are not necessary principal stresses as $S_{\theta w}$, a shear stress tangential to the borehole wall, is not necessary equal to zero. In order to compute the principal stress at wellbore wall, let consider the stress perpendicular to a lineament in the plane tangential to the borehole walls. This lineament makes an angle ω with the borehole axis. ω is defined between -90° and $+90^\circ$. The sign of ω is defined as on Figure D.2. The stress perpendicular to this lineament is given in

function of ω and the state of stress at borehole walls by the following equation:

$$S_t = \frac{1}{2}(S_{\theta\theta} + S_{ww}) + \frac{1}{2}(S_{\theta\theta} - S_{ww}) \cos 2\omega + S_{\theta w} \sin 2\omega \quad (\text{D.13})$$

S_t is a periodic function of ω reaching one maximum and one minimum in the $[-90^\circ 90^\circ]$. To find the minimal and maximal stresses at the borehole wall, one has to derive (D.13) after ω and solve the equation for 0, as following:

$$\dot{S}_t = -(S_{\theta\theta} - S_{ww}) \sin 2\omega + 2S_{\theta w} \cos 2\omega \quad (\text{D.14})$$

$$\begin{aligned} \dot{S}_t &= -(S_{\theta\theta} - S_{ww}) \sin 2\omega_o + 2S_{\theta w} \cos 2\omega_o = 0 \\ 2S_{\theta w} \cos 2\omega_o &= (S_{\theta\theta} - S_{ww}) \sin 2\omega_o \\ \frac{(S_{\theta\theta} - S_{ww})}{2S_{\theta w}} \tan 2\omega_o &= 1 \\ \tan 2\omega_o &= \frac{2S_{\theta w}}{(S_{\theta\theta} - S_{ww})} \end{aligned}$$

$$\begin{aligned} \omega_o^1 &= \frac{1}{2} \arctan \left[\frac{2S_{\theta w}}{(S_{\theta\theta} - S_{ww})} \right] \\ \omega_o^2 &= \frac{1}{2} \arctan \left[\frac{2S_{\theta w}}{(S_{\theta\theta} - S_{ww})} \right] + 90^\circ \quad \text{if } \omega_o^1 < 0 \\ \text{else } \omega_o^2 &= \frac{1}{2} \arctan \left[\frac{2S_{\theta w}}{(S_{\theta\theta} - S_{ww})} \right] - 90^\circ \end{aligned} \quad (\text{D.15})$$

Equation (D.15) give the angles where the stresses at the borehole wall are minimum or maximum. To know exactly which of ω_o^1 or ω_o^2 correspond to a maximum or a minimum, one has to check the result with equation (D.13).

Substituting (D.15) into (D.13) permit to calculate the magnitude of the maximum and minimum stresses tangential to the borehole wall and so the principal stress at borehole wall are given by:

$$S_t^{min} = \frac{1}{2}(S_{\theta\theta} + S_{ww}) - \frac{1}{2} \sqrt{(S_{\theta\theta} - S_{ww})^2 + 4S_{\theta w}^2} \quad (\text{D.16})$$

$$S_t^{max} = \frac{1}{2}(S_{\theta\theta} + S_{ww}) + \frac{1}{2} \sqrt{(S_{\theta\theta} - S_{ww})^2 + 4S_{\theta w}^2} \quad (\text{D.17})$$

$$S_{rr} = P_p + \Delta P \quad (\text{D.18})$$

So it is possible to compute S_t^{min} and S_t^{max} for an array of θ value in the range $[0^\circ \ 180^\circ[$ and find out θ_t where compression is minimal and θ_c where compression is maximal. Tension fracture fractures may occur at θ_t^1 and $\theta_t^2 = \theta_t^1 + 180$ with $\omega_0^2 = -\omega_0^1$. Breakouts may occur at the angles θ_c^1 and $\theta_c^2 = \theta_c^1 + 180$. Note also that $\theta_c^1 - \theta_t^1 = \theta_c^2 - \theta_t^2 = 90^\circ$.

D.3 Thermal stress component

An other component that affects the stress state at wellbore wall is the stresses induced by the cooling of the newly created borehole walls while drilling. This cooling occurs because of the circulation of cold drilling mud and it induces thermal stresses which are axisymmetric to the borehole. The temperature perturbation penetrates the rock mass with time due to thermal conduction and convection. Considering conduction only, it is possible to show (e.g. *Stephens and Voight, 1982*) that at borehole wall the induced thermal stress is not time-dependant but is function of the temperature difference and the thermo-elastic parameters only. So at borehole wall, the induced thermal stress tangential to the wellbore ($S_{\Delta T}$) is given after *Stephens and Voight (1982)* by the following equations:

$$S_{\Delta T} = \frac{\alpha_o E \Delta T}{1 - \nu} \quad (\text{D.19})$$

where α_o is the coefficient of thermal expansion. E and ν are the Young modulus and respectively the poisson ratio. If the temperature perturbation is negative (cooling) the resultant tangential thermal stress is negative, i.e. tensile.

E Fifth appendix - Strength and elastic properties of the Soultz granite

STRENGTH and elastic properties of the Soultz granite were measured in order to assess the wellbore failure. This appendix documents these tests. It is drawn from a conference paper we presented at Soultz in 2006 (*Valley and Evans, 2006b*).

E.1 Abstract

Twelve uniaxial tests were performed on Soultz granite in order to acquire its uniaxial compressive strength and static Young's modulus. Uniaxial compressive strength, a property never tested before on Soultz granite, ranges from 100 to 130 MPa for unaltered granite, and is unaffected by the strength of the pervasive alteration. One sample with significant vein alteration had a uniaxial compressive strength about 8MPa lower than the weaker unaltered sample. The Young's modulus of 'unaltered' Soultz granite is 54 ± 2 GPa, regardless of the degree of pervasive alteration. However, two samples with vein alteration showed a significantly lower modulus of 39 GPa.

E.2 Introduction and previous works

Twelve uniaxial compressive tests have been performed in order to determine some poorly known petrophysical properties of the Soultz granite: specifically, uniaxial compressive strength (*UCS*) and static Young's modulus. Although there are several determinations of Young's modulus reported in the literature, these are the first tests we are aware of that measure *UCS*.

Previous measurements of the Young's modulus on the Soultz granite are presented in Table E.1. The only direct static measurements are from *Schäfer* (1990) from triaxial tests on 20 samples with 40 MPa confinement. Thirteen of them show no evidence of a type of hydrothermal alteration described later and referred to as 'vein alteration'. Such samples without vein alteration are usually called 'unaltered', although they invariable host a second type of alteration which will be referred to as 'pervasive alteration'. The mean E-modulus of samples without vein alteration was

Table E.1: Literature review of E-modulus determinations of Soultz granite

	Source	Type of measurement	Nb of data	E-mod [GPa] mean±std /min/max	
Static modulus	Schäfer (1990)	Triaxial – 40MPa confinement	without vein alt.	13	49±4 / 43 / 56
			with vein alt.	4	30±14 / 14 / 48
	Rummel, et al. (1989)	Three point bending test on 62mm cores	without vein alt.	28	73±6 / 57 / 86
			with vein alt.	1	53
		Three point bending test on 30mm cores	without vein alt.	16	70±6 / 57 / 80
			with vein alt.	7	53±4 / 45 / 58
Dynamic modulus	Schäfer (1990)	Ultrasonic velocity measurement on dried cores		20	62±5 / 44 / 69
		Ultrasonic velocity measurement on saturated cores		14	88±4 / 86 / 94
	Rummel & König (1991)	Ultrasonic velocity measurement on cores		335	64±8 / 24 / 99
	Rummel, et al. (1992)	Ultrasonic velocity measurement on cores		4	71±5 / 63 / 76
	Rummel & Schreiber (1993)	Ultrasonic velocity measurement on cores	radial	8	65±10 / 46 / 84
			Axial	6	59±6 / 53 / 70
	Schlumberger sonic and density between 1949 and 3492 m in GPK1				73±9 / 26 / 106

49±4 GPa. Schäfer (1990) also tested four samples which showed vein alteration and found a lower Young’s modulus of 30±14 GPa. Rummel et al. (1989) derived static Young modulus from three points bending test on 62 mm and 30 mm diameter samples. Their summary makes no mention of the Young’s modulus results of their tests on 60mm cores, but gives 83±4.7 GPa for their tests on 30 mm core. This appears to be in error as the highest value of Young’s modulus listed in their results table is 80 GPa. Rummel (1991) later summarised the results of the 3-point bending tests and reports that the static Young’s modulus of 29 tests was 38.0±8.5 MPa. This also appears to be in error as the smallest value in the dataset is 51 GPa. To clarify the situation, the mean and single standard deviation of the Young’s modulus values listed in the results tables of Rummel et al. (1989) were computed. For 28 tests on 62 mm granite samples without vein alteration, the static Young’s modulus was 73±6 GPa, whereas for 16 tests of 30 mm granite samples without vein alteration, the value was 70±6 GPa. Rummel et al. (1989) also conducted a few tests on samples with vein alteration. All tests yielded values lower than obtained for unaltered samples. One test on the 60 mm diameter samples yielded an value of 53 GPa, and seven on 30 mm samples gave values of 53±4 GPa.

The dynamic Young’s modulus of the Soultz granite has been estimated from p-

and s-wave velocity and density measurements derived either from laboratory tests or borehole logs. *Schäfer* (1990) performed measurements on 20 dry and 14 saturated cores in unconfined conditions and report values of 62 ± 5 GPa and 88 ± 4 GPa, respectively. *Rummel and König* (1991) made measurements on 335 granite cores taken from borehole EPS1 between the granite top to 2227 m and found an E-modulus of 64 ± 8 GPa. *Rummel and Schreiber* (1993) measured p- and s-wave velocities in the axial and radial directions on granite core sample K21 taken from borehole GPK1 (3522.58-3525.88 m depth). These permit to highlight a slight anisotropy in the P- and S- wave velocities leading to lower axial E-modulus than radial E-modulus, i.e. 59 ± 6 GPa and 65 ± 10 GPa respectively. Dynamic elastic moduli have also been derived by combining precisely depth-matched sonic and density logs in well GPK1 over the depth interval 1949 to 3492 m. The average E-modulus between 1950 m and 3500 m was found to be 73 ± 9 GPa with values dipping as low as 30 GPa within cataclastic shear zones where vein alteration is strongly present. The values in sections relatively free of vein alteration zones typically ranged between 73 GPa and 80 GPa. These values generally agree with the laboratory estimates of dynamic modulus if the stiffening effects of saturation are taken into consideration. They are also in agreement with the static E-modulus estimates derived from the 3-point bending tests, but not with the values from triaxial tests which are significantly lower. Generally speaking, static E-modulus values are usually substantially lower than the dynamic values, and so the results of the 3-point bending are somewhat surprising. Thus, the direct measurements of Young's modulus presented in this report are of some considerable interest.

E.3 Sample description and preparation

Twelve 78 mm diameter core pieces of the Soultz granite were tested under uniaxial compression. The samples were selected to represent various type and degrees of alterations. The details of the samples, including alteration type and degree, and the core identification numbers and depths of origin, are given in the six first columns of Table E.2.

As noted earlier, the samples are affected by two different types of alteration called 'pervasive' and 'vein alteration' (*Genter and Traineau, 1992*). The pervasive alteration is a very early event that is probably related to reactions with magmatic fluids. It affects all of the granite so far explored at the Soultz site. This alteration is characterized by low grade alteration of biotite to chlorite and plagioclase to epidote (saussuritization). K-Feldspars are also affected and become reddish. Rock texture is not modified. The second type of alteration, vein alteration, is related to hydrothermal fluid circulation within fractures. It is characterized by the illitization of biotite and plagioclases, which usually imparts a yellowish color to the granite. Fractures which show vein alteration are sealed with quartz (occasionally geodic), calcite, illite,

Table E.2: Properties of samples

Sam- ple n°	Core n°	Core piece n°	Core piece btm depth [m]	Perv- asive alt.	Vein alt.	UCS	Eavg	Emin	Emax	Comments
1	K136	3270	1792.10	L	N	invalid test				
2	K136	3275	1794.72	L	N	131.14	invalid test			Failure not influenced by pre-existing cracks
3	K136	3279	1796.02	L	N	123.13	56.15	49.35	63.71	Failure not influenced by pre-existing cracks
4	K157	3794	1950.76	L	N	109.05	51.57	48.22	67.08	Failure not influenced by pre-existing cracks
5	K162	3914	1987.37	L	N	105.75	52.78	48.14	57.69	Failure not influenced by pre-existing cracks
6	K149	3634	1902.58	H	L	89.10	52.42	48.37	60.64	Failed along pre-existing cracks
7	K149	3628	1901.08	H	L	109.62	52.63	46.37	59.38	Failure not influenced by pre-existing cracks
8	K163	3933	1993.60	L-M	N	invalid test	55.88	50.00	61.88	Failure occurred in two load step with unloading in between. Then UCS is not reliable.
9	K107	2744	1626.00	M	L	101.52	54.98	45.70	59.07	Failed along pre-existing cracks
10	K113	2853	1657.63	M	M	98.28	39.24	34.19	48.87	Failure not influenced by pre-existing cracks
11	K101	2638	1598.78	M	N	129.66	58.35	47.39	61.35	Failure not influenced by pre-existing cracks
12	K113	2846	1656.57	H	H	65.47	39.81	33.24	47.38	Failed along pre-existing cracks

chlorite, sulfides, barite or hematite.

The degree to which the samples are affected by each of the two alteration types is indicated by four levels: ‘none’ (N), ‘low’ (L), ‘medium’ (M) or ‘high’ (H). The definition underlying this grading is given in Table E.3, and the grades for each sample listed in Table E.2.

The samples were prepared from the original 78 mm diameter cores by sawing them to length and grinding the ends to produce a right circular cylinder that was as close as possible to the ISRM norms (*Bieniawski and Bernede, 1979*). Two specifications of this norm were occasionally not quite attained: (1) the specification that the size of the largest grain in the rock should be related to the sample diameter with a ratio of at least 10:1. In the case of the Soultz granite with decametric K-Feldspath porphyroclasts this wasn’t possible. (2) The specifications concerning the perpendicularity of the sample faces with the axis, and the mutual parallelism of the two faces could not quite be achieved for samples 2 and 4, although they was met for the other samples. This reflects the difficulty of machining heterogeneous materials like

Table E.3: Classification of alteration

Pervasive alteration	
None (N)	Unaltered biotite K-Feldspar and plagioclase. This case is never met.
Low (L)	Biotites are black showing only little alteration into chlorite, plagioclases are milky and K-feldspars are grey or pink.
Medium (M)	Biotites become greenish showing advanced alteration into chlorite, plagioclase show beginning of greenish coloring reflecting alteration in epidote and K-Feldspars are less pink and more reddish.
High (H)	Biotites are totally transformed into chlorite, plagioclases are dark green trough transformation in epidote and K-Feldspars are reddish to orange.
Vein alteration	
None (N)	No visible trace of vein alteration.
Low (L)	Small fractures present a yellowish halo of vein alteration which does not penetrate the whole sample.
Medium (M)	Former biotites and plagioclases are yellowish, reflecting alteration to illite. No major fractures cross the sample.
High (H)	The sample is traversed by fractures and biotites and plagioclases are totally altered to illite.

the Soultz granite. However, the deviation of samples 2 and 4 from the norms was not considered to be large enough to significantly influence the test results.

E.4 Tests description

The tests were performed at constant strain-rate of about 0.075mm/min and comprised three loading cycles (Figure E.1). The first cycle extended to about 1/3 of the expected UCS , the second to about 2/3 of UCS ; and the third continued until the sample failed. Each test took 30 to 40 minutes to perform. Unfortunately, samples 1 and 2 were tested with incorrect strain measurement settings and so it was not possible to estimate the Young's modulus of these samples. Moreover, the loading rate for sample 1 was too fast and so the UCS measurement is not considered valid.

All samples except sample 8 were tested on a loading frame where axial shortening was measured by displacement sensors on either side of the loading platens. For practical reasons, steel cylinders were placed between the loading frame platen and the sample (Figure E.2). Thus, to determine the displacement across the sample it is necessary to remove the displacements across the steel cylinders and the interfaces. Once this was done, the sample strain was determined by dividing net sample length change by the sample length. Sample 8 was tested on another machine which allowed the sample axial strain to be directly measured with clip-on 'blade' strain gages. This permitted a comparison of results and a check calibration.

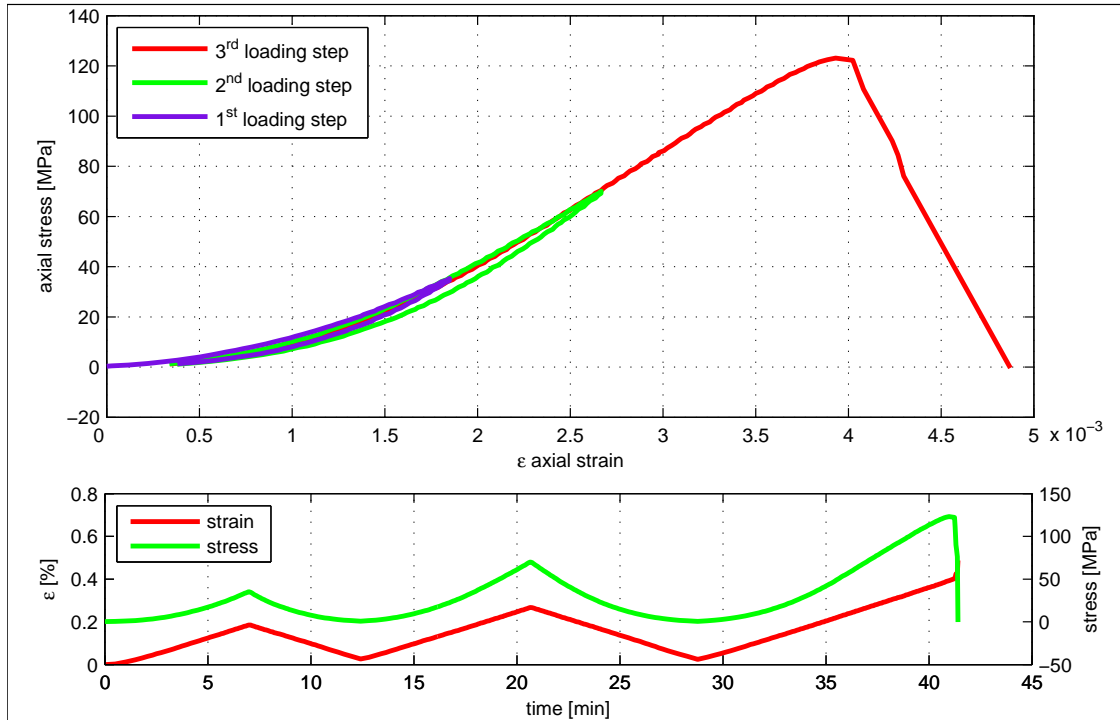


Figure E.1: Example of a test record for sample 3. The upper frame shows axial stress vs. axial strain for the 3 loading/unloading cycles performed during the test, each of which is shown with a different colour. The lower frame presents the history of stress (green) and strain (red) during the test. It is evident that the test is strain controlled as the strain curve has precisely linear segments, in contrast to the axial stress curve (in green).

UCS was taken as being the highest stress value obtained during the testing of each samples. Three different Young Modulus estimates were determined from the slopes of the strain-stress curves. The one called E-average is taken as the slope of the linear part of the last loading cycle. E-min corresponds to the slope of the curve at the end of the last but one loading cycle. This is always slightly less than E-average. E-max is the slope of the curve at the beginning of the last unloading cycle. This is always slightly more than E-average. This procedure provides a realistic range for the Young's modulus value which includes all other candidate E-modulus estimators such as the secant modulus.

E.5 Calibration and corrections of E-modulus

As noted earlier, the estimation of axial sample strain from axial displacement of the platens requires the effect of steel cylinders at the end of the sample to be removed.

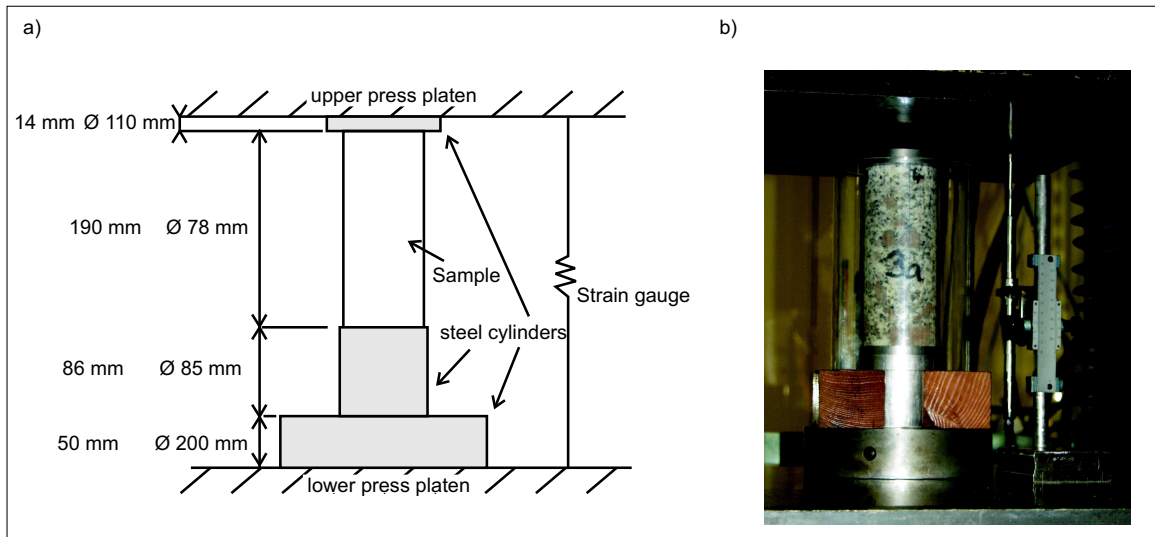


Figure E.2: a) sketch of the test settings b) picture of sample 3 just before testing. The steel cylinder can be seen below the sample.

This correction is not a trivial matter as the geometry of the cylinders is not precisely the same as the sample. Moreover, the compliance of the various interfaces in the load train also enters into the calculation but is unknown. To keep the analysis simple, we make the initial hypothesis that the effects of the interfaces are negligible, and that the diameters of the sample and cylinders are identical which is not the case as one can see on the sketch of Figure E.2a. The validity of these assumptions will be checked later. In the simplified case, the E-modulus of the complete stack can be expressed as a function of the E-modulus of each stack element and their length by:

$$\frac{l_{tot}}{E_{tot}} = \frac{l_1}{E_1} + \frac{l_2}{E_2} + \frac{l_3}{E_3} + \dots \quad (\text{E.1})$$

The E-modulus of the steel is precisely known as 210 GPa, and the lengths of the sample and steel cylinders are also known. Thus, the E-modulus of the sample can be estimated.

The validity of the assumptions made in obtaining the estimates was checked in two ways. First, the axial strain on sample 8 was measured relatively directly and so the concerns arising from the steel cylinder corrections do not apply. The E-modulus of this unaltered granite sample was in good agreement with the corrected E-modulus of the other unaltered granite samples. Second, and more definitively, a sample of fused quartz was tested in the load frame with the steel cylinders. The E-modulus of this sample was precisely known as 74 GPa (i.e. the E-modulus for crystal quartz). The estimate of E-modulus obtained from equation 1 for this sample was 73.7 GPa, which is within 1% of the true value. Thus, we conclude that the

simplifying assumptions inherent in equation E.1 do not have a significant effect of the resulting E-modulus estimates.

E.6 Results and discussion

E.6.1 Uniaxial compressive strength

The estimates of *UCS* obtained from the tests are listed in column 7 of Table E.2 and are plotted in Figure 3a and 4a. In interpreting these values it is important to know whether sample failure involved the fracture of ‘intact’ rock or activation of a preexisting fracture. This information is given in column 11 of Table E.2, and is included in Figure 3a and 4a by distinguishing points relating to activation of a pre-existing feature by open circles. Evidently, all but three tests involved the failure of intact rock. The *UCS* values obtained for these ‘intact rock failure’ samples ranged between 98.3 MPa and 131.1 MPa.

The relation between the *UCS* of samples which involved failure of intact rock and alteration grade is shown in Figure 4a. Samples with no vein alteration have relatively high *UCS* values ranging between 105.8 MPa and 131.1 MPa, regardless of whether the degree of pervasive alteration is high or low. Of the samples that involved intact rock failure, only sample 10 has a significantly high degree of vein alteration, and this has a *UCS* of 98.3 MPa, which is 8 MPa lower than the weakest sample without significant vein alteration. The result is consistent with the hypothesis that vein alteration tends to reduce the *UCS*, although more tests would be needed to establish this.

Three samples (6, 9 and 12) failed through the activation of a pre-existing fracture which was favourably-oriented for shear failure. In two of these cases (6 and 9), the pre-existing fractures were sealed by quartz, and the *UCS* values of 89.1 and 101.5 MPa were relatively high. In contrast, the pre-existing fracture that failed in sample 12 had a black sealing, probably made of sulfide, and was much weaker, with a *UCS* of 65.47 MPa.

The *UCS* estimates obtained in this study cannot be compared with literature values as none exist. All that can be said is that the estimates lie in the lower range of values typical of granites, which may be due to the porphyric nature of the Soultz granite.

E.6.2 Young’s modulus

The estimates of Young’s modulus for all samples except 10 and 12 range between 50 and 60 GPa with a mean and single standard deviation of 54.2 GPa. Samples 10 and 12 are the only samples with significant vein alteration (i.e. medium or high grade), and their Young’s modulus is 39 GPa, which is much lower.

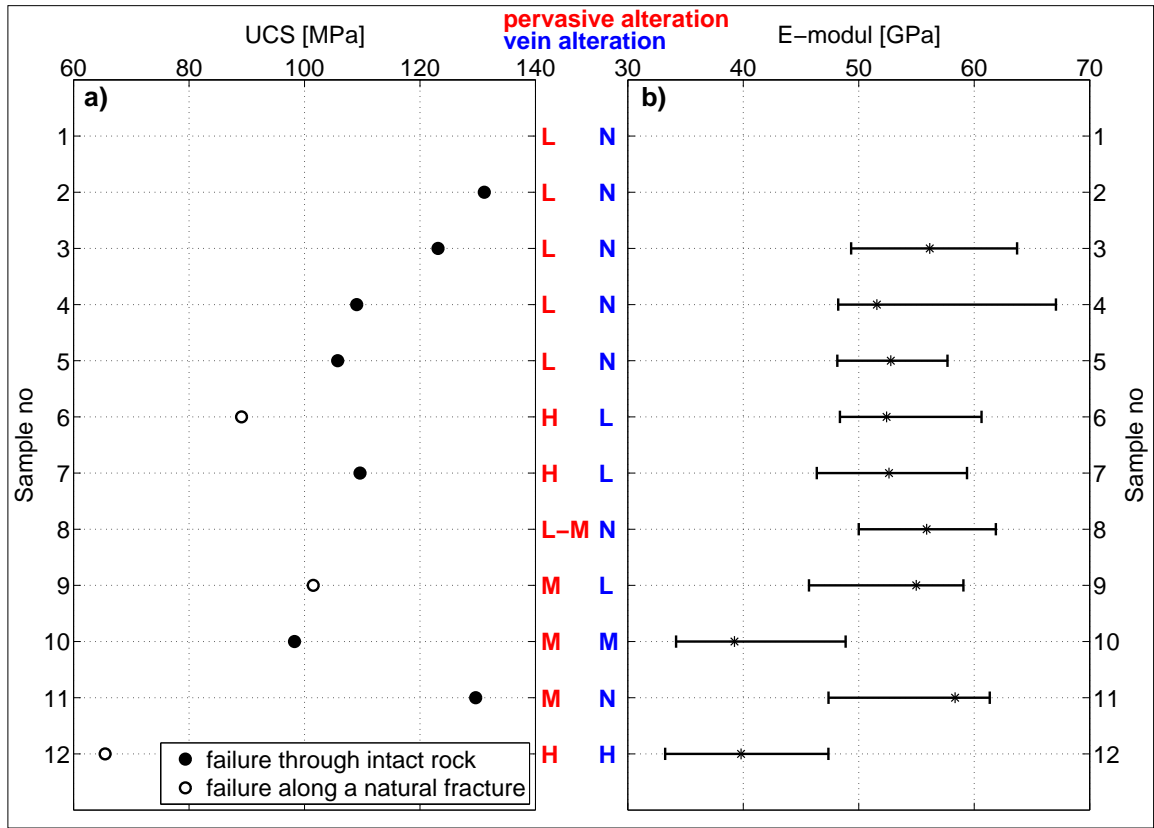


Figure E.3: Illustration of the test results. a) Results for UCS . Failure of intact rock or activation of a natural fracture are denoted by close and open circles respectively. The letters in the middle of the figure denote the degree of pervasive and vein alteration. b) Results for E-modulus. The ranges extend from E_{min} to E_{max} and the stars denote E_{avg} .

The E-modulus estimates obtained in this study are in reasonable accord with the values obtained by Schäfer (1990) from triaxial tests with 40 MPa confining pressure (see Table E.1). Our estimates (and those of Schäfer) are significantly lower than the values reported by Rummel *et al.* (1989) from three-point bending tests. Given that our estimates and those of Schäfer constitute direct measurements of Young's modulus, whereas those of Rummel *et al.* (1989) are indirect, it would appear that the latter are affected by some form of systematic error. A corollary of this is that the static E-modulus of the Soultz granite is of the order of 30% lower than the dynamic E-modulus, which is consistent with the literature (e.g. Eissa and Kazi, 1988). Finally there can be no doubt that rock which has suffered from vein alteration has a lower Young's modulus. This has been found in all tests, regardless of whether they measure static and dynamic modulus.

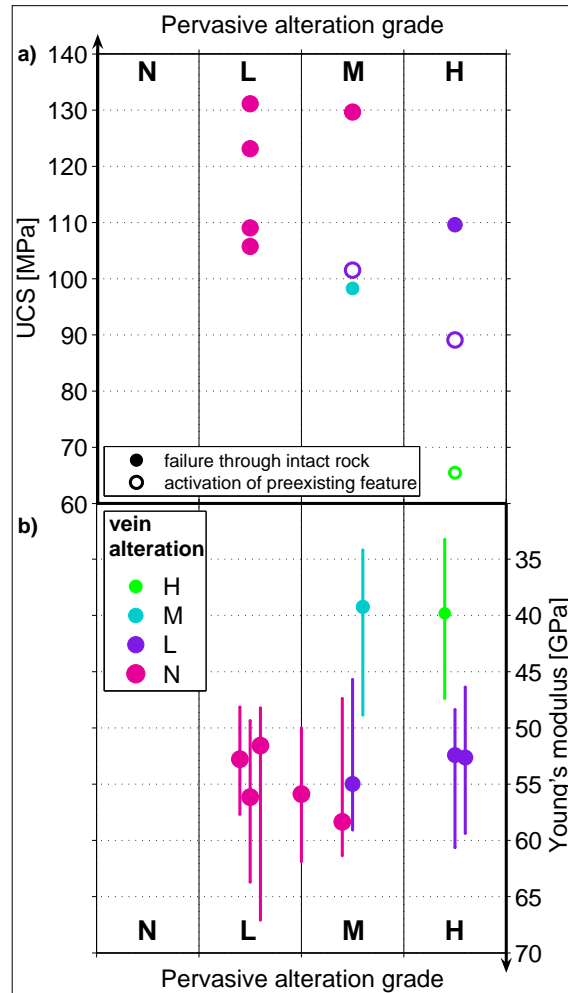


Figure E.4: Illustration of the effect of the two types of alteration on the test results. The degree of pervasiveness is indicated by the column, and the degree of vein alteration is denoted by both the colour and the size of the circles a) Results for UCS . Tests where sample failure occurred in intact rock are denoted as closed circles whereas those that involved activation of a natural fracture are indicated by open circles. b) Results for E-modulus. The ranges extend from E_{min} to E_{max} , and the circles denote E_{avg} .

E.7 Conclusions

The *UCS* of unaltered Soultz granite ranges between 100 and 130 MPa. Pervasive alteration does not appear to affect the strength of the granite. However, limited data suggests that the presence of vein alteration may reduce the strength slightly, although the data are too few to establish this firmly. The test also show that fractures with quartz sealing can be almost as strong as the intact rock. However, one sample that had a favorably oriented fracture filled with a dark material that was probably sulfide failed at about 65 MPa. The static Young's Modulus of Soultz granite that has suffered little or no vein alteration is 54 ± 2 GPa (average and single standard deviation of 8 samples). Two samples with significant vein alteration show substantially lower values of about 39 GPa. The static E-modulus of rock without vein alteration is about 75% of the estimates of dynamic E-modulus derived from both lab testing and wireline logs.

Acknowledgments

Thanks are due to Erich Pimentel and Thomas Jaggi from IGT-ETH Zürich for the help in performing of the tests. We are grateful to Jean-François Mathier and Laurent Gastaldo from LMR-EPF Lausanne who helped with the sample preparation.

Curriculum Vitae

Benoît Christian Valley



Personal Data

date of birth March 2, 1979
place of birth Boudeviliers, Switzerland
citizen of Chevenez (JU), Switzerland

Benoît Valley obtains his first degree in 2002 in the University of Neuchâtel (Switzerland). He wrote his Diploma thesis under the direction of Prof. Martin Burkhard. The topic was 3D modelling and restoration of non-cylindrical folds in the Jura Fold and Thrust belt. Since 2002, he works in the group of Engineering Geology of ETH Zürich. His first project was related to the characterization and modelling of a shallow landslide in soil. In 2007, he candidates to complete his PhD study on the thematic of fracture network and stress characterisation in the 5 km deep seated granite of Soultz-sous-Forêts (European geothermal project).

Education and Stages

2004–2007 ETH Zürich, Geological Institute, Engineering Geology. PhD thesis in the group of Prof. S. Löw.
2002–2004 ETH Zürich, Geological Institute, Engineering Geology. Junior researcher with project related to slope stability.
1997–2002 University of Neuchâtel, Geological Institute. Studies in earth sciences and Diploma thesis with Prof. M. Burkhard.

- 1994–1997 High school in Neuchâtel.
1985–1994 Elementary and secondary School in Neuchâtel.

Titles

- 2002 Diploma BeNeFri in earth sciences, section geology, with ‘mention très bien’ and awarded with the prizes Jean Landry and Bernard Kübler.
1997 Swiss Federal Maturity type C (scientific) with ‘mention bien’ and price in French Literature.

Projects

- Soultz-sous-Forêts Benoît Valley has been involve in that project from 2004 to 2007 and wrote his PhD thesis with data from that project. He has been involved in the characterisation of the natural fracturing as well as the stress induced wellbore failure on acoustic borehole images.
- GeoPower Basel Benoît Valley has been involved in the Geothermal Project GeoPower Basel for a short term consulting contract in 2006. The goal was to characterise the state of stress from detailed analysis of stress induced wellbore failure.
- Lutzenberg The two year project Lutzenberg aimed to analyse the causes of a shallow soil slide which took place in 2002 in Switzerland. This project involved Benoît Valley into geotechnical mapping, soil characterisation on field and in laboratory, geological model building and numerical modelling. That project was founded by the Swiss Geological Survey.
- TDR In 2003, Benoît Valley has been also involved in the proposal writing for a project aiming to use the TDR technology to monitor landslides.
- Teaching From 2002 to 2007, Benoît Valley has been active in teaching tasks within the Geological Institute of ETH Zürich. He has been responsible for practicals and field courses in Engineering Geology.

Swiss Virtual Campus Benoît Valley participated to the project objectif terre (<http://objectif-terre.unil.ch/>) part of the Swiss Virtual Campus project, a e-learning project of the Swiss federal government.

Vallée des Ponts Benoît Valley wrote is Diploma thesis on the project Vallée des Ponts. The aims and tasks realised were geological mapping and modelling, 3D-structural modelling and tectonic interpretations.